

Thermostructural Problem of Hypersonic Airbreathing Flight Systems – Modeling and Simulation

Christian Messe

**INSTITUT FÜR
STATIK UND DYNAMIK
DER LUFT- UND
RAUMFAHRTKONSTRUKTIONEN**

UNIVERSITÄT STUTTGART

Thermostructural Problem
of
Hypersonic Airbreathing Flight Systems
—
Modeling and Simulation

A thesis accepted by the Faculty of Aerospace Engineering and Geodesy of the University of Stuttgart in partial fulfillment of the requirements for the degree of Doctor of Engineering Sciences (Dr.-Ing.)

by

Christian Messe

born in Stuttgart, Germany

main referee: Prof. Dr.-Ing. habil. Bernd Kröplin

co-referee: Prof. Dr.-Ing. Thomas Wallmersperger

date of defense: August 4th 2017

Institute of Statics and Dynamics of Aerospace Structures
University of Stuttgart

2017

D93

ISBN 978-3-942807-05-0

Dieses Werk ist urheberrechtlich geschützt. Die dadurch begründeten Rechte, insbesondere die der Übersetzung, des Nachdrucks, des Vortrags, der Entnahme von Abbildungen und Tabellen, der Funksendung, der Mikroverfilmung oder der Vervielfältigung auf anderen Wegen und der Speicherung in Datenverarbeitungsanlagen, bleiben, auch bei nur auszugsweiser Verwertung, vorbehalten. Eine Vervielfältigung dieses Werkes oder von Teilen dieses Werkes ist auch im Einzelfall nur in den Grenzen der gesetzlichen Bestimmungen des Urheberrechtsgesetzes der Bundesrepublik Deutschland vom 9. September 1965 in der jeweils geltenden Fassung zulässig. Sie ist grundsätzlich vergütungspflichtig. Zuwiderhandlungen unterliegen den Strafbestimmungen des Urheberrechtsgesetzes.

© Institut für Statik und Dynamik der Luft- und Raumfahrtkonstruktionen,
Universität Stuttgart, Stuttgart, 2017

Dieser Bericht kann über das Institut für Statik und Dynamik der Luft- und Raumfahrtkonstruktionen, Universität Stuttgart, Pfaffenwaldring 27, 70569 Stuttgart, Telefon: (0711) 6856-63612, Fax: (0711) 6856-63706, bezogen werden.

Acknowledgment

I have learned to use the word 'impossible' with the greatest caution.

–Wernher von Braun

THIS work was created during my time at the German Research Training Group GRK 1095 and the Institute of Statics and Dynamics of Aerospace Structures at the University of Stuttgart, Germany. It might be impossible to thank all the people that have advised and supported me during the years. Nevertheless, it shall be tried in the following:

I'd like to thank my supervisor Prof. Bernd Kröplin, who taught me the bravery and Prof. Thomas Wallmersperger, who taught me the diligence needed to conduct this work, as well as Prof. Reinhard Reichel for his support and advice, and for being a great boss.

From NASA, I'd like to thank Helen J. Hall for her efforts and advice, and from the former research training group, I'd like to thank Prof. Bernhard Weigand, for his dedication as project leader and his useful comments on my documentation, and Johannes Groß, Daniel Kliche, Oana Petrache and Birgit Reinartz for the productive work and the good times we had.

From the Institute of Aircraft Engines, I'd like to thank Prof. Stephan Staudacher for being a great mentor, Manfred Zippel and Martin Rose for the interesting and motivating discussions, and Martin Marx and Björn Weigel for their constant support, and for being great friends. Same goes for Dave T. Haslam from the Space Systems institute.

From my former students, I'd like to point out Eva Weißbecher, Stefano Ruberto, Tim Belschler, Moritz Geiger and Matthias Schuff for their inspiring ideas, and thank them for their good work.

From the Institute of Statics and Dynamics of Aerospace Structures, I'd especially like to thank Gunther Faust, Manfred Hahn, H. Matthias Deuschle, Karsten Keller, Andrea Berghammer and Stephan Rudolph and the group of data processing for the interesting and insightful discussions, and the good time, Sabine Brüßing for helping me out with the English language, and Rafael Jarzabek and Michael Reck for being great colleagues that I felt honored to work with, and privileged to call my friends.

This institute and its people have been my home for a long time, and although I am happy for the new things to come, leaving such a place is tough. Nevertheless, it feels good to know that following a long lean spell of a vacant chair, a new head and team is taking over. I believe that with Prof. Tim Ricken, Lena Lambers, Lukas Moj and the others, the institute and its students are in very capable hands, and I wish them all the best for the future.

Finally, I'd like to thank my brother Adrian and my mom Renate for being there.

Stuttgart in November 2017

Christian Messe

Contents

Nomenclature	xviii
Kurzfassung	xxiii
Abstract	xxv
1. Introduction	1
1.1. Scramjet Working Principle	1
1.1.1. Process Cycle Reference States	2
1.1.2. Hypersonic Flight Corridor and Total Temperature	3
1.2. Historical Overview	5
1.2.1. World War II and Before	6
1.2.2. Flight Experiments and Research During the Space Race	6
1.2.3. Conceptual Studies During the 1980s	6
1.2.4. Post Cold War Flight Experiments	7
1.2.5. Post Cold War Basic Research in Germany	8
1.2.6. Hypersonic Flight in the Present and the Near Future	9
1.3. Motivation	10
1.3.1. Application as Airbreathing Space Transportation System	10
1.3.2. Fuel Budget Example for a Space Transportation System	10
1.3.3. Purpose of This Work	12
1.4. Scramjet Thermal Management: State of the Art	12
1.4.1. Overview over Considerable Cooling Concepts	12
1.4.2. Cooling Concepts of Flown and Upcoming Vehicles	15
1.4.3. Scramjet Thermal Management: Literature for Consideration	15
1.5. Structure of This Work	16
2. Aerothermodynamic Fundamentals	19
2.1. Governing Equations and Physical Quantities	20
2.1.1. Fluid Equations of State	20
2.1.2. Thermodynamic Coefficients	21

2.1.3.	Caloric Properties of Pure Fluids	22
2.1.4.	Isentropic State Transition and Total States of Moving Fluids	24
2.1.5.	Transport Properties of a Newtonian Fluid	26
2.1.6.	Conservation Equations for a Flow Field	27
2.1.7.	A Note on Numerical Solving of the Navier-Stokes Equations	28
2.1.8.	Similarity Parameters in Aerothermodynamics	30
2.2.	Boundary Layer Theory and Heat Transfer	35
2.2.1.	Naming Conventions in this Section	36
2.2.2.	Boundary Layer Thicknesses	38
2.2.3.	Laminar Incompressible Flat Plate	39
2.2.4.	Laminar Compressible Flat Plate	40
2.2.5.	Turbulent Incompressible Flat Plate	41
2.2.6.	Turbulent Incompressible Channel Flow	44
2.2.7.	Turbulent Compressible Flat Plate Problem	45
2.2.8.	Turbulent Compressible Channel Flow	47
2.2.9.	Channel Differential Equations	55
2.3.	Compression and Expansion Shocks	58
2.3.1.	Normal Compression Shocks	58
2.3.2.	Oblique Compression Shocks	58
2.3.3.	Prandtl-Meyer Expansion	61
3.	Combustion and Radiation	63
3.1.	Combustion Modeling	63
3.1.1.	Chemical Kinetics	63
3.1.2.	Modeling of Fuel Injection	66
3.2.	Thermal Radiation Fundamentals	66
3.2.1.	Emissivity, Absorbitivity and Reflectivity of Technical Surfaces	66
3.2.2.	Surface Visibility	68
3.2.3.	Interaction of Multiple Surfaces	69

4. Finite Element Method	71
4.1. Thermal Field Formulation	71
4.1.1. The Weak Formulation of the Thermal Energy Balance . . .	71
4.1.2. Finite Element Discretization of the Thermal Energy Balance	72
4.1.3. Backward Euler Time-stepping	73
4.2. Mechanical Field Formulation	74
4.2.1. Weak Formulation of the Momentum Balance	74
4.2.2. Hooke's Law, Engineering Strains and Voigt Notation . . .	75
4.2.3. Hooke's Law with Thermal Deformation	77
4.2.4. Finite Element Discretization	78
4.2.5. Stress Calculation	79
5. Inlet Heat Load Investigation	81
5.1. Introduction	81
5.2. General Thoughts on Regenerative Cooling	83
5.3. CFD Simulation	86
5.3.1. Investigation of Unstarting Behavior	86
5.3.2. Similarity Parameters for Thermal Heat Loads	87
5.3.3. Verification of the Perfect Gas Approach	90
5.3.4. Investigation of the External Flow Field around the Cowl . .	92
5.4. Finite Element Simulation	94
5.4.1. Simulation of Uncooled Configuration	94
5.4.2. Simulation of Regeneratively Cooled Configuration	94
5.5. Discussion of Results	95
5.6. Modeling Limitations	96
6. Combustor Heat Load Investigation	99
6.1. Geometry Definition	99
6.1.1. Combustor Geometry Definition and Fuel Injection	99
6.2. Central Injector	100
6.3. Code Validation	103
6.4. Finite Element Simulation	108

7. Cooling Channel Investigation	115
7.1. Modeling Problems and Thermal Boundary Conditions	115
7.2. Mechanical Bearing	118
7.3. Thermal Stress Calculation	119
8. Conclusion and Outlook	127
A. Finite Element Formulation	131
A.1. Definition of Shape Functions	131
A.2. Numerical Integration and Differentiation	134
A.3. Spatial Derivatives in Finite-Element-Analysis	135
B. Material Characterization of C/C-SiC	136
B.1. The Problem of Mechanical Modeling of C/C-SiC	136
B.1.1. The Self-Consistent Homogenization Approach	137
B.1.2. Modeling of Fiber Degeneration	139
B.1.3. Modeling of Matrix Degeneration	140
B.1.4. Mechanical Properties of the Composite	141
B.2. Tsai-Wu Failure Criterion for C/C-SiC	142
B.3. Thermal Conductivity of C/C-SiC	144
B.4. Specific Heat Capacity of C/C-SiC	145
B.5. Thermal Expansion of C/C-SiC	146
C. Caloric and Transport Properties of Dry Air	147
C.1. Caloric Properties of Dry Air	147
C.2. Transport Properties of Dry Air	148
D. Inlet Design Methodology	149
E. Hydrogen–Air Combustion Mechanism	154
Bibliography	181

Nomenclature

Acronyms

Symbol	Description
CFRP	carbon fiber reinforced plastic
DARPA	Defense Advanced Research Projects Agency
DLR	Deutsches Zentrum für Luft- und Raumfahrt
DNS	direct numerical simulation
FEM	finite element method
GRK	Graduiertenkolleg (German Research Training Group)
HIFiRE	Hypersonic International Flight Research Experimentation
HOTOL	Horizontal Take-off and Landing Satellite Launcher
ISD	Institut für Statik und Dynamik
LEO	low Earth orbit
LES	large eddy simulation
NASA	National Aeronautics and Space Administration
NASP	National Aero-Space Plane
PAN	polyacrylonitrile (resin used in the production of carbon fibers)
PTAH-SOCAR	Paroi Tissée Application Hypersonique - Simple Operational Composite for Advanced Ramjet
RANS	Reynolds averaged Navier stokes simulation

SAE	Society of Automotive Engineers
SFB	Sonderforschungsbereich (German Research Collaborative Center)
SHEFEX	Sharp Edge Flight Experiment
SLV	Small Launch Vehicle
SPARTAN	Scramjet Powered Accelerator for Reusable Technology Advancement
SSTO	single-stage-to-orbit
TSTO	two-stage-to-orbit
UML	Unified Modeling Language
USAF	United States Air Force

Greek Symbols

Symbol	Description	Dimensions	Units
α	α -function for cubic EOS, see (2.2)	—	—
α	angle	—	rad
α	isobaric thermal expansion	Θ^{-1}	K^{-1}
α	tangent thermal expansion coefficient, see Eq. (4.34)	—	—
β	angle	—	rad
β	isochoric stress coefficient	Θ^{-1}	K^{-1}
δ	boundary layer thickness, see Eq. (2.62)	L	m
δ^*	displacement thickness, see Eq. (2.59)	L	m

$\dot{\eta}$	area specific emitted radiation load	$M T^{-3}$	$W m^{-2}$
$\dot{\upsilon}$	area specific incident radiation load	$M T^{-3}$	$W m^{-2}$
$\dot{\omega}$	area specific Planck radiation	$M T^{-3}$	$W m^{-2}$
ϵ	mean spectral emissivity	—	—
η	efficiency	—	—
η_{comb}	combustion efficiency	—	—
$\eta_{\text{mix,inj}}$	fuel mixing efficiency of injector	—	—
γ	adiabatic exponent, see Eq. (2.19ff)	—	—
γ	engineering shear strain (elastic), see Eq. (4.25)	—	—
λ	specific heat conductivity	$L M T^{-3} \Theta^{-1}$	$W m^{-1} K^{-1}$
κ	isothermal compressibility	$L T^2 M^{-1}$	Pa^{-1}
κ	von Kármán constant	—	—
λ	wavelength	L	m
Γ	Kelvin-Christoffel stiffness, see Eq. (B.5)	$L^{-1} M T^{-2}$	Pa
μ	Mach angle, see Eq. (2.164)	—	rad
μ	dynamic shear viscosity	$L^{-1} M T^{-1}$	Pa s
μ	thermal deformation, see Eq. (4.33)	—	—
μ_{st}	stoichiometric air-fuel mass ratio	—	—

ν	Poisson's ratio	—	—
ν	Prandtl-Meyer function, see Eq. (2.171)	—	rad
ν''	combustion product	—	—
ν'	combustion educt	—	—
Ω	integration domain	L^3	m^3
$\partial\Omega$	surface of integration do- main	L^2	m^2
ϕ	shape function component	—	—
ϕ	stoichiometric equivalence ratio, see Eq. (5.15)	—	—
ρ	density	$L^{-3} M$	$kg\ m^{-3}$
σ	stress	$L^{-1} M\ T^{-2}$	$N\ m^{-2}$
τ	shear stress	$L^{-1} M\ T^{-2}$	$N\ m^{-2}$
θ	momentum thickness, see Eq. (2.60)	L	m
Δ	shock standoff distance, see Fig. D.4	L	m
ε	normal strain (elastic), see Eq. (4.24)	—	—
ζ	Reynolds analogy factor, see Eq. (2.50)	—	—
\mathcal{E}	Species contributing to elementary reaction, see Eq. (3.1)	—	—
ζ	dynamic bulk viscosity	$L^{-1} M\ T^{-1}$	$Pa\ s$

Script Symbols

Symbol	Description		
g	molar gibbs potential	$L^2 M T^{-2} N^{-1}$	$J mol^{-1}$
h	molar enthalpy	$L^2 M T^{-2} N^{-1}$	$J mol^{-1}$
s	molar entropy	$L^2 M T^{-2} \Theta^{-1} N^{-1}$	$J mol^{-1} K^{-1}$
\mathcal{C}	elasticity tensor, see Eq. (4.20)	$L^{-1} M T^{-2}$	Pa
\mathcal{I}	identity tensor, see Eq. (B.3)	—	—
\mathcal{A}	influence tensor, see Eq. (B.2)	—	—
\mathcal{B}	compliance influence, see Eq. (B.15)	—	—
\mathcal{C}	viscosity tensor, see Eq. (2.27f)	$L^{-1} M T^{-1}$	Pa s
\mathcal{D}	damage tensor, see Eqs. (B.6) and (B.7)	—	—
\mathcal{F}	Tsai-Wu tensor, see Eq. (B.8)	$L^2 T^4 M^{-2}$	Pa^{-2}
\mathcal{f}	Tsai-Wu origin, see Eq. (B.8)	$L M^{-1} T^2$	Pa^{-1}
\mathcal{M}	compliance tensor, see Eq. (B.17)	$L M^{-1} T^2$	Pa^{-1}
\mathcal{P}	Hill polarization tensor, see Eq. (B.4)	—	—
$\dot{\mathcal{Q}}$	local coldgas heat flux derivative, see Eqs. (7.2) and (7.3).	$L M T^{-3}$	$W m^{-1}$

g	Tsai-Wu criterion, see Eq. (B.8)	—	—
s	energy error, see Eq. (7.4)	—	—

Roman Symbols

Symbol	Description	Dimensions	Units
c_f	local skin friction coefficient, see Eq. (2.44)	—	—
C_p	pressure coefficient, see Eq. (2.43)	—	—
c_p	specific heat capacity at constant pressure	$L^2 T^{-2} \Theta^{-1}$	$J kg^{-1} K^{-1}$
c_v	specific heat capacity at constant volume	$L^2 T^{-2} \Theta^{-1}$	$J kg^{-1} K^{-1}$
\dot{b}	volumetric heat load	$L^{-1} M T^{-3}$	$W m^{-3}$
\dot{i}	momentum flux, see Eq. (2.111)	$L M T^{-2}$	$kg m s^{-1}$
\dot{m}	mass flux	$M T^{-1}$	$kg s^{-1}$
\dot{q}	area specific heat load	$M T^{-3}$	$W m^{-2}$
\dot{H}_t	energy flux, see Eq. (2.115)	$L^2 M T^{-3}$	$J s^{-1}$
I_{sp}	specific impulse, see Eq. (1.2)	T	s
Ma	Mach number, see Eq. (2.41)	—	—
\mathbf{C}	elasticity matrix, see Eq. (4.28)	$L^{-1} M T^{-2}$	Pa

J	Jacobian matrix	variable	variable
Pr	Prandtl number, see Eqs. (2.46), (2.47) and (2.48)	—	—
Re	Reynolds number, see Eq. (2.42)	—	—
St	Stanton number, see Eq. (2.45)	—	—
\tilde{A}	Arrhenius frequency factor, see Eq. (3.4)	T^{-1}	s^{-1}
\tilde{E}	Arrhenius activation en- ergy, see Eq. (3.4)	$L^2 M T^{-2} N^{-1}$	$J mol^{-1}$
A	cross section	L^2	m^2
a	acceleration vector, see Eq. (2.32)	$L T^{-2}$	$m s^{-2}$
c	mass concentration	$M^{-3} N$	$mol cm^{-3}$
c	specific heat capacity of solid	$L^2 T^{-2} \Theta^{-1}$	$J kg^{-1} K^{-1}$
C_d	drag coefficient	—	—
c_e	effective exhaust velocity, see Eq. (1.2)	$L T^{-1}$	$m s^{-1}$
C_r	internal inlet compression ratio, see Eqs. (D.5) and (D.6)	—	—
$C_{mix,inj}$	injector mixture param- eter after Pulsonetti, see Eq. (3.19)	—	—
d	duct height	L	m

D_h	hydraulic diameter, see Eq. (2.93)	L	m
d_θ	inviscid duct height	L	m
E	Young's modulus	$L^{-1} M T^{-2}$	Pa
F	force	$L M T^{-2}$	N
G	Shear modulus	$L^{-1} M T^{-2}$	Pa
g^+	wake contribution to u^+ , see Eqs. (2.87) and (2.122)	—	—
k''	backward reaction rate coefficient, see Eq. (3.9)	variable	mol, m, s
k'	forward reaction rate coefficient, see Eq. (3.4)	variable	mol, m, s
l	length	L	m
M	molar mass	$M N^{-1}$	$kg mol^{-1}$
P	perimeter	L	m
r	radius	L	m
r	recovery factor, see Eq. (2.55)	—	—
s	coordinate along surface	L	m
t	time	T	s
u, v, w	velocity components	$L T^{-1}$	$m s^{-1}$
u^+	dimensionless velocity parallel to wall, see Eqs. (2.79) and (2.98)	—	—
x, y, z	spacial coordinates	L	m

Y	mass fraction	—	—
y^+	dimensionless wall distance, see Eqs. (2.80) and (2.99)	—	—

Superscripts

Symbol	Description
◦	caloric property at reference pressure
★	incompressible adiabatic reference state
—	cross section averaged value

Subscripts

Symbol	Description
cg	coldgas
δ	condition at edge of boundary layer
hg	hotgas
∞	freestream condition
M	mixed laminar and turbulent property
r	condition at recovery state
T	turbulent property
t	caloric property at stagnation condition
w	condition at wall
cinj	central injector
winj	wall injector

Indices

Symbol	Description
z	index for timestep or iteration loop
d	index for node
e	index for finite element
i, j, k, l	index for spacial dimensions
m	number of elements
n	number of nodes
p, q	index for integration point
r, s	index for degree of freedom
v, w	index for Voigt notation

Constants

Symbol	Description and Value	Dimensions
\mathcal{R}	universal gas constant $\mathcal{R} = 8.314\,459\,8 \text{ J mol}^{-1} \text{ K}^{-1}$	$\text{L}^2 \text{M T}^{-2} \Theta^{-1} \text{N}^{-1}$
σ	Stefan-Boltzman constant, see Eq. (3.23) $\sigma = 5.670\,367 \times 10^{-8} \text{ W m}^{-2} \text{ K}^{-4}$	$\text{M T}^{-3} \Theta^{-4}$
g_0	mean gravitational acceleration on earth's surface $g_0 = 9.806\,65 \text{ N kg}^{-1}$	L T^{-2}

List of Figures

1.1.	Scramjet system component names and reference station numbers.	1
1.2.	Flight corridor for various stratospheric vehicles.	3
1.3.	T_t vs. Ma for various flight experiments.	4
1.4.	Experimental vehicles X-43A (top) and X-51A (bottom).	8
1.5.	Configuration of a generic airbreathing space transportation system.	11
1.6.	General modeling approach of this work.	17
2.1.	T_t and p_t of air at 30 km vs. Ma	25
2.2.	Comparison between flat plate flow and channel flow or pipe flow. .	35
2.3.	Order and evolution of important boundary layer models.	37
2.4.	Velocity profile in a turbulent boundary-layer, smooth flat plate. . .	42
2.5.	UML activity diagram for the modified van Driest method.	53
2.6.	Velocity triangles of an oblique compression shock.	59
2.7.	Shock angles for various reflection angles and Mach numbers. . . .	60
2.8.	Prandtl-Meyer expansion fan along a convex corner.	61
2.9.	Velocity triangle for the Prandtl-Meyer expansion.	62
3.1.	Hottel's method of crossed strings.	69
5.1.	Variables for the inlet geometry.	82
5.2.	Working principle of a regenerative fuel cycle system.	84
5.3.	C/C-SiC sandwich structure with cooling channels.	85
5.4.	Kinetic adiabatic efficiency for various isothermal wall temperatures.	87
5.5.	Separation bubble, started and unstarted operation mode.	88
5.6.	St and C_p along the wetted inlet surface.	89
5.7.	Pressure coefficient distribution along the blunted nose.	91
5.8.	Stanton number distribution along the blunted nose.	92
5.9.	Overpressurization near the blunted leading edge.	92
5.10.	Simplified flow field around the external cowl.	93
5.11.	Stanton numbers along the external cowl.	93
5.12.	Finite element mesh for the inlet simulation.	94
5.13.	Cooling channels on inlet geometry.	95
5.14.	Equilibrium surface temperatures of inlet, hull side.	97
5.15.	Thermal interaction between flow field and structure, with $\phi = 1$. .	97
5.16.	Equilibrium surface temperatures of inlet	98
6.1.	General dimensions of the combustion chamber, dimensions in mm.	99
6.2.	Isometric view of the injector geometry, dimensions in mm.	100
6.3.	Back side of the fuel injector, dimensions in mm.	100
6.4.	Simplified inviscid shock system around central injector.	101
6.5.	Estimated mean injector temperature over fuel temperature	102
6.6.	Development of T and Ma for $\phi = 0$	104

6.7.	Development of p and p_t for $\phi = 0.65$	105
6.8.	Development of T and Ma for $\phi = 0.65$	106
6.9.	Development of T and Ma for $\phi = 0.85$	107
6.10.	The two-staged fuel cooling and injection system of the combustor.	108
6.11.	Combustor static temperature and Mach number	110
6.12.	Combustor static pressure and velocity	111
6.13.	Combustor equilibrium surface temperatures.	112
6.14.	Convective and radiative heat loads.	113
7.1.	Example of a regeneratively cooled C/C-SiC panel.	116
7.2.	Simulated structure domains in the y - z plane and x - y -plane.	116
7.3.	Boundary conditions: $T_w = \text{const.}$ and $St = \text{const.}$	117
7.4.	Symmetrical half model of C/C-SiC panel	119
7.5.	Relation between maximum Tsai-Wu criterion vs. $T_{w,\text{hot}} - T_{\text{cg}}$	120
7.6.	UML activity diagram for cooling channel investigation.	121
7.7.	Inlet calculation along x -coordinate.	122
7.8.	Combustor calculation along x -coordinate.	123
7.9.	Temperature field (left) and Tsai-Wu criterion, inlet.	124
7.10.	Temperature field (left) and Tsai-Wu criterion, combustor.	125
A.1.	Local coordinate system of the QUAM9 and TRIM6.	131
A.2.	Shape functions of the QUAM9 element.	132
A.3.	Shape functions of the TRIM6 element.	133
B.1.	Simplified model of the C/C-SiC material.	137
B.2.	Ellipsoid shape representing an inclusion or void.	138
B.3.	Modeled degeneration of carbon fibers.	139
B.4.	Modeled degeneration of composite matrix.	140
B.5.	Thermal conductivity of C/C-SiC and polynomial.	144
B.6.	Experimental data for the specific heat of C/C-SiC and polynomial.	145
B.7.	Experimental data and polynomials for thermal expansion of C/C-SiC.	146
D.2.	Sharp-edged external shock system.	150
D.3.	Inviscid blunt edged external shock system.	151
D.4.	Shock system around a blunted edge.	152

List of Tables

1.1.	Overview over various research projects related to hypersonic flight.	5
1.2.	Mass budget for a generic airbreathing space transportation system.	11
1.3.	Possible cooling methods for hot structures in hypersonic vehicles.	14
2.1.	Calibration parameters for important cubic equation models.	20
5.1.	Geometry parameters for the investigated configuration.	82
5.2.	Preliminary flow data for $T_w = 600$ K.	83
5.3.	Boundary conditions for CFD simulations.	86
5.4.	Mean flow states for Fig. 5.10.	93
5.5.	Boundary conditions for the inlet calculations.	96
6.1.	Calculating the injector temperature using the method of van Driest.	102
6.2.	Combustor inflow conditions for the Hohn inlet.	103
6.3.	Boundary conditions for the combustor calculations.	109
6.4.	Combustor cooling channel exit conditions.	109
B.1.	Mechanical properties of Toho Tenax HTA40 E13.	139
B.2.	Matrix composition of C/C-SiC XB and elastic matrix properties. . .	140
B.3.	Elastic properties of C/C-SiC XB.	141
B.4.	Tsai-Wu parameters for C/C-SiC XB.	143
B.5.	Polynomial coefficients for the thermal conductivity of C/C-SiC. . .	144
B.6.	Polynomial coefficients for the specific heat capacity of C/C-SiC. . .	145
B.7.	Polynomial coefficients for thermal expansion of C/C-SiC.	146
C.1.	Polynomial coefficients for the specific heat capacity of air.	147
C.2.	Calibration parameters for the Sutherland and Hansen correlations.	148
E.1.	Hydrogen–Air Reaction Scheme	154

Kurzfassung

Luftatmende Raumtransportsysteme stellen eine interessante Alternative zu den klassischen, rein raketentriebenen Raumtransportsystemen dar. Da die erste Stufe eines solchen luftatmenden Systems den Sauerstoff der Atmosphäre für die Verbrennung nutzen würde, müsste im Gegensatz zur Rakete kein Oxidator mitgeführt werden. Theoretisch könnten so bis zu drei Viertel des explosiven Treibstoffes eingespart werden, und damit die Sicherheit des Systems verbessert werden. Nachdem derartige Systeme lange Zeit nur in der Theorie bekannt waren, konnte in den 2010er Jahren experimentell nachgewiesen werden, dass ein sogenannter Supersonic Combustion Ramjet zumindest über einen kurzen Zeitraum hinweg tatsächlich in der Lage ist, den Verbrennungsprozess stabil zu unterhalten und positiven Schub zu erzeugen.

Aufgrund der hohen Wärmelasten, denen ein derartiges System ausgesetzt wäre, besteht eine große Herausforderung darin, ein System zu bauen, das über einen längeren Zeitraum hinweg betrieben werden kann. Für eine Modellierung dieses Problems müssen aerodynamische, thermodynamische und mechanische Phänomene berücksichtigt werden, die stark miteinander wechselwirken. Im Rahmen der vorliegenden Arbeit wird ein Modellierungsansatz vorgeschlagen, anhand dessen die auftretenden Wärmeströme, Wandtemperaturen, und thermischen Spannungen innerhalb der Struktur abgeschätzt werden können. Für eine Fluggeschwindigkeit von Mach 8 bei einer Flughöhe von 30 km wird eine zweidimensionale Beispielkonfiguration des Einlauf-Brennkammer-Systems definiert und auf ihre thermische und mechanische Beständigkeit hin untersucht.

Das Strömungsfeld des Einlaufsystems wird mit einem reynoldsgemittelten Navier-Stokes-Löser berechnet, wobei das Turbulenzmodell nach Menter zum Einsatz kommt. Die numerische Lösung des Strömungsfelds wird anhand verfügbarer semiempirischer Lösungen validiert. Die berechneten lokalen Wandwärmeströme werden nach einem Ähnlichkeitsmechanischen Ansatz dimensionslos gemacht und anschließend als Randbedingungen an die thermische Struktursimulation übergeben.

Basierend auf den Arbeiten von Shapiro, Walther, und Scheuermann wird das chemisch reagierende Strömungsfeld in der Brennkammer vereinfacht als eindimensionale Kanalströmung modelliert. Für die chemische Verbrennung wurde das Reaktionsschema nach Jachimowski eingesetzt. Zur vereinfachten Berechnung der Reibung und des Wärmeübergangs von der Strömung auf die Struktur wird aufbauend auf den Ansätzen von Crocco und van Driest ein neues Grenzschichtmodell vorgeschlagen. Dieses wird anhand dreidimensionaler Rechnungen von Rabadán Santana validiert. Es wird angenommen, dass die Struktur ähnlich einer Raketenbrennkammer regenerativ mit Treibstoff gekühlt wird. Dazu soll kyogener Wasserstoff eingesetzt werden, der mittels des Modells von Leachman et. al. modelliert wird.

Die Wärmeleitung innerhalb der Struktur wird mit der Methode der Finiten Elemente simuliert. Als Zeitschrittverfahren kommt ein implizites Euler-Verfahren zum Einsatz. Da die Struktur zweidimensional modelliert wird, wird die Wärmestrahlung nach dem Ansatz von Hottel simuliert. Aufgrund seiner hohen Hitzebeständigkeit wird als Werkstoff die faserverstärkte Keramik C/C-SiC ausgewählt. Neben den Temperaturen, die sich in der Struktur im thermischen Gleichgewicht einstellen, werden auch die thermomechanischen Spannungen innerhalb der Struktur bestimmt. Als Versagensmodell der mechanischen Analyse wird das Kriterium von Tsai und Wu eingesetzt.

Es wird gezeigt, dass für einen Mach 8 Flug ein thermodynamisches Gleichgewicht erreicht werden kann, ohne dass ein strukturelles Versagen oder ein Zusammenbruch des thermodynamischen Kreislaufs zu erwarten ist. Zum Schluss wird diskutiert, wie sich die in dieser Arbeit gewonnen Erkenntnisse auf den weiteren Konstruktions- und Modellierungsprozess eines Scramjet-Antriebssystems auswirken.

Abstract

Airbreathing space transportation systems are an interesting alternative to classical, purely rocket driven space transportation systems. Since the first stage of such an airbreathing system is able to use the oxygen from the atmosphere for the combustion process, it would, in contrast to a rocket, not need to carry any oxidizer around. Theoretically, up to three quarters of the explosive rocket fuel could be saved this way, which would increase the safety of the system. For a long time, such a system was only known as a theoretical concept. In the 2010s, it could be experimentally proven that a supersonic combustion ramjet is, at least for a short time, actually able to maintain a stable combustion process and generate positive thrust.

Due to the high heat loads such a system is exposed to, building a system which is able to operate for a longer time is a major challenge. For the modeling of this problem it is necessary to regard aerodynamical thermodynamical and mechanical phenomena, which all strongly interact.

Within the present work, a modeling approach is suggested which allows estimating heat fluxes, surface temperatures and thermal stresses within the structure. Applied to a cruise velocity of Mach 8 and a flight altitude of 30 km, a two-dimensional example configuration for the inlet-combustor system is defined and investigated regarding its thermal and mechanical stability.

The flow field in the inlet was calculated with a Reynolds-averaged Navier-Stokes solver, in which the turbulence model from Menter was used. The numerical solution of the flow field was validated against available semi-empirical approaches. The local wall heat fluxes obtained were made dimensionless by using a similitude approach, and afterwards committed as boundary conditions to the thermostructural simulation.

Based on the works of Shapiro, Walther, and Scheuermann, the reacting flow field in the combustion chamber is simplified as one-dimensional channel flow. The scheme of Jachimowski was used to model the chemical combustion. For a simplified calculation of friction and heat transfer between the flow and the structure, a new boundary layer model is suggested, based on the works of Crocco and that of van Driest. It is validated against three-dimensional calculations, which have been performed by Rabadán Santana. Similarly to the combustion chamber of a rocket, it is assumed that the structure is regeneratively cooled with fuel. For that purpose, cryogenic hydrogen is chosen, which is modeled by an approach suggested by Leachman et al.

The thermal conduction within the structure is modeled using the finite element method. For the time-stepping, an implicit Euler method is used. Since the structure is modeled two-dimensionally, the model by Hottel is used for the thermal radiation. Due to its high thermal resistance, the fiber-reinforced ceramic C/C-SiC is

chosen. Apart from the equilibrium temperatures of the structure, thermomechanical stresses are calculated as well. As failure model for the mechanical analysis, the criterion by Tsai and Wu is used.

It is shown that for the case of a Mach 8 flight it is possible to achieve a thermal equilibrium without a failure of structural integrity, or a failure of the thermodynamic cycle being expected. Finally, it is discussed in what way the results of the present work could influence future design and modeling approaches of a scramjet propulsion system.

1. Introduction

The concept of an airbreathing space transportation system has been discussed since the 1950s at least, and it remains an interesting alternative to conventional rocket systems. The discussion remains in spite of the fact, that the realization of such a system requires mastering huge challenges in almost all fields of engineering sciences. One challenge regards the fact that the thermal loads on the structure increase with the square of the cruise velocity of the vehicle. The present work investigates whether a thermally balanced scramjet-powered flight at $Ma = 8$ is physically possible, and if so, how it can be modeled and numerically simulated. A two-dimensional example geometry is defined, and a thermomechanical investigation is performed and discussed.

1.1. Scramjet Working Principle

The supersonic combustion ramjet is an airbreathing aircraft propulsion system, which creates thrust by compression, heating, and expansion of air. Scramjet engines can only operate in the hypersonic flow region, ranging from approximately $Ma \gtrsim 5$ to $Ma \lesssim 10$. Secondary engines are necessary to accelerate a vehicle up to this speed range. Typically, turbine engines or solid rocket boosters are being considered for this purpose. Dual mode scramjets can also operate with subsonic combustion down to speeds of approximately $Ma \approx 2$. The engine can be podded into a nacelle, similarly to turbine engines in modern airliners. These variants are usually rotationally symmetric. In another variant, the external compression and expansion processes are performed along the vehicle's hull. The advantage of this construction is that it creates less drag than an engine nacelle. The shape of such an airframe integrated engine is illustrated in Fig. 1.1.

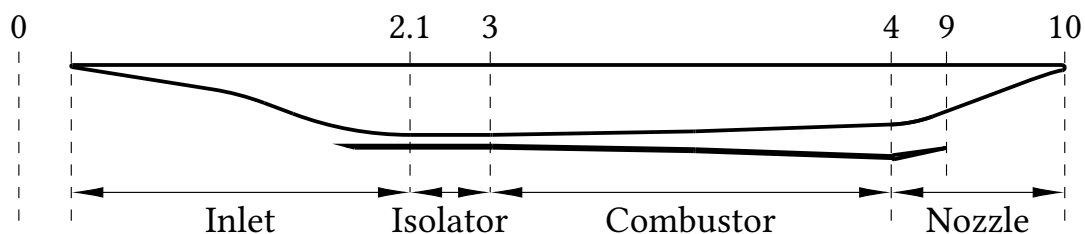


Figure 1.1: Scramjet system component names and reference station numbers.

See Sec. 1.1.1 for station number description.

1.1.1. Process Cycle Reference States

To characterize the thermodynamic process of the engine, the cycle determining parameters like temperature, pressure and flow velocity are averaged across certain cross areas perpendicular to the general direction of the flow. The denotations of these reference stations are based on the SAE standard AS755F,¹ although minor variations are found in literature when applied to the scramjet engine. The main reference stations are :

- **freestream condition**

The freestream condition is defined by the cruising speed Ma_0 and the flight altitude. The static temperature T_0 and pressure p_0 are determined on the basis of a standard atmospheric model.²

- **compression**

Along the inlet structure, compression is achieved by a series of oblique compression shocks. Since the compression process is assumed to end at position (2.1), while a series of oblique compression shocks and expansion, the *shock train*, may occur in the isolator, which ends at position (3). It is a matter of point of view whether the isolator has to be regarded as a part of the inlet or as a separate system component. During the design process of the inlet, the latter is preferred since the length of the isolator depends on the maximal pressure in the combustion chamber, which has to be determined separately. Once the isolator length is known, inlet performance parameters are usually referred to station (3) instead of (2.1) to facilitate the analysis of the thermodynamic cycle of the engine.

- **combustion**

The fuel injector is placed in the center of the entrance of the combustion chamber in order to induce perturbations that support the mixing process. Other variants consider a fuel injection from the wall, or a combination of central and wall injection.

- **expansion**

The chemical process of the combustion is usually modeled until the flow reaches the combustor exit at station (4). From the nozzle onwards, a frozen combustion is often assumed, where the gas composition does no longer change due to combustive effects, and no chemical heat is released.

1.1.2. Hypersonic Flight Corridor and Total Temperature

The definition of the flight corridor helps to choose an appropriate flight altitude for a desired cruise velocity. Considering aeronautical engineering applications, lift and drag of a vehicle moving through the atmosphere depend almost linearly on the dynamic pressure

$$q_0 = \frac{\rho_0 u_0^2}{2}, \quad (1.1)$$

where ρ_0 is the atmospheric density and u_0 the cruising speed. Since the density of the air decreases with the altitude, the vehicle must fly low enough to create sufficient lift, yet high enough to prevent mechanical or thermal failure caused by drag and friction. The optimal flight altitude of a stratospheric aircraft depends on the chosen Mach number and the required dynamic pressure q_0 , which should be between roughly 20 and 90 kPa.³ This *flight corridor* is illustrated in Fig. 1.2 along with operating points for various stratospheric vehicles.

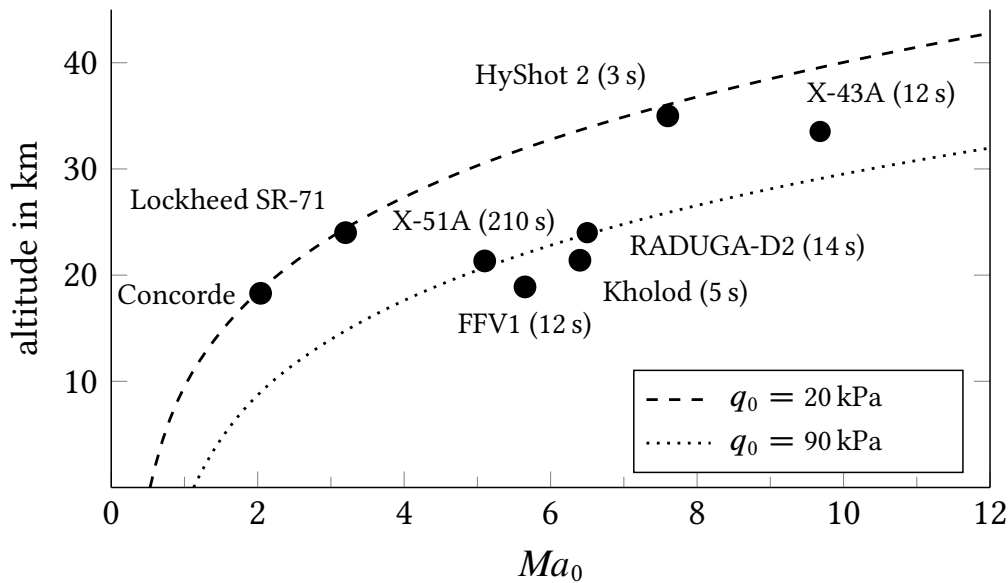


Figure 1.2: Flight corridor for various stratospheric vehicles, the dynamic pressure is referred to the US 1976 standard atmosphere.

The total temperature $T_{t,0}$ allows a first estimation of the maximal wall temperatures that are to be expected on the external surfaces of the vehicle, see Fig. 1.3. For this estimation, it is assumed that there is no thermal radiation and that the external surfaces are thermally isolated from the supporting structure. The physical meaning of the total temperature can easily be explained as follows: from the viewpoint of the vehicle, the air is moving with a velocity of u_0 . If the air was fully stopped, the kinetic energy would be fully converted into caloric energy, thus heating up the air to the total temperature.

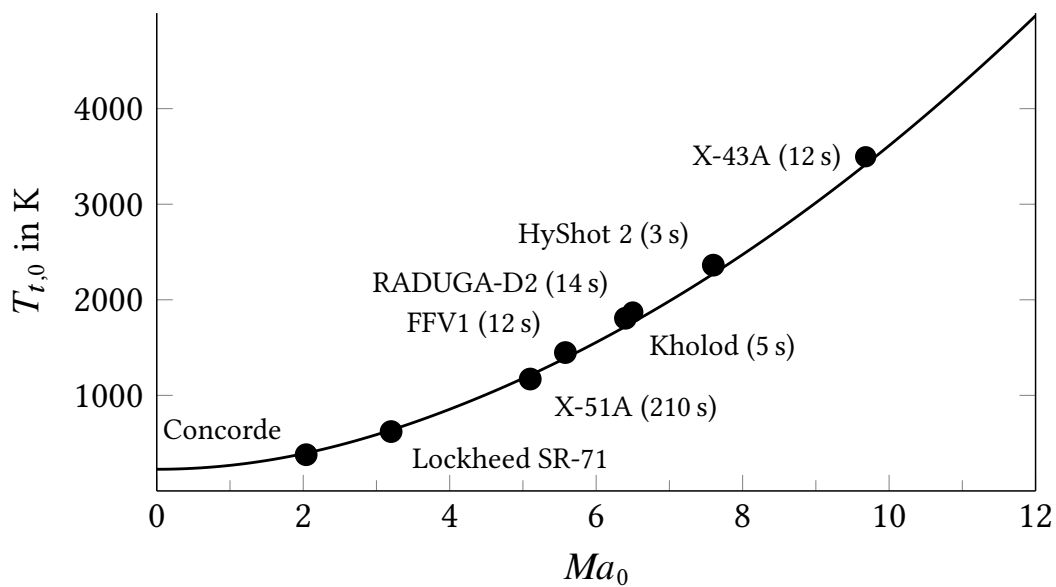


Figure 1.3: Total temperature versus Mach number for various flight experiments.

1.2. Historical Overview

The history of hypersonic flight can be roughly divided into four eras. The first era covers the concept phases before and during World War II. The second phase was dominated by the beginning of the American X-Plane programs as well as various French ramjet flight experiments. Furthermore, fundamental research programs were initiated by the former Soviet Union, the United Kingdom, and Japan. Research declined after the end of the Apollo Program, which marks the end of the second era. The third era can be described as the era of conceptual single and two-stage to orbit vehicles. Various of these had been investigated in the 1980s and early 1990s. Although none of these studies had actually resulted in a flying vehicle, the conducted basic research had influenced the research projects of the late 1990s and the 2000s. The beginning of the fourth era was marked by the Russian Hypersonic Flying Laboratory *Kholod*, and peaked in the flight of the American X-43A test vehicle in 2001. An incomplete overview over various research projects related to hypersonic flight is shown in Tab. 1.1.

Table 1.1: Overview over various research projects related to hypersonic flight. Bold names mark flight experiments actually flown, italic names mark ramjet-powered missiles.

	USA	France	Germany	Russia	Australia
1940			Silbervogel Me P.1100	Borovkov-Florov D	
Post WW II	1950	X-1 X-5 <i>Pluto</i>			
	1960	X-15 SR-71 SCRAM			
	1970	HRE			
	1980	Space Shuttle X-30			
Post Apollo	1950				
	1960				
Post Cold War	1990				
	2000	X-43A FFV1 X-37 X-51A			
	2010				
	2010				

1.2.1. World War II and Before

Several jet engine patents had been granted across Europe until the mid 1930s,⁴ but it wasn't until World War II, when the the British engineer Frank Whittle and his German counterpart Hans Joachim Pabst von Ohain almost independently developed the first working turbojet engines to actually power airplanes, namely the *Messerschmitt Me 262* by the Luftwaffe and the *Gloster E.28/39* by the Royal Airforce. Nazi Germany was performing many highly anticipated studies on supersonic and hypersonic flight, one especially worth of mentioning was the *Silbervogel* proposed by Eugen Sänger and his wife Irene Bredt. It was a conceptual rocket driven sub-orbital bomber, meant to start from Europe, cross the Atlantic within 150 minutes, and drop a 4000 kg bomb over the United States.⁵ Dozens more ramjet and rocket driven fighter concepts were investigated during the last year of World War II. Although most of these concepts were never to leave the drawing board, the Allied Forces would adopt many key technologies after the war was over.

1.2.2. Flight Experiments and Research During the Space Race

The most prominent example of a German fighter concept adopted by the Allied Forces is the *Messerschmitt P.1101*, which was built and flown by the United States Air Force (USAF) as a so-called *X-Plane*, namely the X-5 by Boeing in 1951. The X-5 flight can probably be considered as one of the first supersonic ramjet flights. A first subsonic ramjet flight was performed in France by the Leduc 0.1 in 1947, the same year in which Chuck Yeager had broken the sound barrier piloting the Bell X-1. Other noteworthy X-vehicles from that area are the unmanned X-7 by Lockheed, which was used as a flying testbed for ramjet flights, and the X-20 Dyna-Soar. Although officially never actually built, the X-20 project was a huge contribution to the science hypersonic flight. Many developments would flow into the the X-15 by North American Aviation. The X-15 was mainly used to conduct flight experiments to support the American space program during the 1960s.⁶ Many more research projects on ramjet and rocket driven vehicles followed in the subsequent years, predominantly in the USA, France, the Soviet Union, and Japan. France, Britain and the Soviet union also built the first ramjet powered missiles.⁷

1.2.3. Conceptual Studies During the 1980s

During the 1980s and early 1990s, conceptual studies for various single-stage-to-orbit (SSTO) vehicles were performed, including the American *National Aero-Space Plane X-30 (NASP)*, and the Soviet *Tupolev Tu-2000*. In the mid 1990s, Japan also started conceptual studies on an SSTO vehicle. Eugen Sänger's early studies on a two-stage-to-orbit (TSTO) vehicle led to both the British *Horizontal Take-off and*

Landing Satellite Launcher (HOTOL) and the European vehicle *Sänger-II*. Similar studies were performed by the Soviet Union during the *Ayaks* project.⁸ Unfortunately, none of these projects actually succeeded, since the intended flight conditions could neither be achieved in a test bed nor numerically simulated with the desired accuracy. The highly promising field of computational fluid dynamics (CFD) turned out to be either too inaccurate or too costly by means of calculation power. Especially turbulence modeling turned out to be a great issue. Thermally balanced flight experiments on the other hand were impossible due to the lack of the necessary heat resistant materials.⁹

1.2.4. Post Cold War Flight Experiments

A major breakthrough had been achieved in November 1991, when Russia's *Hypersonic Flying Laboratory (HFL) Kholod* was the first recorded vehicle to achieve supersonic combustion in flight, reaching a cruise velocity of $Ma = 5.2$ for twelve seconds. More flight experiments on Kholod followed during the 1990s, in cooperation with France and the United States.^{10,11} France had maintained its reusable launcher program *PREPHA* until 1996. It was followed by the military *PROMETHEE* program¹²

In 1994, one year after the failure of the NASP X-30, the United States initiated the Hyper-X Program. This highly successful program focused on developing a down-scaled version of the X-30, namely the X-43A flight experiment (see Fig. 1.4, top). It was hydrogen fueled, and was able to generate positive net thrust at $Ma = 9.66$ for about twelve seconds.¹³ The Australian HyShot Program was initiated in the early 2000s at the University of Queensland¹⁴ and featured four hypersonic flight tests which were launched between 2001 and 2006, as well as the collaborative Australia-United States HyCAUSE experiment, which flew in June 2007.

The Hyper-X and HyShot test programs had successfully proven that an air-breathing flight vehicle can not only achieve supersonic combustion, but also generate positive net thrust. Up until then, all test vehicles had maintained their high speed for a few seconds only, but the problem of a sustained, thermally balanced flight persisted until the X-51A *Waverider* (see Fig. 1.4, bottom) was developed on the basis of the initiated but canceled X-43C test vehicle. The X-51A Waverider was a collaboration between the United States Air Force (USAF) and the Defense Advanced Research Projects Agency (DARPA). Two successful flights were performed in May 2010 and May 2013, the latter of which achieving 210 seconds of hypersonic flight at $Ma = 5.1$.¹⁵ The X-51A did not combust hydrogen but JP-7, a special hydrocarbon based fuel. A similar research program called *LEA* was conducted in France from 2003 to 2015.¹⁶

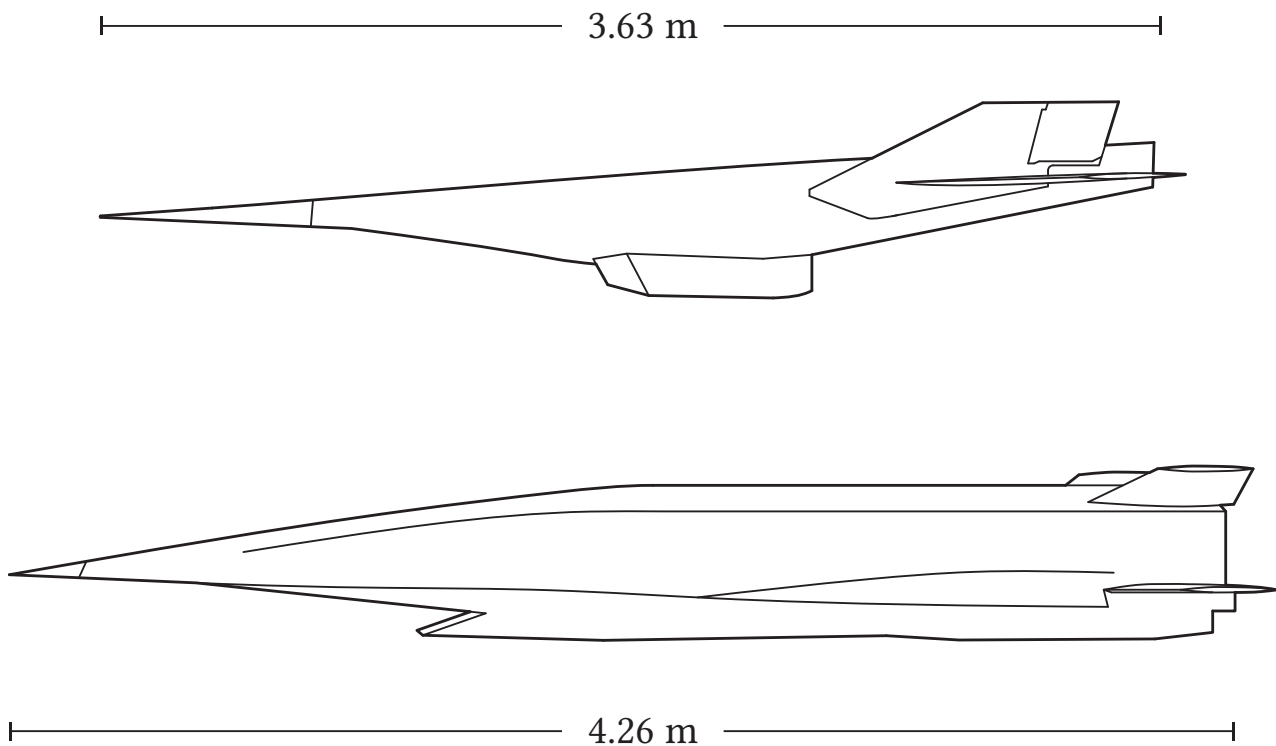


Figure 1.4: Experimental vehicles X-43A (top) and X-51A (bottom).

1.2.5. Post Cold War Basic Research in Germany

Continuing the heritage of Sanger II, the *German Hypersonics Technology Program* was initiated in the 1990s. Apart from basic investigations, the program also contained several flight experiments of a scramjet testbed, which was mounted on the Russian RADUGA-D2 rocket^{17,18} ^a. During the same period, the *German Research Collaborative Centres*, SFB 253, SFB 255 and SFB 259 were founded. They focused on basic research regarding aerodynamics and thermodynamics, flight mechanics and control, high-temperature materials as well as overall design aspects of SSTO and TSTO space transportation systems.¹⁹ After their expiration in the mid 2000s, the project was followed by the *German Research Training Group GRK 1095*,²⁰ which focused on basic aerothermodynamic vehicle design, and the *Transregio 40 Collaborative Research Centre*, which focused on modeling and manufacturing of high temperature materials. A German contribution in the field of material sciences was achieved by the DLR through the *Sharp Edged Flight Experiments SHEFEX* and *SHEFEX II*, which were launched in October 2005 and June 2012 and featured high enthalpy flight experiments on carbon fiber reinforced ceramics and transpirational cooling.²¹⁻²³

^aРадуга (raduga) is the Russian word for *rainbow*

1.2.6. Hypersonic Flight in the Present and the Near Future

During the time this work was written, a third SHEFEX mission aimed to reach $Ma = 20$ was being planned.²⁴ In May 2016, Australia launched the HIFire 5B flight experiment, which was developed in cooperation with the US military. The three dimensional inlet geometry consists of a ramp with sidewalls, which gradually merges in an elliptic isolator structure.²⁵ It reached Ma 7.5. With HIFiRE 8, Australia has announced a C/C-SiC structured waverider experiment, which aims at reaching a 30 second hypersonic flight.^{26,27} Another flight experiment to be expected in the near future is the Brazilian Waverider *Hypersonic Aerospace Vehicle 14-X S*.^{28,29}

In collaboration with Airbus, the American company Aerion is currently developing the supersonic business jet AS2, which is supposed to reach $Ma = 1.5$, and is expected to be shipped in 2023. In November 2015, the Bombardier Aerospace subsidiary Flexjet placed a 2.4 billion dollar order on 20 airplanes of that type.³⁰ Both the American companies Lockheed Martin, and Spike Aerospace, as well as the British company HyperMach and the Russian Sukhoi Company have announced similar projects. In June 2015, NASA announced to grant over 4.6 million dollars to industrial and academic funding in research on supersonic commercial passenger transport.³¹ One month later, Airbus was granted a US patent of a possible Concorde successor which would be hydrogen-fueled and could transport 20 passengers at $Ma = 4.5$.^{32,33}

The Boeing Company has announced the *Small Launch Vehicle*, a four stage air-breathing space transportation system which will be developed in cooperation with *Scaled Composites*. The patent was granted in 2015.³⁴ In June 2016, a similar project called *SPARTAN* has been announced in Australia.³⁵ Continuing the heritage of Sanger I and HOTOL, the British Company Reaction Engines Limited is developing a single stage to orbit space transportation system called *Skylon*. Similar to the upper stage of Boeing's SLV, the engine of Skylon will compress the incoming air and decelerate it to subsonic speed. The air will pass a heat exchanger and be cooled down to 120 K, before being passed into a classical turbojet engine.^{36,37} The Skylon project is very ambitious, and it might take some time until all technical challenges are overcome.^{38,39}

The scramjet technology has also a strategical relevance. Due to its high maneuverability and potential stealth capabilities, a hypersonic glide vehicle could overcome a satellite supported missile defense shield far easier than a classical missile. It is therefore not surprising that the lessons learned from the Boeing X-51A Waverider will flow into the development of so called *Conventional Prompt Global Strike Weapons*, maneuverable stealth missiles, which are said to be capable of reaching velocities of up to $Ma = 6$.^{40,41} It is furthermore not a secret that Russia, India, and China are working on similar projects.⁴²

1.3. Motivation

This section consists of three parts. The first part discusses why the scramjet should be considered as an engine for a space transportation system, in spite of its technical challenges. It is followed by an example fuel budget in order to demonstrate the benefit of the scramjet approach. The short explanation of the flight path and the concept of total temperatures illustrate the thermal problem that comes with hypersonic flight. That section is followed by a short explanation of the contributions this work hopes to provide for future investigations.

1.3.1. Application as Airbreathing Space Transportation System

The attractiveness of an airbreathing system is that it would require significantly less fuel than a conventional rocket. This could potentially lead to a more reliable and less expensive system.^{43,44} This reduced fuel consumption is owed to the vehicle's capability of extracting the atmospheric oxygen required for combustion. The overall efficiency of the system will therefore depend on the maximum velocity at which the atmospheric oxygen can be used. This makes the scramjet engine a good candidate for the propulsion system. Apart from space transportation, such an engine could become interesting for commercial passenger transport as well as defense applications.

1.3.2. Fuel Budget Example for a Space Transportation System

The effective exhaust velocity c_e , and respectively the specific Impulse I_{sp} ,

$$c_e = g_0 I_{sp} = \frac{F}{\dot{m}_f}, \quad (1.2)$$

are used to describe the capability of a rocket engine to generate thrust by expelling fuel. Herein, F is the thrust, and \dot{m}_f the fuel mass flow. Traditionally, the effective exhaust velocity c_e is divided by the gravitational acceleration at sea level g_0 in order to avoid confusion between engineers using metric and imperial systems of measurement, thus resulting in the specific impulse I_{sp} , which is measured in seconds.

The cost of a spaceflight mission is described as Δv , which measures the amount momentum needed during the mission. A flight from the surface of the Earth to the low Earth orbit (LEO) for example, costs about $10\,000 \text{ m s}^{-1}$.^{45,46} The fuel budget of a rocket consisting of n stages can be determined by the Tsiolkovsky rocket equation

$$\Delta v = \sum_{i=1}^n c_{e,i} \ln \frac{m_{0,i}}{m_{b,i}}, \quad (1.3)$$

where $m_{0,i}$ is the total wet mass of the rocket at the ignition of the stage, and $m_{b,i}$ the burnout mass of the stage. Fig. 1.5 depicts a theoretical space transportation system, which could transport the X-37B experimental vehicle to LEO.

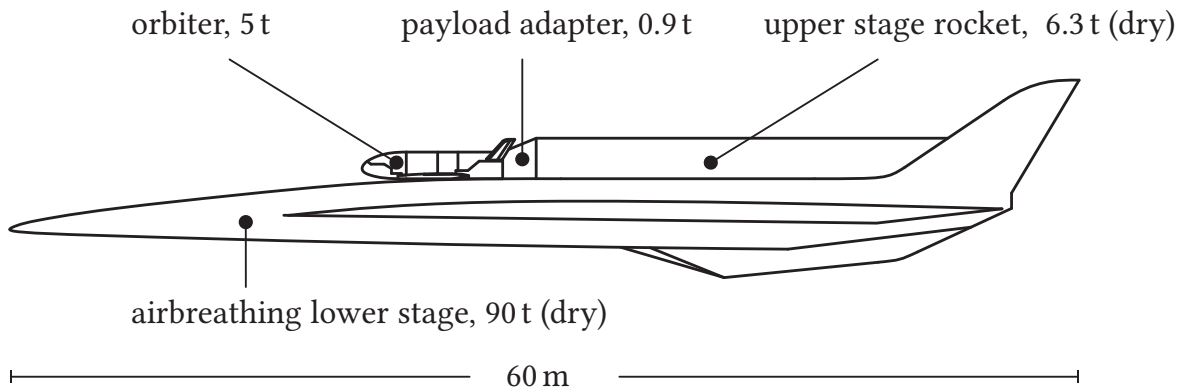


Figure 1.5: Configuration of a generic airbreathing space transportation system.

A possible mass budget for Eq. (1.3) is shown in Tab. 1.2. The assumed dry masses are 90 t for the airbreathing stage and 7.3 t for the upper stage including engine and payload adapter. The mass budget shows that 72 t of fuel would be required. In the present, the X-37B vehicle is launched with an *Atlas V 501* system, which requires over 300 t of fuel for the same mission.

Table 1.2: Mass budget for a generic airbreathing space transportation system.

		I_{sp} s	Ma_b	m_0 t	m_b t	m_f t	Δv m/s
1a	Turbojet	4000	2	174.3	171.7	2.6	590
1b	Ramjet	3000	5	171.7	166.6	5.1	885
1c	Scramjet	2000	8	166.6	159.1	7.5	900
2	Rocket	450		69.1	12.2	56.8	7625
3	Payload			5.0			
	total					72	10000

1.3.3. Purpose of This Work

It is easy to see from Fig. 1.3 that the total temperature exceeds any maximum service temperature of most common materials, so that active cooling concepts are necessary if a thermally balanced flight is desired. Apart from the regeneratively cooled X-51A flight experiment, which flew in the low hypersonic regime, no flight experiment was able to achieve a thermal equilibrium, especially not in the regimes of $Ma = 8$ and above. The purpose of this work is to create a thermal model of a generic two-dimensional inlet-combustor geometry, and prove that a thermally balanced flight at $Ma = 8$ is possible, if the structure is actively cooled. Furthermore, the appearing thermal stresses within the cooled structure are predicted. If the flow field along a scramjet structure is to be modeled viscously, which means that aerodynamic friction is regarded, most models require the local temperatures of the wetted surfaces as imposed boundary conditions. Their diligent estimation often poses a challenge to the aerodynamicist. The information provided by the model in this work can facilitate that estimation. The model also provides the thermal loads, which will help the material scientist to determine thermal deformations and mechanical stresses within the structure, so that more detailed investigations on the mechanical strength of the structure will be possible. The thermal losses predicted by the present model will contribute to the overall system knowledge that is needed for investigations on the performance and robustness of the engine's thermodynamic cycle.

1.4. Scramjet Thermal Management: State of the Art

This section provides an overview over various cooling methods that can be considered for the application of a scramjet engine. Cooling methods of previously flown and upcoming flight experiments are briefly discussed. The section closes with a short overview over some noteworthy theoretical works.

1.4.1. Overview over Considerable Cooling Concepts

In the concept of regenerative cooling, fuel is pumped through cooling channels along the structure. This way, the fuel acts as a coolant and absorbs the heat through forced convection. When the fuel is injected into the combustion, a part of the absorbed heat energy is returned into the combustion process. Originally suggested by Konstantin Tsiolkovsky,⁴⁷ regenerative cooling is probably the oldest and most evaluated method for the cooling of rocket combustion chambers. As an alternative to cooling channels, so-called *pin fins* can be used, which can be more efficient, but are also subjected to higher pressure losses.⁴⁸ If a hydrocarbon fuel such as JP-7 is used, the heat energy can also be used to refine the fuel, which additionally eases

the combustion. This process is called *thermal cracking*.⁴⁹ Due to the heating, the fuel in the channels accelerates. To prevent thermal choking, it must be ensured that the coolant velocity always remains below the speed of sound. A closer look at the mass balance and coolant equation of state reveals that this can be achieved by choosing a high channel pressure. Since the required pressures are usually higher than those in lightweight fuel tanks, an additional fuel feed and compression system is needed which increases the system complexity.^{50,51}

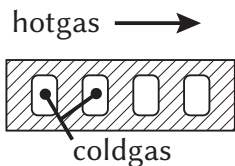
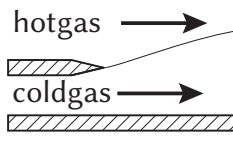
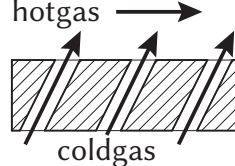
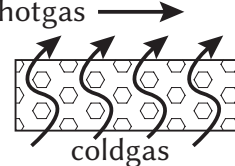
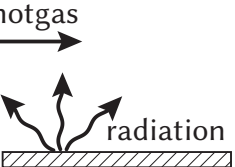
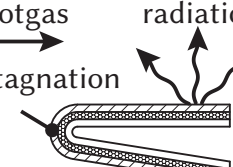
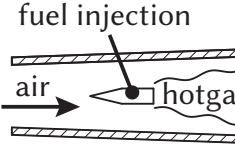
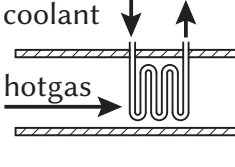
There are three cooling concepts, which are frequently used in gas turbine engines and can be characterized as *film cooling*: wall jet cooling, effusion cooling and transpiration cooling. In wall jet cooling, the coolant, mostly fuel, is injected parallel to the flow, thus forming a protective cooling film on the surface.⁵² In effusion cooling, the coolant is injected through drill holes perpendicular to the flow, so that a more uniform boundary layer is created.^{53,54} Effusion cooling is also often applied in turbine blades,⁵⁵ using air as coolant. In transpiration cooling, the coolant is pressed through a porous structure instead of drilled holes, so that the structure is cooled in a more homogeneous way.⁵⁶ Another, yet manageable, technical challenge is that the anti-oxidation coating on the porous structure also needs to be porous.⁵⁷ Since the coolant pressure needs to be only slightly higher than the hotgas pressure, the required coolant feed systems for film cooling turn out to be less complex than those for regenerative cooling.

Radiative cooling works mainly on external structures because a heat sink, for example the environment, is needed to absorb the emitted radiation. The cooling effect is rather low but increases with the power of four with the surface temperature.

Heat pipes have been considered as passive cooling systems for leading edges.^{58,59} A working fluid, for example lithium, transports the heat from the stagnation area to a heat sink where the energy can be led away radiatively. When applied to a scramjet, however, the cooling effect is rather low. Furthermore, heat pipes have poor off-design capabilities.

Core burning means that the flow is designed so that the combustion flames are kept away from the walls. As already approved in modern gas turbines, this technology is also under consideration for low hypersonic scramjet engines.⁶⁰ Precooling is for example used in the Sabre engine by Reaction Engines.³⁶ The compressed air is cooled by using a helium driven heat exchanger. An overview over various cooling techniques for hot structures is given in Tab. 1.3.

Table 1.3: Possible cooling methods for hot structures in hypersonic vehicles.

	Active Cooling Methods			
	Regenerative	Wall Jet Cooling	Effusion	Transpiration
				
cooling effect	high	high	high	very high
system complexity	high	medium	medium	medium
	+ field-tested in rocket engines + can use fuel as coolant - requires high channel pressure - complex pump system required	+ field-tested in gas turbines + can use fuel as coolant - requires high coolant mass flux	+ field-tested in gas turbines + can use fuel as coolant - requires high coolant mass flux	+ more efficient than effusion - requires porous surface coating - requires high coolant mass flux
	Passive Cooling Methods		Other Cooling Methods	
	Radiative	Heat Pipe	Core Burning	Precooling
				
cooling effect	medium	low	low	very high
system complexity	low	medium	low	very high
	+ very robust - requires heatsink (e.g. environment) - works mainly on external surfaces	+ robust - requires heatsink - limited operating range - works mainly on leading edges	+ field-tested in gas turbines + combinable with other methods - low hypersonic regime only	- requires high coolant mass flux - reduces engine performance - heavily increases system mass

1.4.2. Cooling Concepts of Flown and Upcoming Vehicles

The engine of the X-43A experimental vehicle, which passed three short-timed test flights between 2001 and 2004, was mainly made out of a water cooled copper alloy, which would work as a heat sink during the time of the experiment.⁶¹

The X-51A low hypersonic demonstrator vehicle, which conducted five long-duration flight tests between 2010 and 2013, was mainly built out of standard aerospace metals such as aluminum, steel, inconel and titanium. The leading edges were protected by carbon/carbon composites, critical areas were protected by silica-based ceramic tiles.⁶² The hydrocarbon jet fuel was pumped through cooling channels along the hot ceramic structures, which reached a maximum temperature of 2150 K.^{37,63}

An experimental transpiration cooling system was flown on the SHEFEX-II vehicle, where a porous C/C structure was cooled with nitrogen.²³ A successor experiment is planned on the upcoming SHEFEX III flight experiment.⁶⁴ The upcoming HIFiRE 8 experiment, which is expected to reach $Ma = 6$, will not be equipped with active cooling.²⁶

1.4.3. Scramjet Thermal Management: Literature for Consideration

The problem of thermal management is briefly mentioned in the standard works on the scramjet engine by Heiser and Pratt,³ and Segal.⁶⁵ A general overview over considerable cooling strategies and appropriate materials can be found in the Work of Bouchez,^{66,67} and Glass.⁶⁸

There is however very little literature about overall system considerations on scramjet thermal management. The regenerative concept has been addressed by Pagel and Warmbold,⁶⁹ discussing general feasibility and possible cooling channel pressures. Kanda et al.,^{50,70,71} and Qin et al.⁷² investigated the applicability of a turbopump powered cooling cycle for an overall scramjet system. Focusing on the combustion chamber, Zander and Morgan,^{73,74} numerically investigated a combination of radiative and regenerative cooling.

In order to estimate the convective heat loads, all of these works relied on the Eckert's empiric *Reference Enthalpy* model,⁷⁵ or at least a slightly modified version of it,⁷⁶ which is known to be rather inaccurate for the turbulent high enthalpy flows which occur in a typical scramjet engine.⁷⁷ More accurate investigations of the short-timed HyShot II experiment computational fluid dynamics have been performed by Crow et al.⁷⁸ In a similar work, Capra et al.⁷⁹ investigated the $Ma = 8$ reentry of the SCRAMSPACE vehicle. According to the author's knowledge, a coupled thermostructural investigation for proving that a thermally balanced $Ma = 8$ flight is theoretically possible has not been published so far.

1.5. Structure of This Work

In order to estimate the equilibrium temperatures and resulting thermal stresses within the structure, the physical fields of structural mechanics, aerothermodynamics, chemical combustion and thermal radiation must be regarded, see Fig. 1.6. When such strongly interdependent physical models need to be implemented into a computer program, it is necessary to keep the structure and processing needs of the generated data within a maintainable scale.

Apart from the FLOWer program, which was used to model the inlet flow field, and kindly provided by DLR, none of the available software packages seemed to be suitable for approaching this problem in an efficient way. It was therefore decided to create the necessary computer program from scratch, using the Fortran 2003 programming language.

To allow a traceability of the calculations performed in this work, the next three chapters will cover the aerodynamic, thermal and mechanical fundamentals which were needed to create this program.

The theoretical chapters are followed by an investigation into the thermal field of the inlet in chapter five, the combustion chamber in chapter six. Thermomechanical deformation and stresses are discussed in chapter seven. The work closes with a conclusion and an outlook. A detailed material model can be found in the appendix.

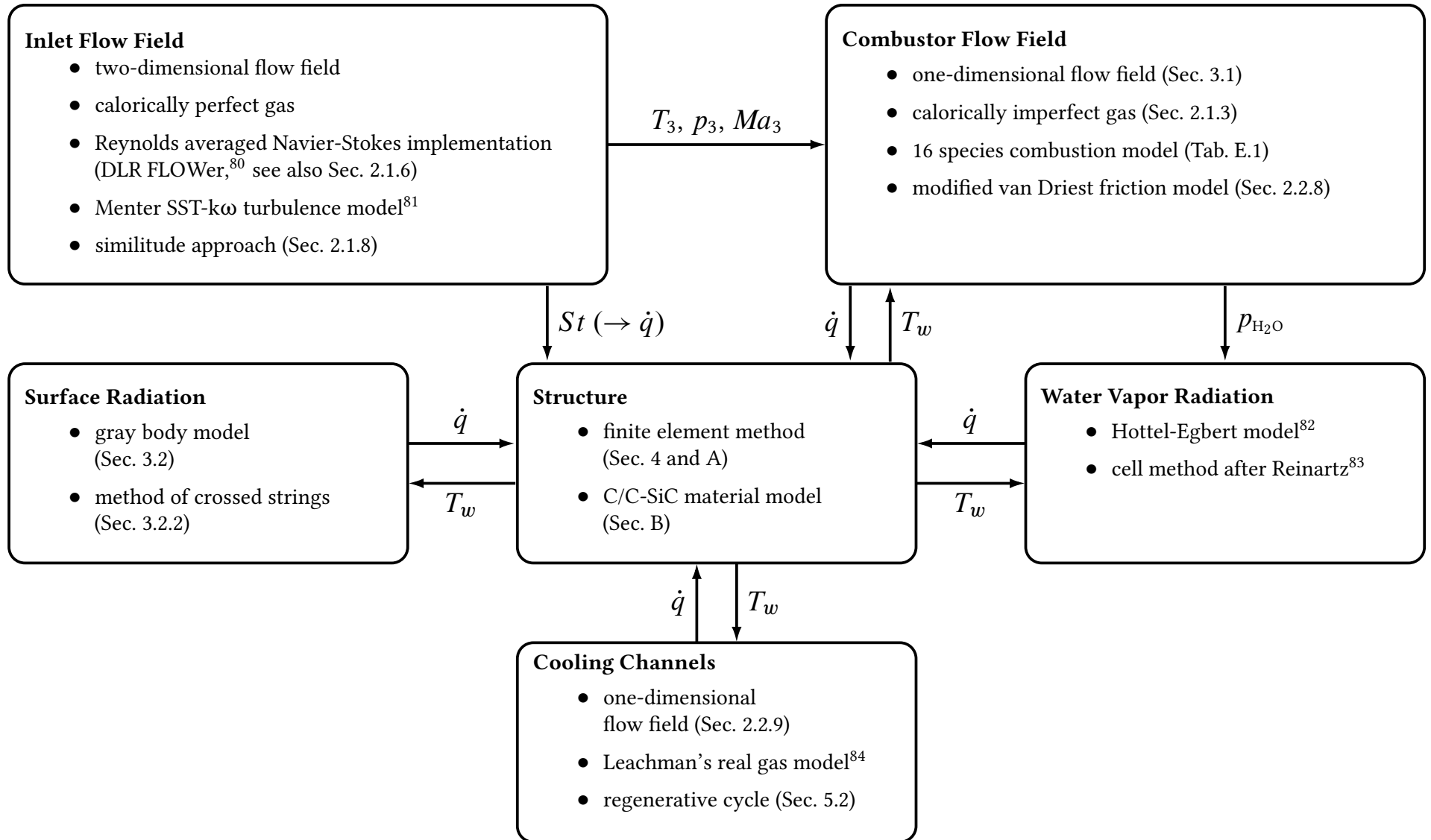


Figure 1.6: General modeling approach, interdependencies and references to relevant sections within this work.

2. Aerothermodynamic Fundamentals

The field of aerothermodynamics deals with the description of the aerodynamic and thermal behavior of fluids. To do so, the balance equations for mass, momentum and energy need to be solved in respect to the given boundary conditions. A fluid is physically characterized by its abilities to store and transport kinetic and thermal energy, which are expressed by the fluids' density ρ (or the specific volume $v = \rho^{-1}$), its heat capacity c_p , the dynamic viscosity μ and the thermal conductivity λ (in Anglo-Saxon also denoted as k). The relation between temperature T , pressure p and density ρ is expressed by an *equation of state*.

The solution of the momentum balance, which is often described by the *Navier-Stokes-Equations*, is very costly in terms of calculation power, however reasonable simplifications can be made in many cases. The most important simplification is the *boundary layer theory*. This theory contains descriptions for velocity and temperature distributions close to the wall, from which conclusions on local friction and heat transfer effects between the fluid and the wall can be drawn. A special type of the boundary layer theory is the theory by *van Driest*, which allows the modeling of compressible and supersonic boundary layers on external surfaces.

In order to give represent the internal flow field of the combustion chamber in a better way, a modification for van Driest's theory for channel flows is suggested in this work. Dimensionless *similarity parameters* are often used in aerodynamics in order to reduce the number of unknowns in the relevant equations. If a relation between two similarity parameters cannot be expressed analytically, it can be approximated by a regression curve through experimental data or data provided by a direct solution of the Navier-Stokes equations. In order to be able to estimate the local friction and heat loads on the structure, the present section will give an overview of the necessary equations. Finally, an overview over the supersonic compression and expansion processes, which are needed during the design process of the inlet, is given.

2.1. Governing Equations and Physical Quantities

The energy storage and transport within a fluid can be characterized by its caloric and transport properties. Once these properties are known, the conservation equations and the equation of state can be set up and the flow field can be determined.

2.1.1. Fluid Equations of State

The thermodynamic state of a fluid can be described by its temperature T , pressure p and specific volume v . A *thermal equation of state* relates these three variables over a function. A common rule of thumb is, that for pressures below 10 bar, and temperatures above 200 K, the *ideal gas law*

$$p v = R T \quad (2.1)$$

can be applied. If intermolecular attractions are to be considered, for example at high pressures or very low temperatures, *cubic equations of state* in the shape of

$$p = \frac{R T}{v - b} - \frac{a \alpha(T)}{(v - b r_1)(v - b r_2)} \quad (2.2)$$

give good results.⁸⁵ Herein, α is an empirical function of the temperature. It is customized for the chosen cubic equation of state and the considered fluid. The constants a and b depend on the critical temperature T_c and critical pressure p_c of the fluid, so that

$$a = \Omega_a \frac{(R T_c)^2}{p_c}, \quad (2.3)$$

and

$$b = \Omega_b \frac{R T_c}{p_c}. \quad (2.4)$$

For important cubic equations, the parameters r_1 , r_2 , Ω_a and Ω_b are listed in Tab. 2.1.

Table 2.1: Calibration parameters for important cubic equation models.

	van der Waals	Soave-Redlich-Kwong ⁸⁶	Peng-Robinson ⁸⁷
r_1	0	0	$-1 - \sqrt{2}$
r_2	0	-1	$-1 + \sqrt{2}$
Ω_a	$27/64$	$X/9$	$(40 X + 24)/(147 - 37 X)$
Ω_b	$1/8$	$X/3$	$X/(X + 9)$
X	-	$2^{1/3} - 1$	$(6\sqrt{2} + 8)^{1/3} - (6\sqrt{2} - 8)^{1/3} - 1$

Literature provides a huge variety of empirical α -functions other than those suggested in the original papers. In the case of the Soave-Redlich-Kwong approach, however, most modifications are not significantly better than the one suggested in Soave's original paper.⁸⁸ For the Peng-Robinson model, the model of Aznar and Telles,⁸⁹ which was mainly designed for hydrocarbons, gives very satisfying results.⁹⁰ A detailed explanation of the handling of mixtures of gases and liquids is given by Jaubert and Privat.⁹¹ *Virial equations of state* try to approach the surface in the p - v - T space by several high order polynomials. An important example of a virial equation of state is the Lee-Kessler equation, which is used to model hydrocarbon fuels such as kerosene.^{92,93} Another approach is to model the equation of state over the *free Helmholtz energy*. This is done for example in the model by Leachman et al.,⁸⁴ which in this work is used to model cryogenic hydrogen.

2.1.2. Thermodynamic Coefficients

In order to simplify the thermodynamic description of real gases, it is expedient to introduce the isobaric thermal expansion coefficient α , which is not to be confused with the α -function in Eq. (2.2), the isochoric stress coefficient β and the isothermal compressibility coefficient κ . They depend on the chosen equation of state, and read for a constant mass composition Y_i ⁹⁴

$$\alpha = \frac{1}{v} \left(\frac{\partial v}{\partial T} \right)_p, \quad (2.5)$$

$$\beta = \frac{1}{p} \left(\frac{\partial p}{\partial T} \right)_v, \quad (2.6)$$

$$\kappa = -\frac{1}{v} \left(\frac{\partial v}{\partial p} \right)_T, \quad (2.7)$$

and are connected over the general relation

$$\alpha = p \beta \kappa. \quad (2.8)$$

For an ideal gas, the thermodynamic coefficients simplify to $\alpha = \beta = 1/T$ and $\kappa = 1/p$.

2.1.3. Caloric Properties of Pure Fluids

To describe a thermodynamic process, it is necessary to know the caloric properties of the considered fluid. Frequently used magnitudes are the specific heat capacities which denote the partial derivative of the internal energy e at a constant specific volume v with respect to temperature

$$c_v = \left(\frac{\partial e}{\partial T} \right)_v = T \left(\frac{\partial s}{\partial T} \right)_v, \quad (2.9)$$

and the temperature derivative of the specific enthalpy at a constant pressure p

$$c_p = \left(\frac{\partial h}{\partial T} \right)_p = T \left(\frac{\partial s}{\partial T} \right)_p. \quad (2.10)$$

Both heat capacities are linked over the relation

$$c_p - c_v = \underbrace{p v T \alpha \beta}_{=R, \text{ if ideal gas}}. \quad (2.11)$$

The specific heats are generally both temperature and pressure dependent. By creating the total derivatives of h and s

$$dh = \left(\frac{\partial h}{\partial T} \right)_p dT + \left(\frac{\partial h}{\partial p} \right)_T dp, \quad (2.12)$$

$$ds = \left(\frac{\partial s}{\partial T} \right)_p dT + \left(\frac{\partial s}{\partial p} \right)_T dp, \quad (2.13)$$

it can be seen that the change of enthalpy and entropy have both temperature dependent and pressure dependent parts. It is best practice to uncouple both dependencies as follows: a model for the temperature-dependent specific heat capacity c_p° at reference pressure is created. From Eq. (2.10), an integral for the specific enthalpy in relation to a reference temperature T° at a reference pressure p° can be obtained

$$h^\circ = \int_{T^\circ}^T c_p^\circ d\tilde{T} + h_{\text{ref}}^\circ. \quad (2.14)$$

Similarly, the function for the specific entropy s° at a reference pressure p° reads

$$s^\circ = \int_{T^\circ}^T \frac{c_p^\circ}{T} d\tilde{T} + s_{\text{ref}}^\circ. \quad (2.15)$$

The pressure dependence is then incorporated into the model over the so called *departure functions*. From Eqs. (2.8) and (2.12) it follows for the enthalpy that⁹⁵

$$\begin{aligned} h - h^\circ &= \int_0^p \left(\frac{\partial h}{\partial \tilde{p}} \right)_T d\tilde{p} \\ &= \int_0^p \left[v - T \left(\frac{\partial v}{\partial T} \right)_{\tilde{p}} \right]_T d\tilde{p} \\ &= p v - R T + \int_\infty^v \left[T \left(\frac{\partial p}{\partial T} \right)_{\tilde{v}} - p \right]_T d\tilde{v}, \end{aligned} \quad (2.16)$$

and for the entropy

$$\begin{aligned} s - s^\circ &= \int_0^p \left(\frac{\partial s}{\partial \tilde{p}} \right)_T d\tilde{p} \\ &= \int_0^p \left[\frac{R}{\tilde{p}} - \left(\frac{\partial v}{\partial T} \right)_{\tilde{p}} \right]_T d\tilde{p} \\ &= R \ln \left(\frac{p v}{R T} \right) + \int_\infty^v \left[\left(\frac{\partial p}{\partial T} \right)_{\tilde{v}} - \frac{R}{\tilde{v}} \right]_T d\tilde{v}. \end{aligned} \quad (2.17)$$

Finally, the temperature and pressure dependent specific heat capacity c_p reads

$$c_p - c_p^\circ = \left(\frac{\partial(h-h^\circ)}{\partial T} \right)_p. \quad (2.18)$$

It is easy to see that if a gas follows the ideal gas relation in Eq. (2.1), the departure functions become zero, meaning that for an ideal gas, neither the enthalpy nor the specific heat capacity depend on pressure. Since in thermodynamics a *real gas* is any gas that does not follow Eq. (2.1), one might identify the pressure dependence of the caloric properties as *real gas effects*. However, Hirschel⁹⁶ pointed out that there is some confusion regarding the term *real gas effects* in literature. Sometimes it is feasible to neglect the temperature dependence of the caloric properties of an ideal gas, thus achieving a *calorically perfect* gas description. While in their original definition *real gas effects* denote the pressure dependence of the caloric properties, which is a consequence of Van-der-Waals forces that are not perceived in the ideal gas approach, a wide-spread practice is to use the expression in order to point out that the gas is not calorically perfect. This however is a little inaccurate, because an ideal gas is still not a real gas, even though it can be calorically imperfect. For

specific heats and entropies most fluids of technical relevance are published in the *JANAF Joint Army-Navy-Airforce thermodynamical tables*.⁹⁷ A digital version of this database that is implemented in many codes is Gordon and McBride's *Computer Program for Calculation of Complex Chemical Equilibrium Compositions and Applications*,^{98,99} which refers all polynomials to $T^\circ = 298.15\text{ K}$ and $p^\circ = 1\text{ bar}$. Although Gordon and McBride's tables provide good approximations to the JANAF database, their correlations are not continuous, which can under some conditions prevent some algorithms from converging. In the present investigation, best performance and stability was achieved by spline-interpolating Gordon and McBride's correlations.

Similar relations also exist for high pressure viscosity $\mu - \mu^\circ$ and thermal conductivity $\lambda - \lambda^\circ$, however, one might prefer empirical models such as summarized by Kleiber and Joh.¹⁰⁰

2.1.4. Isentropic State Transition and Total States of Moving Fluids

For a steady fluid, two flow states (T_1, p_1, v_1) and (T_2, p_2, v_2) are called *isentropic* if they have the same specific entropy, so that $s_1 = s_2$. From the equations of the last section, it can be shown, that for moderate state changes, the entropy of two states is equal if their pressures and specific volumes fulfill the relation¹⁰¹

$$p_1 v_1^{\gamma_1} = p_2 v_2^{\gamma_2}, \quad (2.19)$$

where the *adiabatic exponent* γ (sometimes called κ) follows the general relation

$$\gamma = -\frac{c_p}{c_v} \frac{v}{p} \left(\frac{\partial p}{\partial v} \right)_T = \frac{c_p}{c_v} \frac{\beta}{\alpha}, \quad (2.20)$$

which for an ideal gas simplifies to the temperature dependent *ratio of specific heats*

$$\gamma = \frac{c_p}{c_v} = \frac{c_p}{c_p - R}. \quad (2.21)$$

To perform balance investigations of a moving fluid, the specific kinetic energy is added to the enthalpy, this yields in the *total enthalpy*

$$h_t = h + \frac{u^2}{2}, \quad (2.22)$$

where u is the velocity of the flow. Generally, the *total temperature* is to be obtained from Eqs. (2.14) and (2.16), while the corresponding *total pressure* is received from Eq. (2.19) and the chosen equation of state.

If air is considered, the well known simplifications

$$\frac{T_t}{T} \approx 1 + \frac{\gamma - 1}{2} Ma^2 \quad (2.23)$$

and

$$\frac{p_t}{p} \approx \left(1 + \frac{\gamma - 1}{2} Ma^2\right)^{\frac{\gamma}{\gamma - 1}} \quad (2.24)$$

should not be used in the hypersonic flow region ($Ma \gtrsim 5$), since the 'real gas effects' cause significant deviations (see Fig. 2.1). However, they may be useful to calculate initial values to start a numerical iteration process of T_t and p_t .

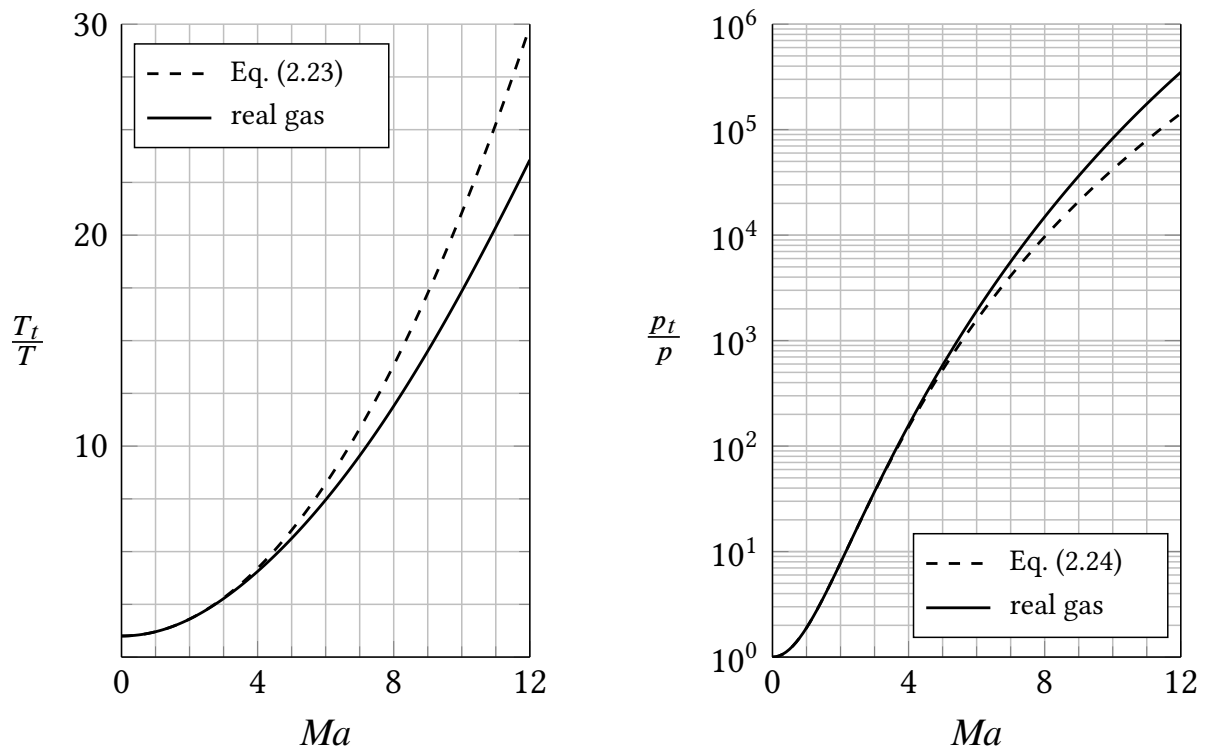


Figure 2.1: Total temperature (left) and total pressure (right) of air at 30 km altitude versus Ma , calculated with both the perfect and the imperfect model.

2.1.5. Transport Properties of a Newtonian Fluid

In analogy to solid mechanics, the mechanical stress state of a fluid can be described by Cauchy's stress tensor

$$\boldsymbol{\sigma} = \begin{pmatrix} \sigma_{xx} & \sigma_{xy} & \sigma_{xz} \\ & \sigma_{yy} & \sigma_{yz} \\ \text{sym.} & & \sigma_{zz} \end{pmatrix} = \begin{pmatrix} \sigma_{xx} & \tau_{xy} & \tau_{xz} \\ & \sigma_{yy} & \tau_{yz} \\ \text{sym.} & & \sigma_{zz} \end{pmatrix}. \quad (2.25)$$

Generally, the stress tensor contains a hydrostatic and a deviatoric contribution

$$\sigma_{ij} = -p \delta_{ij} + \sigma'_{ij}, \quad (2.26)$$

where δ_{ij} is the Kronecker delta. In fluid mechanics, the deviatoric part $\boldsymbol{\sigma}'$ is caused by inner frictions between the particles of a moving fluid and is also called *viscous stress*. In a *Newtonian* fluid, the viscous stress is assumed to depend linearly on the velocity gradient¹⁰²

$$\sigma'_{ij} = \mathcal{C}_{ijkl} \frac{1}{2} \left(\frac{\partial u_k}{\partial x_l} + \frac{\partial u_l}{\partial x_k} \right). \quad (2.27)$$

For most cases of technical relevance, the viscosity of the fluid is isotropic, so that the viscosity tensor \mathcal{C} can be defined by two parameters,

$$\mathcal{C}_{ijkl} = 3\zeta \delta_{ij} \delta_{kl} + 2\mu \left(\delta_{ik} \delta_{jl} + \delta_{il} \delta_{jk} - \frac{2}{3} \delta_{ij} \delta_{kl} \right), \quad (2.28)$$

with ζ being the bulk viscosity and μ the shear viscosity of the fluid. Both properties depend strongly on temperature, and weakly on pressure. While the shear viscosity of most fluids is known very well, and extensive data is available for example in the Gordon-McBride database,^{98,99} very little data is available on the bulk viscosity. Stokes' hypothesis that the bulk viscosity is very small and can be neglected seems to be suitable for many cases in practice. However, this is not necessarily the case for extreme flow conditions like high enthalpy flows.¹⁰³ In those cases, the application of Stokes' hypothesis is not empirically verified, but rather a consequence of a lack of data. It is especially known that Stokes hypothesis is not appropriate for Carbon Dioxide.¹⁰⁴

Fourier's law provides a relation between the temperature gradient and the heat flux. In a general continuum, the heat flux vector reads

$$\dot{q}_i = -\lambda_{ij} \frac{\partial T}{\partial x_j}. \quad (2.29)$$

In an isotropic medium, the thermal conductivity matrix λ reduces to a scalar value λ , so that Eq. (2.29) simplifies to

$$\dot{q}_i = -\lambda \frac{\partial T}{\partial x_i}. \quad (2.30)$$

As with the dynamic viscosity, the thermal conductivity λ strongly depends on temperature and weakly on pressure.

2.1.6. Conservation Equations for a Flow Field

To provide the full description of a flow field, velocity vector, density, temperature and pressure of the fluid need to be determined at each point of the considered domain. If the fluid's caloric and transport properties are known, the flow state can be determined by considering the conservation laws of mass, momentum, and energy. Additionally, an equation of state is needed that provides a relation between temperature, pressure and density. In continuum mechanics, movement can be described from two different points of view. In the approach of Lagrange, the position vector of a mass increment is tracked over time, while from Euler's point of view, mass fluxes through a fixed volume are investigated. Based on the shape of the problem, Lagrange's point of view has proven to be convenient in solid mechanics, while in fluid mechanics, Euler's approach is usually preferred.

The relation between velocity and density is achieved through the continuity equation, which demands conservation of mass

$$\frac{D\rho}{Dt} + \rho \frac{\partial u_i}{\partial x_i} = \frac{\partial \rho}{\partial t} + u_i \frac{\partial \rho}{\partial x_i} + \rho \frac{\partial u_i}{\partial x_i} = \frac{\partial \rho}{\partial t} + \frac{\partial (\rho u_i)}{\partial x_i} = 0. \quad (2.31)$$

It follows from Euler's approach that the acceleration of a moving particle through a fixed volume is the material derivative of the velocity vector \mathbf{u}

$$a_i = \frac{Du_i}{Dt} = \frac{\partial u_i}{\partial t} + u_j \frac{\partial u_i}{\partial x_j}. \quad (2.32)$$

Inserting Eq. (2.32) into Cauchy momentum equation yields

$$\rho \left(\frac{\partial u_i}{\partial t} + u_j \frac{\partial u_i}{\partial x_j} \right) = \rho g_i + \frac{\partial \sigma_{ij}}{\partial x_j}, \quad (2.33)$$

where \mathbf{g} is the acceleration caused by an external force field (e.g. gravitation), ρ the density, and $\boldsymbol{\sigma}$ the Cauchy stress tensor. Assuming a Newtonian fluid with zero bulk viscosity, one can insert Eq. (2.28) in Eq. (2.26), and Eq. (2.26) in Eq. (2.33) to get

the well known *Navier-Stokes* equations, which provide a relation between velocity and pressure of the flow

$$\rho \left(\frac{\partial u_i}{\partial t} + u_j \frac{\partial u_i}{\partial x_j} \right) = \rho g_i + \frac{\partial}{\partial x_j} \left[\mu \left(\frac{\partial u_i}{\partial x_j} + \frac{\partial u_j}{\partial x_i} - \frac{2}{3} \frac{\partial u_k}{\partial x_k} \delta_{ij} \right) \right] - \frac{\partial p}{\partial x_i}. \quad (2.34)$$

Due to energy conservation, the enthalpy of the fluid will change in dependence of heat flux, and change of hydraulic and deviatoric pressure

$$\rho \frac{Dh_t}{Dt} = - \frac{\partial \dot{q}_i}{\partial x_i} + \frac{\partial p}{\partial t} + \frac{\partial}{\partial x_i} (\sigma'_{ij} u_j). \quad (2.35)$$

Inserting Fourier's law from Eq. (2.30), the total differential of the enthalpy in Eq. (2.35) delivers a formulation for the energy balance in dependence of temperature¹⁰⁵

$$\rho c_p \left(\frac{\partial T}{\partial t} + u_i \frac{\partial T}{\partial x_i} \right) = \frac{\partial}{\partial x_i} \left(\lambda \frac{\partial T}{\partial x_i} \right) + \alpha T \left(\frac{\partial p}{\partial t} + u_i \frac{\partial p}{\partial x_i} \right) + \sigma'_{ij} \frac{\partial u_i}{\partial x_j}, \quad (2.36)$$

with α from Eq. (2.5). For a Newtonian and ideal gas, Eq. (2.36) simplifies to

$$\begin{aligned} \rho c_p \left(\frac{\partial T}{\partial t} + u_i \frac{\partial T}{\partial x_i} \right) &= \frac{\partial}{\partial x_i} \left(\lambda \frac{\partial T}{\partial x_i} \right) + \left(\frac{\partial p}{\partial t} + u_i \frac{\partial p}{\partial x_i} \right) \\ &+ \mu \frac{\partial}{\partial x_i} \left[\left(\frac{\partial u_i}{\partial x_j} + \frac{\partial u_j}{\partial x_i} - \frac{2}{3} \frac{\partial u_k}{\partial x_k} \delta_{ij} \right) u_j \right]. \end{aligned} \quad (2.37)$$

2.1.7. A Note on Numerical Solving of the Navier-Stokes Equations

Determining the flow field of a fluid at given boundary conditions requires to find the temperature, pressure and velocity field that satisfy the mass balance Eq. (2.31), momentum balance Eq. (2.34), and energy balance Eq. (2.37) at any point within the considered domain. However, these equations have turned out to be very complicated. Even for an incompressible case with given initial and boundary conditions, it is not known whether the Navier-Stokes equations actually provide a deterministic description of the flow field.

In fact, finding the mathematical proof of this question is widely considered as one of the most challenging mathematical problems of our time.¹⁰⁶

In most cases, the domain of the considered flow field is discretized using the finite volume method or the finite difference method. Sometimes, but less often, finite element approaches are chosen. The resolution of the discretization is of significant importance.

An obvious approach is the *Direct Numerical Simulation (DNS)*, where the domain is discretized in such a fine resolution, that every significant microstructural swirl (*eddy*) is captured by the model. This approach allows a very deep insight into the microstructure of a flow field, but the capacity limits of available high performance computers reduce its application to very small and simple problems. For most applications of technical relevance, the discretization needs to be coarsened to more economic length scales. Since the influence of eddies can not be captured by coarse grids, a typical approach are *Reynolds Averaged Navier Stokes (RANS)*-simulations, where turbulence models provide simplifying time-averaged statistical approximations of the energy transportation phenomena on a subgrid level.

If more detailed solutions are required, a reasonable compromise between DNS and RANS is to perform a *Large Eddy Simulation (LES)*, where a low pass filtering on the Navier-Stokes equations is performed to capture large vortices, while unresolved swirls are homogenized by statistical subgrid models similar to the turbulence models used in RANS. For some problems, friction and heat transfer of a flow may be insignificant. By setting the thermal conductivity λ , as well as both viscosities ζ and μ , and therefore the viscosity tensor \mathfrak{C} , to zero, the conservation equations for mass, momentum, and energy are simplified to the *Euler-Equations*.

A significant problem occurs when the aerodynamic heating of a structure is investigated, since the time scales of the individual domains of fluid and structure differ by four to six orders of magnitude. An economic remedy is provided by the theory of *similarity mechanics*. Herein, the flow field is calculated only once, where the surface temperature is assumed to be constant and isotropic. Then, the aerodynamic friction forces and heat fluxes are made dimensionless and impinged as boundary condition on the thermostructural models. In many cases, the dependence of friction and heat transfer on the surface temperature is canceled out this way.

This *similitude* approach, however, doesn't provide reliable results when structural deformation or chemical combustion are present. As long as the flow field is simple enough, a remedy can be found in the *boundary layer theory*, where one-dimensional solutions of the Navier-Stokes equations are combined with similitude approaches.

2.1.8. Similarity Parameters in Aerothermodynamics

In order to realize an engineering concept, the physical dimensions of the variables defining that concept must be known. Sometimes however, it is easier to rearrange the variables into dimensionless expressions, and perform the necessary calculations in this dimensionless space. In case of an aerospace vehicle, an engineer might be interested for example in the dimensional quantities of lift, drag, flight speed, flight altitude, fuel consumption and so on. If ξ_1 was one of these quantities, its actual magnitude could be determined from other dimensional, positive real variables ξ_i . Their relation would form an equation in the shape of

$$f(\xi_1, \xi_2, \dots, \xi_n) = 0. \quad (2.38)$$

The modern interpretation of Buckingham's Π -Theorem¹⁰⁷ is, that if such a relation $f(\xi_i) = 0$ exists, it can be transformed to a corresponding dimensionless relation

$$F(\pi_1, \pi_2, \dots, \pi_m) = 0, \quad (2.39)$$

where the dimensionless *similarity parameters* π_j can be determined by a product such as

$$\pi_j = \xi_{r+j} \prod_{i=1}^r \xi_i^{\alpha_{ji}}, \quad (2.40)$$

with $m = n - r$. Here, r is the number of base dimensions *length, mass, time* and *temperature* present in the function f . Non-base dimensions on the other hand are dimensions that can be created from a combination of base dimensions, for example *pressure, speed, energy* and *momentum*. The real constants α_{ji} can be determined through an analysis of all base and non-base dimensions of the participating variables x_i . The benefit of this method is that for many cases, the number of unknowns is reduced.¹⁰⁸ Additionally, the isolation of dimensions eases the comparison of different but similar problems. In the theory of aerodynamics, the most important similarity parameters are:

- **Mach Number**

Describing the flow speed u relative to the speed of sound c , see also Eq. (2.151), the Mach number is a measure for the transportation speed of pressure information through a fluid

$$Ma = \frac{u}{c}. \quad (2.41)$$

- **Reynolds Number**

The Reynolds number describes the relation between momentum and friction forces within a fluid. It is generally defined as

$$Re_x = \frac{\rho u x}{\mu}, \quad (2.42)$$

where density, speed and shear viscosity can be defined in reference to freestream conditions, the edge of the boundary layer or any uniquely defined reference state. The length scale x is determined by the bounding wall, but other favorable reference lengths are possible.

- **Pressure Coefficient**

The pressure Coefficient C_p , which is not to be confused with the specific heat capacity c_p , is used to compare pressure rising effects in the boundary layer independent of the flow conditions at a given position

$$C_p = \frac{p_e - p_\infty}{\frac{\rho_\infty}{2} u_\infty^2}. \quad (2.43)$$

- **Skin Friction Coefficient**

The skin friction coefficient is a measurement for friction losses in relation to the fluid's kinetic energy.

$$c_f = \frac{\tau_w}{\frac{\rho_\infty}{2} u_\infty^2}, \quad (2.44)$$

where τ_w is the wall shear stress, and ρ_∞ the density of the fluid at freestream conditions.

- **Stanton Number**

The Stanton number St (sometimes denoted as C_h), is a dimensionless measurement of the ratio of convective heat fluxes between a flow and a wall with respect to the flow's caloric energy,

$$St = \frac{\dot{q}_w}{\rho_\infty u_\infty (h_r - h_w)} \approx \frac{\dot{q}_w}{\rho_\infty u_\infty c_p (T_r - T_w)}, \quad (2.45)$$

assuming $u_\infty > 0$. In case of an adiabatic wall, the wall temperature T_w equals the recovery temperature T_r . In this case, \dot{q}_w equals zero, and thus St is not defined.

- **Prandtl Number**

Viscosity describes the ability of a fluid to transport momentum information caused by friction, while the specific heat and thermal conduction describe the ability to store and transport caloric energy. Due to the the immediate connection between friction and heat generation, the Prandtl number allows deductions concerning the relation of velocity and temperature gradients near a wall.

$$Pr = \frac{\mu c_p}{\lambda}. \quad (2.46)$$

Apart from this Prandtl number, which is sometimes also called the *laminar* Prandtl number, there is also a turbulent Prandtl number Pr_T and a mixed Prandtl number Pr_M . In turbulent flows there are perturbations, or eddies, which are sometimes too small to be captured by the calculation grid used. In order to model the shear stress near wall regions of such a flow, two new magnitudes, namely the *eddy viscosity* μ_T and the *eddy conductivity* λ_T , are introduced. The turbulent Prandtl number is then defined as

$$Pr_T = \frac{\mu_T c_p}{\lambda_T}, \quad (2.47)$$

while the mixed Prandtl number reads

$$Pr_M = \frac{\mu + \mu_T}{\lambda + \lambda_T} c_p. \quad (2.48)$$

The determination of the eddy transport properties μ_T and λ_T can be achieved by an appropriate turbulence model. One very popular method to estimate Pr_T is given by Kays and Crawford¹⁰⁹

$$Pr_T^{-1} = \frac{1}{2 Pr_{T,\infty}} + \frac{0.3 Pr}{\sqrt{Pr_{T,\infty}}} \left(\frac{\mu_T}{\mu} \right) - \left[0.3 Pr \left(\frac{\mu_T}{\mu} \right) \right]^2 \cdot \left[1 - \exp \left(- \frac{1}{0.3 Pr \left(\frac{\mu_T}{\mu} \right) \sqrt{Pr_{T,\infty}}} \right) \right]. \quad (2.49)$$

A typical value for the infinite turbulent Prandtl number is $Pr_{T,\infty} = 0.85$, while for scramjet-applications, the value $Pr_{T,\infty} = 0.89$ is sometimes found.¹¹⁰ See also Kays¹¹¹ for further reading.

- **Reynolds-Colburn Analogy Factor**

Similarity investigations of various experimental data indicate, that there must be a connection between friction coefficient c_f , and the Stanton number St . This relation is defined over the Reynolds Analogy Factor

$$\zeta = \frac{c_f}{2 St}. \quad (2.50)$$

In his original publication, Colburn¹¹² suggested the relation

$$\zeta = Pr^{\frac{2}{3}} \text{ for } Pr \text{ near } 1, \quad (2.51)$$

where there is a little variation in the exponent over Pr in literature. At least for the laminar case, this *Reynolds-Colburn Analogy* provides very good results over a range of $0.01 \leq Pr \leq 100$.¹¹³ For turbulent flows, this analogy is less accurate. An analytical formulation for ζ^a was given by van Driest¹¹⁴

$$\zeta = \frac{1}{u_\infty} \int_0^\delta Pr_M \exp\left(-\int_0^y \frac{1 - Pr_M}{\tau} \frac{\partial \tau}{\partial \tilde{y}} d\tilde{y}\right) \frac{\partial u}{\partial y} dy \quad (2.52)$$

where τ is the shear stress of the flow within the boundary layer

$$\tau = (\mu + \mu_T) \frac{du}{dy}, \quad (2.53)$$

and y is the direction perpendicular to the wall distance. Combining similarity considerations with experimental data from Nikuradse,¹¹⁵ van Driest developed a semi-empirical correlation from Eq. (2.52) for a turbulent flow over a flat plate, which depends on the friction factor c_f

$$\begin{aligned} \zeta Pr_{T,\infty}^{-1} &= 1 + 5 \sqrt{\frac{c_f}{2}} \left\{ \left(\frac{1 - Pr_{T,\infty}}{5\kappa} \right) \left[\frac{\pi^2}{6} + \frac{3}{2} (1 - Pr_{T,\infty}) \right] \right. \\ &\quad \left. + \left(\frac{Pr}{Pr_{T,\infty}} - 1 \right) + \ln \left[1 + \frac{5}{6} \left(\frac{Pr}{Pr_{T,\infty}} - 1 \right) \right] \right\}, \quad (2.54) \end{aligned}$$

for $0.7 < Pr_{T,\infty} < 1$. Although being originally developed for incompressible flows, Eq. (2.54) gives good values even for higher Mach numbers.

^aNote that in the original paper,¹¹⁴ van Driest integrated by substituting y with τ . Mathematically, this is not correct, since the function $\tau(y)$ is not bijective. This mistake has been corrected in Eqs. (2.52) and (2.56).

- **Recovery Factor**

The total enthalpy h_t is the sum of the specific enthalpy and kinetic energy of a fluid. The total temperature T_t is the temperature a moving fluid would have if the kinetic energy was fully converted to caloric energy. Anticipating Prandtl's boundary layer concept, which is described in the next chapter, it is assumed that the fluid is fully stopped in areas infinitesimally close to a wall. Excluding heat losses through the wall for this consideration, it is observed that thermal diffusion and viscous effects prevent the fluid in this area to actually reach the total temperature. For air and combustion gases, only a part $r < 1$ of this kinetic energy can be *recovered* at this point, a slightly lower *recovery temperature* or *adiabatic wall temperature* T_r , can be reached physically. The recovery factor is defined as

$$r = \frac{h_r - h_\infty}{h_t - h_\infty}, \quad (2.55)$$

where h_r is the enthalpy of the fluid at T_r , and h_∞ the enthalpy at freestream condition. For turbulent flows, the recovery factor is generally defined as¹¹⁴

$$r = \frac{2}{(u_\infty)^2} \int_0^\delta Pr_M \exp\left(-\int_0^y \frac{1 - Pr_M}{\tau} \frac{\partial \tau}{\partial \tilde{y}} d\tilde{y}\right) \left[\int_0^y \exp\left(\int_0^{\tilde{y}} \frac{1 - Pr_M}{\tau} \frac{\partial \tau}{\partial \tilde{y}} d\tilde{y}\right) \frac{\partial u}{\partial \tilde{y}} d\tilde{y} \right] \frac{\partial u}{\partial y} dy \quad (2.56)$$

For preliminary estimations, Ackermann's correlation¹¹⁶ is widely accepted,

$$r = \begin{cases} \sqrt{Pr} & \text{if the flow is laminar,} \\ \sqrt[3]{Pr} & \text{if the flow is turbulent.} \end{cases} \quad (2.57)$$

Consistent with Eq. (2.54), an approximation for the turbulent flat plate is

$$\begin{aligned} r Pr_{T,\infty}^{-1} &= 1 + \frac{2}{\kappa} \sqrt{\frac{c_f}{2}} (1 - Pr_{T,\infty}) \left[\frac{\pi^2}{6} + \frac{3}{2} (1 - Pr_{T,\infty}) \right] \\ &+ 25 \frac{c_f}{2} \left\{ \left(\frac{Pr}{Pr_{T,\infty}} - 1 \right) + 2 \ln \left[1 + \frac{5}{6} \left(\frac{Pr}{Pr_{T,\infty}} - 1 \right) \right] \right. \\ &\left. + \ln 6 \ln \left[1 + \frac{7}{8} \left(\frac{Pr}{Pr_{T,\infty}} - 1 \right) \right] - \ln 6 \ln \left[1 + \frac{1}{4} \left(\frac{Pr}{Pr_{T,\infty}} - 1 \right) \right] \right\}. \end{aligned} \quad (2.58)$$

2.2. Boundary Layer Theory and Heat Transfer

If the differential equation for the energy balance in Eq. (2.37) is to be solved, a wall temperature distribution is required as boundary condition. The wall temperatures however depend on the convective and radiative heat loads on the wall, and the thermal behavior of the structure. This way, an interdependence between the flow field and the thermal field within the structure is created.

In the absence of chemical reaction, the local values of c_f and therefore St depend very weakly on the local wall temperature, and can even be determined sufficiently if only a rough estimation of the wall temperature is available. Thus, the problem of flow and structure can be easily decoupled. This changes if a combustion is present in the flow field. In this case the calculations of the structure and the combustive flow have to be iterated. In order to save the calculation cost of solving the full conservation equations for mass (2.31), momentum (2.34), and energy (2.37), a simplified representation of the flow field is chosen. This approach is the *boundary layer theory*.

The concept of the boundary layer was introduced by Ludwig Prandtl in 1904,¹¹⁷ and is based on the idea that friction and heat transfer effects in a flow are only significant in areas very close to the wall. The boundary layer theory provides similarity methods for estimating velocity, pressure and temperature gradients in areas very close to the wall. This information allows the estimation of aerodynamic friction and wall-fluid heat exchange. There are four different types of boundary layer shapes, which are relevant for the present investigation namely the *flat plate*, the two-dimensional *channel flow*, and the axisymmetric *pipe flow* (see Fig. 2.2).

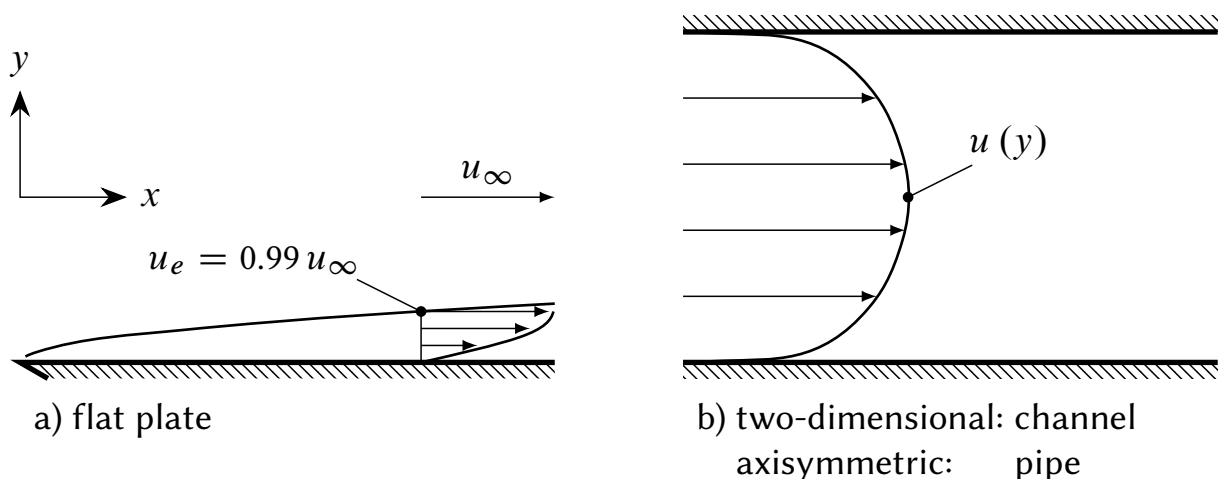


Figure 2.2: Comparison between flat plate flow and channel flow or pipe flow.

For the application on the scramjet engine, the flat plate case is suitable for preliminary investigations on the external surfaces such as the double ramp of the inlet and the nose, as well as manual verifications of CFD calculations. The axisymmetric pipe flow model is used for the cooling channels in the structure. If secondary effects like internal compression shocks and expansion waves are neglected, the flow field within the combustor can be simplified as a turbulent, compressible channel flow problem.

Important boundary layer models have been arranged in Fig. 2.3 according to their attributes of being internal or external, laminar or turbulent, and incompressible or compressible. These boundary layer problems build on each other, with the laminar, incompressible flat plate problem being the simplest, and the compressible channel flow problem being the most complex one. Since latter one is not part of standard literature, a new model is proposed within this work, which combines the pipe flow model by Kármán¹¹⁸ and Prandtl¹¹⁹ with the compressible flat plate model by Crocco¹²⁰ and van Driest.¹²¹ In order to understand this new model, its originating models as illustrated in Fig. 2.3 need to be understood first. These models are explained in the following sections. For the sake of completeness, Eckert's *Reference Enthalpy Method*⁷⁵ is briefly discussed as well.

2.2.1. Naming Conventions in this Section

For better readability, the index notation in the conservation equations is dropped, and the velocities and coordinates are renamed as follows

$$\begin{aligned} x_1 &\rightarrow x, & u_1 &\rightarrow u, \\ x_2 &\rightarrow y, & u_2 &\rightarrow v. \end{aligned}$$

Additionally, the following indices will be used:

- **freestream condition** (∞) :
Flow state in a space of infinite distance to the wall.
- **edge of the boundary layer** (δ) :
State of the flow at the edge of the boundary layer.
- **wall** (w) :
State of the flow at the wall, where $y = 0$.
- **incompressible adiabatic state** (\star) :
The star-index will be used to indicate that an incompressible flow state is considered, where $Ma \approx 0$, and $T_w \approx T_\infty \approx T_r$.

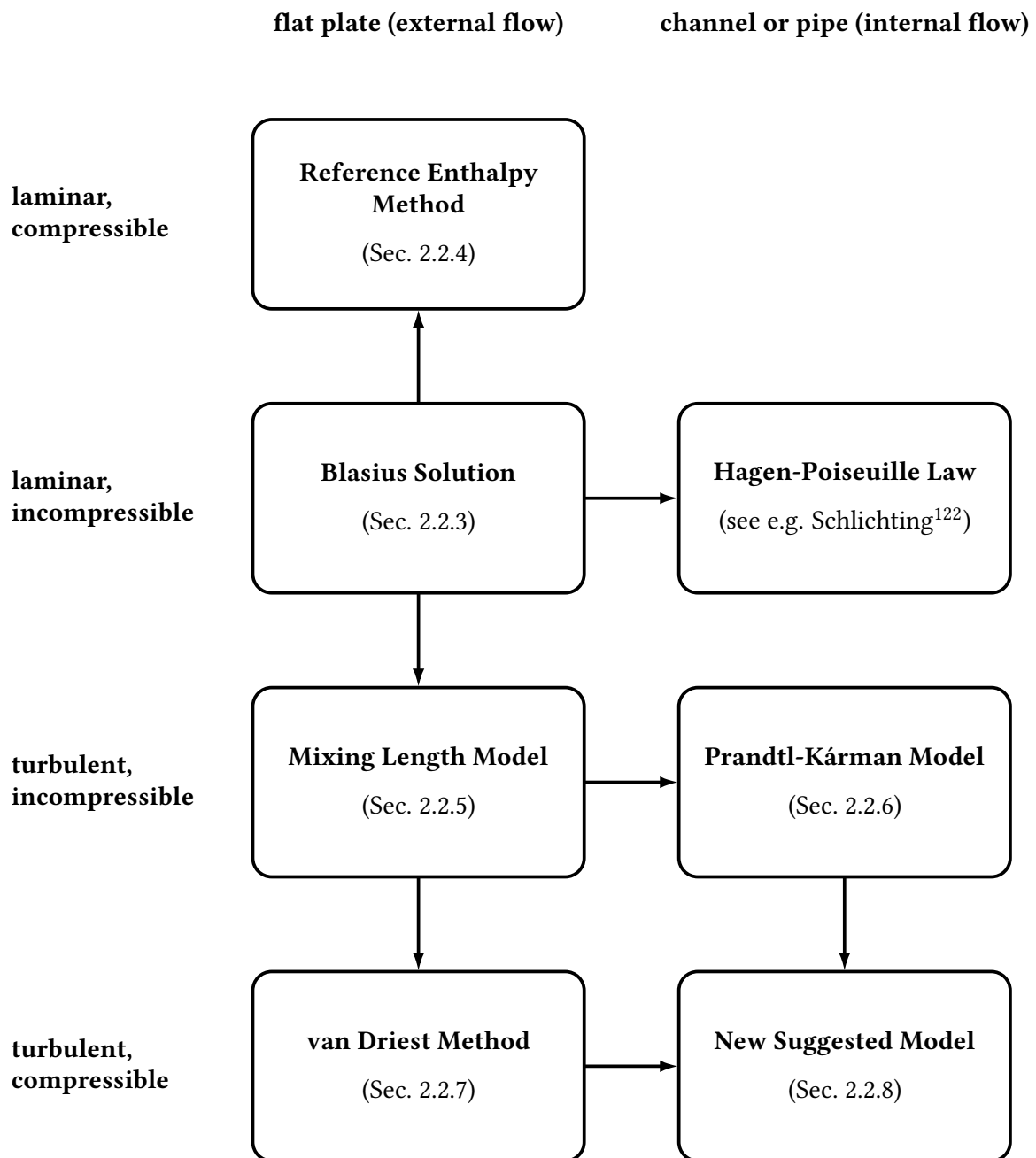


Figure 2.3: Order and evolution of important boundary layer models.

2.2.2. Boundary Layer Thicknesses

The physical behavior of a boundary layer is characterized by the velocity profile $u(y)$ and the density profile $\rho(y)$. Knowledge of these profiles does not only allow the prediction of effects related to viscosity, such as heat transfer, it also facilitates the prediction of laminar to turbulent transition, boundary layer separation, and also the description of shock-boundary-layer-interactions.

If the flow is calculated inviscidly, the surface has to be thickened by the *displacement thickness* to generate the same flow rate as the viscous flow along the unthickened surface. The definition of the displacement thickness reads¹²³

$$\delta^* = \int_0^{\infty} \left(1 - \frac{\rho u}{\rho_{\infty} u_{\infty}} \right) dy. \quad (2.59)$$

Similarly, adding the *momentum loss thickness*, θ , (usually abbreviated to *momentum thickness*), to the surface when performing an inviscid calculation generates the same momentum as the viscous calculation¹²³

$$\theta = \int_0^{\infty} \frac{\rho}{\rho_{\infty}} \frac{u}{u_{\infty}} \left(1 - \frac{u}{u_{\infty}} \right) dy. \quad (2.60)$$

In practice, the integrals in Eqs. (2.59) and (2.59) can not be evaluated up to infinity. Demanding a velocity profile where

$$\lim_{y \rightarrow \infty} u(y) = u_{\infty}, \quad (2.61)$$

the edge of the boundary layer δ is used as upper limit for the integrals, where

$$u_{\delta} = u(y = \delta) \equiv 0.99 u_{\infty}. \quad (2.62)$$

Both δ^* and θ are related to the local friction coefficient c_f over the *van Kármán momentum integral equation*¹²⁴

$$\frac{c_f}{2} = \frac{\partial \theta}{\partial x} + \frac{(\delta^* + 2\theta)}{u_{\infty}} \frac{\partial u_{\infty}}{\partial x} = \frac{\partial \theta}{\partial x} - \frac{(\delta^* + 2\theta)}{\rho_{\infty} u_{\infty}^2} \frac{\partial p}{\partial x}, \quad (2.63)$$

For a pipe flow or a channel flow, see Fig. 2.2, Eq. (2.63) simplifies to¹²⁵

$$\frac{c_f}{2} = \frac{D_h}{4 \bar{\rho} \bar{u}^2} \frac{\partial p}{\partial x}. \quad (2.64)$$

2.2.3. Laminar Incompressible Flat Plate

A two-dimensional flow is considered, which runs parallel to a hydraulically smooth plane surface. Following Prandtl's original considerations of an incompressible flow field, where $\rho(y) = \rho^* = \text{const}$, and $\mu(y) = \mu^* = \text{const}$, and assuming $v \ll u$, the *boundary layer equations* are obtained¹¹⁷

$$\rho^* \left(u \frac{\partial u}{\partial x} + v \frac{\partial u}{\partial y} \right) = -\frac{\partial p}{\partial x} + \mu^* \frac{\partial^2 u}{\partial y^2} \quad (2.65)$$

$$\frac{\partial u}{\partial x} + \frac{\partial v}{\partial y} = 0 \quad (2.66)$$

$$0 = -\frac{\partial p}{\partial y}, \quad (2.67)$$

where the following boundary conditions are postulated

$$u_w = 0, \quad \text{for } y = 0, \quad (2.68)$$

$$v_w = 0, \quad \text{for } y = 0, \quad (2.69)$$

$$\lim_{y \rightarrow \infty} u = u_\infty, \quad (2.70)$$

$$\frac{\partial p}{\partial x} = 0, \quad \forall y. \quad (2.71)$$

An analytical solution of this problem was provided by Blasius,¹²⁶ who could show that the above equations are fulfilled, if

$$\left. \frac{\partial u}{\partial y} \right|_{y=0} \approx 0.332 \frac{\rho^* u_\infty^2}{\mu^* \sqrt{Re_x^*}}, \quad (2.72)$$

which together with Eqs. (2.44) and (2.26) result in the friction factor

$$c_f^* \approx \frac{0.664}{\sqrt{Re_x^*}}. \quad (2.73)$$

For a similar solution for non-zero pressure gradients, $\partial p / \partial x \neq 0$, one may refer to the work of Falkner and Skan.¹²⁷

2.2.4. Laminar Compressible Flat Plate

Under compressible flow conditions, in case of air $Ma \gtrsim 0.3$, density and shear viscosity vary within the boundary layer, which leads to a loss of the similarities described by these correlations. Experimental investigations support the assumption, that the Reynolds - skin friction similarity can be regained if an incompressible correlation of the shape

$$c_f^* = f(Re_x^*) \quad (2.74)$$

is scaled in an appropriate way. Introducing the scaling factors F_{c_f} and F_{Re_x} , the actual skin friction coefficient for the compressible flow state can be determined by performing a coordinate transformation of Eq. (2.74)¹²⁸ so that

$$c_f^* = F_{c_f} c_f = f\left(\underbrace{F_{Re_x} Re_x}_{=Re_x^*}\right). \quad (2.75)$$

In his *Reference Enthalpy Method*, Eckert suggested to average the specific enthalpy⁷⁵

$$h^* = c_\infty h_\infty + c_r h_r + c_w h_w, \quad (2.76)$$

and evaluate the corresponding viscosity μ^* and density ρ^* at the reference temperature T^* , where the reference pressure is equal to the pressure at the wall and the pressure at the edge of the boundary layer ($p^* = p_w = p_\infty$). The corresponding scaling factors read

$$F_{c_f} = \frac{\rho_\infty}{\rho^*} \quad (2.77)$$

$$F_{Re_x} = \frac{1}{F_{c_f}} \frac{\mu_\infty}{\mu^*}. \quad (2.78)$$

For dry air under laminar flow, Meador and Smart⁷⁷ recommend the calibration parameters $c_\infty = 0.29$, $c_r = 0.16$, and $c_w = 0.55$, and $c_\infty = 0.34$, $c_r = 0.16$, and $c_w = 0.50$ for the turbulent case. While Eckert's method gives reasonable results for laminar flow, it underpredicts the skin friction coefficient by as much as thirty percent when applied to a correlation for turbulent flow.^{77,128,129} For the turbulent case it should therefore be used for rough preliminary estimations only.

2.2.5. Turbulent Incompressible Flat Plate

Based on Prandtl's original thoughts, his postgraduate student von Kármán¹¹⁸ postulated that in an area very close to the wall, the velocity profile of an incompressible boundary layer could be described by a similarity approach. First, a dimensionless velocity

$$u^+ = \frac{u}{u_\tau^*}, \quad (2.79)$$

and a dimensionless wall distance

$$y^+ = \frac{\rho^* u_\tau^* y}{\mu^*}, \quad (2.80)$$

which is in fact a Reynolds number, are introduced, with the *shear velocity* being

$$u_\tau^* = \sqrt{\frac{\tau_w^*}{\rho^*}} = u_\infty \sqrt{\frac{c_f^*}{2}}. \quad (2.81)$$

Herein, τ_w^* is the shear stress at the wall, and the star (\star) indicates that as with the incompressible laminar case, constant density $\rho(y) = \rho^* = \text{const}$, and viscosity $\mu(y) = \mu^* = \text{const}$, and constant pressure $p(y) = \text{const}$ are assumed. The differential equation reads

$$\frac{\partial u^+}{\partial y^+} = \frac{\partial f^+}{\partial y^+} + \frac{\partial g^+}{\partial y^+}, \quad (2.82)$$

where f^+ is called *law of the wall*, and g^+ is the *law of the wake*. Experimental data (see Fig. 2.4 suggest that Eq. (2.82) can be approximated at least partly by Prandtl's *mixing length model*

$$\frac{\partial u^+}{\partial y^+} = \frac{1}{\kappa y^+}, \quad (2.83)$$

with κ being the *von Kármán constant*. Integrating Eq. (2.83) over y^+ leads to the *logarithmic law of the wall*

$$u^+ \approx f^+ \approx \frac{1}{\kappa} \ln y^+ + B^+, \quad (2.84)$$

where the integration constant B^+ , as well as the von Kármán constant κ , have to be found experimentally. The logarithmic law approximates f^+ very well within a range of $30 \lesssim y^+ \lesssim 500$, while in areas very close to the wall, $y^+ \lesssim 10$, the *laminar sublayer*, the approach

$$u^+ \approx y^+ \quad (2.85)$$

is more appropriate.

For numerical application, one may prefer the transcendent equation by Spalding,¹³⁰ which is continuous and over the full range of y^+

$$y^+ = f^+ + e^{-\kappa B^+} \left[e^{\kappa f^+} - \sum_{k=0}^4 \frac{(\kappa f^+)^k}{k!} \right]. \quad (2.86)$$

Although they are called *constants*, κ and B^+ are not universally constant, but seem to depend on other flow parameters such as the Reynolds number. An experimental investigation performed in the year 2000 by Österlund¹³¹ suggests that in case of a flat plate, the parameters $\kappa = 0.38$ and $B^+ = 4.1$ should give good results, thus confirming Schultz-Grunow's investigation from 1941, who found $\kappa = 0.388$ and $B^+ = 4.07$.¹³² A comparison of Eq. (2.84), respectively Eq. (2.86), with experimental results reveals that in the range from $y^+ \gtrsim 500$, there is a major deviation between the equations and experimental data (see Fig. 2.4).

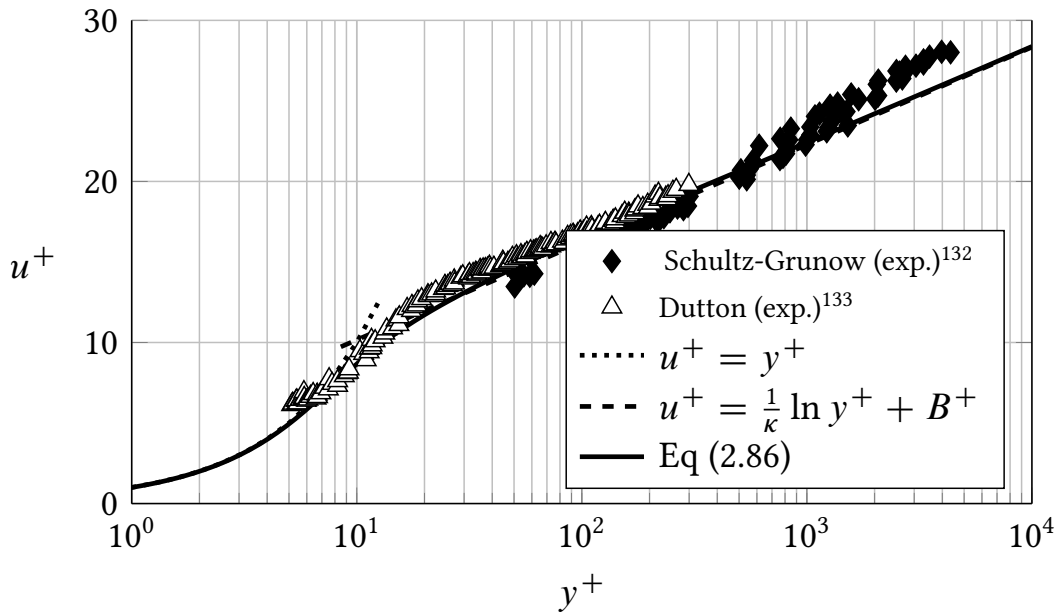


Figure 2.4: Velocity profile in a turbulent boundary-layer over a smooth flat plate.

The *law of the wake* g^+ corrects this deviation. According to Coles, g^+ can be physically interpreted as a large-scale mixing process similar to flow in a wake. Coles suggested the function¹³⁴

$$g^+ = \frac{2\Pi}{\kappa} \left[3 \left(\frac{y}{\delta} \right)^2 - 2 \left(\frac{y}{\delta} \right)^3 \right]. \quad (2.87)$$

where δ is the boundary layer thickness as defined by Eq. (2.62), and the *wake parameter* Π needs to be determined experimentally.

Once the wake parameter Π is known, Eq. (2.82) can be written in an integral form

$$u^+ = f^+(y^+) + g^+\left(\Pi, \frac{y}{\delta}\right). \quad (2.88)$$

For the case of a zero pressure gradient, $\frac{\partial p}{\partial x} = 0$, the momentum integral equation Eq. (2.63) leads to

$$c_f^* = 2 \frac{\partial \theta}{\partial x}. \quad (2.89)$$

Eqs. (2.62), (2.60) and Eqs. (2.100) to (2.88) can be rearranged so that an implicit relation for c_f^* is found

$$c_f^* = \frac{2 \left[0.98 \kappa - \sqrt{2 c_f^*} (1 + \Pi) \right] \exp \left(0.99 \kappa \sqrt{\frac{2}{c_f^*}} - \kappa B^+ - 2 \Pi \right)}{Re_x^* \kappa^2}, \quad (2.90)$$

which for a *wake parameter* of $\Pi = 0.29$ agrees very well with Schultz-Grunow's explicit correlation for zero pressure gradients $\frac{\partial p}{\partial x} = 0$

$$c_f^* \approx \frac{0.370}{(\log_{10} Re_x^*)^{2.584}}. \quad (2.91)$$

For $\frac{\partial p}{\partial x} = 0$, the wake parameter Π can be correlated to Re_θ ¹³⁵

$$\Pi = 0.55 \left\{ 1 - \exp \left[-0.243 \left(\frac{Re_\theta^*}{425} - 1 \right)^{\frac{1}{2}} - 0.298 \left(\frac{Re_\theta^*}{425} - 1 \right) \right] \right\}, \quad (2.92)$$

which for large Re_θ approaches $\Pi = 0.55$. For nonzero pressure gradients, the wake parameter Π becomes a function of $\frac{\partial p}{\partial x}$. One may refer to Das,¹³⁶ and Schlichting and Gersten¹³⁷ for further reading.

2.2.6. Turbulent Incompressible Channel Flow

Consider a two-dimensional flow field, which is confined by two opposing parallel flat plates, and let b be the distance, the duct height, between both plates (see Fig. 2.2). For symmetry reasons, the boundary layer thickness δ cannot grow bigger than $\frac{b}{2}$. For similarity considerations, the Reynolds number is therefore referred to the hydraulic diameter D_h

$$D_h = \frac{4A}{P}. \quad (2.93)$$

where A is the cross section, and P the perimeter. For a channel flow, D_h becomes twice the distance b between both plates, while for a circular pipe, D_h is the circle's diameter. After some rearrangements of the logarithmic law of the wall from Eq. (2.84), one obtains the following transcendent equation for a channel flow

$$\frac{1}{\sqrt{\frac{c_f^*}{2}}} = \frac{1}{\kappa} \ln \left(\frac{Re_{D_h}^*}{4} \sqrt{\frac{c_f^*}{2}} \right) + B^+, \quad (2.94)$$

with $\kappa = 0.38$ and $B^+ = 4.1$ being the same coefficients as in the flat plate flow. For the circular pipe, the equation changes only by one factor

$$\frac{1}{\sqrt{\frac{c_f^*}{2}}} = \frac{1}{\kappa} \ln \left(\frac{Re_{D_h}^*}{8} \sqrt{\frac{c_f^*}{2}} \right) + B^+, \quad (2.95)$$

which for the historical values $\kappa = 0.4$ and $B^+ = 5.2$ almost exactly yields the well known Prandtl-Kármán correlation¹¹⁹

$$\frac{1}{\sqrt{4c_f^*}} \approx 2 \log_{10} \left(Re_{D_h}^* \sqrt{4c_f^*} \right) - 0.8. \quad (2.96)$$

More recent investigations indicate that in case of a circular pipe, one should rather choose $\kappa = 0.43$.¹³⁸ Comparing this value with Eq. (2.96) suggests a value of $B^+ \approx 6$ for the pipe flow. For a non-adiabatic wall, $Re_{D_h}^*$ and c_f^* are, similarly to Eckert's approach from Eq. (2.75), referred to the wall temperature $T^* = T_w$. The friction factor \bar{c}_f with respect to the mean gas temperature \bar{T} is found over the transformation functions Eq. (2.75) and Eq. (2.77). For pipes, the Reynolds analogy factor ζ was correlated by Petukhov as¹³⁹

$$\zeta \approx (1 + 13.6 \bar{c}_f) + \left(11.7 + 1.8 \bar{Pr}^{-\frac{1}{3}} \right) \left(\bar{Pr}^{\frac{2}{3}} - 1 \right) \sqrt{\frac{\bar{c}_f}{2}}. \quad (2.97)$$

2.2.7. Turbulent Compressible Flat Plate Problem

The boundary layer model of Edward R. van Driest¹²¹ is a widely used method to estimate aerodynamic friction and heating of flat external surfaces. Mentionable contributions were made by Fernholz,¹⁴⁰ who discussed the problem of gasses with $Pr \neq 1$, and Bradshaw,¹⁴¹ who provided a better description for the wake parameter Π under compressible flow. In the compressible case, it can not be assumed that density and viscosity are constant, $\rho(y) \neq \text{const}$, $\mu(y) \neq \text{const}$. The constant pressure assumption $p(y) = \text{const}$ is still justifiable for most cases. With the assumption that the function $u(y)$ is bijective, the similarity parameters for Eq. (2.82) now read

$$u^+ = \frac{1}{u_\tau} \int_0^\infty \sqrt{\frac{\rho}{\rho_w}} \frac{\partial u}{\partial y} dy = \frac{1}{u_\tau} \int_{u_w}^{u_\infty} \sqrt{\frac{\rho}{\rho_w}} du, \quad (2.98)$$

and

$$y^+ = \frac{\rho u_\tau y}{\mu}, \quad (2.99)$$

with the shear velocity being

$$u_\tau = \sqrt{\frac{\tau_w}{\rho_w}} = u_\infty \sqrt{\frac{c_f}{2}}. \quad (2.100)$$

Following the suggestion of Crocco¹²⁰ and Busemann,¹⁴² it is assumed that the density ρ and the velocity u are related over a parabola such as

$$\frac{\rho_w}{\rho} = 1 + \psi^+ \left(\frac{u}{u_\infty} \right) - \varphi^+ \left(\frac{u}{u_\infty} \right)^2. \quad (2.101)$$

Demanding *no slip*, meaning $u_w = 0$, it follows from the Newtonian fluid assumption, Eqs. (2.27), the definition of the friction factor, Eq. (2.44), Fourier's law Eq. (2.30), and the definition of the Stanton number, (2.45), that

$$\varphi^+ = 1 + \psi^+ - \frac{\rho_w}{\rho_\infty}, \quad (2.102)$$

$$\psi^+ = \underbrace{\frac{2 St}{c_f} \frac{\mu_w}{\lambda_w} (h_r - h_w)}_{=\zeta^{-1}} \underbrace{\rho_w \frac{\partial \left(\frac{1}{\rho} \right)}{\partial T}}_{=\frac{1}{T_w}, \text{ if ideal gas}}. \quad (2.103)$$

Note that in contrast to Eq. (2.30), the sign of the heat load is chosen so that a positive \dot{q}_w means heating of the wall.

Inserting the *Crocco-Busemann* relation, Eq. (2.101), into Eq. (2.98) yields for the right hand side after integration

$$u^+ = \frac{u_\infty/u_\tau}{\sqrt{\varphi^+}} \left\{ \sin^{-1} \left[\frac{2\varphi^+ (u/u_\infty) - \psi^+}{\sqrt{(\psi^+)^2 + 4\varphi^+}} \right] + \sin^{-1} \left[\frac{\psi^+}{\sqrt{(\psi^+)^2 + 4\varphi^+}} \right] \right\}. \quad (2.104)$$

For zero pressure gradients perpendicular to the wall, $\partial p/\partial x = 0$, it follows from the von Kármán momentum integral equation, Eq. (2.63), that

$$\tau_w = \frac{\rho_\infty u_\infty^2}{2} c_f = \frac{\partial}{\partial x} \left[\int_0^\infty \rho u (u_\infty - u) dy \right]. \quad (2.105)$$

Van Driest has shown,¹²¹ that Eq. (2.105) can be transformed into a shape similar to the one found in the Reference Enthalpy Method

$$c_f^* = F_{c_f} c_f = f \left(\underbrace{F_{Re_x} Re_x}_{=Re_x^*} \right), \quad (2.75)$$

where F_{c_f} and F_{Re_x} are approximated over a Taylor series as

$$F_{c_f} \approx \frac{T_r/T_\infty - 1}{\left\{ \sin^{-1} \left[\frac{2\varphi^+ - \psi^+}{\sqrt{(\psi^+)^2 + 4\varphi^+}} \right] + \sin^{-1} \left[\frac{\psi^+}{\sqrt{(\psi^+)^2 + 4\varphi^+}} \right] \right\}^2}, \quad (2.106)$$

$$F_{Re_x} \approx \frac{1}{F_{c_f}} \frac{\mu_\infty}{\mu_w}. \quad (2.107)$$

Originally, van Driest applied this transformation to a correlation based on measurements of friction on short plates in water, performed in 1924.¹⁴³ To achieve a more consistent model, one should prefer Eq. (2.90) for the determination of c_f^* . A fully consistent solution can be achieved by numerically solving the von Kármán momentum integral equation, Eq. (2.63), using Eqs. (2.59) and (2.60).

2.2.8. Turbulent Compressible Channel Flow

Van Driest's method was originally developed for flat plate flows. Huang and Coleman argued, that this method can also be used for channel flows, if the equations are referred to the peak density $\hat{\rho}$, and velocity \hat{u} rather than the far field values ρ_∞ and u_∞ , which do not exist in a channel or pipe flow.^{144,145} In the case of a channel flow, the peak values are found at the center of the duct if the surface temperatures of the opposing walls have the same temperature, otherwise, their position \hat{y} will shift to the side of the cooler wall.¹⁴⁶

In cross-section averaged calculations, like the combustor model that is used in this work, the averaged magnitudes $\bar{\rho}$ and \bar{u} are given, while the required peak parameters $\hat{\rho}$ and \hat{u} need to be determined in order to calculate the local shear stress τ_w at each wall and the corresponding heat load \dot{q}_w . It is shown in this section that both demanded parameters can be found by using the balance equation of mass and momentum, which are combined with a model of the velocity profile $u(y)$. After an overview over all given and demanded parameters, the compressible channel flow problem is approached into six steps. First, the definitions of c_f and St are modified to the needs of the channel flow. Next, the cross section averaging method is discussed. Steps three and four consider the necessary modifications of the Crocco-Busemann relation and the law of the wake. In step five, the determination of the Reynolds analogy factor ζ and the recovery factor r is explained. In the sixth step, a nonlinear equation system is created, which can be solved by a Newton-Raphson method.

Step 0: Given and Demanded Parameters

For the general compressible, non-adiabatic channel flow problem, the surface temperature T_w , the mean density $\bar{\rho}$, and the mean velocity \bar{u} , the mean Temperature \bar{T} , and the cross section A need to be given at a specific coordinate x . Generally, constant pressure $\partial p / \partial y = 0$ is assumed, where $\bar{\rho}$ is found over the equation of state. There are two unknown parameters, which can either be expressed as shear stress τ_w and heat load \dot{q}_w on the wall, or alternatively, over the reference velocity \hat{u} and density $\hat{\rho}$, which are explained in Step 3.

Step 1: Definition of c_f and St

The friction factor c_f and the Stanton Number St can be either referred to the cross section averaged density and velocity $\bar{\rho}$ and \bar{u} or the peak density and velocity \hat{u} and the density $\hat{\rho}$. For a numerical implementation, former one is more practical, while latter one is more useful for engineering purposes. Both definitions are allowed, they must, however, not be confused.

The definitions for the friction factor c_f and the Stanton number St read

$$\tau_w = \mu_w \left. \frac{\partial u}{\partial y} \right|_w = \frac{\hat{c}_f}{2} \hat{\rho} \hat{u}^2 = \frac{\bar{c}_f}{2} \bar{\rho} \bar{u}^2, \quad (2.108)$$

and

$$\dot{q}_w = \lambda_w \left. \frac{\partial T}{\partial y} \right|_w = \hat{St} \hat{\rho} \hat{u} (h_r - h_w) = \bar{St} \bar{\rho} \bar{u} (h_r - h_w). \quad (2.109)$$

As in the flat plate case, the sign of (2.109) is swapped with respect to Eq. (2.30), so that a positive \dot{q}_w means heating of the wall.

Step 2: Cross-Section Averaging

The integral equations of the balances of mass and momentum read¹⁴⁷

$$\dot{m} = \int_A \rho u \, dA = \bar{\rho} \bar{u} A, \quad (2.110)$$

and

$$\dot{i} = \int_A p + \rho u^2 \, dA = (\bar{p} + \bar{\rho} \bar{u}^2) A. \quad (2.111)$$

From the chosen definition for the cross section averaged pressure

$$\bar{p} \equiv \frac{1}{A} \int_A p \, dA, \quad (2.112)$$

it follows from Eqs. (2.110) and (2.111) that the cross section averaged velocity and density must read

$$\bar{u} = \frac{\int_A \rho u^2 \, dA}{\int_A \rho u \, dA}, \quad (2.113)$$

and

$$\bar{\rho} = \frac{1}{A} \frac{[\int_A \rho u \, dA]^2}{\int_A \rho u^2 \, dA}. \quad (2.114)$$

There are two variants to define the cross section averaged enthalpy \bar{h} . Either, one can demand energy conservation

$$\dot{H}_t = \int_A \left(h + \frac{u^2}{2} \right) \rho u \, dA = \left(\bar{h} + \frac{\bar{u}^2}{2} \right) \dot{m}, \quad (2.115)$$

which together with Eqs. (2.114) and (2.113) leads to the definition

$$\bar{h} = \frac{\int_A h \rho u \, dA + \frac{1}{2} \int_A \rho u^3 \, dA}{\int_A \rho u \, dA} - \frac{1}{2} \left[\frac{\int_A \rho u^2 \, dA}{\int_A \rho u \, dA} \right]^2. \quad (2.116)$$

Alternatively, one could rely on the the caloric model, Eqs. (2.14) and (2.16), and the chosen equation of state in order to demand

$$\bar{h} = \bar{h}(\bar{\rho}, \bar{p}). \quad (2.117)$$

If implemented correctly, both variants must lead to the same result within the accuracy of numerical discretization.

Step 3: Modifying the Crocco-Busemann Relation

Two new reference states \hat{u} and $\hat{\rho}$ are introduced, which later need to be determined iteratively. The Crocco-Busemann profile is modified to

$$\frac{\rho_w}{\rho} = 1 + \psi^+ \left(\frac{u}{\hat{u}} \right) - \varphi^+ \left(\frac{u}{\hat{u}} \right)^2, \quad (2.118)$$

and φ^+ is modified to

$$\varphi^+ = 1 + \psi^+ - \frac{\rho_w}{\hat{\rho}}, \quad (2.119)$$

while ψ^+ is the same as for the flat plate equation

$$\psi^+ = \underbrace{\frac{2 \hat{S}t}{\hat{c}_f}}_{=\hat{\zeta}^{-1}} \frac{\mu_w}{\lambda_w} (h_r - h_w) \underbrace{\rho_w \frac{\partial \left(\frac{1}{\rho} \right)}{\partial T}}_{=\frac{1}{T_w}, \text{ if ideal gas}} \Big|_w. \quad (2.103)$$

The recovery enthalpy h_r can be determined over either the peak or the averaged parameters

$$h_r = \hat{h} + \hat{r} \frac{\hat{u}^2}{2} = \bar{h} + \bar{r} \frac{\bar{u}^2}{2}, \quad (2.120)$$

where former one is preferred here. The dimensionless velocity u^+ now reads

$$u^+ = \frac{\hat{u}/u_\tau}{\sqrt{\varphi^+}} \left\{ \sin^{-1} \left[\frac{2\varphi^+ (u/\hat{u}) - \psi^+}{\sqrt{(\psi^+)^2 + 4\varphi^+}} \right] + \sin^{-1} \left[\frac{\psi^+}{\sqrt{(\psi^+)^2 + 4\varphi^+}} \right] \right\}. \quad (2.121)$$

Step 4: Modifying the Wake Law g^+

For the law of the wall, f^+ , Spalding's wall law Eq. (2.86) is used without modification, with y^+ being defined after Eq. (2.99). The law of the wake, g^+ needs to be modified. Discussing experimental studies by Lindgren,¹⁴⁸ White¹⁴⁹ pointed out that the wake parameter can be neglected for pipe and channel flows, so that $\Pi \approx 0$. Gou and Julien¹⁵⁰ on the other hand argued that for symmetry reasons, a correction is still needed in order to have $\partial u/\partial y = 0$ in the center of the duct. Therefore, the following wake function is suggested at this point

$$g^+ = \frac{1}{\kappa} \left[(6\Pi + 1) \left(\frac{y}{\hat{y}} \right)^2 - (4\Pi + 1) \left(\frac{y}{\hat{y}} \right)^3 \right], \quad (2.122)$$

where $\Pi = 0$ is assumed. The definition of \hat{y} in Eq. (2.122) depends on the kind of the flow. For a pipe, \hat{y} is half of the hydraulic diameter D_h , which is calculated after Eq. (2.93). For a two-dimensional channel flow, \hat{y} is half of the duct size if the opposing walls have the same surface temperature. If that is not the case, \hat{y} has to be determined iteratively.¹⁴⁶

Step 5: Modifying the Reynolds analogy factor ζ and the recovery factor r

General equations for the Reynolds Analogy Factor ζ and the Recovery Factor r for the flat plate were given by van Driest,¹¹⁴ see Eqs. (2.52) and (2.56). The integration limits of both equations need to be modified. Instead of up to the edge of the boundary layer $y = \delta$, the modified equations now integrate up to the reference height $y = \hat{y}$.

The definitions for the Reynolds-Colburn analogy $\hat{\zeta}$ and the recovery factor \hat{r} read

$$\hat{\zeta} = \frac{1}{\hat{u}} \int_0^{\hat{y}} Pr_M \exp \left(- \int_0^y \frac{1 - Pr_M}{\tau} \frac{\partial \tau}{\partial \tilde{y}} d\tilde{y} \right) \frac{\partial u}{\partial y} dy \quad (2.123)$$

and

$$\hat{r} = \frac{2}{\hat{u}^2} \int_0^{\hat{y}} Pr_M \exp \left(- \int_0^y \frac{1 - Pr_M}{\tau} \frac{\partial \tau}{\partial \tilde{y}} d\tilde{y} \right) \cdot \left[\int_0^y \exp \left(\int_0^{\tilde{y}} \frac{1 - Pr_M}{\tau} \frac{\partial \tau}{\partial \tilde{y}} d\tilde{y} \right) \frac{\partial u}{\partial \tilde{y}} d\tilde{y} \right] \frac{\partial u}{\partial y} dy \quad (2.124)$$

For both Eq. (2.123) and Eq. (2.124), the shear stress τ needs to be evaluated at every y -position. It reads

$$\tau = (\mu + \mu_T) \frac{\partial u}{\partial u^+} \frac{\partial u^+}{\partial y^+} \frac{\partial y^+}{\partial y}. \quad (2.125)$$

A turbulence model is needed in order to determine μ_T and λ_T , respectively Pr_M . A very simple hypothesis the turbulent shear viscosity μ_T , which was fitted against experimental data in pipe flows, reads^{115, 151}

$$\mu_T = \mu \kappa y^+, \quad (2.126)$$

with κ being the *von Kármán constant*, see Eq. (2.83). For the turbulent conductivity λ_T , the Kays-Crawford relation in Eq. (2.49) can be used in combination with Eq. (2.47). Subsequently, the mixed Prandtl number Pr_M in Eqs. (2.123) and (2.124) is calculated using Eq. (2.48).

Step 6: Application of the Newton-Raphson Algorithm

In order to find the shear stress τ_w and the heat flux \dot{q}_w at the wall, the reference velocity \hat{u} and the reference density $\hat{\rho}$ must be iterated until the balances equations for mass and momentum, Eqs. (2.110) and (2.111), are fulfilled, respectively, the expressions

$$\Delta \dot{m} = \bar{\rho} \bar{u} A - \int_A \rho u \, dA \quad (2.127)$$

and

$$\Delta \dot{I} = (\bar{p} + \bar{\rho} \bar{u}^2) A - \int_A p + \rho u^2 \, dA \quad (2.128)$$

become zero.

The iteration is performed over a Newton-Raphson method

$$\begin{bmatrix} \hat{u} \\ \hat{\rho} \end{bmatrix}^{k+1} = \begin{bmatrix} \hat{u} \\ \hat{\rho} \end{bmatrix}^k - \omega \mathbf{J}^{-1} \begin{bmatrix} \Delta \dot{m} \\ \Delta \dot{I} \end{bmatrix}^k, \quad (2.129)$$

where k is the iteration step, and $0 < \omega \leq 1$ a relaxation factor. The Jacobian matrix \mathbf{J} is numerically approximated through

$$\mathbf{J} = \begin{bmatrix} \frac{\Delta \dot{m}(\hat{u} + \Delta \hat{u}, \hat{\rho}) - \Delta \dot{m}(\hat{u} - \Delta \hat{u}, \hat{\rho})}{2 \Delta \hat{u}} & \frac{\Delta \dot{m}(\hat{u}, \hat{\rho} + \Delta \hat{\rho}) - \Delta \dot{m}(\hat{u}, \hat{\rho} - \Delta \hat{\rho})}{2 \Delta \hat{\rho}} \\ \frac{\Delta \dot{I}(\hat{u} + \Delta \hat{u}, \hat{\rho}) - \Delta \dot{I}(\hat{u} - \Delta \hat{u}, \hat{\rho})}{2 \Delta \hat{u}} & \frac{\Delta \dot{I}(\hat{u}, \hat{\rho} + \Delta \hat{\rho}) - \Delta \dot{I}(\hat{u}, \hat{\rho} - \Delta \hat{\rho})}{2 \Delta \hat{\rho}} \end{bmatrix}, \quad (2.130)$$

where $\Delta \hat{u}$ and $\Delta \hat{\rho}$ are incremental steps, fore example

$$\Delta \hat{u} = \frac{\bar{u}}{10000}, \quad (2.131)$$

$$\Delta \hat{\rho} = \frac{\bar{\rho}}{10000}. \quad (2.132)$$

For the initial step $k = 0$ the following values can be chosen

$$\hat{u}^{k=0} = \bar{u}, \quad (2.133)$$

$$\hat{\rho}^{k=0} = \bar{\rho}, \quad (2.134)$$

$$\zeta^{k=0} = Pr^{\frac{2}{3}}, \quad (2.135)$$

$$r^{k=0} = Pr^{\frac{1}{3}}. \quad (2.136)$$

The initial value of τ_w follows from Eqs. (2.108) with $c_f^{k=0}$ being guessed using the simple but weak *Dittus-Boelter correlation*¹⁵²

$$c_f^{k=0} = 0.046 \left(\frac{\rho_w}{\bar{\rho}} \right) \left(\frac{\rho_w \bar{u} D_h}{\mu_w} \right)^{-0.2}. \quad (2.137)$$

The full algorithm is illustrated in Fig. 2.5.

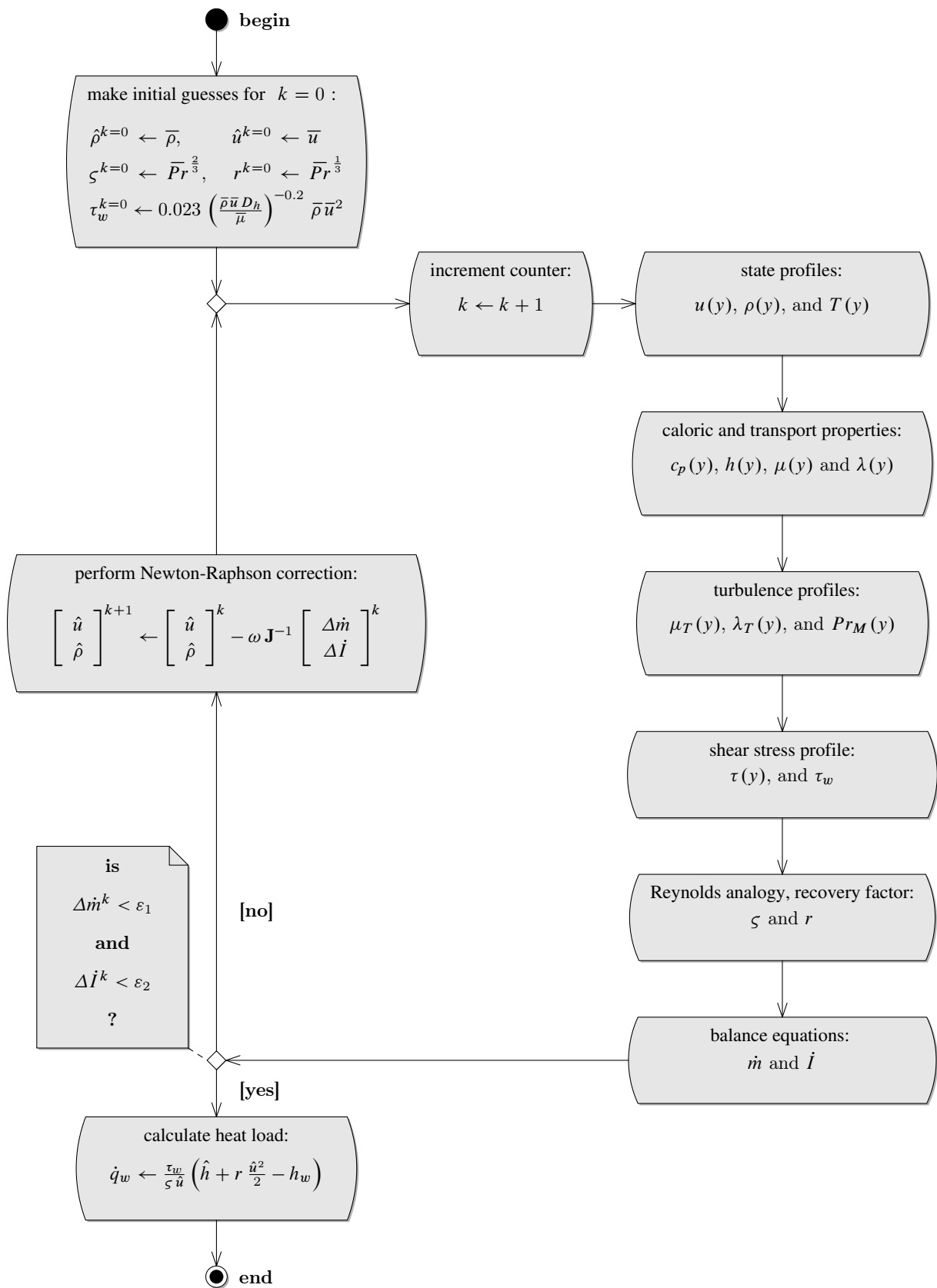


Figure 2.5: UML activity diagram for the modified van Driest method.

If there is a two-dimensional channel flow, the opposing walls can have different surface temperatures, $T_{w1} \neq T_{w2}$. If this is the case, the new variable \hat{y} is introduced, which marks the position of the peak values \hat{u} and $\hat{\rho}$, and via the equation of state implicitly \hat{T} . For geometrical reasons, the values \hat{y}_1 and \hat{y}_2 of both walls must add up to the height d of the channel

$$\hat{y}_1 + \hat{y}_2 = \frac{D_h}{2} = d. \quad (2.138)$$

Due to the nature of Spalding's law of the wall, Eq. (2.86), the peak velocity $u(\hat{y})$ calculated using Eqs. (2.121) will slightly differ from \hat{u} . This difference will be less than one percent, and is therefore less relevant from a modeling point of view. Demanding continuity, however, it is important that the peak velocities of both wall profiles are identical. By defining the velocity error

$$\Delta\hat{u} = u_1(\hat{y}_1) - u_2(\hat{y}_2) \quad (2.139)$$

between both wall profiles, a third continuity condition is found. The modified Newton-Raphson scheme now reads

$$\begin{bmatrix} \hat{u} \\ \hat{\rho} \\ \hat{y}_1 \end{bmatrix}^{k+1} = \begin{bmatrix} \hat{u} \\ \hat{\rho} \\ \hat{y}_1 \end{bmatrix}^k - \omega \mathbf{J}^{-1} \begin{bmatrix} \Delta\dot{m} \\ \Delta\dot{I} \\ \Delta\hat{u} \end{bmatrix}^k, \quad (2.140)$$

with the Jacobian matrix being

$$\mathbf{J} = \begin{bmatrix} \frac{\Delta\dot{m}(\hat{u} + \Delta\hat{u}, \hat{\rho}, \hat{y}_1) - \Delta\dot{m}(\hat{u} - \Delta\hat{u}, \hat{\rho}, \hat{y}_1)}{2\Delta\hat{u}} & \frac{\Delta\dot{m}(\hat{u}, \hat{\rho} + \Delta\hat{\rho}, \hat{y}_1) - \Delta\dot{m}(\hat{u}, \hat{\rho} - \Delta\hat{\rho}, \hat{y}_1)}{2\Delta\hat{\rho}} & \frac{\Delta\dot{m}(\hat{u}, \hat{\rho}, \hat{y}_1 + \Delta\hat{y}_1) - \Delta\dot{m}(\hat{u}, \hat{\rho}, \hat{y}_1 - \Delta\hat{y}_1)}{2\Delta\hat{y}_1} \\ \frac{\Delta\dot{I}(\hat{u} + \Delta\hat{u}, \hat{\rho}, \hat{y}_1) - \Delta\dot{I}(\hat{u} - \Delta\hat{u}, \hat{\rho}, \hat{y}_1)}{2\Delta\hat{u}} & \frac{\Delta\dot{I}(\hat{u}, \hat{\rho} + \Delta\hat{\rho}, \hat{y}_1) - \Delta\dot{I}(\hat{u}, \hat{\rho} - \Delta\hat{\rho}, \hat{y}_1)}{2\Delta\hat{\rho}} & \frac{\Delta\dot{I}(\hat{u}, \hat{\rho}, \hat{y}_1 + \Delta\hat{y}_1) - \Delta\dot{I}(\hat{u}, \hat{\rho}, \hat{y}_1 - \Delta\hat{y}_1)}{2\Delta\hat{y}_1} \\ \frac{\Delta\hat{u}(\hat{u} + \Delta\hat{u}, \hat{\rho}, \hat{y}_1) - \Delta\hat{u}(\hat{u} - \Delta\hat{u}, \hat{\rho}, \hat{y}_1)}{2\Delta\hat{u}} & \frac{\Delta\hat{u}(\hat{u}, \hat{\rho} + \Delta\hat{\rho}, \hat{y}_1) - \Delta\hat{u}(\hat{u}, \hat{\rho} - \Delta\hat{\rho}, \hat{y}_1)}{2\Delta\hat{\rho}} & \frac{\Delta\hat{u}(\hat{u}, \hat{\rho}, \hat{y}_1 + \Delta\hat{y}_1) - \Delta\hat{u}(\hat{u}, \hat{\rho}, \hat{y}_1 - \Delta\hat{y}_1)}{2\Delta\hat{y}_1} \end{bmatrix}. \quad (2.141)$$

2.2.9. Channel Differential Equations

The differential equations needed in order to model the axial progression of a channel flow are based on the conservation equations for mass, momentum and energy. All properties are referred to cross averaged values, \bar{T} , $\bar{\rho}$, and \bar{u} . In the following notation the overbars are omitted for better readability. For a flow with constant mass flux \dot{m} , the differential equations for the conservation of mass, momentum^b and energy read

$$0 = \frac{1}{A} \frac{\partial A}{\partial x} + \frac{1}{u} \frac{\partial u}{\partial x} - \frac{1}{v} \frac{\partial v}{\partial x}, \quad (2.142)$$

$$0 = \frac{1}{p} \frac{\partial p}{\partial x} + \frac{u^2}{p v} \frac{1}{u} \frac{\partial u}{\partial x} + \tau_w \frac{4}{D_h}, \quad (2.143)$$

$$0 = \frac{\partial h}{\partial x} + u^2 \frac{1}{u} \frac{\partial u}{\partial x} + \frac{4 A}{D_h} \frac{\dot{q}}{\dot{m}}. \quad (2.144)$$

For a reacting gas with $\partial Y/\partial x \neq 0$, the pressure gradient reads

$$\begin{aligned} \frac{\partial p}{\partial x} &= \left(\frac{\partial p}{\partial T} \right)_{v, Y_i} \frac{\partial T}{\partial x} + \left(\frac{\partial p}{\partial v} \right)_{T, Y_i} \frac{\partial v}{\partial x} + \sum_i \left(\frac{\partial p}{\partial Y_i} \right)_{v, T} \frac{\partial Y_i}{\partial x} \\ &= p \beta \frac{\partial T}{\partial x} - \frac{1}{\kappa} \frac{1}{v} \frac{\partial v}{\partial x} + \sum_i \left(\frac{\partial p}{\partial Y_i} \right)_{v, T} \frac{\partial Y_i}{\partial x}. \end{aligned} \quad (2.145)$$

With the relation

$$\left(\frac{\partial h}{\partial p} \right)_T = v - T \left(\frac{\partial v}{\partial T} \right)_p = v (1 - T \alpha), \quad (2.146)$$

as well as the definitions for the specific heat capacities at constant volume and pressure, Eqs. (2.9) and (2.10), the following enthalpy gradient is found

^bIn the original source,¹⁵³ a superfluous contribution $\frac{1}{A} \frac{\partial A}{\partial x}$ is written in the momentum balance. This mistake has been corrected in Eq. (2.143). The author apologizes for any inconvenience.

$$\begin{aligned}
\frac{\partial h}{\partial x} &= \left(\frac{\partial h}{\partial T} \right)_{p, Y_i} \frac{\partial T}{\partial x} + \left(\frac{\partial h}{\partial p} \right)_{T, Y_i} \frac{\partial p}{\partial x} + \sum_i \left(\frac{\partial h}{\partial Y_i} \right)_{T, p} \frac{\partial Y_i}{\partial x} \\
&= (c_v + p v \beta) T \frac{1}{T} \frac{\partial T}{\partial x} + \frac{v}{\kappa} (T \alpha - 1) \frac{1}{v} \frac{\partial v}{\partial x} \\
&\quad + \sum_i \left[h_i + v (1 - T \alpha) \left(\frac{\partial p}{\partial Y_i} \right)_{v, T} \right] \frac{\partial Y_i}{\partial x}.
\end{aligned} \tag{2.147}$$

Using the relations found for the gradients in Eqs. (2.145) and (2.142), (2.147), the balance equations (2.143) and (2.144) can be rearranged into an equation system of the shape

$$\mathbf{A} \cdot \begin{pmatrix} \frac{1}{v} \frac{\partial v}{\partial x} \\ \frac{1}{u} \frac{\partial u}{\partial x} \\ \frac{1}{T} \frac{\partial T}{\partial x} \end{pmatrix} = \mathbf{f}, \tag{2.148}$$

where

$$\mathbf{A} = \begin{pmatrix} 1 & -1 & 0 \\ -\frac{\beta}{\alpha} & \frac{u^2}{p v} & \beta T \\ \frac{v}{\kappa} (T \alpha - 1) & u^2 & (c_v + p v \beta) T \end{pmatrix}, \tag{2.149}$$

and

$$\mathbf{f} = \begin{pmatrix} \frac{1}{A} \frac{\partial A}{\partial x} \\ -\frac{4}{D_h} \frac{\tau_w}{p} \\ -\frac{4A}{D_h} \frac{\dot{q}}{\dot{m}} \end{pmatrix} - \sum_i \begin{pmatrix} 0 \\ \frac{1}{p} \left(\frac{\partial p}{\partial Y_i} \right)_{v, T} \\ h_i + v (1 - T \alpha) \left(\frac{\partial p}{\partial Y_i} \right)_{v, T} \end{pmatrix} \frac{\partial Y_i}{\partial x}. \tag{2.150}$$

If the velocity u coincides with the speed of sound c , the matrix \mathbf{A} becomes singular,

$$\det \mathbf{A} = 0 \Leftrightarrow u = c = \sqrt{-v^2 \left(\frac{\partial p}{\partial v} \right)_s} = \left[p v \frac{\beta}{\alpha} \frac{c_p}{c_v} \right]^{\frac{1}{2}}. \quad (2.151)$$

In this situation, the specific entropy s of the flow will reach a local maximum, and *thermal choking* will occur.

In case of an ideal gas, the matrix \mathbf{A} and the vector \mathbf{f} simplify to

$$\mathbf{A}_{(idgas)} = \begin{pmatrix} 1 & -1 & 0 \\ -1 & \frac{u^2}{RT} & 1 \\ 0 & u^2 & c_p T \end{pmatrix}, \quad (2.152)$$

and

$$\mathbf{f}_{(idgas)} = \begin{pmatrix} \frac{1}{A} \frac{\partial A}{\partial x} \\ -\frac{4}{D_h} \frac{\tau_w}{p} \\ -\frac{4A}{D_h} \frac{\dot{q}}{\dot{m}} \end{pmatrix} - \sum_i \begin{pmatrix} 0 \\ \frac{M}{M_i} \\ h_i \end{pmatrix} \frac{\partial Y_i}{\partial x}. \quad (2.153)$$

While Eq. (2.148) can be extended to regard changes in the mass flux, $\partial \dot{m} / \partial x$, the application discussed in the present work requires a mass injection at one discrete point. If two flows (1) and (2) are intended to be mixed to a flow (3), the integral form of the balance equations are solved:

$$\dot{m}_1 + \dot{m}_2 = \dot{m}_3 \quad (2.154)$$

$$p_1 A_1 + \dot{m}_1 u_1 + p_2 A_2 + \dot{m}_2 u_2 = p_3 A_3 + \dot{m}_3 u_3 \quad (2.155)$$

$$\dot{m}_1 h_{t,1} + \dot{m}_2 h_{t,2} = \dot{m}_3 h_{t,3}, \quad (2.156)$$

where

$$A_1 + A_2 = A_3. \quad (2.157)$$

The gradient of mass fractions $\partial Y_i / \partial x$ will be discussed in Chapter 3.1.

2.3. Compression and Expansion Shocks

The concept of supersonic compression shocks and expansions is an essential component of the theory of hypersonic flight, well known and well documented in standard literature. This chapter therefore only covers the general relations. One may refer to Hayes and Probstein,¹⁵⁴ Anderson¹⁵⁵ or Hirschel⁹⁶ for further reading.

2.3.1. Normal Compression Shocks

In a moving gas, every supersonic one-dimensional flow state (T_1, p_1, u_1) has a subsonic counterpart (T_2, p_2, u_2) with equal fluxes of mass, momentum and energy. The entropy of the subsonic counterpart is however higher.¹⁵⁶ Under certain conditions, a supersonic flow state can change into the subsonic state instantaneously without violating mass, momentum and energy conservation. Due to the entropy rise during such a *normal compression shock*, jumps from the subsonic to the supersonic state are forbidden by the second law of thermodynamics. For any real gas, these mass, momentum and energy conservation laws are

$$\rho_1 u_1 = \rho_2 u_2, \quad (2.158)$$

$$p_1 + \rho_1 u_1^2 = p_2 + \rho_2 u_2^2, \quad (2.159)$$

$$h_1 + \frac{u_1^2}{2} = h_2 + \frac{u_2^2}{2}. \quad (2.160)$$

Since these conservation laws need to be solved iteratively, the perfect gas relations of Eq (2.23), as well as the relation¹⁵⁵

$$Ma_2^2 \approx \frac{1 + \left(\frac{\gamma-1}{2}\right) Ma_1^2}{\gamma Ma_1^2 - \frac{\gamma-1}{2}} \quad (2.161)$$

can be used to estimate good starting values for the iteration process.

2.3.2. Oblique Compression Shocks

When a supersonic flow is deflected at a concave corner, an oblique shock is created. It can be seen from the velocity triangles in Fig. 2.6 that the velocity vector \mathbf{w} can be split into a component \mathbf{u} normal to the shockwave, and a parallel component \mathbf{v} . Along the shockwave, the parallel component remains unchanged, so that $\mathbf{v}_1 = \mathbf{v}_2$. The normal component \mathbf{u} experiences a normal shock and follows the conservation conditions of Eqs. (2.160) to (2.159). From the velocity triangles, a relation between normal velocities, ramp and shock angle can be found

$$\frac{\tan(\beta - \alpha)}{\tan \beta} = \frac{u_2}{u_1}. \quad (2.162)$$

which for a calorically perfect gas simplifies to the β - α - Ma -relation¹⁵⁵

$$\tan \alpha = 2 \cot \beta \left[\frac{Ma_1^2 \sin^2 \beta - 1}{Ma_1^2 (\gamma + \cos 2\beta) + 2} \right]. \quad (2.163)$$

In order to find the state after the shock, the conservation equations for mass (2.158), momentum (2.159), and energy (2.160), the geometry condition (2.162) and the equation of state must be solved iteratively. In theory, there are two states that fulfill these equations (see Sec. 2.3.1), a *strong* solution, where w_2 is always subsonic, and a *weak* solution, where w_2 is in most cases supersonic. Usually, the weak solution is to be expected. It is known that the shock angle β for the weak solution can not fall under the Mach angle μ_1 , where μ is defined as

$$\sin \mu = \frac{1}{Ma}, \quad (2.164)$$

while there is a critical shock angle β_{crit} , where the strong and the weak solution coincide.

$$\left. \frac{\partial \alpha}{\partial \beta} \right|_{Ma_1, \beta_{crit}} = 0 \quad (2.165)$$

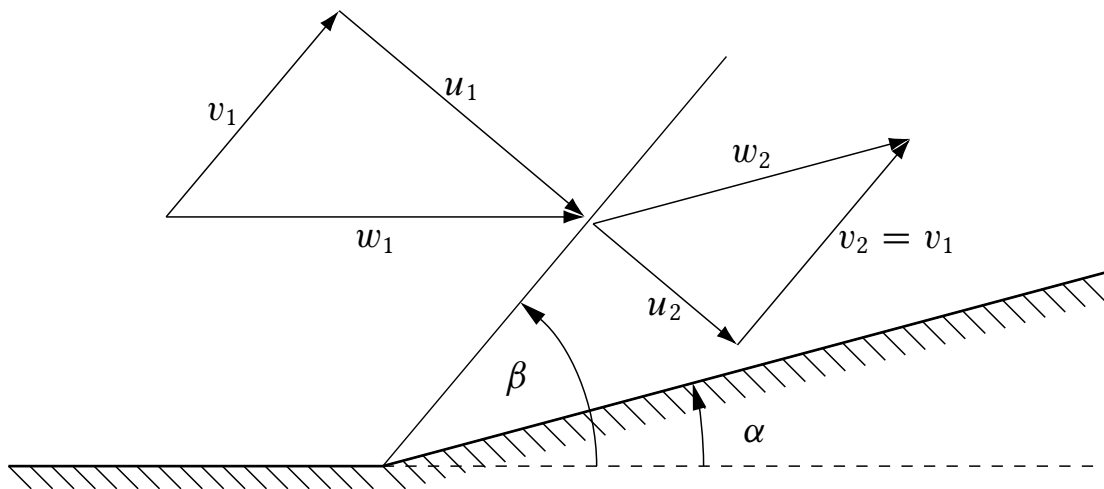


Figure 2.6: Velocity triangles of an oblique compression shock.

For a calorically perfect gas, this critical shock angle β_{crit} can be found by analytically solving Eq. (2.163) to α , deriving the result to β , and solving Eq. (2.165) numerically. Since β_{crit} is only needed as a starting value for iterating Eq. (2.163) and the conservation conditions, an approximate estimation of β_{crit} is usually sufficient. For a calorically perfect gas with $\gamma = 1.4$ and $Ma > 1.4$, the following correlation predicts β_{crit} with a deviation of approximately 0.1%:

$$\beta_{crit} \approx -0.1189 Ma_1^{-4} + 1.1617 Ma_1^{-3} - 0.7708 Ma_1^{-2} + 1.1832. \quad (2.166)$$

In order to accelerate the calculation, the initial condition

$$\mu_1 < \beta < \beta_{max}, \quad (2.167)$$

can be used in order to find β for the calorically perfect gas, using Eq. (2.163). The solution can be used as initial value to find the real-gas solution with Eq. (2.162).

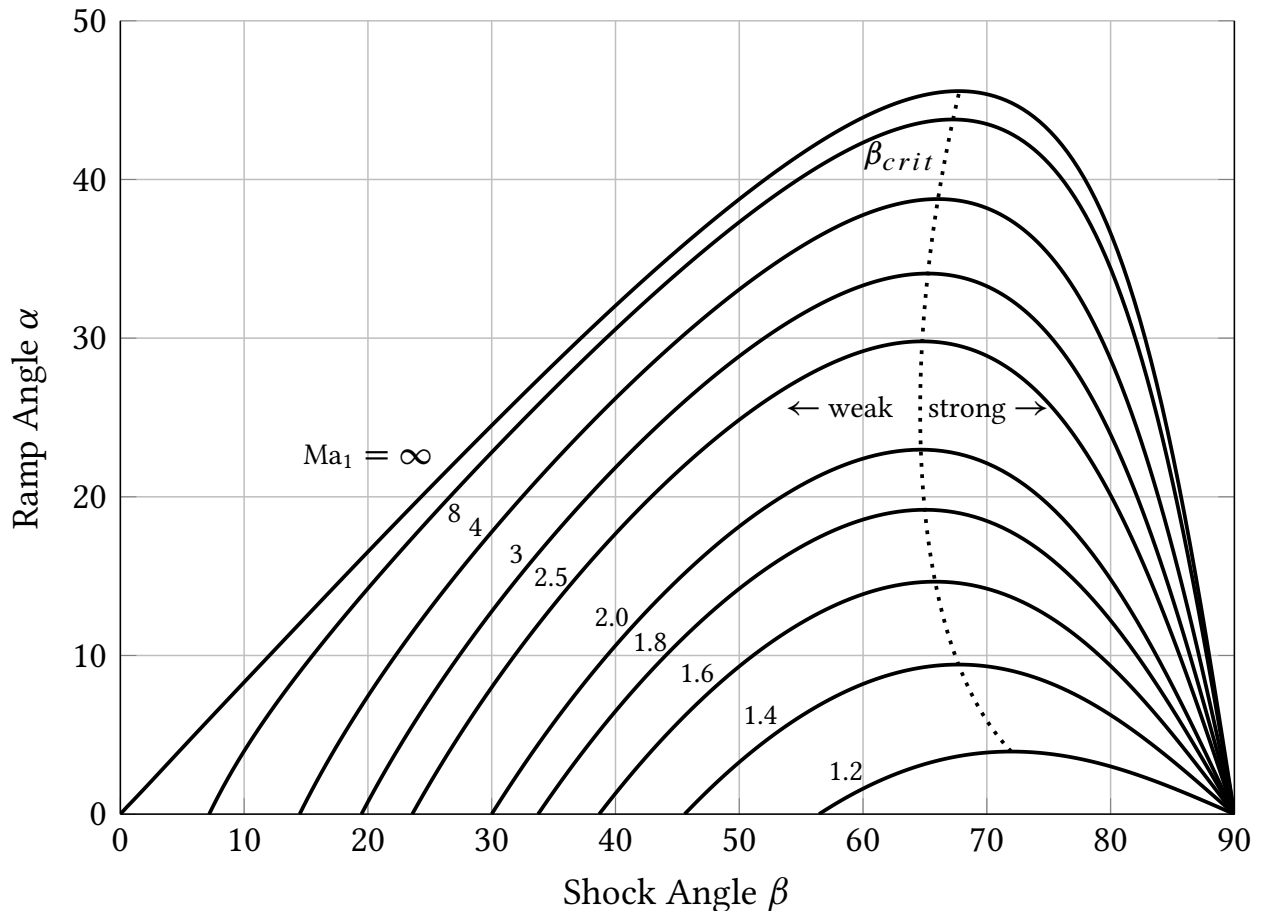


Figure 2.7: Shock angles for various reflection angles and Mach numbers.

2.3.3. Prandtl-Meyer Expansion

The Prandtl-Meyer expansion can be considered as the opposite of an oblique shock wave. A supersonic flow is expanded and accelerated along a kink, see Fig. 2.8. Usually, the flow state (T_1, p_1, Ma_1) as well as the opening angle α are known, while the flow state (T_2, p_2, Ma_2) is wanted. The expansion process is assumed to be isentropic.

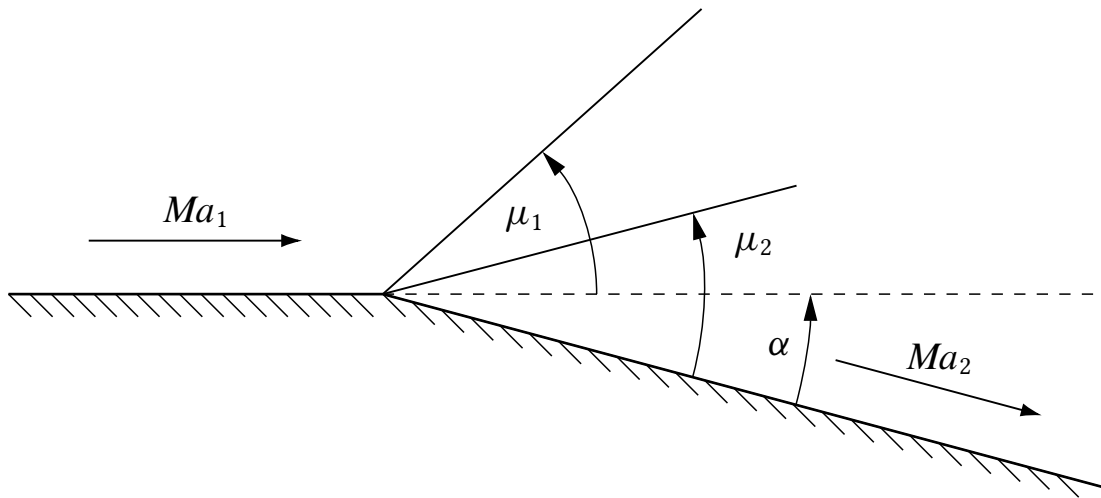


Figure 2.8: Prandtl-Meyer expansion fan along a convex corner.

From geometrical considerations as illustrated in Fig. 2.9, it can be shown that the velocity increment dw and the angle increment $d\alpha$ are related through the Mach angle from Eq. (2.164) so that

$$\frac{w + dw}{w} = \frac{\cos \mu}{\cos (\mu + d\alpha)} \approx \frac{1}{1 - d\alpha \tan \mu}. \quad (2.168)$$

After performing a Taylor series, where second and higher order terms are neglected, the integral

$$\alpha = \int_{w_1}^{w_2} \frac{1}{\tan \mu} \frac{dw}{w} \quad (2.169)$$

is found. For a calorically perfect gas, it simplifies to

$$\alpha = \int_{Ma_1}^{Ma_2} \frac{\sqrt{Ma^2 - 1}}{1 + \frac{\gamma-1}{2} Ma^2} \frac{dMa}{Ma}. \quad (2.170)$$

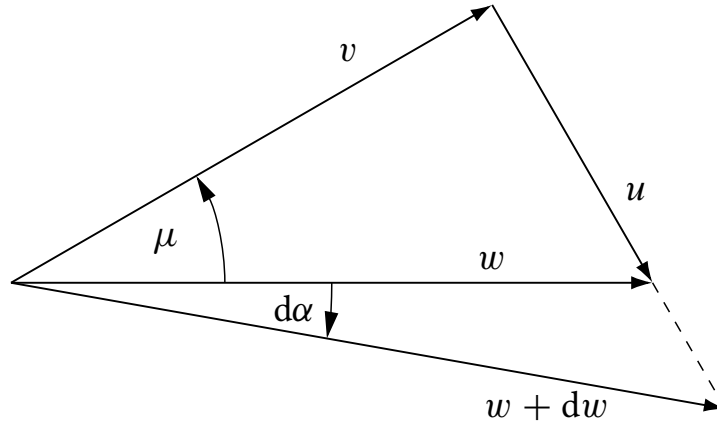


Figure 2.9: Velocity triangle for the Prandtl-Meyer expansion.

Introducing the *Prandtl-Meyer function*

$$\begin{aligned}
 v &= \int_1^{Ma} \frac{\sqrt{Ma^2 - 1}}{1 + \frac{\gamma-1}{2} Ma^2} \frac{dMa}{Ma} \\
 &= \sqrt{\frac{\gamma+1}{\gamma-1}} \arctan \sqrt{\frac{\gamma-1}{\gamma+1} (Ma^2 - 1)} - \arctan \sqrt{Ma^2 - 1},
 \end{aligned} \tag{2.171}$$

the expansion problem can be solved by numerically solving the equation

$$\alpha = v(Ma_2) - v(Ma_1) \tag{2.172}$$

to Ma_2 . If a Newton-Raphson scheme is chosen, the iteration sequence reads

$$Ma_2^{k+1} = Ma_2^k - \frac{v(Ma_2^k) - v(Ma_1) - \alpha}{\frac{\partial v}{\partial Ma}(Ma_2^k)}, \tag{2.173}$$

with the derivative

$$\frac{\partial v}{\partial Ma} = \frac{Ma \left(\frac{\gamma+1}{\gamma-1} \right)}{\sqrt{Ma^2 - 1} \left[(Ma^2 - 1) + \left(\frac{\gamma+1}{\gamma-1} \right) \right]} - \frac{1}{Ma \sqrt{Ma^2 - 1}}. \tag{2.174}$$

Since the expansion is assumed to be isentropic and calorically perfect, the values of T_2 and p_2 can be estimated using Eqs. (2.23) and (2.24). See also Hayes¹⁵⁴ and Anderson¹⁵⁷ for further reading.

3. Combustion and Radiation

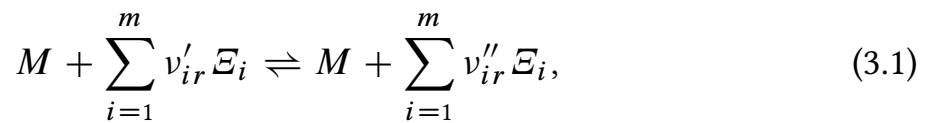
This chapter covers the one-dimensional equations which have been used to model a simplified description of the combustion process. Since thermal radiation becomes relevant for high surface temperatures, the modeling approach is described in this chapter as well. One problem related to the radiation model is the visibility between the radiating surfaces of the investigated geometry. The determination of surface visibilities is briefly explained. In addition to the thermal radiation of the surface, radiative effects of water vapor have been investigated, using the model of Hottel and Egbert.⁸² It turned out however, that gas radiation plays a negligible role in the combustor heat budget. Therefore, it will not be discussed within the present work. Concerning the problem of gas radiation, one may refer to Vortmeyer and Kabelac¹⁵⁸ for further reading.

3.1. Combustion Modeling

The combustion simulation is performed on two scales. On the macroscale, where $\delta x \approx 0.1$ mm, the system of differential equations as given in Eq. (2.148) is solved using an explicit fifth order Runge-Kutta-Fehlberg approach.¹⁵⁹ The contribution of $\frac{\partial Y}{\partial x}$ in Eq. (2.150) respectively Eq. (2.153) is calculated in a microscale, which is between two and three orders of magnitudes below the macroscale.

3.1.1. Chemical Kinetics

Let the reactive fluid consist of n several species i , each one having a mass fraction Y_i , and describe the combustion through a set of m elementary reactions r . The general form of a elementary reaction r reads



with ν' being the molar multiples for of educts and ν'' those of the products of the contributing species \mathcal{E} . In Eq. (3.1) and only Eq. (3.1), the symbol M , stands for an optional inert collision partner. It is not to be confused with the molar Mass M . The temporal derivative of each mass fraction Y_i reads¹⁶⁰

$$\frac{\partial Y_i}{\partial t} = v M_i \sum_{r=1}^m \left[(\nu''_{ir} - \nu'_{ir}) \left(k'_r \prod_{q=1}^{n+1} c_q^{\nu'_{qr}} - k''_r \prod_{q=1}^{n+1} c_q^{\nu''_{qr}} \right) \right], \quad (3.2)$$

with k' and k'' being the forward and backward reaction speeds,

and c_q being the molar concentrations

$$c_q = \frac{Y_q}{v M_q}. \quad (3.3)$$

The $(n + 1)^{\text{th}}$ index in the sum of Eq. (3.2) occurs if an inert collision partner exists in the considered reaction. In the present model, the speed k'_r of the r^{th} reaction, is modeled over an Arrhenius approach

$$k'_r = \tilde{A}_r T^{\tilde{n}_r} e^{-\frac{\tilde{E}_r}{\mathcal{R}T}}, \quad (3.4)$$

where the coefficients \tilde{A}_r , \tilde{E}_r and \tilde{n}_r are given by the chosen combustion model (see Tab. E.1). The speed of the backward reaction k''_j is not given in the combustion model and needs no be calculated. First, the molar Gibbs potential

$$\Delta_f g_i^\circ = \Delta_f h_i^\circ - T \Delta_f s_i^\circ \quad (3.5)$$

of each species i at reference pressure p° needs to be determined from the molar formation enthalpy h_i° and entropy s_i° . For a general species $C_w H_x N_y O_z$, these properties read

$$\Delta_f h^\circ = h^\circ_{(C_w H_x N_y O_z)} - \frac{1}{2} \left[2w h^\circ_{(C)} + x h^\circ_{(H_2)} + y h^\circ_{(N_2)} + z h^\circ_{(O_2)} \right], \quad (3.6)$$

$$\Delta_f s^\circ = s^\circ_{(C_w H_x N_y O_z)} - \frac{1}{2} \left[2w s^\circ_{(C)} + x s^\circ_{(H_2)} + y s^\circ_{(N_2)} + z s^\circ_{(O_2)} \right], \quad (3.7)$$

The molar gibbs free energy $\Delta_r g^\circ$ of the r^{th} reaction at reference pressure p° reads

$$\Delta_r g^\circ = \sum_i v''_{ir} \Delta_f g_i^\circ - \sum_i v'_{ir} \Delta_f g_i^\circ \quad (3.8)$$

Having $\Delta_r g^\circ$, the backwards reaction speed can be calculated using the *law of mass actions*

$$\frac{k''_r}{k'_r} = \left(\frac{p^\circ}{\mathcal{R}T} \right)^{(\sum_i v'_{ir} - \sum_i v''_{ir})} \exp \left(\frac{\Delta_r g^\circ}{\mathcal{R}T} \right). \quad (3.9)$$

A common pitfall in modeling combustion processes is the consistency of units. For historical reasons, the reaction models are usually given in thermochemical calories, where $1 \text{ cal}_{\text{th}} = 4184 \text{ J}$, and cubic centimeters, where $1 \text{ ccm} = 10^{-6} \text{ m}^3$. If this is the case, the activation energy \tilde{E}_r in Eq. (3.4) needs to be converted to Joule, while the specific volume v in Eqs. (3.2) and (3.3) has the unit ccm/kg and the term $p^\circ/\mathcal{R}T$ in Eq. (3.9) has the unit mol/ccm .

Neglecting losses on the microscale, the enthalpy gradient reads (see also Eq. (2.147))

$$\begin{aligned} \frac{\partial h}{\partial t} &= \left(\frac{\partial h}{\partial T} \right)_{p, Y_i} \frac{\partial T}{\partial t} + \left(\frac{\partial h}{\partial p} \right)_{T, Y_i} \frac{\partial p}{\partial t} + \sum_i \left(\frac{\partial h}{\partial Y_i} \right)_{T, p} \frac{\partial Y_i}{\partial x} \\ &= c_p \frac{\partial T}{\partial t} + v (1 - T \alpha) \frac{\partial p}{\partial t} + \sum_i h_i \frac{\partial Y_i}{\partial t} = 0. \end{aligned} \quad (3.10)$$

Specializing for an ideal gas, it follows that the temperature gradient reads

$$\frac{\partial T}{\partial t} = -\frac{1}{c_p} \sum_i h_i \frac{\partial Y_i}{\partial t}. \quad (3.11)$$

For the integration of Y_i within the microscale, Walther developed the implicit scheme¹⁶¹

$$\left[\begin{array}{c|c} \delta_{ij} - C_1 \frac{\partial^2 Y_i}{\partial Y_j \partial t} & -C_1 \frac{\partial^2 Y_i}{\partial T \partial t} \\ \hline -C_1 \frac{\partial^2 T}{\partial Y_j \partial t} & 1 - C_1 \frac{\partial^2 T}{\partial T \partial t} \end{array} \right]^z \left[\begin{array}{c} \Delta Y_j \\ \Delta T \end{array} \right]^{z+1} = C_1 \left[\begin{array}{c} \frac{\partial Y_i}{\partial t} \\ \frac{\partial T}{\partial t} \end{array} \right]^z + C_2 \left[\begin{array}{c} \Delta \xi_i \\ \Delta T \end{array} \right]^z, \quad (3.12)$$

with the constants

$$C_1 = \frac{2}{3} \frac{\widetilde{\Delta x}}{u}, \quad (3.13)$$

$$C_2 = \frac{1}{3}, \quad (3.14)$$

where $\widetilde{\Delta x}$ is the spacial step of the microscale. Note that counterintuitively, it is due to the non-orthogonality of Y_i

$$\frac{\partial^2 Y_i}{\partial Y_i \partial t} \neq 0. \quad (3.15)$$

On the macroscale with the stepsize Δx , the change of mass fractions needed for Eq. (2.153) read

$$\frac{\partial Y_i}{\partial x} \approx \frac{\Delta Y_i}{\Delta x}, \quad (3.16)$$

where ΔY_i is the finite change calculated along a group of steps on the microscale.

3.1.2. Modeling of Fuel Injection

The fuel is injected at a discrete point in the combustor, and therefore contributes to the inertial properties of the flow instantaneously. To prevent an unrealistically fast combustion, however, only a fraction η_{fuel} of the fuel mass is allowed to contribute to the chemical reaction. Following a model by Murthy,¹⁶² and Scheuermann et.al,¹⁶³ an exponential mixing function was chosen

$$\eta_{\text{fuel}}(x) = \begin{cases} \eta_{\text{mix,inj}} \left[1 - (1 - \hat{\eta}_{\text{mix,inj}})^{\frac{x-x_{\text{inj}}}{l_{\text{mix,inj}}}} \right] & \text{if } x > x_{\text{inj}} \\ 0 & \text{else,} \end{cases} \quad (3.17)$$

where x_{inj} is the position of the fuel injection, $\hat{\eta}_{\text{mix,inj}} = 0.99$ a constant, $\eta_{\text{mix,inj}}$ the mixing efficiency of the injector, and the mixing length $l_{\text{mix,inj}}$ the position where the following condition is fulfilled:

$$\eta_{\text{fuel}}(x_{\text{inj}} + l_{\text{mix,inj}}) = \hat{\eta}_{\text{mix,inj}} \eta_{\text{mix,inj}}. \quad (3.18)$$

The mixing length depends on the stoichiometric fuel ratio ϕ_{inj} and the geometry of the injector. A frequently used empirical correlation for the mixing length was suggested by Pulsonetti¹⁶⁴

$$l_{\text{mix,inj}} \approx 0.179 d_{\theta} C_{\text{mix,inj}} e^{1.72 \phi_{\text{inj}}}, \text{ where } 0 \leq \phi_{\text{inj}} \leq 1. \quad (3.19)$$

In a first approximation, the inviscid duct height d_{θ} can be set equal to the geometric duct height d_3 .

3.2. Thermal Radiation Fundamentals

Using the previously discussed methods, one will find that the expected convective heat loads on the structure will be in the same order of magnitude as those heat fluxes caused by thermal radiation. A distinction is made between radiation from surface to surface, respectively surface to environment, and combustion gas radiation. As it turns out however, the latter will have a very small effect on the thermal state of the surface.

3.2.1. Emissivity, Absorbtivity and Reflectivity of Technical Surfaces

Any technical surface emits thermal radiation across several wavelengths in the electromagnetic spectrum. The area-specific heat \dot{w}_{λ} emitted over a wavelength λ can be modeled through Planck's law¹⁶⁵

$$\dot{w}_\lambda = \epsilon_\lambda \frac{2 \pi h c^2}{\lambda^5 \left(e^{\frac{hc}{\lambda k_B T}} - 1 \right)}, \quad (3.20)$$

with T being the surface temperature, h being the Planck constant, c the speed of light and k_B the Boltzmann constant. The spectral emissivity $0 < \epsilon_\lambda \leq 1$ is a temperature-dependent material parameter which has to be determined experimentally. A *black body* has an ideal surface emissivity of $\epsilon_\lambda = 1$. In the *gray body* model, the spectral emissivity ϵ_λ is averaged over the wave spectrum so that

$$\epsilon = \frac{\int_0^\infty \epsilon_\lambda \frac{2 \pi h c^2}{\lambda^5 \left(e^{\frac{hc}{\lambda k_B T}} - 1 \right)} d\lambda}{\int_0^\infty \frac{2 \pi h c^2}{\lambda^5 \left(e^{\frac{hc}{\lambda k_B T}} - 1 \right)} d\lambda}. \quad (3.21)$$

With the emissivity ϵ being independent of the wavelength λ , Eq. (3.20) can be integrated analytically, which leads to the Stefan-Boltzmann law

$$\dot{w} = \epsilon_\lambda \int_0^\infty \frac{2 \pi h c^2}{\lambda^5 \left(e^{\frac{hc}{\lambda k_B T}} - 1 \right)} d\lambda = \epsilon \sigma T^4, \quad (3.22)$$

with the Stefan-Boltzmann constant

$$\sigma = \frac{2 \pi^5 k_B^4}{15 c^2 h^3}. \quad (3.23)$$

Regarding availability, scattering and measurement accuracy of experimental data, it is in many cases sufficient to neglect the temperature dependence of ϵ .

Now let an opaque surface be exposed to an incident radiation load \dot{v} . The fraction $\alpha \dot{v}$ is absorbed and the remaining part $(1 - \alpha) \dot{v}$ is reflected. The total heat load on the surface results from the balance is

$$\dot{q} = \alpha \dot{v} - \dot{w}, \quad (3.24)$$

while the total radiation emitted by a surface reads

$$\dot{\eta} = (1 - \alpha) \dot{v} + \dot{w}. \quad (3.25)$$

In general, the radiative absorptivity of the surface depends on the wavelength of the incident heat load, and is averaged similarly to ϵ_λ ¹⁶⁵

$$\alpha \approx \frac{\int_0^\infty \alpha_\lambda \dot{v}_\lambda d\lambda}{\int_0^\infty \dot{v}_\lambda d\lambda}. \quad (3.26)$$

According to Kirchhoff's law, emissivity and absorptivity must be identical to allow the surface to reach a thermal equilibrium

$$\alpha_\lambda = \epsilon_\lambda. \quad (3.27)$$

In case of a gray body model, Eq. (3.27) leads to the conclusion that also the averaged values of emissivity and absorptivity must be identical

$$\alpha \approx \epsilon. \quad (3.28)$$

This assumption however is restricted to the case where incident and emitted radiation have similar wavelengths, say infrared radiation. In case of a combination of infrared radiation and visible sunlight, for example, Eq. (3.28) can not be applied.

Apart from being dependent on wavelength and temperature, the emissivity and absorptivity also depend on the angle of incidence, respectively the angle of view. Many nonconducting and semiconducting materials like ceramics and other non-metals can be modeled as a *diffuse radiator*, where the aligned intensity of radiation can be modeled through Lambert's cosine law

$$\dot{\eta}_\theta = \dot{\eta} \frac{\cos \theta}{\pi}, \quad (3.29)$$

where θ is the angle between the direction of perspective and the surface normal.

3.2.2. Surface Visibility

Consider an arbitrary surface increment dA_k emitting the thermal radiation $\dot{\eta}_k$ and another increment dA_j receiving a fraction F_{kj} , $\dot{\eta}_k$ so that

$$\dot{v}_{kj} dA_j = F_{kj} \dot{\eta}_k dA_k. \quad (3.30)$$

In case of diffuse emission and reception, the view factor F_{kj} between two finite surfaces A_k and A_j is directly found from Eq. (3.29)¹⁶⁶

$$F_{kj} = \frac{1}{\pi A_k} \int_{A_k} \int_{A_j} \frac{\cos \theta_j \cos \theta_k}{r^2} dA_j dA_k, \quad (3.31)$$

where r is the distance between the emitting and the receiving increments of the surfaces. Solving Eq. (3.31) costs a lot of calculation power, especially if the view

between the two surface increments is partially blocked. For three-dimensional problems, Monte Carlo calculations, where individual rays are fired randomly from the sending surface have proven to be more efficient than a direct solution.¹⁶⁷ Hottel's method of crossed strings¹⁶⁸ provides a very easy solution for two-dimensional problems. Let a surface 1 be determined by the line \overline{AB} and a surface 2 be determined by the line \overline{CD} , as illustrated in Fig. 3.1. Then, if the view between the surfaces is not blocked, the view factor can be determined by the distances

$$F_{12} = \frac{\overline{AC} + \overline{BD} - \overline{AD} - \overline{BC}}{\overline{AB}}. \quad (3.32)$$

In a more general formulation, even if the view is partially blocked by a third surface like on the right part of Fig. 3.1, F_{12} can be found by the sum of all crossed strings minus the sum of all uncrossed strings divided by the length of the emitting surface.

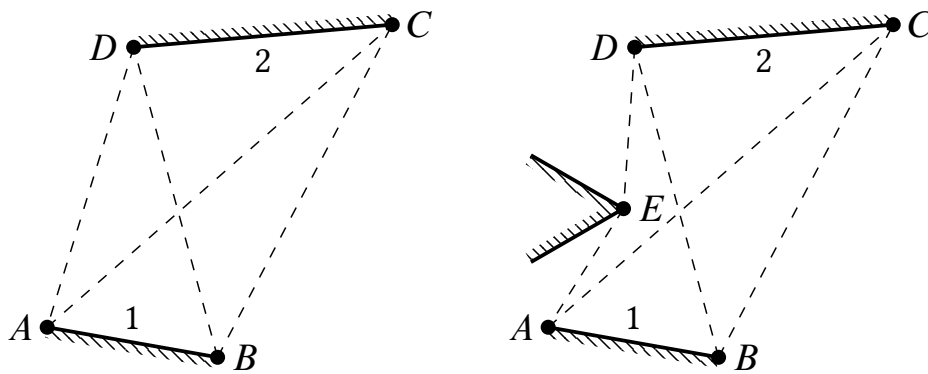


Figure 3.1: Hottel's method of crossed strings.

3.2.3. Interaction of Multiple Surfaces

Let a geometry be discretized in n finite opaque surfaces, and the average temperature T_j and emissivity ϵ_j as well as all viewfactors F_{kj} be known. Then, each surface j will emit and reflect thermal radiation following Eqs. (3.20) and (3.25), and transmit a heat load \dot{q}_j following Eq. (3.24) into the bulk material. After some algebraic manipulation of these equations, the area specific heat loads \dot{q}_j are found by solving the linear equation system¹⁶⁹

$$\left(F_{kj} \frac{1 - \epsilon_j}{\epsilon_j} - \frac{\delta_{kj}}{\epsilon_j} \right) \dot{q}_j = (\delta_{kj} - F_{kj}) \sigma T_j^4, \quad (3.33)$$

where δ_{kj} is the Kronecker delta.

4. Finite Element Method

With the growing availability of computing systems in the 1950s and 1960s, scientists have begun to investigate methods for numerically solving problems in mechanical engineering. Having originally been developed to perform structural simulations of aircraft structures,^{170,171} the finite element method was established as a powerful tool to solve differential equations. This chapter provides a brief overview of the underlying balance equations for thermal and mechanical field formulation. The interpolation functions for the chosen elements can be found in App. A. The chapter closes with a description of the modeling of thermal radiation.

One may refer to standard literature like Bathe,¹⁷² Zienkiewicz et al,¹⁷³ Brenner and Scott,¹⁷⁴ and Argyris and Mlejnek¹⁷⁵ for further reading.

4.1. Thermal Field Formulation

This section covers the Galerkin-approach which is used to model the heat conduction problem with finite elements. The backward Euler method is explained, which is used for the transient analysis. The spacial dimensions are indexed using i and j ; nodal degrees of freedom are indexed by r and s . The timestep is indexed using the letter z .

4.1.1. The Weak Formulation of the Thermal Energy Balance

The energy balance equation for thermal conduction reads in its Lagrangian form¹⁷⁶

$$\rho c \frac{\partial T}{\partial t} + \frac{\partial \dot{q}_i}{\partial x_i} - \dot{b} = 0, \quad (4.1)$$

where ρ is the density, c the specific heat capacity, \dot{q} the directed area specific heat flux, and \dot{b} the volumetric heat load of heat that is generated within the bulk material. According to the *fundamental lemma of calculus of variations*, the differential equation (4.1) is also fulfilled for a whole domain Ω , if it is multiplied with an arbitrary function δT before integration, so that

$$\int_{\Omega} \delta T \left(\rho c \frac{\partial T}{\partial t} + \frac{\partial \dot{q}_i}{\partial x_i} - \dot{b} \right) dV = 0. \quad (4.2)$$

From partial integration and Gauss's theorem, it follows for the heat flux term

$$\int_{\Omega} \delta T \frac{\partial \dot{q}_i}{\partial x_i} dV = - \int_{\Omega} \frac{\partial \delta T}{\partial x_i} \dot{q}_i dV + \int_{\partial \Omega} \delta T \dot{q}_i n_i dA. \quad (4.3)$$

Herein, the first term describes the heat flux through the structure and the second term describes the heat flux along the surface $\partial\Omega$, where \mathbf{n} is the normal vector pointing away from the surface. Replacing the former term with Fourier's law from Eq. (2.29) yields the *weak formulation* of the energy balance^c

$$\int_{\Omega} \delta T \rho c \frac{\partial T}{\partial t} dV + \int_{\Omega} \frac{\partial \delta T}{\partial x_i} \lambda_{ij} \frac{\partial T}{\partial x_j} dV + \int_{\partial\Omega} \delta T \dot{q}_i n_i dA - \int_{\Omega} \delta T \dot{b} dV = 0. \quad (4.4)$$

4.1.2. Finite Element Discretization of the Thermal Energy Balance

The goal of the method of Galerkin is to represent Eq. (4.4) by a system of equations that can be solved numerically. In order to construct the system of equations, the domain Ω is subdivided into finite elements

$$\Omega = \bigcup_{e=1}^m \Omega^e. \quad (4.5)$$

Within each element e , the weak formulation from Eq. (4.4) is discretized and the contributions to the vectors and matrix for the equation system representing the whole domain Ω are determined. Introducing the shape function N^e , the real and virtual temperatures are approximated through

$$\delta T \approx \delta \hat{T}_r^e N_r^e, \quad (4.6)$$

$$T \approx N_s^e \hat{T}_s^e, \quad (4.7)$$

where \mathbf{N} contains the shape function components ϕ_r

$$\mathbf{N}^e = [\phi_1 \mid \phi_2 \mid \dots \mid \phi_n], \quad (4.8)$$

and $\delta \hat{T}_r^e$ respectively \hat{T}_s^e are the virtual and real temperatures at the nodes of each element. The shape function components ϕ_r are shown in Appendix A.1. The spatial derivatives are approximated using the function \mathbf{B}^e , so that

^cNote that by definition, it is $\dot{q}_w = -\dot{q}_i n_i$. See also Eqs. (2.45) and (2.109).

$$\frac{\partial \delta T}{\partial x_i} \approx \delta \hat{T}_r^e B_{ir}^e, \quad (4.9)$$

$$\frac{\partial T}{\partial x_j} \approx B_{js}^e \hat{T}_s^e, \quad (4.10)$$

where the \mathbf{B} -matrix reads

$$\mathbf{B}^e = \left[\begin{array}{c|c|c|c} \frac{\partial \phi_1}{\partial x_1} & \frac{\partial \phi_2}{\partial x_1} & \cdots & \frac{\partial \phi_n}{\partial x_1} \\ \frac{\partial \phi_1}{\partial x_2} & \frac{\partial \phi_2}{\partial x_2} & \cdots & \frac{\partial \phi_n}{\partial x_2} \end{array} \right]. \quad (4.11)$$

Specializing for a problem with zero volumetric heat load, $\dot{b} = 0$, The weak formulation in Eq. (4.4) for a finite element reads in its discretized form

$$\underbrace{\delta \hat{\mathcal{T}}_r^e \int_{\Omega^e} N_r^e \rho c N_s^e dV^e}_{D_{rs}^e} \frac{\partial \hat{T}_s^e}{\partial t} + \underbrace{\delta \hat{\mathcal{T}}_r^e \int_{\Omega^e} B_{ir}^e \lambda_{ij} B_{js}^e dV^e}_{K_{rs}} \hat{T}_s^e \approx \underbrace{\delta \hat{\mathcal{T}}_r^e \int_{\delta \Omega^e} -N_r^e n_i \dot{q}_i dA^e}_{f_r^e}. \quad (4.12)$$

After assembling, the space-discretized problem for the domain Ω is represented by a vector-matrix system, so that

$$D_{rs} \frac{\partial \hat{T}_s}{\partial t} + K_{rs} \hat{T}_s = f_r. \quad (4.13)$$

4.1.3. Backward Euler Time-stepping

In the analysis of transient heat conduction, the nodal temperatures \hat{T}^z are known at a given timestep t^z , and the nodal temperatures \hat{T}^{z+1} at the next timestep t^{z+1} are to be found. Using the approximation

$$\frac{\partial \hat{T}_s}{\partial t} \approx \frac{\hat{T}_s^{z+1} - \hat{T}_s^z}{\Delta t} \quad (4.14)$$

Eq. (4.12) can be rearranged so that a linear equation system of the shape

$$\left[D_{rs}^{z+1} + \Delta t K_{rs}^{z+1} \right] \hat{T}_s^{z+1} = D_{rs}^{z+1} \hat{T}_s^z + \Delta t f_r^{z+1} \quad (4.15)$$

is created,¹⁷⁷ where the matrices \mathbf{D} and \mathbf{K} and the load vector \mathbf{f} are evaluated with respect to the new temperature vector $\hat{\mathbf{T}}^{z+1}$. Due to its low oscillation behavior, the backward Euler method is known to be very robust. Although sometimes claimed otherwise, this method is not unconditionally stable, and fails if the timestep Δt is chosen too large. This is especially the case if the load vector \mathbf{f} is a nonlinear function of $\hat{\mathbf{T}}$. The implicit nature of Eq. (4.15) can be approached by a relaxed Newton-Raphson-Method, while a significant efficiency gain is achieved if an iterative solving algorithm such as a stabilized biconjugate gradient method¹⁷⁸ is used.

4.2. Mechanical Field Formulation

An index notation is used in order to be consistent with Chapter 2. As is the thermal field, the degrees of freedom are indexed by r and s . The spacial dimensions are indexed using i, j, k, l , the Voigt notation is indexed using the letters v and w .

4.2.1. Weak Formulation of the Momentum Balance

The momentum balance of an undamped problem reads in its Lagrangian form

$$\rho \frac{\partial^2 u_i}{\partial t^2} - \frac{\partial \sigma_{ji}}{\partial x_j} - \psi_i = 0, \quad (4.16)$$

with σ being the Cauchy stress tensor and ψ_i being body forces such as gravity or magnetism, see also Eq. (2.33). Applying the fundamental lemma of calculus of variations in the same way as done in the heat equation, Eq. (4.1), one obtains

$$\int_{\Omega} \delta u_i \left(\rho \frac{\partial^2 u_i}{\partial t^2} - \frac{\partial \sigma_{ji}}{\partial x_j} - \psi_i \right) dV = 0, \quad (4.17)$$

where δu_i is an arbitrary function. Similarly to Eq. (4.3), one finds that

$$- \int_{\Omega} \delta u_i \frac{\partial \sigma_{ji}}{\partial x_j} dV = \int_{\Omega} \frac{\partial \delta u_i}{\partial x_j} \sigma_{ji} dV - \int_{\partial \Omega} \delta u_i \sigma_{ji} n_j dA, \quad (4.18)$$

so that the virtual work equation reads

$$\int_{\Omega} \delta u_i \rho \frac{\partial^2 u_i}{\partial t^2} dV + \int_{\Omega} \frac{\partial \delta u_i}{\partial x_j} \sigma_{ji} dV - \int_{\partial \Omega} \delta u_i \sigma_{ji} n_j dA - \int_{\Omega} \delta u_i \psi_i dV = 0. \quad (4.19)$$

4.2.2. Hooke's Law, Engineering Strains and Voigt Notation

The field of linear mechanics considers structural problems with small deformations. Introducing the fourth order elasticity tensor \mathbf{C} , Cauchy's stress tensor $\boldsymbol{\sigma}$ from Eq. (2.25) is found by relating \mathbf{C} to the spacial derivatives of the local displacements as follows¹⁷⁹

$$\sigma_{ij} = C_{ijkl} \frac{1}{2} \left(\frac{\partial u_k}{\partial x_l} + \frac{\partial u_l}{\partial x_k} \right). \quad (4.20)$$

Mathematically, Hooke's law is very similar to the Newtonian fluid assumption (2.27), except that here u_k are displacements and not velocities. Specializing for a static problem without body forces, so that $\ddot{\mathbf{u}} = 0$ and $\boldsymbol{\psi} = 0$, Eq. (4.19) simplifies to

$$\int_{\Omega} \frac{\partial \delta u_i}{\partial x_j} \sigma_{ji} dV = \int_{\partial\Omega} \delta u_i \sigma_{ji} n_j dA. \quad (4.21)$$

Due to the symmetry of the stress tensor, $\sigma_{ij} = \sigma_{ji}$, it follows that

$$\int_{\Omega} \frac{\partial \delta u_i}{\partial x_j} \sigma_{ji} dV = \int_{\Omega} \frac{1}{2} \left(\frac{\partial \delta u_i}{\partial x_j} + \frac{\partial \delta u_j}{\partial x_i} \right) \sigma_{ij} dV + \underbrace{\int_{\Omega} \frac{1}{2} \left(\frac{\partial \delta u_i}{\partial x_j} - \frac{\partial \delta u_j}{\partial x_i} \right) \sigma_{ij} dV}_{=0}, \quad (4.22)$$

and therefore for Eq. (4.21)

$$\int_{\Omega} \frac{1}{2} \left(\frac{\partial \delta u_i}{\partial x_j} + \frac{\partial \delta u_j}{\partial x_i} \right) C_{ijkl} \frac{1}{2} \left(\frac{\partial u_k}{\partial x_l} + \frac{\partial u_l}{\partial x_k} \right) dV = \int_{\partial\Omega} \delta u_i \sigma_{ij} n_j dA. \quad (4.23)$$

In order to make Eq. (4.23) handier, the *engineering strain* relations are introduced, reading

$$\varepsilon_{kk} = \frac{\partial u_k}{\partial x_k} \quad (4.24)$$

$$\gamma_{kl} = 2 \varepsilon_{kl} = \frac{\partial u_k}{\partial x_l} + \frac{\partial u_l}{\partial x_k}, \quad \forall k \neq l, \quad (4.25)$$

and for their virtual counterparts

$$\delta\varepsilon_{ii} = \frac{\partial\delta u_i}{\partial x_i} \quad (4.26)$$

$$\delta\gamma_{ij} = 2\delta\varepsilon_{ij} = \frac{\partial\delta u_i}{\partial x_j} + \frac{\partial\delta u_j}{\partial x_i}, \forall i \neq j. \quad (4.27)$$

Using these definitions, Eq. (4.20) can be rewritten in *Voigt notation*

$$\underbrace{\begin{bmatrix} \sigma_{11} \\ \sigma_{22} \\ \sigma_{33} \\ \tau_{23} \\ \tau_{13} \\ \tau_{12} \end{bmatrix}}_{\sigma_v} = \underbrace{\begin{bmatrix} C_{11} & C_{12} & C_{13} & C_{14} & C_{15} & C_{16} \\ & C_{22} & C_{23} & C_{24} & C_{25} & C_{26} \\ & & C_{33} & C_{34} & C_{35} & C_{36} \\ & & & C_{44} & C_{45} & C_{46} \\ & \text{sym.} & & & C_{55} & C_{56} \\ & & & & & C_{66} \end{bmatrix}}_{C_{vw}} \underbrace{\begin{bmatrix} \varepsilon_{11} \\ \varepsilon_{22} \\ \varepsilon_{33} \\ \gamma_{23} \\ \gamma_{13} \\ \gamma_{12} \end{bmatrix}}_{\varepsilon_w}, \quad (4.28)$$

where the entries C_{vw} of the elasticity matrix are called *engineering constants*. Unfortunately, the order of the engineering shear strains, here $\gamma_{23} - \gamma_{13} - \gamma_{12}$ is not consistent across literature. If the engineering constants C_{vw} are given, the order of the shear strains they are referred to should always be mentioned as well. For a material that is orthotropic along the x_1 , x_2 , and x_3 axis, the elasticity matrix \mathbf{C} can be determined from the Young's moduli E_k , the Poisson ratios ν_{kl} and the shear moduli G_k

$$\mathbf{C}^{-1} = \begin{bmatrix} 1/E_1 & -\nu_{21}/E_2 & -\nu_{31}/E_3 & 0 & 0 & 0 \\ -\nu_{12}/E_1 & 1/E_2 & -\nu_{32}/E_3 & 0 & 0 & 0 \\ -\nu_{13}/E_1 & -\nu_{23}/E_2 & 1/E_3 & 0 & 0 & 0 \\ 0 & 0 & 0 & 1/G_{23} & 0 & 0 \\ 0 & 0 & 0 & 0 & 1/G_{13} & 0 \\ 0 & 0 & 0 & 0 & 0 & 1/G_{12} \end{bmatrix}. \quad (4.29)$$

While the definition in Eq. (4.29) refers to the common Anglo-Saxon notation, literature from the German-speaking area usually notes the indices kl in reverse order. When literature data is used, special caution is required, since due to the symmetry of the elasticity matrix \mathbf{C} , the Poisson numbers ν_{ij} and ν_{ji} are only equal if the Young's moduli E_i and E_j are equal as well.

For a two-dimensional problem, the *plane stress* assumption is usually applied. Here, the tensile stress σ_{33} and the shear stresses τ_{13} and τ_{23} are neglected, and the third and sixth row and column of the compliant matrix \mathbf{C}^{-1} in Eq. (4.29) are canceled. Hooke's law for an orthotropic material in two dimensions then reads

$$\begin{bmatrix} \sigma_{11} \\ \sigma_{22} \\ \tau_{12} \end{bmatrix} = \begin{bmatrix} \frac{1}{E_1} & -\frac{\nu_{21}}{E_2} & 0 \\ -\frac{\nu_{12}}{E_1} & \frac{1}{E_2} & 0 \\ 0 & 0 & \frac{1}{G_{12}} \end{bmatrix}^{-1} \begin{bmatrix} \varepsilon_{11} \\ \varepsilon_{22} \\ \gamma_{12} \end{bmatrix}. \quad (4.30)$$

In Voigt notation, the left hand side of Eq. (4.21) becomes rather compact

$$\int_{\Omega} \delta \varepsilon_v C_{vw} \varepsilon_w dV = \int_{\partial\Omega} \delta u_i \sigma_{ij} n_j dA. \quad (4.31)$$

4.2.3. Hooke's Law with Thermal Deformation

Temperature changes cause the material to expand or contract, so that Hooke's law from Eq. (4.28) needs to be modified to

$$\sigma_v = C_{vw} (\varepsilon_w - \delta_{wj} \mu_j) \quad \forall \quad 1 \leq j \leq 3. \quad (4.32)$$

Herein, μ_j denotes the thermal deformation in j -direction, and δ_{wj} the Kronecker delta. The thermal strains of $\boldsymbol{\mu}$ are in relation to a reference temperature T° defined as

$$\mu_j = \exp \left(\int_{T^\circ}^T \alpha_j dT \right) - 1, \quad (4.33)$$

with α_i being the tangent thermal expansion coefficient. It is defined as the thermal change of the length l_j in j -direction

$$\alpha_j = \frac{1}{l_j} \frac{dl_j}{dT}, \quad (4.34)$$

which must not be confused with the linear thermal expansion coefficient $\tilde{\alpha}_j$,

$$\tilde{\alpha}_j = \frac{l_j - l_j^\circ}{l_j^\circ (T - T^\circ)}, \quad (4.35)$$

which is often found in literature instead of α_j .

4.2.4. Finite Element Discretization

As with the thermal field, the domain Ω is subdivided into elements Ω^e , in which the displacements and their virtual counterparts are interpolated. If Lagrangian elements are used only, each element e has n nodes, and each node has one degree of freedom per spacial dimension, which are summarized in the vector $\hat{\mathbf{q}}^e$ and its virtual counterpart $\delta\hat{\mathbf{q}}^e$. In case of a two-dimensional problem they read

$$\hat{\mathbf{q}}^e = \left[\hat{u}_{11}^e \quad \hat{u}_{12}^e \mid \hat{u}_{21}^e \quad \hat{u}_{22}^e \mid \dots \mid \hat{u}_{n1}^e \quad \hat{u}_{n2}^e \right]^T, \quad \text{and} \quad (4.36)$$

$$\delta\hat{\mathbf{q}}^e = \left[\delta\hat{u}_{11}^e \quad \delta\hat{u}_{12}^e \mid \delta\hat{u}_{21}^e \quad \delta\hat{u}_{22}^e \mid \dots \mid \delta\hat{u}_{n1}^e \quad \delta\hat{u}_{n2}^e \right]^T, \quad (4.37)$$

where \hat{u}_{js}^e is the displacement of the s^{th} node of the e^{th} element, in the j^{th} direction, and $\delta\hat{u}_{ir}^e$ is the virtual counterpart. The interpolation matrix \mathbf{N}^e is introduced, which allows the interpolations

$$\delta u_i \approx \delta\hat{q}_r^e N_{ir}^e, \quad (4.38)$$

$$u_j \approx N_{js}^e \hat{q}_s^e, \quad (4.39)$$

within the domain Ω^e . For an element with n nodes, the interpolation matrix has the shape

$$\mathbf{N}^e = \left[\begin{array}{cc|cc|ccc|cc} \phi_1 & 0 & \phi_2 & 0 & \dots & \phi_n & 0 \\ 0 & \phi_1 & 0 & \phi_2 & \dots & 0 & \phi_n \end{array} \right], \quad (4.40)$$

The components of the engineering strain vector $\boldsymbol{\varepsilon}$ and its virtual counterpart $\delta\boldsymbol{\varepsilon}$ are interpolated by using the rules

$$\delta\varepsilon_v \approx \delta\hat{q}_r^e B_{vr}^e, \quad (4.41)$$

$$\varepsilon_w \approx B_{ws}^e \hat{q}_s^e, \quad (4.42)$$

where the \mathbf{B} -Matrix has the shape

$$\mathbf{B}^e = \left[\begin{array}{cc|cc|ccc|cc} \frac{\partial\phi_1}{\partial x_1} & 0 & \frac{\partial\phi_2}{\partial x_1} & 0 & \dots & \frac{\partial\phi_n}{\partial x_1} & 0 \\ 0 & \frac{\partial\phi_1}{\partial x_2} & 0 & \frac{\partial\phi_2}{\partial x_2} & \dots & 0 & \frac{\partial\phi_n}{\partial x_2} \\ \frac{\partial\phi_1}{\partial x_2} & \frac{\partial\phi_1}{\partial x_1} & \frac{\partial\phi_2}{\partial x_2} & \frac{\partial\phi_2}{\partial x_1} & \dots & \frac{\partial\phi_n}{\partial x_2} & \frac{\partial\phi_n}{\partial x_1} \end{array} \right]. \quad (4.43)$$

Inserting the shape functions into Eq. (4.31) results in an approximated solution of the virtual work which is performed in the domain Ω_e

$$\underbrace{\delta \hat{\mathbf{q}}_r^e \int_{\Omega^e} B_{vr}^e C_{vw} B_{ws}^e dV^e}_{K_{rs}^e} \hat{q}_s^e \approx \underbrace{\delta \hat{\mathbf{q}}_r^e \left[\int_{\Omega^e} B_{vr}^e C_{vw} \delta_{wj} \mu_j dV^e - \int_{\partial\Omega^e} N_{ir}^e \sigma_{ij} n_j dA^e \right]}_{f_r^e} \quad (4.44)$$

Finally, the elemental stiffness matrices \mathbf{K}^e and load vectors \mathbf{f}^e are assembled

$$\mathbf{K} = \bigcup_{e=1}^m \mathbf{K}^e, \quad (4.45)$$

$$\mathbf{f} = \bigcup_{e=1}^m \mathbf{f}^e, \quad (4.46)$$

and so are the vectors which represent the virtual and real degrees of freedom

$$\delta \hat{\mathbf{q}} = \bigcup_{e=1}^m \delta \hat{\mathbf{q}}^e, \quad (4.47)$$

$$\hat{\mathbf{q}} = \bigcup_{e=1}^m \hat{\mathbf{q}}^e, \quad (4.48)$$

so that the virtual work Equation (4.31) is approximated by

$$K_{rs} \hat{q}_s = f_r, \quad (4.49)$$

where the virtual nodal degrees of freedom are canceled. Solving Eq. (4.49) reveals the local displacements \hat{u}_{sj} in the spacial directions x_j at the s^{th} node.

4.2.5. Stress Calculation

The local stress at an arbitrary point within the domain Ω^e of an element e can be determined by combining Eqs. (4.32) and (4.42), so that

$$\sigma_v = C_{vw} B_{ws}^e (\hat{q}_s^e - \delta_{sj} \mu_j). \quad (4.50)$$

Usually, one is interested in the nodal stresses σ_v^d , which leads to a problem if Lagrangian elements such as QUAM9 and TRIM6 are used. Within the considered domain Ω^e , the displacements \mathbf{q}^e are interpolated by the shape functions of the finite elements. If an edge or a node is shared by more than one element, the shape functions and therefore the interpolated displacement field of the adjoining elements coincide along that edge or at that node. The Lagrangian formulation however, does not allow a continuous spacial derivative, which will result in the fact that the stress calculation at the same node or edge within two different elements will give two different results. One possible way of interpolating a smoothed stress solution is given in Appendix A.3.

5. Inlet Heat Load Investigation

The physics of aerothermodynamic heating of a vehicle moving with hypersonic speed is relatively well known and understood. As for scramjet inlets, however, there seems to be very little literature available on the equilibrium surface heat loads and temperatures that occur under stationary flight conditions, which emerge after a few minutes of hypersonic flight. On the one hand, it must be investigated whether it is possible to build a structure that is able to sustain the expected thermal loads. On the other hand, it must be assured that the flow field remains stable across the whole spectrum of expected wall temperatures.

5.1. Introduction

Most two-dimensional inlet designs mentioned in literature are designed for short-timed experiments (see Figs. 1.2 and 1.3). To reduce complexity and cost, a geometry for that purpose is usually designed with sharp corners, and metal is used for the construction. If the inlet is intended to reach a thermal equilibrium, which can take several minutes, another material such as carbon fiber reinforced ceramics should be considered. The utilization of carbon fiber reinforced ceramics on a scramjet inlet has originally been suggested by Kochendörfer and Krenkel.¹⁸⁰ Wind tunnel tests on a scramjet combustor made out of this material have been performed by Glass et al.²⁶ If such a material is chosen, the geometry needs to be more continuous, evincing round corners and blunt edges. In the present investigation, a two-dimensional scramjet inlet meeting those requirements was developed from a sharp edged configuration by Häberle and Gülhahn.¹⁸¹ The chosen geometry and its dimensions are shown in Fig. 5.1 and Tab. 5.1. Guidelines for the design of such a geometry are given in Appendix D.

The transient heating process of the structure was investigated. The simulations were performed in three steps. In the first step, an isothermal wall temperature was assumed and a computational fluid dynamics simulation was performed. The isothermal wall temperature was varied between 600 K and 2000 K. From these investigations, local heat transfer coefficients were extracted and used as boundary condition in the second step, in which the transient heating process of the structure was investigated. Critical areas on the surface have been identified, and actively cooled in the third step. The flow field was simulated using the structured Reynolds averaged Navier-Stokes code *FLOWer*¹⁸² from the German Aerospace Centre (DLR). These transient heating off the structure performed using an implicit time-stepping method (see Sec. 4.1.3), which was implemented in a custom finite element code. The maximum service temperature of the chosen carbon fiber reinforced ceramic C/C-SiC is about 2200 K.¹⁸³ Approximately at this temperature, the silicon carbide

in the matrix of the material softens and loses its capability to sustain mechanical loads. An anti oxidation coating, which consists of yttrium silicate, was successfully tested at temperatures up to 1923 K.¹⁸⁴ According to the results of the present work, this limit is closely reached within a few seconds.

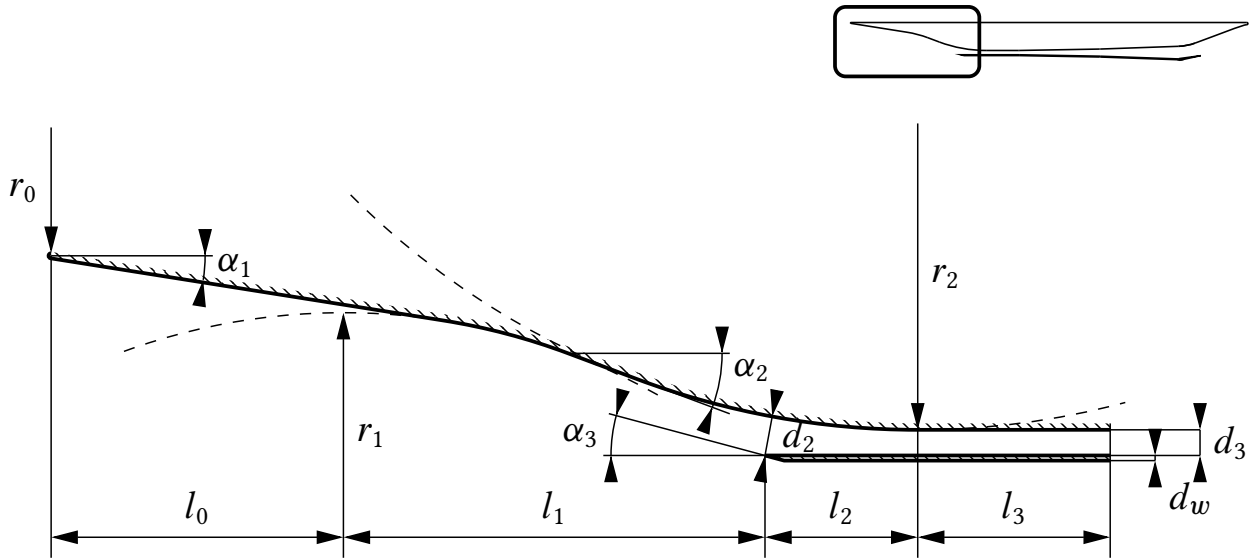


Figure 5.1: Variables for the inlet geometry.

Table 5.1: Geometry parameters for the investigated configuration.

description	name	value
first ramp angle	α_1	9.0°
second ramp angle	α_2	20.5°
lip angle	α_3	15.0°
nose radius	r_0	4 mm
radius of first circle	r_1	1000 mm
radius of second circle	r_2	1250 mm
height of combustor entrance	d_3	40 mm
vertical position of first circle midpoint	-	1089 mm
axial position of first circle midpoint	l_0	455 mm
distance between lip and first circle midpoint	l_1	657 mm
distance between lip and second circle midpoint	l_2	238 mm
isolator length	l_3	300 mm

The risk of material failure is less critical than the risk the surface temperatures causing the inlet to unstart. The terminology of a *started* and an *unstarted* operation mode is used in literature to describe the state of the internal flow field.¹⁸⁵ In a started operation mode, the internal flow field is predominantly supersonic and does not influence the mass flow rate significantly. In an unstarted operation mode, the internal contraction reaches a critical magnitude, which decelerates the flow to sonic speed. This way, a normal shock wave is generated which significantly reduces the mass flow and performance characteristics. If the fuel for the combustion can be used to cool the inlet structure,^{186,187} the surface can be constantly cooled down below a critical wall temperature, so that an unstarting of the inlet is prevented.

Numerical values for the flow conditions needed for the equations listed above are summarized in Tab. 5.2 (for the station numbers, see also Fig. 1.1).

Table 5.2: Preliminary flow data for $T_w = 600$ K
(see also Fig. 1.1 for station numbering)

station	description	T in K	p in Pa	Ma
0	freestream conditions	226.5	1181	8.00
st	conditions at stagnation point	2647	90939	0.37
1	first ramp, oblique shock relation	383.4	5426	6.00
2	second ramp, oblique shock relation	643	23191	4.51
2.1	isolator entry, CFD simulation	1110	43602	2.92
3	combustor entry, CFD simulation	1160	43228	2.77

5.2. General Thoughts on Regenerative Cooling

Regenerative cooling is a widely spread concept in the construction of rocket engines. The basic idea is to use the fuel as cooling fluid and recirculate the heat which is dissipated through the walls back into the combustion process. A few general considerations of the design of the fuel feed system are necessary in order to estimate reasonable boundary conditions for the cooling flow. A possible fuel feed concept, similar to the one suggested by Kanda,^{50,51} is illustrated in Fig. 5.2.

Similarly to the design of the Boeing X-43A, see Fig. 1.4, a vehicle of approximately 2.5 m length and 1 m width is considered. The hydrogen, which would be used as fuel for such a vehicle, would be stored in liquid form.¹⁸⁸ The hydrogen tank could be made out of carbon fiber reinforced plastics (CFRPs), and store the liquid

Following Bernoulli's principle,¹⁹⁵ it is possible to estimate an off-design channel pressure over a parabolic equation

$$p_{\text{ch},3} = p_{\text{tank}} + \left(p_{\text{cg},3} \Big|_{\phi=1} - p_{\text{tank}} \right) \phi^2. \quad (5.2)$$

The chosen channel design is illustrated in Fig. 5.3. It was inspired by the designs investigated French *PTAH-SOCAR* research program.^{196,197} The horizontal hachures in Fig. 5.3 illustrate the planar direction of fabric layers in the carbon fiber reinforced structure. For geometrical reasons, neither the cooling of the nose nor the cooling of the external side of the engine is feasible.

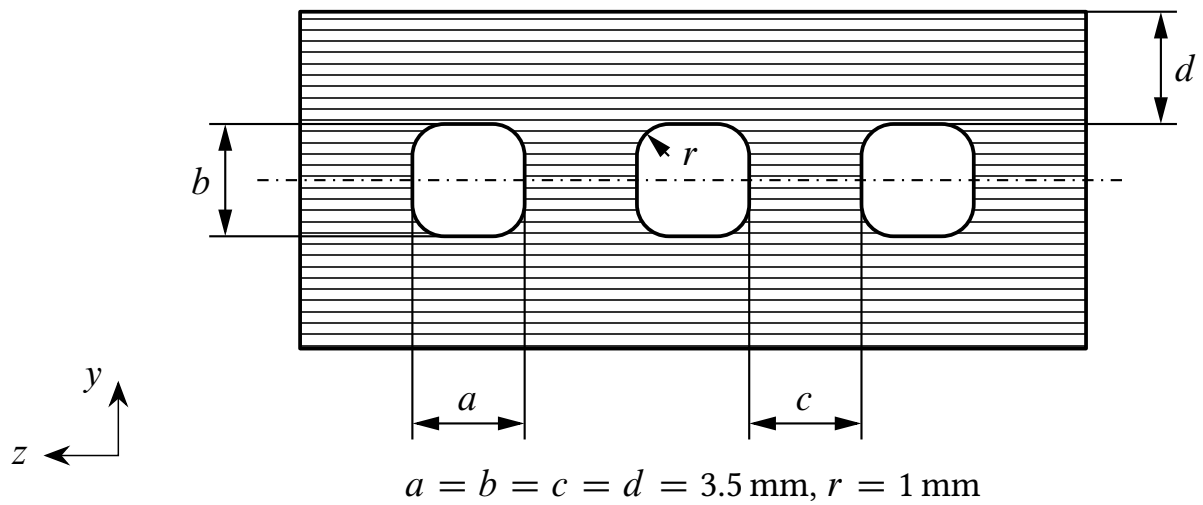


Figure 5.3: C/C-SiC sandwich structure with cooling channels.

The heating process within the cooling channels was modeled using the channel differential equations given in Sec. 2.2.9. A real gas model needs to be used for the cooling channel flow, since hydrogen does not behave like an ideal gas under cryogenic conditions. The caloric properties of cryogenic hydrogen strongly depend on the mixture if the two spin isomers of hydrogen, namely orthohydrogen and parahydrogen. This influence is considered for example in the state equation by Leachman et al.⁸⁴ For temperatures of room temperature and above, a constant mixture of 75% parahydrogen and 25% orthohydrogen can be assumed.¹⁹⁸ In this temperature region, the Soave-Redlich-Kwong equation of state,⁸⁶ Eq. (2.2), is sufficient, while costing far less calculation power than the model of Leachman et al.

Since the flow in the cooling channels remains in the incompressible flow domain, the Prandtl-Kámán model, see Sec. 2.2.6, is sufficient to model the friction and the heat transfer. Therefore, the similarity factor for friction c_f was modeled using Eq. (2.95), the transformation functions Eq. (2.77) and Eq. (2.78). The Reynolds Analogy ζ and the recovery factor r were determined by using Eq. (2.97) and Eq. (2.57).

5.3. CFD Simulation

Based on preceding investigations by Krause et al.,¹¹⁰ Reinartz et al.,¹⁹⁹ and Frauholz and Reinartz,²⁰⁰ a simulation of the flow field was performed using the *FLOWer*⁸⁰ program, a structured Reynolds averaged Navier-Stokes solver. Menter's two equation shear stress transport model (SST- $k\omega$)⁸¹ was chosen for the turbulence modeling. The grid consisted of approximately 320 000 cells. The transition point at the hull side was arbitrarily chosen. For the cowl side, a fully turbulent boundary layer was assumed. The boundary conditions are listed in Tab. 5.3.

Table 5.3: Boundary conditions for CFD simulations.

description	name	value
freestream temperature	T_0	226.5 K
freestream pressure	p_0	1181 Pa
freestream Mach number	Ma_0	8
isothermal wall temperature	T_w	600 ... 2000 K
ratio of specific heats	γ	1.4
turbulent Prandtl number	$Pr_{T,\infty}$	0.89
Reynolds number per unit length	Re_l	$3.8 \cdot 10^6$ 1/m
laminar to turbulent transition point	x_{trans}	0.2767 m
minimal cell height near wall	Δy_{min}	8.4 μm

5.3.1. Investigation of Unstarting Behavior

Unstarting can be caused by a boundary layer separation phenomenon at the beginning of the internal duct. This separation bubble is induced by the oblique compression shock at the lip hitting the boundary layer on the opposing wall. In the present simulations, it was observed that if the isothermal wall temperature is varied, position and size of the separation bubble remain stable until a critical wall temperature is reached. When the critical wall temperature is exceeded, the separation bubble almost instantly moves upstream and increases in size, thus causing the inlet to unstart. Fischer and Olivier have investigated this phenomenon both experimentally and numerically.²⁰¹ Numerical Schlieren images for both the started and the unstarted flow state are plotted in Fig. 5.5. The adiabatic kinetic efficiency

$$\eta_{\text{kin,ad}} = \frac{h_{t0} - h(p_0, s_3)}{h_{t0} - h_0} \quad (5.3)$$

is a performance parameter which is relatively independent from the wall temperature if the inlet does not switch between started and unstated mode. This behavior makes $\eta_{\text{kin, ad}}$ an appropriate parameter for the numerical detection of inlet unstating. It can be read from the plot in Fig. 5.4 that according to the present model and boundary conditions, the critical wall temperature must be somewhere between 1110 K and 1120 K.

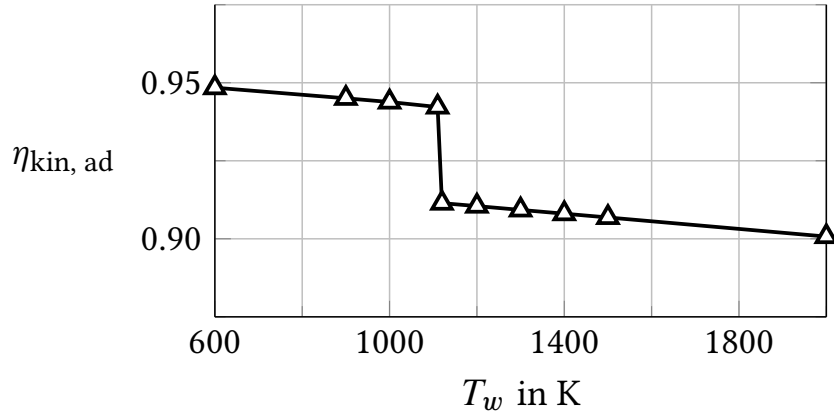


Figure 5.4: Kinetic adiabatic efficiency for various isothermal wall temperatures.

5.3.2. Similarity Parameters for Thermal Heat Loads

The Stanton number is a non-dimensional convective heat flux parameter, which is almost independent of the local surface temperature. In the present case, the Stanton numbers are related to the freestream conditions, so that the Stanton number

$$St_0 = \frac{\dot{q}_w}{\rho_0 u_0 (h_r - h_w)} \quad (5.4)$$

only depends on the location along the wetted surface. Similarly, the pressure coefficient

$$C_p = \frac{p_w - p_0}{q_0} = \frac{p_w - p_0}{\frac{\rho_0}{2} u_0^2} \quad (5.5)$$

is a non-dimensional wall pressure parameter which can be used to describe the mechanical loads on the surface. Both parameters versus x are given in Fig. 5.6. Bear in mind that in boundary layer theory $p_w = p_\delta$ is assumed.

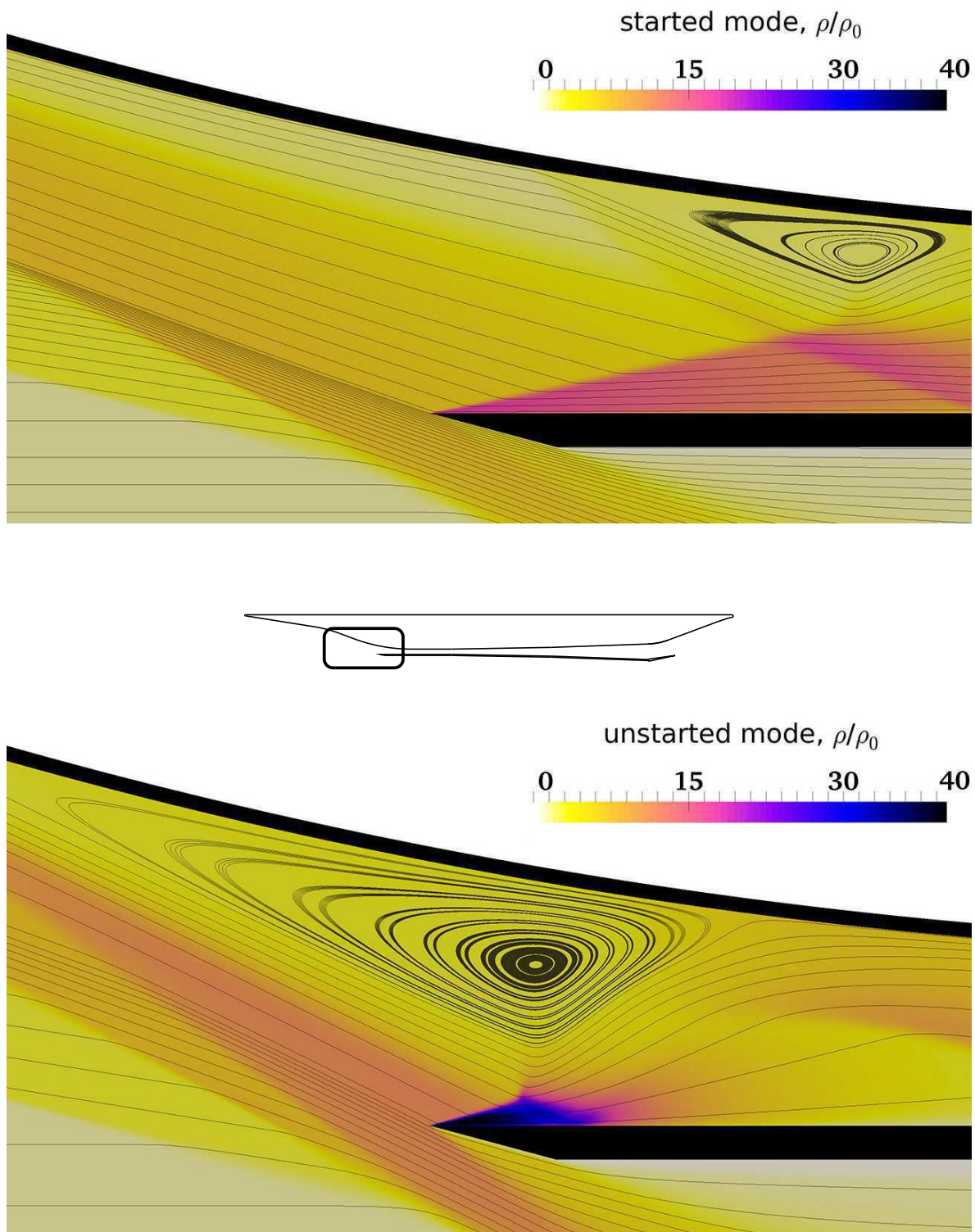


Figure 5.5: Separation bubble in started operation mode (top) and unstarted operation mode (bottom).

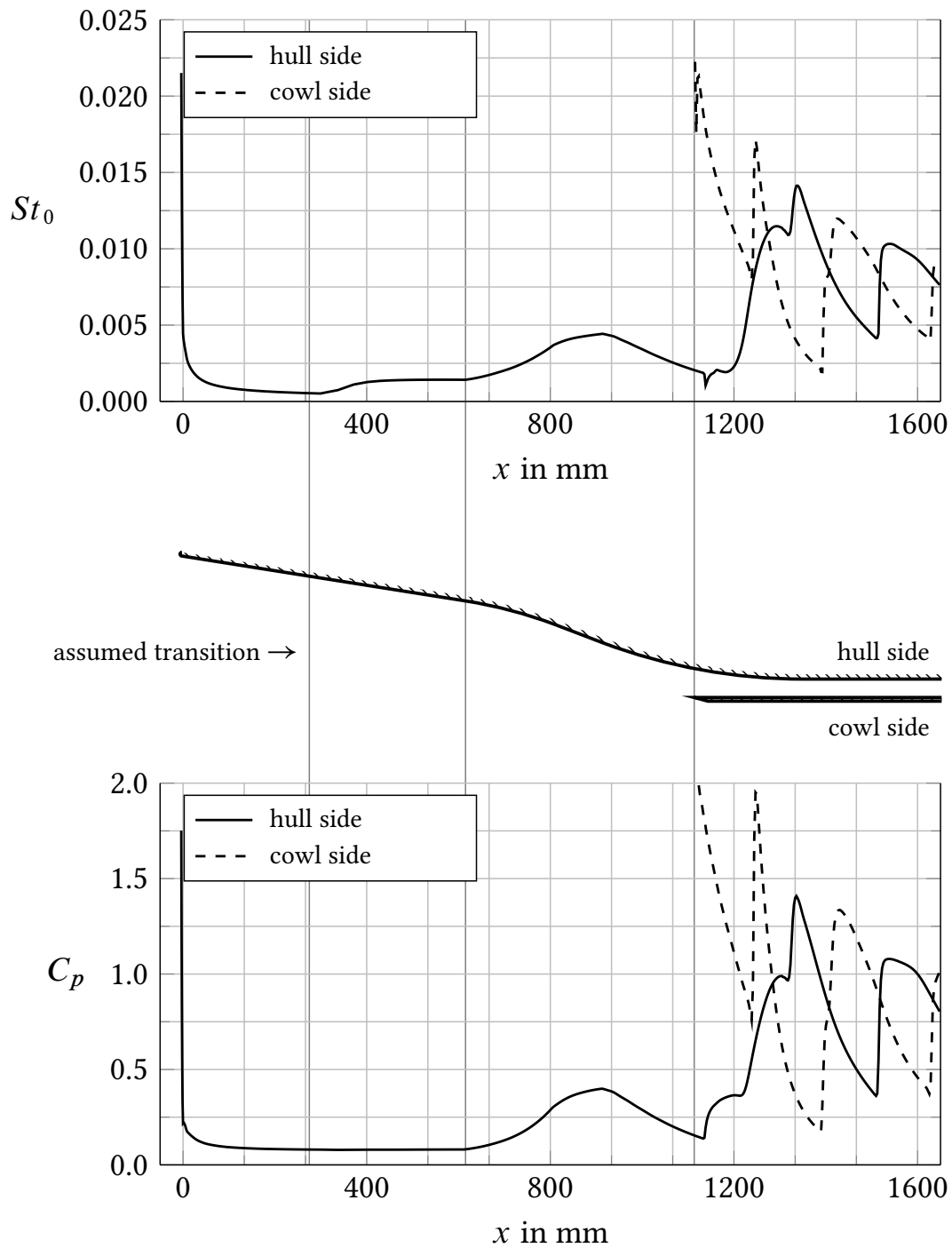


Figure 5.6: Stanton number (top) and pressure coefficient (bottom) versus x , along the wetted inlet surface, CFD calculation.

5.3.3. Verification of the Perfect Gas Approach

The CFD simulation was performed with a calorically perfect gas model. This approach is said to be valid for non-hypersonic velocities below $Ma = 5$.²⁰² This limit is exhausted at the blunted edge. In this paragraph, the calculated similarity parameters C_p and St_0 are compared to semi-empirical methods from literature to ensure the validity of the ideal gas approach. For an uninclined blunted flat plate there is a correlation^d by Lukasiewicz,²⁰³ Baradell and Bertram,²⁰⁴

$$\frac{p_\delta}{p_0} = 0.117 Ma_0^2 \left(\frac{6 r_0 C_d}{7 r_0 + 3 x} \right)^{\frac{2}{3}} + 0.732 \quad \forall x \geq 0, \quad (5.6)$$

from which a correlation for the pressure coefficient along the round nose can be developed. Following Oliver's²⁰⁵ assumption that the maximal pressure coefficient at the tip of the nose can be determined from the stagnation pressure p_{st} , which arises from the perpendicular shock relations, so that

$$C_{p,max} = \frac{p_{st} - p_0}{q_0}, \quad (5.7)$$

an interpolating polynomial

$$C_p \approx a \left(\frac{x}{r_0} \right)^2 + b \left(\frac{x}{r_0} \right) + c \quad \forall x \in [-r_0 \dots 0], \quad (5.8)$$

can be developed, where coefficients read

$$a = C_{p,max} - c + b \quad (5.9)$$

$$b = \left(-0.03016 C_d^{\frac{2}{3}} Ma_0^2 \right) \frac{p_0}{q_0} \quad (5.10)$$

$$c = \left(0.117 C_d^{\frac{2}{3}} Ma_0^2 - 0.268 \right) \frac{p_0}{q_0}. \quad (5.11)$$

Using the analytic solution by Lees²⁰⁶

$$St_0 = \frac{\sqrt{\rho_{st} \mu_{st}}}{2 \rho_0 u_0 Pr^{\frac{2}{3}}} F(s) \quad (5.12)$$

$$F(s) = \frac{\frac{p_\delta}{p_{st}} \frac{\mu_\delta}{\mu_{st}} \frac{T_{st}}{T_\delta} u_\delta}{\sqrt{\int_s \frac{p_\delta}{p_{st}} \frac{\mu_\delta}{\mu_{st}} \frac{T_{st}}{T_\delta} u_\delta ds}}, \quad (5.13)$$

^dthe correlation was modified to be consistent with the coordinate system in Fig. D.4

the distribution of the Stanton numbers can be determined once C_p is known. The pressure coefficient and the Stanton number are plotted in Fig. 5.7 and Fig. 5.8, where the tangential coordinate

$$s = -r_0 \tan^{-1} \frac{y}{x} \quad (5.14)$$

is illustrated in Fig. D.4. A comparison between Eq. (5.8) for $C_d = 1.4$ and the CFD simulation reveals that the pressure coefficient is slightly overpredicted as being near the stagnation point. This can be explained due to the calorically perfect gas model.

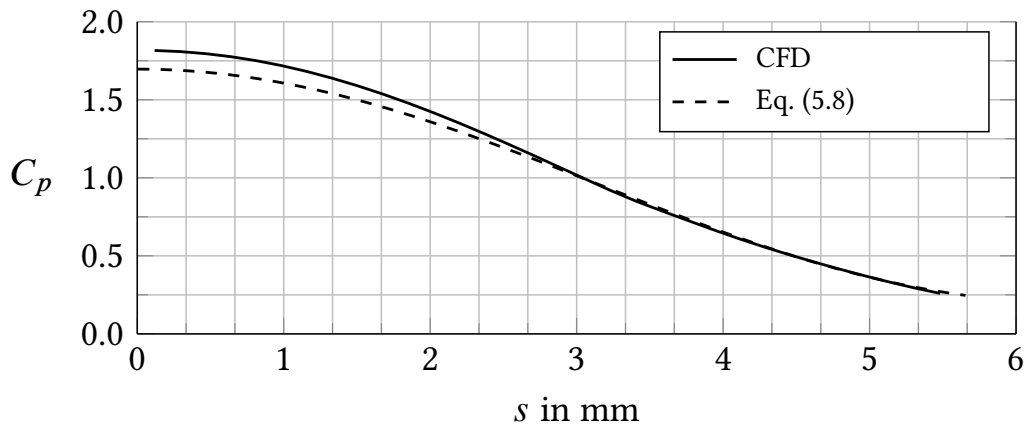


Figure 5.7: Pressure coefficient distribution along the blunted nose.

To find a solution for the temperature T_δ and velocity u_δ at a given coordinate s , the boundary layer was assumed to be adiabatic and isentropic. Apart from the singularity of Eq. (5.12) near the stagnation point, the analytical model and the CFD simulation converge very well. The CFD model might be closer to reality because it might capture secondary effects in the boundary layer which damp the singularity away.

At the point $x = -r_0 \sin \alpha$ (see Fig. D.4), where the blunted edge migrates into the flat ramp, Eq. (5.8) delivers a pressure coefficient of $C_p \approx 0.23$. A comparison of the CFD data (Fig. 5.9) shows that the upstream distribution of the pressure coefficient approaches the value $C_p \approx 0.08$, which is predicted by the oblique shock relation. This overpressurization at the blunt nose is a known effect, which is sometimes referred to as *hypersonic viscous interaction*.²⁰⁷ It is known to influence the upstream development of the boundary layer in terms of skin friction, heat transfer, and transition,¹⁸⁵ so that further comparisons of the CFD simulation with analytical models are not feasible. Both the calculated wall pressure distribution along the blunt edge and the one at the beginning of the first ramp agree very well with the semi-empirical models so that the perfect gas approach in general is appropriate.

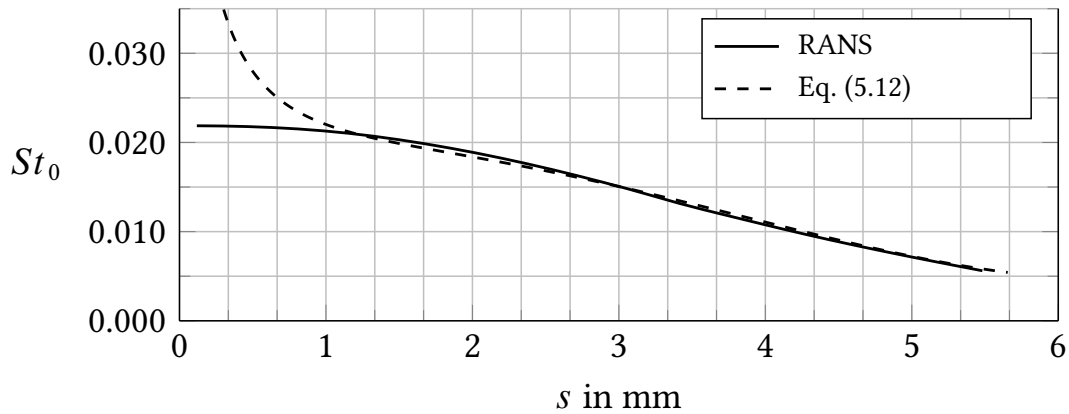


Figure 5.8: Stanton number distribution along the blunted nose.

One restriction that needs to be mentioned is, that the ratio of specific heats has to be set to $\gamma = 1.4$ in order to obtain a realistic external shock system which allows the inlet to start. Due to the higher temperature in the inner region of the duct however, a value of $\gamma \approx 1.3$ would be more appropriate there. This deviation has to be accepted since γ needs to be kept constant if a calorically perfect gas model is chosen.

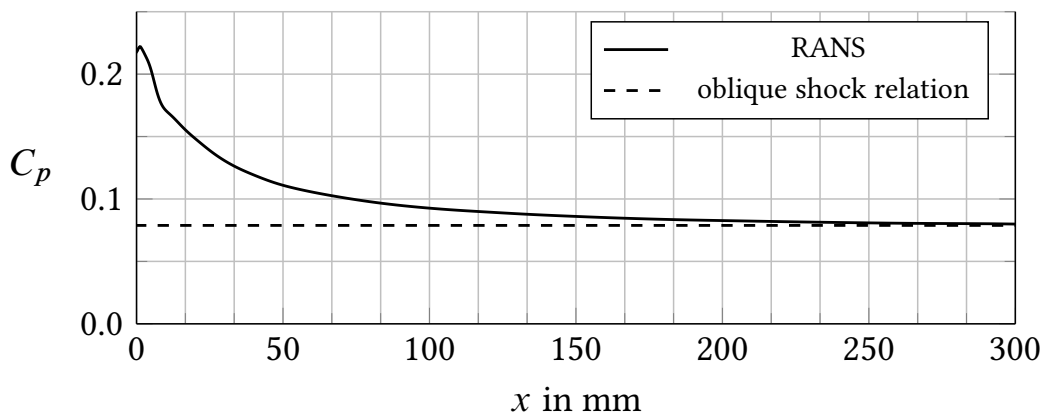


Figure 5.9: Overpressurization near the blunted leading edge.

5.3.4. Investigation of the External Flow Field around the Cowl

The external flow field along the cowl was assumed to be fully turbulent. Due to the simplicity of the flow, it can be easily modeled by two Prandtl-Meyer expansions, as illustrated in Fig. 5.10, the friction coefficient can be estimated using the method of van Driest and Eq. (2.90). The theoretical flow states were calculated using Eq. (2.168), and are listed in Tab. 5.4.

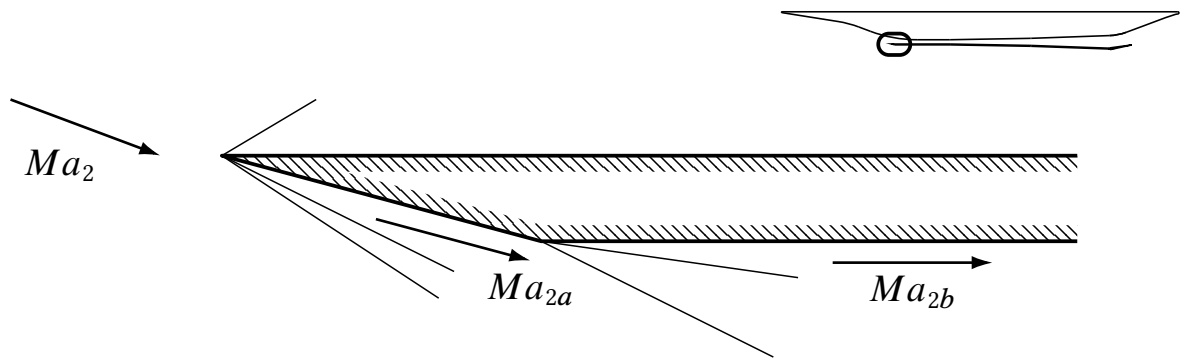


Figure 5.10: Simplified flow field around the external cowl.

Table 5.4: Mean flow states for Fig. 5.10.

		state		
		2	2a	2b
T	K	625.6	523.3	280.0
p	Pa	22893	12854	1595
Ma		4.51	5.01	7.13

A comparison between the theoretical Stanton numbers and the RANS solution for the external wall as shown in Fig. 5.11, reveals that relative to the theoretical solution, the Stanton numbers along the flat plate are underpredicted, but still within acceptable range. The discrepancy along the ramp might be caused by a limitation of the turbulence model not being able to capture the Prandtl-Meyer expansion correctly. This limitation of the turbulence model has been discussed in detail by Nguyen et al.²⁰⁸

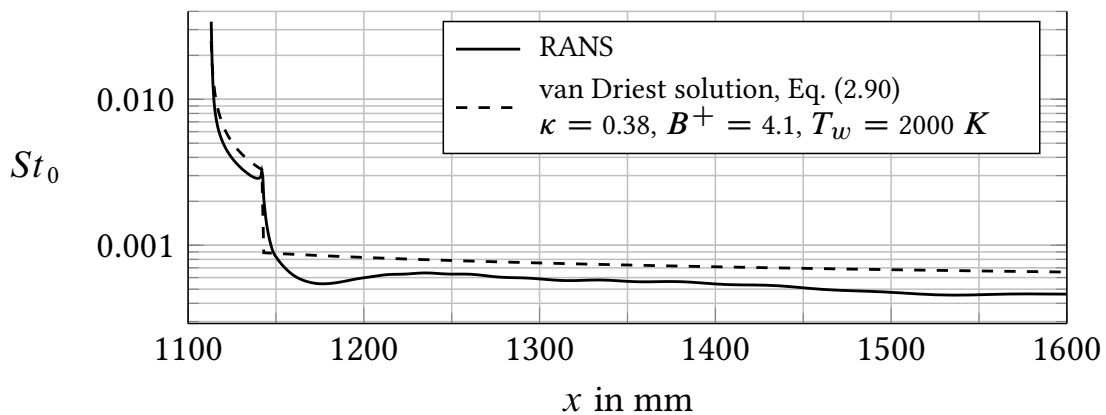


Figure 5.11: Stanton numbers along the external cowl.

5.4. Finite Element Simulation

The heat conduction in the structure was simulated using the finite element method. An implicit Euler scheme was chosen for the time-stepping method. A structured mesh was used which contains both triangular and quadrilateral elements. The spatial discretization was performed with quadratic interpolation functions, see App. A. The mesh consists of approximately ten thousand elements and forty thousand nodes. Two extractions of the mesh are displayed in Fig. 5.12.

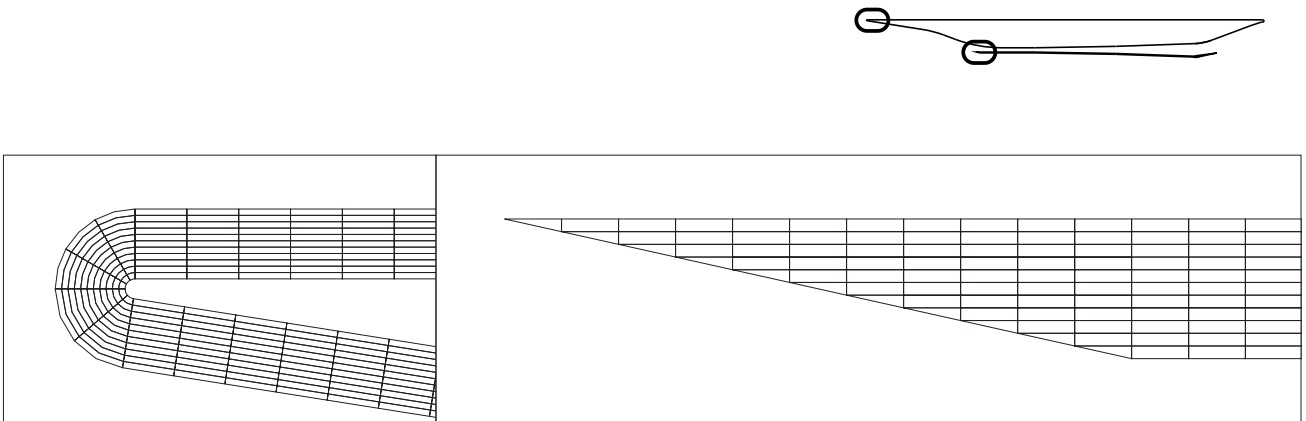


Figure 5.12: Finite element mesh for the inlet simulation.

5.4.1. Simulation of Uncooled Configuration

In the first simulation, the equilibrium temperatures for an uncooled structure were calculated. The Stanton numbers from the CFD calculation were converted to convective heat loads and impinged on the surface. Additionally, radiative heat loads were simulated. The view factors between the radiative surfaces were calculated using Hottel's method of crossed strings.¹⁶⁸ The fluid properties needed to convert the similarity parameters C_p and St_0 to head loads were taken from the Gordon-McBride property database.^{98,99}

5.4.2. Simulation of Regeneratively Cooled Configuration

In the second configuration active cooling was assumed. If the combustor entry conditions are known, see Tab. 5.3, the total mass flow \dot{m}_{cg} in the channels can be estimated using the relation

$$\dot{m}_{cg} = \phi \mu_{st} \dot{m}_3, \quad (5.15)$$

where \dot{m}_3 is the mass flow at the combustor entry, $\mu_{st} \approx 0.0292$ the fuel air mass ratio for stoichiometric combustion, and ϕ the stoichiometric ratio. The cooling channels range from the beginning of the curvature at the kink to the inlet exit, see Fig. 5.13.

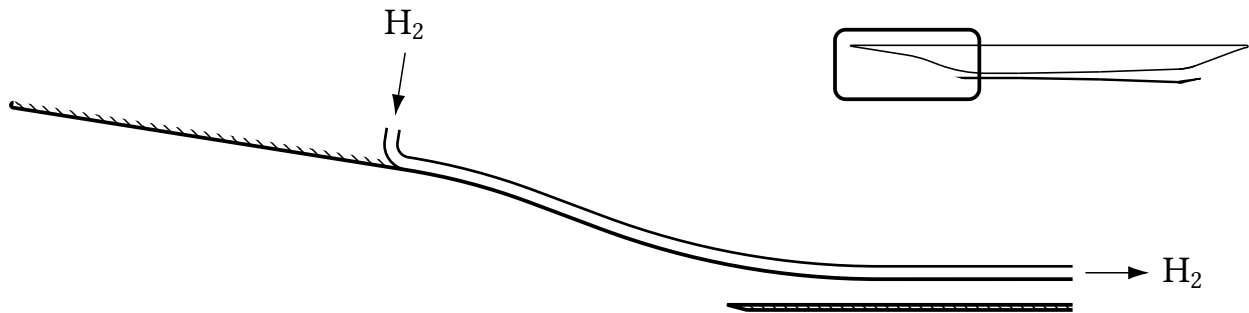


Figure 5.13: Cooling channels on inlet geometry.

5.5. Discussion of Results

The simulations of both the cooled and the uncooled testcase were started with an isothermal wall temperature of 300 K. The chosen timestep was $\Delta t = 0.1$ s. A thermal emissivity of $\epsilon = 0.6$ was assumed for the coated surface.²⁰⁹ The surface temperatures of both the uncooled and the cooled case stagnate after approximately ninety seconds. The equilibrium surface temperatures in Fig. 5.16 are taken after five minutes of simulation time, when a total equilibrium has been achieved. For the uncooled case, the surface temperature in the region of the separation bubble exceeded the critical wall temperature after approximately twenty seconds. At this time, unstarting has to be expected. With the maximum surface temperature exceeding 2200 K in the duct, thermal failure of the structure has to be expected in the uncooled case. The wetted surface of the cooling channels was assumed to be hydraulically smooth. The progression of the surface temperature on the hot gas side, the cold gas side and the coolant temperature for $\phi = 0.6$ and $\phi = 1.0$ are shown in Fig. 5.14.

A section of the relevant area near the separation bubble is displayed in Fig. 5.15. The flow is visualized via streamlines and lines of equal density. The isolines in the wall represent steps of one hundred Kelvin. The surface temperatures on the hull side are kept below the critical temperature of ca. 1100 K, so that wall temperature related unstarting is prevented. Through radiative effects, the cowl side is also cooler than in the uncooled calculation, so that thermal failure of the structure is unlikely. All in all, the suggested cooling concept seems to be very promising.

Table 5.5: Boundary conditions for the inlet calculations.

		Testcase		
		A	B	C
environment Temperature	T_0 K	226.5	226.5	226.5
environment pressure	p_0 Pa	1181	1181	1181
crusing Mach number		8	8	8
stoichiometric ratio	ϕ	0.6	1.0	-
coolant entry temperature	$T_{cg,0}$ K	50	50	-
coolant entry pressure	$p_{cg,0}$ bar	11	20	-
coolant entry velocity	$u_{cg,0}$ m/s	15.7	13.4	-

5.6. Modeling Limitations

A perfect gas approach was adopted in the CFD simulation. A comparison with semi-empirical methods from literature reveals that the CFD model slightly overestimates the pressure coefficient C_p , while it might underestimate the Stanton numbers St_0 in a small area around the stagnation point at the tip of the blunted nose. Unfortunately, experimental data are very rare for the desired boundary conditions. Although the selected turbulence model SST- $k\omega$ was assumed to be suitable in the mentioned literature, actual flight tests are needed to support the validation. In the present calculation, the location of laminar to turbulent transition was chosen arbitrarily but pessimistic. It is a widely known problem that exact location of transition cannot be predicted easily. The sensitivity of the critical wall temperature against the turbulence model and the transition point, as well as off-design behavior, should be part of future investigations. Given the assumption that a hydraulically smooth surface can be realized in the cooling channels, the chosen heat transfer and pressure loss coefficients can be considered trustworthy within a few percent. Another uncertainty is given in the unknown mixture ratio of ortho- to parahydrogen, although the selected ratio of three to one might be a rather pessimistic assumption.

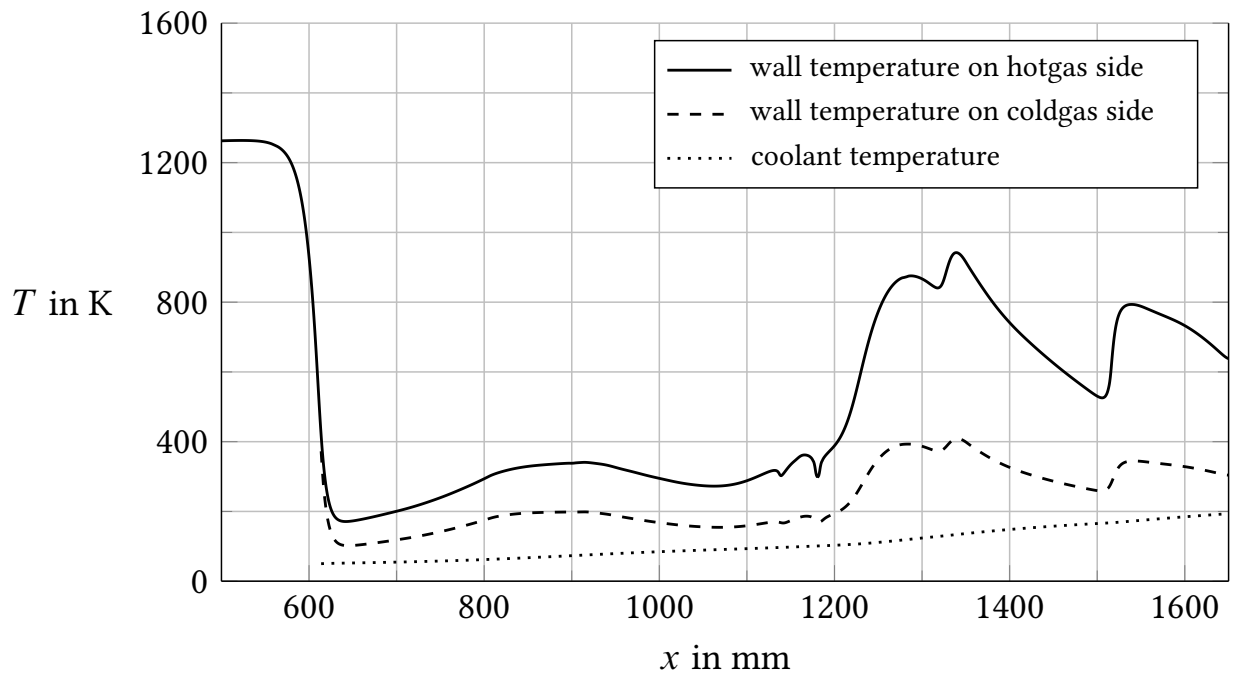


Figure 5.14: Equilibrium surface temperatures of inlet hull side versus x for cooled configuration with a stoichiometric ratio of $\phi = 1$.

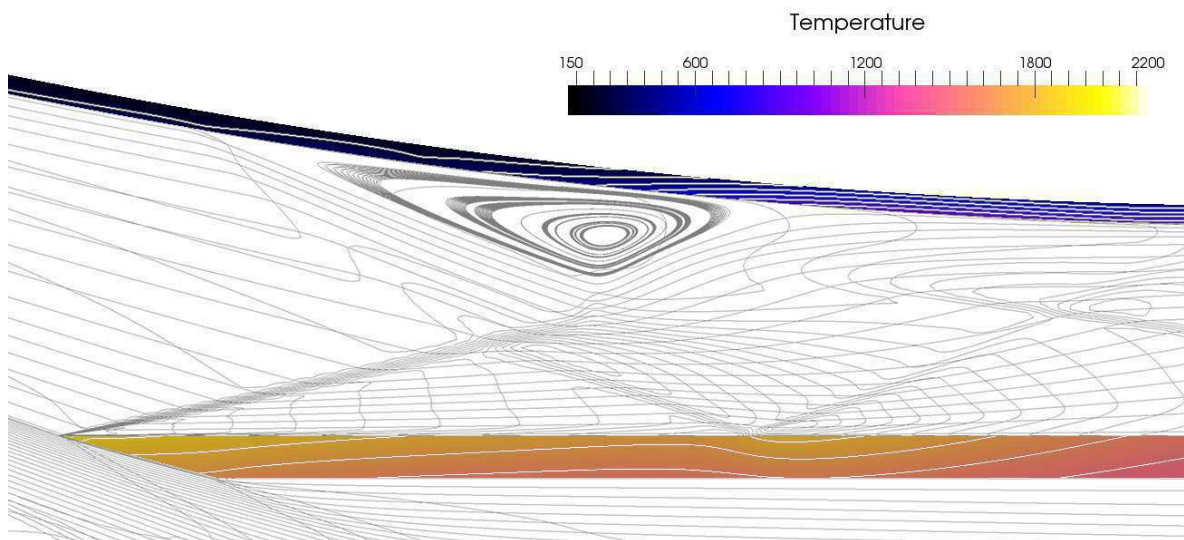


Figure 5.15: Thermal interaction between flow field and structure, with $\phi = 1$.

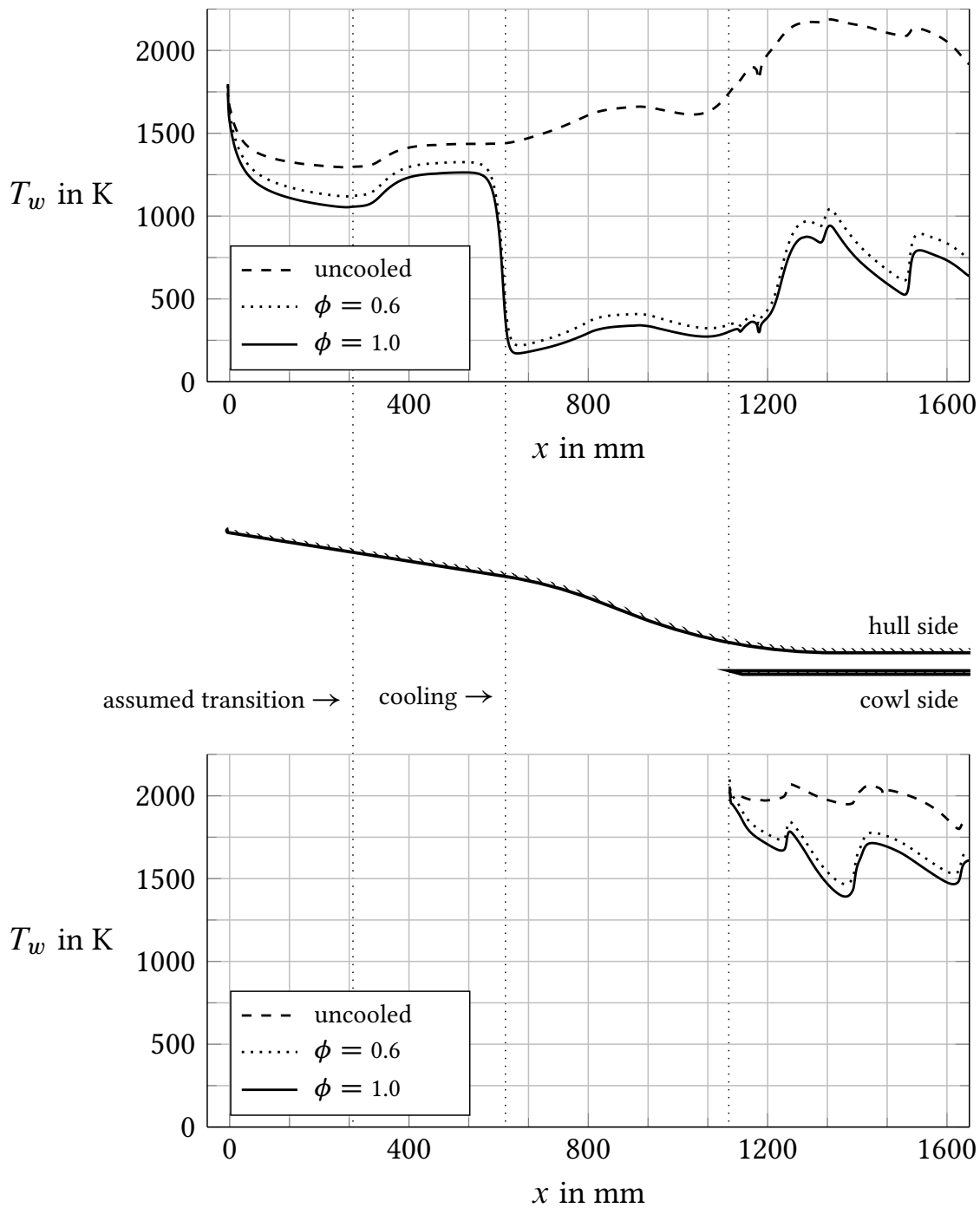


Figure 5.16: Equilibrium surface temperatures of inlet, uncooled and cooled configuration versus x for hull side (top) and cowl side (bottom) .

6. Combustor Heat Load Investigation

In addition to the simulation of the flow field, radiation and active cooling, the chemical process of the combustion has to be modeled. To reduce modeling complexity, the internal system of compression shocks was neglected, and a one-dimensional approach was chosen.

6.1. Geometry Definition

The original GRK 1095 design contains a three-dimensional geometry with the combustor being 65 mm wide. Like in the previous inlet investigation, a two-dimensional geometry with an infinite width is assumed at this point. The used geometry for the duct and the central injector are defined as follows.

6.1.1. Combustor Geometry Definition and Fuel Injection

The geometry of the combustion chamber as illustrated in Fig. 6.1 was derived from a configuration investigated by Rabadán Santana.²¹⁰ The entrance height was chosen to fit the throat height of the inlet; the opening angle is 1° .

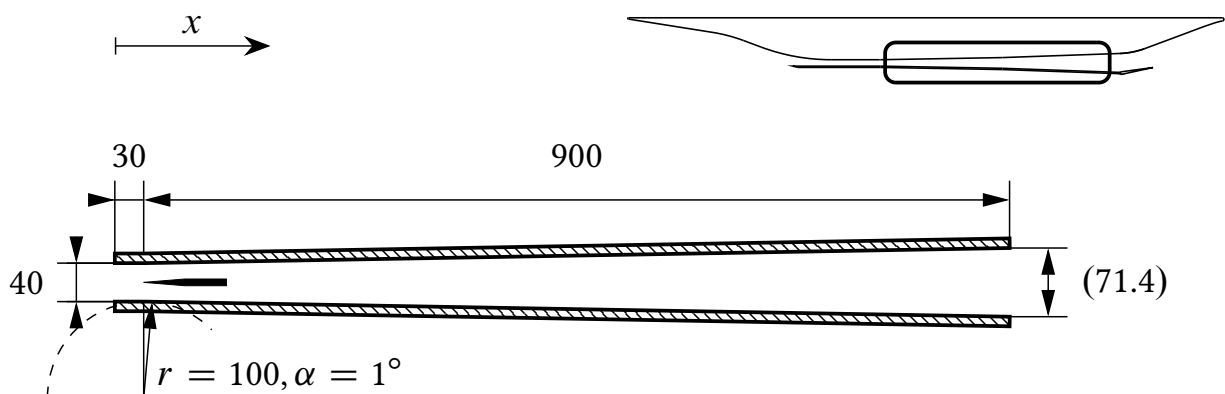


Figure 6.1: General dimensions of the combustion chamber, dimensions in mm.

Continuing the channel geometry of the inlet (Fig. 5.13), the fuel is lead along the inner wall at the hull side of the engine. As with the inlet, the cowl side is uncooled. After being lead along the nozzle, the fuel is injected into the flow over a central injector.

6.2. Central Injector

The central strut injector has been developed during the German SFB 259 Program.²¹¹ The basic dimensions for the central strut injector shown in Fig. 6.2 and 6.3 are derived from Rust et. al.²¹² and Rabadán Santana.²¹⁰ Following the GRK 1095 design, the strut injector is assumed to be placed horizontally in the combustion chamber (see Fig. 6.1). Due to mechanic vibrations however, Fuhrmann²¹³ argues that in case of a broad vehicle similar to the X-43A design, a cluster of vertically placed injectors might be more feasible.

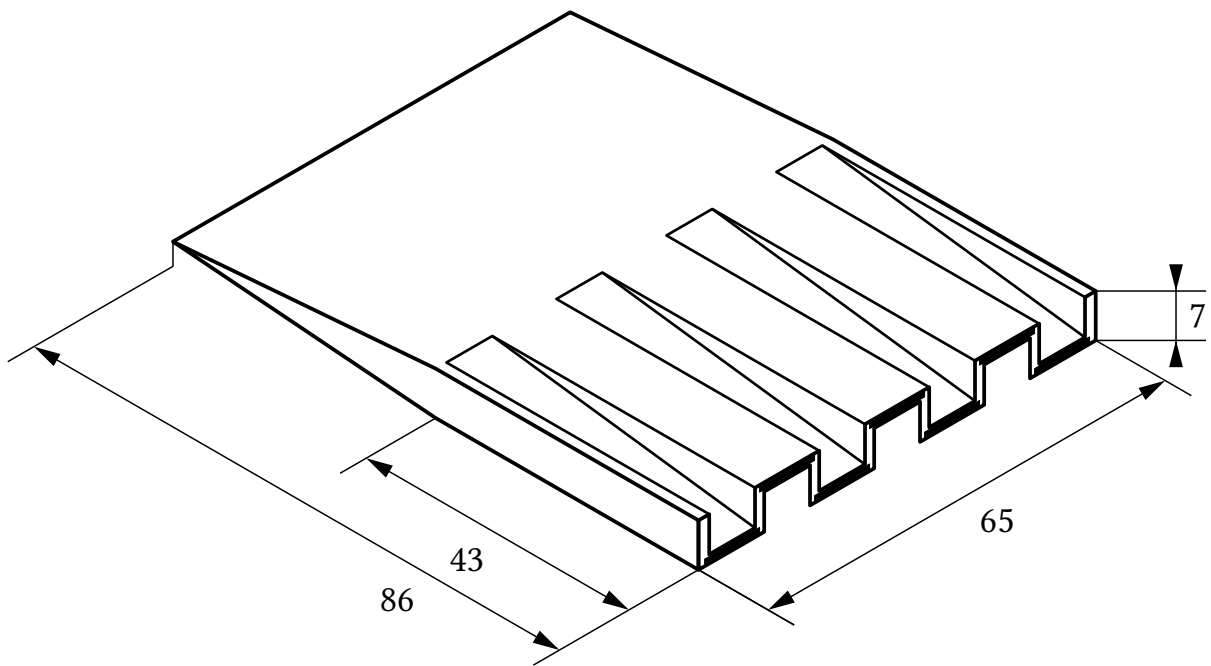


Figure 6.2: Isometric view of the injector geometry, dimensions in mm.

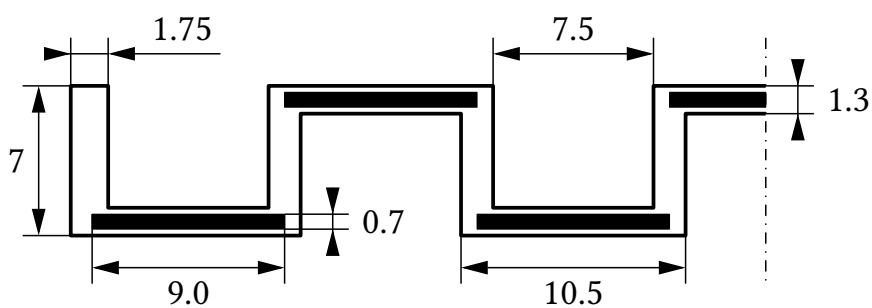


Figure 6.3: Back side of the fuel injector, dimensions in mm.

Knowledge of the surface temperature of the central injector is important not only because the injector itself needs to be kept under the temperature of material failure, but also because it will be a source of thermal radiation that heats up the surrounding sidewalls. In order to predict the surface temperature of the injector, the flow field around it can be simplified to a compression shock and a Prandtl-Meyer expansion fan, see Fig. 6.4. The flow conditions after the oblique compression shock, are found over Eqs. (2.160) to (2.163), and the conditions after the Prandtl-Meyer expansion are found over Eq. (2.171), (2.172), (2.22), and (2.19). Referring to those conditions, and assuming a fully turbulent boundary layer along the surface of the central injector, the local convective heat loads \dot{q}_w can be estimated using the method of van Driest and the friction equation Eq. (2.90). Once \dot{q}_w is known along the injector surface, the average surface temperature $T_{w,\text{cinj}}$ of the injector can be estimated

$$T_{w,\text{cinj}} \approx T_{\text{cg}} + \frac{\int_{\partial\Omega} \dot{q}_w \, d\partial\Omega}{c_{p,\text{cg}} \dot{m}_{\text{cg}}}, \quad (6.1)$$

where T_{cg} and \dot{m}_{cg} are the temperature and mass flow of the injected fuel, which acts as a coolant, and $c_{p,\text{cg}}$ the fuel's specific heat capacity.

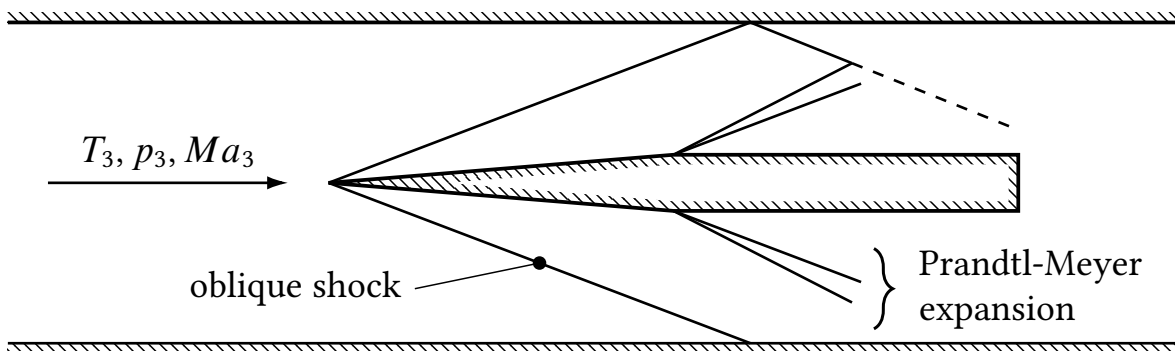


Figure 6.4: Simplified inviscid shock system around central injector.

A numerical simulation for flight conditions with Hydrogen as cooling fluid was performed by Rust et. al.²¹² A second investigation containing both experiments and numerical simulations was performed by Dröske et al.²¹⁴ The boundary conditions extracted from these works and approximate average wall temperatures from these investigations are listed in Tab. 6.1. The combination of the van Driest method with the shock system in Fig. 6.4 agrees very well with Dröske's simulation. The results of Rust's calculation on the other hand are slightly lower than those calculated using van Driest's method. This might be attributed to the fact that thermal radiation was neglected in this simplified calculation, while it was considered by Rust. The third calculation presented in Tab. 6.1 is an example calculation for the boundary conditions found in the inlet calculation.

The fuel will exit the cooling channels in the combustor with a temperature of approximately $T_{cg} = 710$ K for $\phi = 0.6$, and $T_{cg} = 500$ K for $\phi = 1$. However, since the nozzle will need to be cooled as well, an injector entry temperature of $T_{cg} = 1200$ K seems to be a reasonable first assumption. The relation between the estimated mean injector temperature and the fuel temperature for various stoichiometric ratios is drawn in Fig. 6.5.

Table 6.1: Calculating the injector temperature using the method of van Driest.

		Dröske et al. ²¹⁴ (exp. /CFD)	Rust et al. ²¹² (CFD)	example (van Driest)
combustor width	mm	40.0	36.8	1000
combustor height	d_3 mm	35.4	40.0	40.0
hotgas temperature	T_3 K	178	1070	1100
hotgas pressure	p_3 Pa	64000	80450	43000
hotgas Mach number	Ma_3	2.5	2.8	2.77
fuel temperature	T_{cg} K	293	290	1200
specific heat of fuel	$c_{p,cg}$ $\frac{J}{kgK}$	1004.5	14267	15808
stoichiometric ratio	ϕ	-	0.16	0.6
coolant mass flow	\dot{m}_{cg} g/s	18	3.11	17.16
average temp. in literature	T_{cinj} K	≈ 355	≈ 480	-
van Driest calculation	T_{cinj} K	354	521	1500

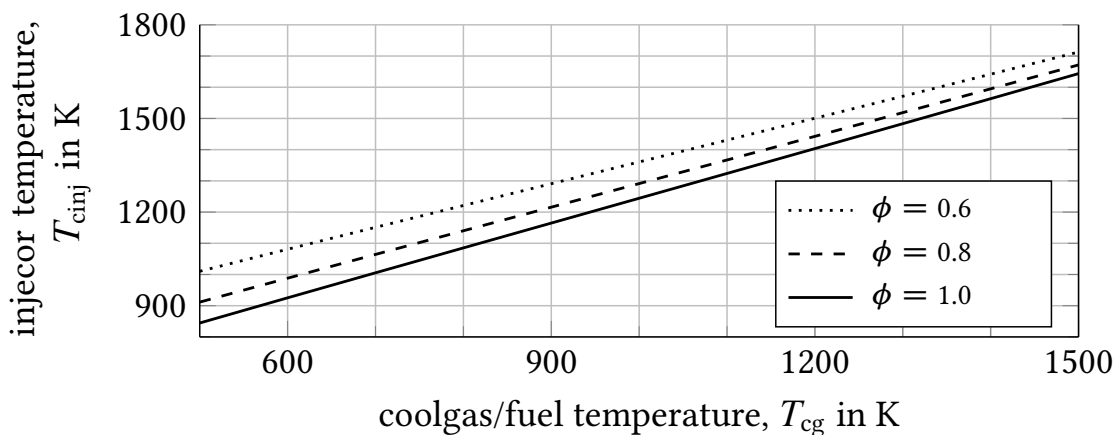


Figure 6.5: Estimated mean injector temperature over fuel temperature for $T_3 = 1100$ K, $p_3 = 43\,000$ Pa, and $Ma_3 = 2.77$.

6.3. Code Validation

In order to validate the one-dimensional friction and combustion models, their results were compared with three-dimensional CFD calculations, which were published by Rabadán Santana.²¹⁰ The CFD calculations were performed with the commercial Riemann solver CFD++ by Metacomp Technologies. The first calculation did not involve fuel injection and combustion, and was performed in order to compare the pressure losses of the CFD solution with the modified van Driest model.

The boundary conditions refer to the three-dimensional inlet by Hohn,²¹⁵ and are listed in Tab. 6.2. The wall temperature was assumed to be isothermal and constant. The axial development of the static temperature, the Mach number and pressure are illustrated in Figs. 6.6 and 6.7. Given the fact that the one-dimensional channel flow model can neither resolve internal shock waves nor expansion fans along the combustion chamber, the agreement between the one-dimensional and three-dimensional model is very satisfying.

The inflow conditions for the reference calculation are given in Tab. 6.2. For the stoichiometric ratio, the values $\phi = 0$, $\phi = 0.65$ and $\phi = 0.85$ were chosen. The mixing efficiency ranges from $0.7 \leq \eta_{\text{mix}} \leq 0.8$, the Pulsonetti parameter C_{mix} (see Eq. (3.19)) was fitted to $C_{\text{mix}} = 15$. A comparison between Rabadán Santana's calculations and the calculations performed with the combustion code of the present work is shown in Figs. 6.8 and 6.9. Although both calculations agree very well, the fitted value of $C_{\text{mix}} = 15$ is unrealistically optimistic, since an expected value would range between $20 \leq C_{\text{mix}} \leq 60$.¹⁶⁴ A very probable explanation could be found in the shape of the three-dimensional DLR inlet, which passes a very anisotropic flow field to the combustion chamber. If the conditions are favorable, the anisotropy of the flow generates a significant increase of the fuel mixing process. Such a behavior is not to be expected when a two-dimensional inlet geometry is used. Therefore, a more moderate value of $C_{\text{mix}} = 25$, which was given by Fuhrmann,²¹³ was assumed for the finite element simulation.

Table 6.2: Combustor inflow conditions for the Hohn inlet.²¹⁵

T_3	K	820
p_3	Pa	42237
Ma_3		3.75
T_w	K	600

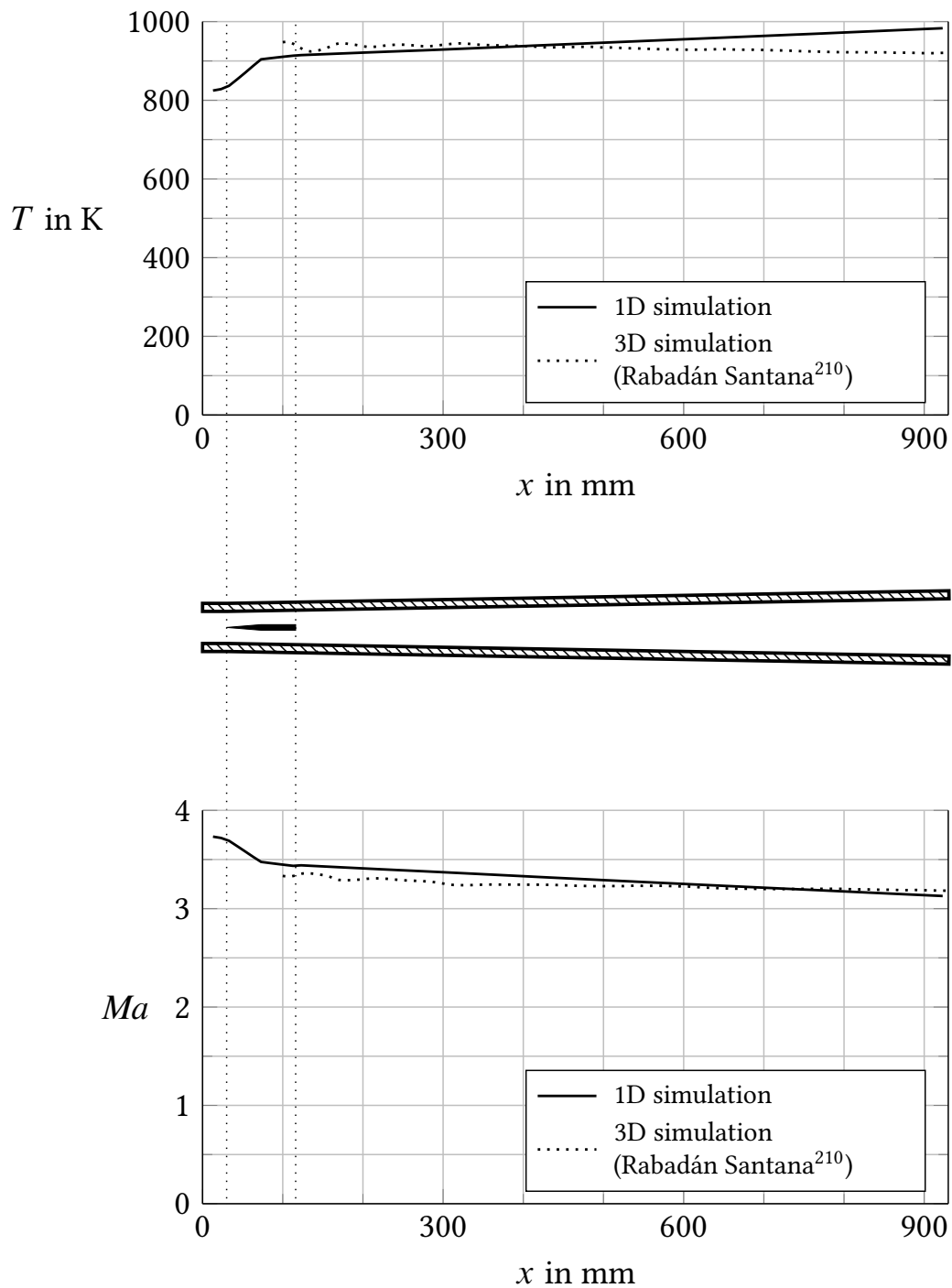


Figure 6.6: Development of static temperature (top) and Mach number (bottom) without fuel injection ($\phi = 0$), versus x . Rabadán Santana's values are mass averaged over the local cross section.

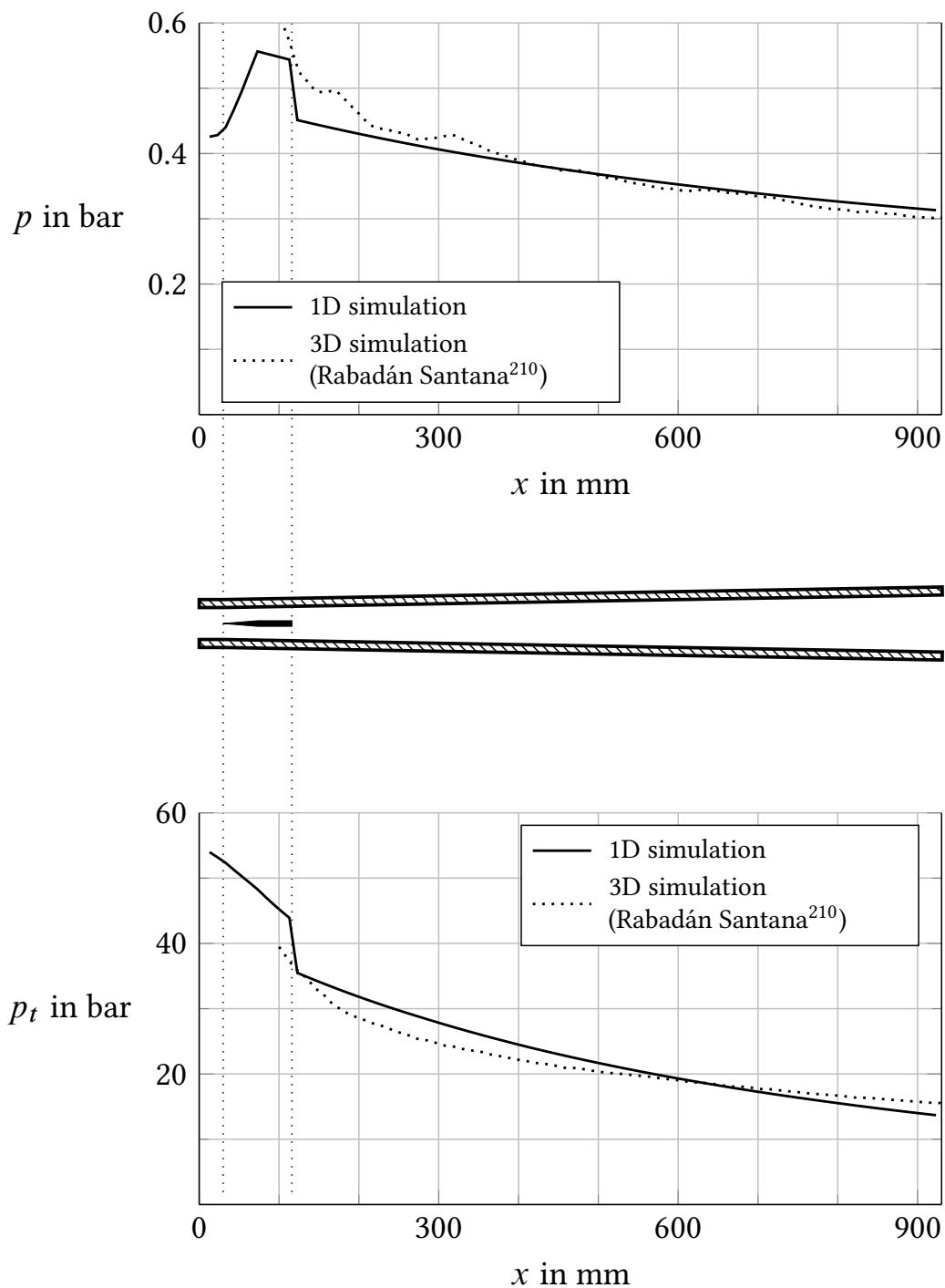


Figure 6.7: Development of static pressure (top) and total pressure (bottom), without fuel injection ($\phi = 0$), versus x . Rabadán Santana's values are mass averaged over the local cross section.

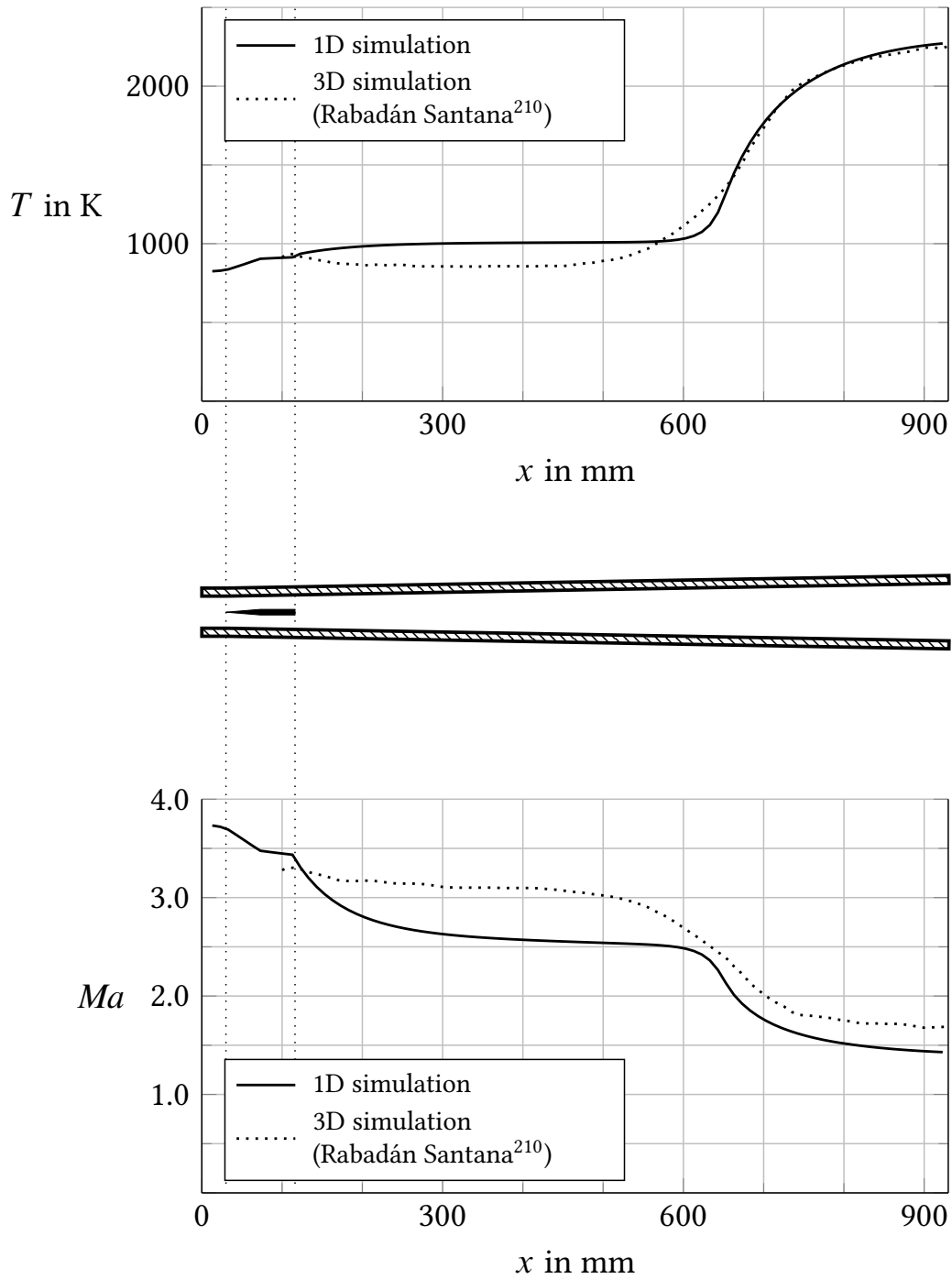


Figure 6.8: Development of static temperature (top) and Mach number (bottom) versus x , with $\phi = 0.65$, $C_{\text{mix}} = 15$, $\eta_{\text{mix}} = 0.8$.

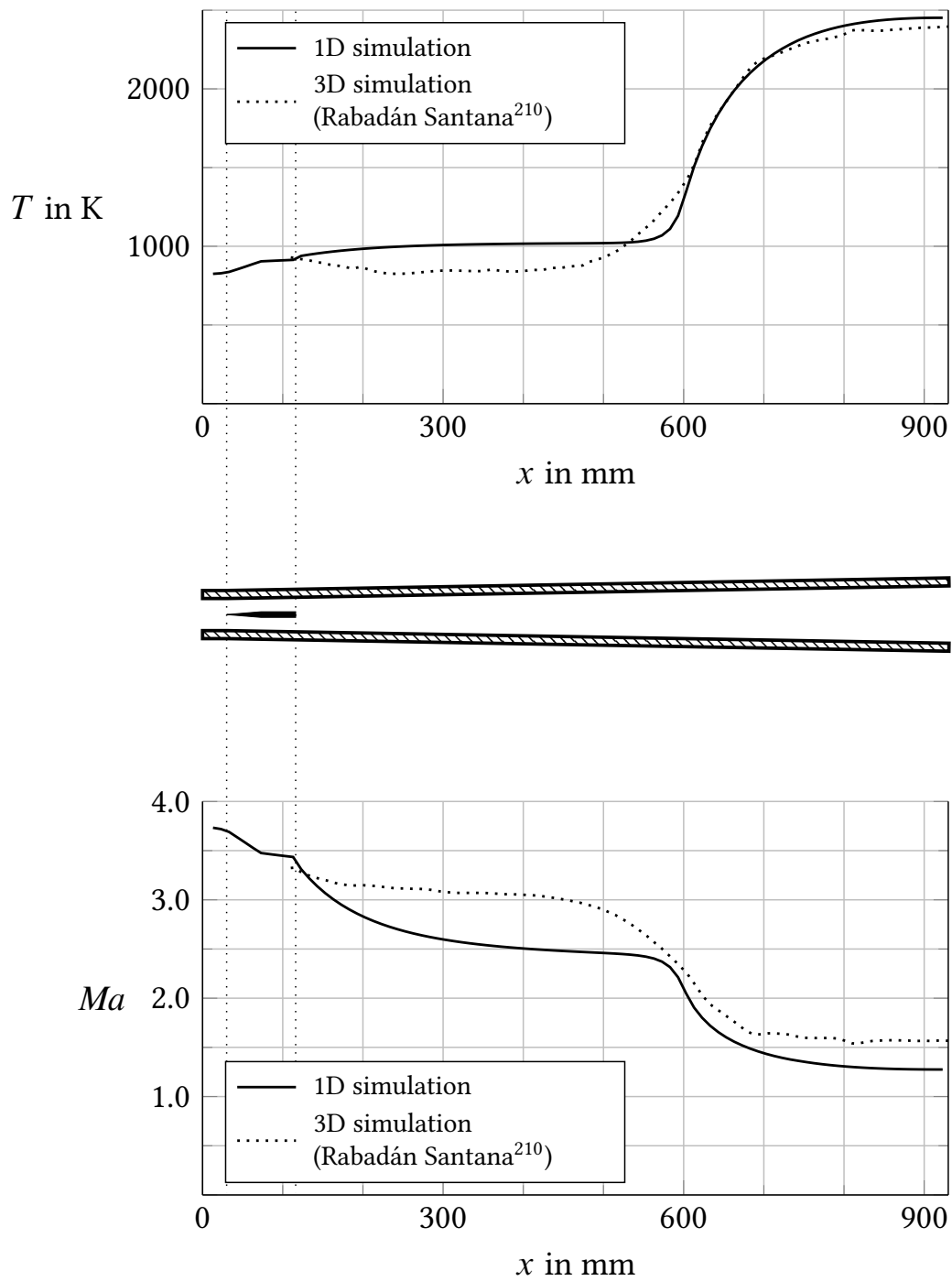


Figure 6.9: Development of static temperature (top) and Mach number (bottom) versus x , with $\phi = 0.85$, $C_{\text{mix}} = 15$, $\eta_{\text{mix}} = 0.7$.

6.4. Finite Element Simulation

Having validated the combustor model, it is now possible to calculate the equilibrium temperatures of the cooled structure. As in the inlet simulation, the cases A and B, with a stoichiometric ratio $\phi = 0.6$ and $\phi = 1.0$, respectively, were chosen as examples of interest, see Tab. 6.3. For comparison, case C represents an uncooled simulation with a stoichiometric ratio of $\phi = 1.0$. Since the combustion model was unable to achieve stoichiometric combustion with one single fuel injection, a two staged injection system as illustrated in Fig. 6.10 was chosen.

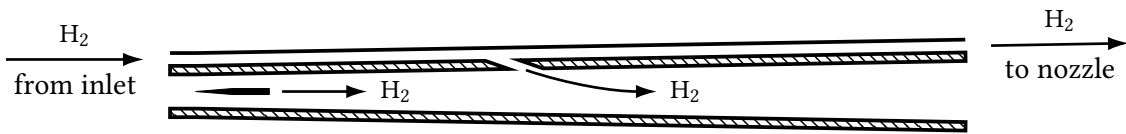


Figure 6.10: The two-staged fuel cooling and injection system of the combustor.

In analogy to Rabadán Santana's configuration, the central fuel injection is positioned at $x_{\text{cinj}} = 160$ mm. The wall injector was chosen to be at $x_{\text{winj}} = 416$ mm. Obviously, the fuel mass, which is injected by the wall injector has to be removed from that channel simulation downstream of the wall injection. Since wall injections are generally less efficient than central injectors, less performant values of $\eta_{\text{mix,winj}}$ and C_{winj} were assumed (see also Scheuermann²¹⁶). The chosen boundary conditions for the finite element simulations are listed in Tab. 6.3.

The sidewalls were assumed to have an initial temperature of 600 K,²¹⁰ the chosen timestep for the implicit Euler simulation was chosen to be $\Delta t = 0.1$ s. Like in the inlet simulation, biquadratic Lagrangian elements of the type QUAM9 (see App. A) were chosen, resolving the structure in Fig. 6.1 with 12 000 elements and 50 000 degrees of freedom. The simulations were stopped after $t = 400$ s, when no significant temperature changes of the temperature field could be observed anymore.

The cross section averaged static temperatures and Mach numbers are shown in Fig. 6.11, the averaged static pressures and velocities are shown in Fig. 6.12. For the cooled case, the wall temperature calculation predicts a surface temperature of roughly 1200 K on the hull side, and 2100 K on the cowl side, see Fig. 6.13. Since the maximum service temperature of 2200 K of the C/C-SiC structure is not exceeded, a thermally balanced flight could be possible! The heat loads are in the order of 1 MW m^{-2} , see Fig. 6.14. The Mach numbers at the exit of the cooling channels listed in Tab. 6.4. They are even in the incompressible regime, and the pressure loss is moderate, so that thermal choking is not to be expected.

The low cooling-channel exit temperatures of $T_{cg,4} = 710$ K for $\phi = 0.6$ and $T_{cg,4} = 500$ K for $\phi = 1$ at the end of the combustor suggest that the combustor temperature of $T_{cinj} = 1500$ K was overestimated, and should more probably be between 1000 K and 1200 K (see Fig. 6.5).

Table 6.3: Boundary conditions for the combustor calculations.

			Testcase		
			A	B	C
combustor entry temperature	T_3	K	1100	1100	1100
combustor entry pressure	p_3	bar	0.43	0.43	0.43
combustor entry Mach number	Ma_3		2.77	2.77	2.77
stoichiometric ratio	ϕ		0.6	1.0	1.0
surface temperature of central injector	T_{cinj}	K	1500	1500	1500
stoichiometric ratio at central injector	ϕ_{cinj}		0.6	0.6	0.6
mixing efficiency of central injector	$\eta_{mix,cinj}$		0.8	0.8	0.8
mixing parameter of central injector	C_{inj}		25	25	25
stoichiometric ratio at wall injector	ϕ_{winj}		-	0.4	0.4
mixing efficiency of wall injector	$\eta_{mix,winj}$		-	0.4	0.4
mixing parameter of wall injector	C_{winj}		-	50	50
coolant entry temperature	$T_{cg,3}$	K	282	194	-
coolant entry pressure	$p_{cg,3}$	bar	10.9	19.9	-

Table 6.4: Combustor cooling channel exit conditions.

			Testcase number	
			A	B
coolant exit temperature	$T_{cg,4}$	K	606.5	517.6
coolant exit pressure	$p_{cg,4}$	bar	10.5	19.7
coolant exit velocity	$u_{cg,4}$	bar	253.7	115.5
coolant exit Mach number	$Ma_{cg,4}$		0.135	0.07

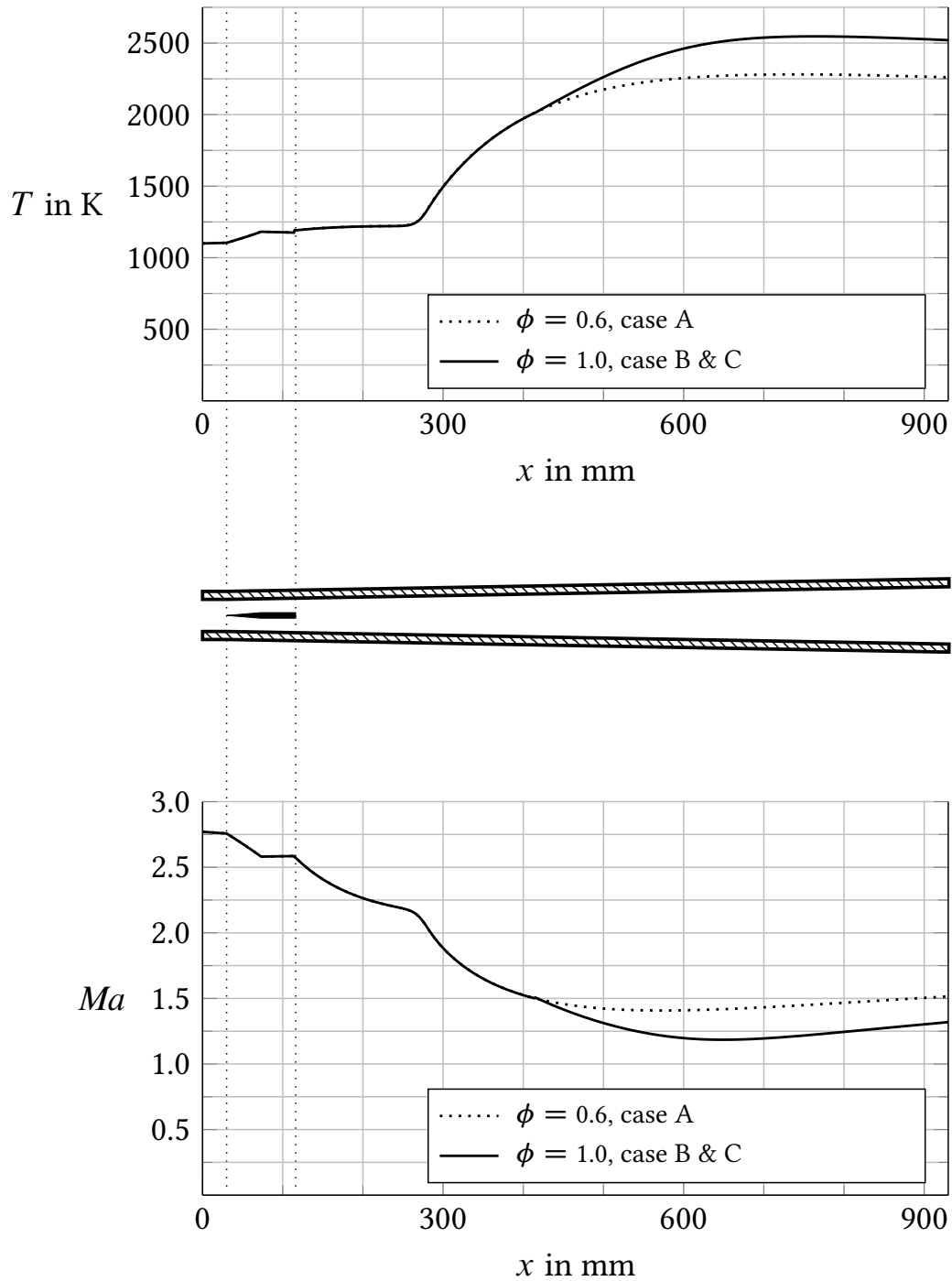


Figure 6.11: Combustor static temperature and Mach number

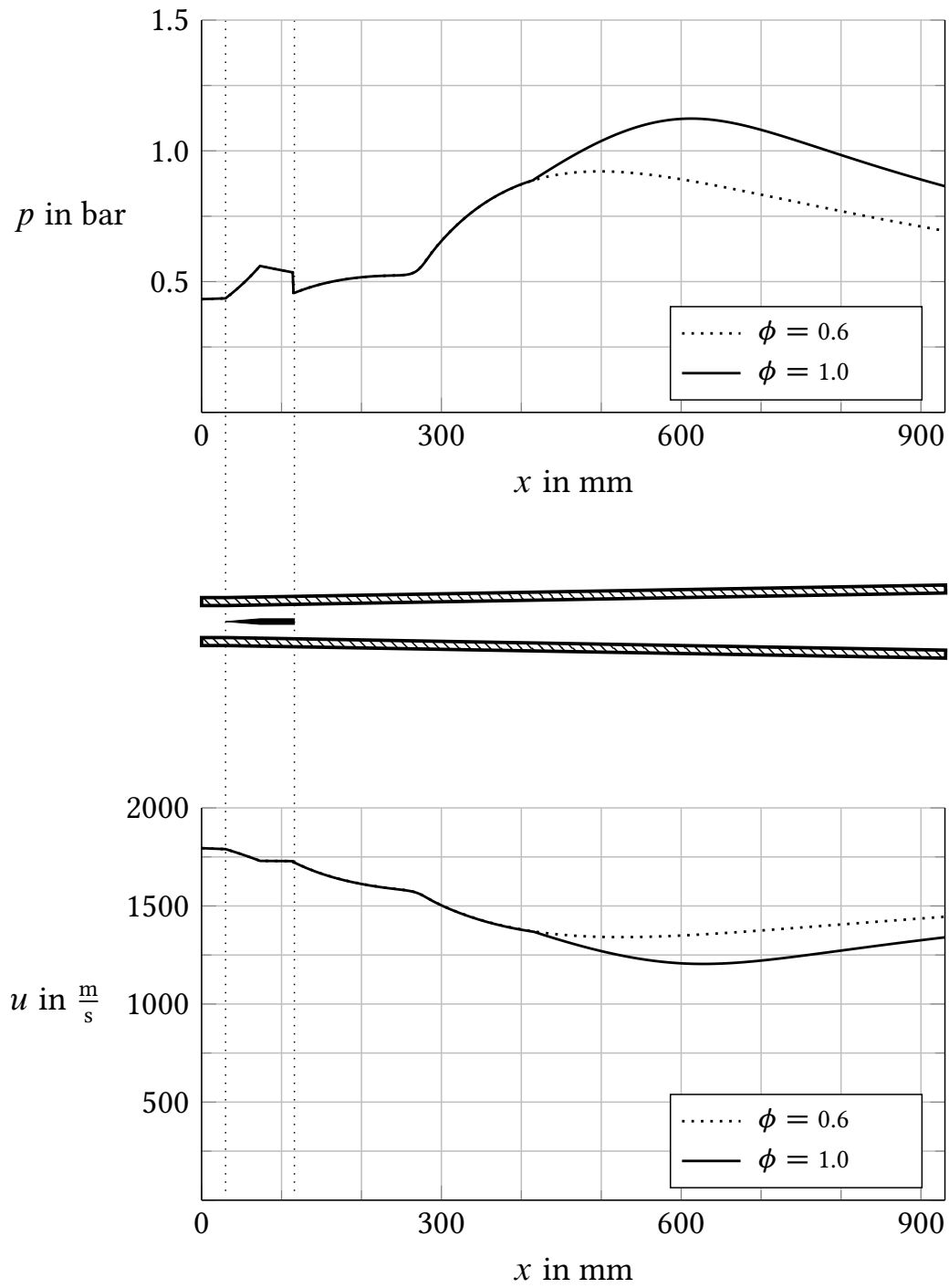


Figure 6.12: Combustor static pressure and velocity

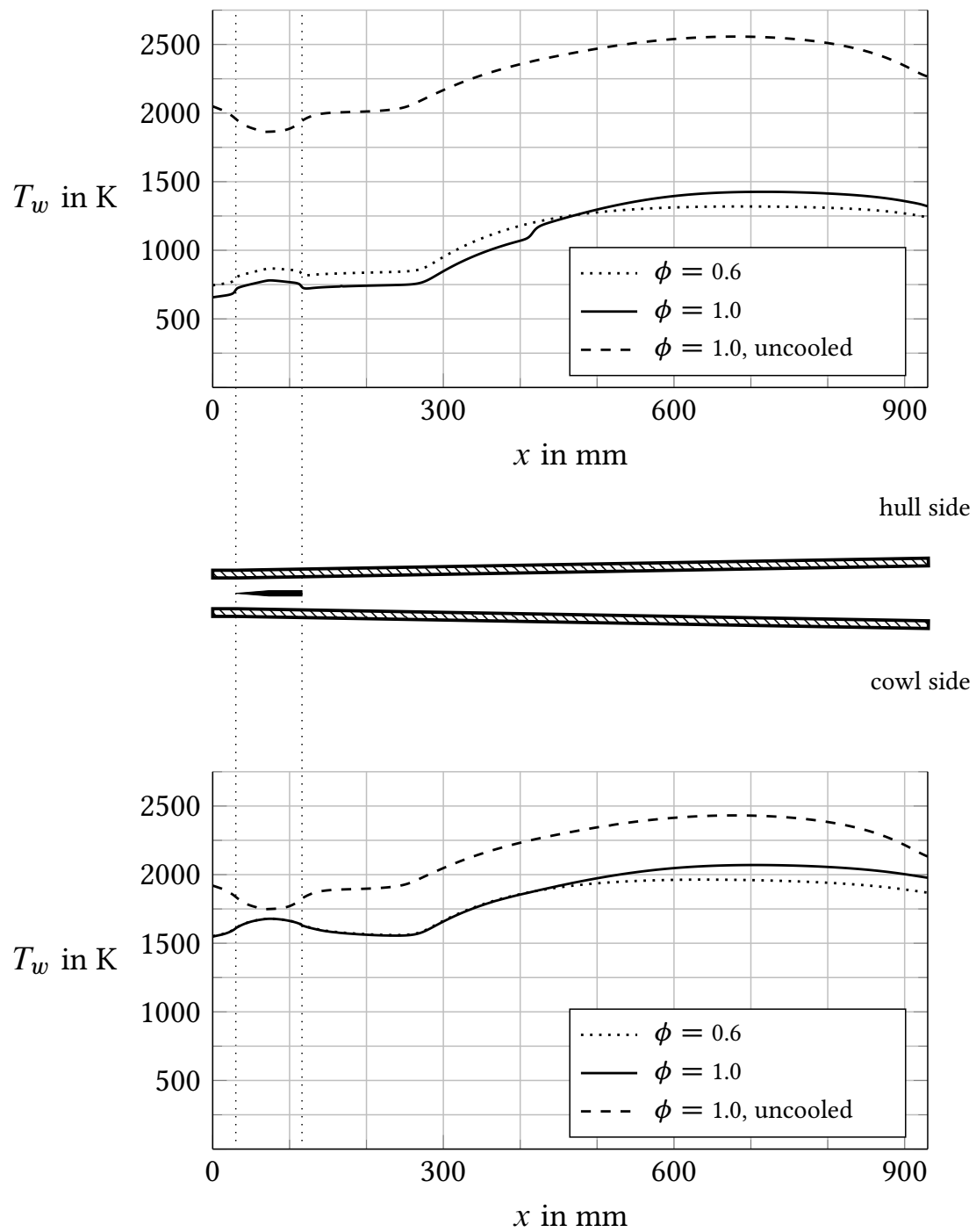


Figure 6.13: Combustor equilibrium surface temperatures for the hull side (top) and cowl side (bottom), versus x , at various stoichiometric ratios.

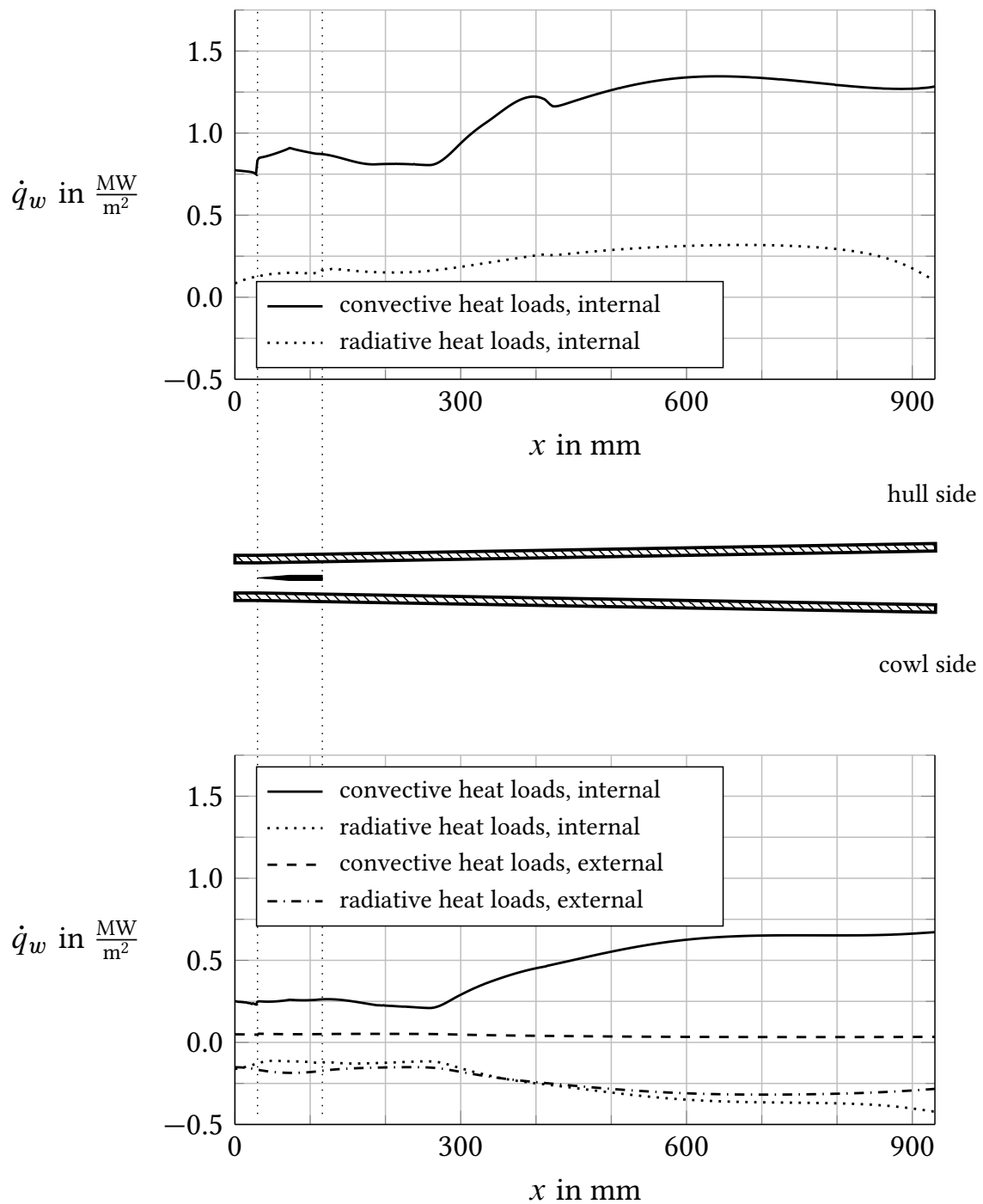


Figure 6.14: Convective and radiative heat loads on hull side walls (top) and cowl side walls (bottom) versus x , for $\phi = 1.0$.

7. Cooling Channel Investigation

The heat transfer analyzes of both the inlet structure in Sec. 5, and the combustor structure in Sec. 6 suggest, that a thermally balanced flight is possible, while the structure is expected to withstand the occurring thermal loads. It is a legitimate question now to ask, whether the structure will be able to suffer the occurring thermal stresses. It is known from regeneratively cooled rocket engine structures, which are comparable to the present technology, that the cooling channels can burst under thermal stress.²¹⁷ Therefore, the thermal stresses in the hull-sided wall, which is regeneratively cooled, see Figs. 5.13 and 6.10, is a logical choice for a first investigation.

In this first investigation, the heat loads obtained from the thermal equilibrium, which are discussed in Sec. 5 and Sec. 6, are imposed as boundary conditions to a thermomechanical investigation, and thermal stresses are evaluated. In order to save calculation power, however, the preceding heat transfer analyzes were modeled two-dimensionally. The errors made by this modeling abstraction are investigated first. Being aware of these errors, the thermal stresses in the structure are calculated and discussed.

7.1. Modeling Problems and Thermal Boundary Conditions

An example of a regeneratively cooled C/C-SiC panel, which could be used in building the hull structure of the scramjet vehicle, is illustrated in Fig. 7.1; see also Fig. 5.3 for dimensions. With respect to the coordinate system shown in Fig. 5.3, the heat transfer analyzes of the inlet in Sec. 5 and the combustor in Sec. 6 have been performed in the x - y -plane, where the x -axis has been the main direction of both the hotgas and the coldgas flow. It can be seen in Fig. 7.2, that the geometry of the structure cannot be represented in a contiguous way if it is cut along the x -axis.

In the present investigation, the local area specific heat flux within the cooling channels, \dot{q}_{cg} , which is a function of x , has been obtained from the Prandtl-Kármán model, see Sec. 2.2.6, and been imposed as boundary condition for \dot{q}_w on the channel flow field model, which is explained in Sec. 2.2.9. In order to deal with the geometry problem shown in Fig. 7.2, and to preserve energy conservation between the model of the channel flow field and a simulation in the x - y -plane, see also Fig. 1.6, this local heat load \dot{q}_{cg} must be scaled before being imposed as boundary condition of the finite-element simulation via Eq. (4.12).

Therefore, let P be the perimeter of the cooling channel, and n be the number of cooling channels in z -direction, and l_z be the width of the panel, which is illustrated in Fig. 7.1.

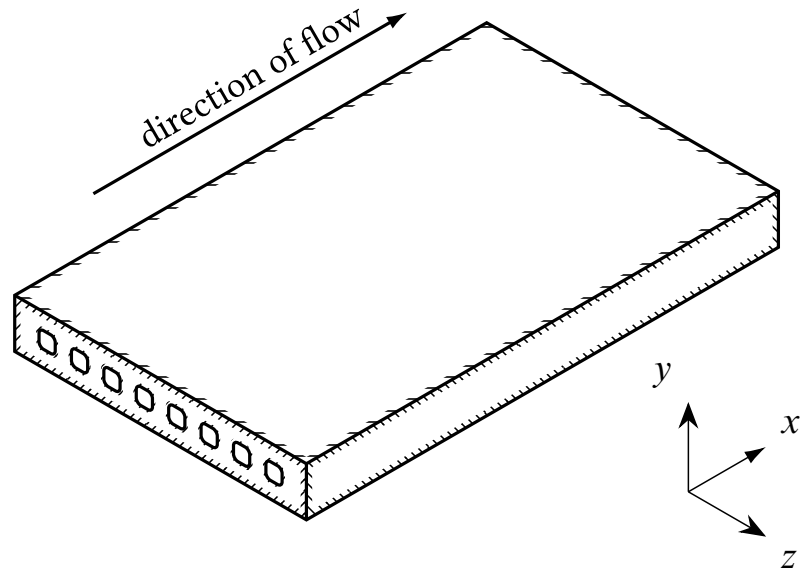


Figure 7.1: Example of a regeneratively cooled C/C-SiC panel.

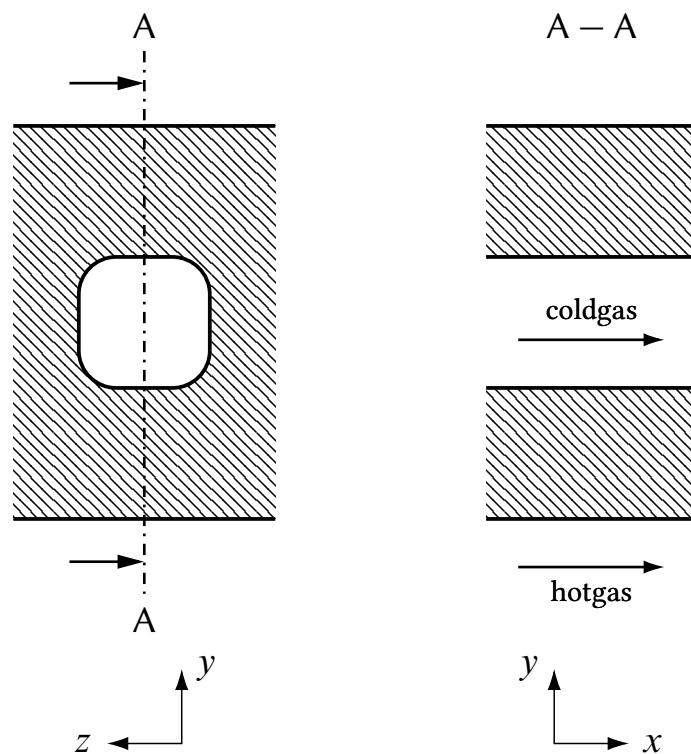


Figure 7.2: Simulated structure domains in the y - z plane (left) and x - y -plane (right). In the latter, only the half on the hotgas side is regarded.

Then, the area specific heat flux $\dot{q}_{cg}^{(xy)}$, which needs to be imposed for \dot{q}_w on the finite-element simulation in the x - y -plane via Eq. (4.12), reads

$$\dot{q}_{cg}^{(xy)} = \frac{n P \dot{q}_{cg}}{l_z}. \quad (7.1)$$

This procedure preserves the energy conservation between the models of the channel flow field and the finite element simulation in the x - y -plane. It also implies that within any x -coordinate, the surface temperature along the perimeter of the cooling channels must be constant. Experience however teaches that this assumption is not realistic.²¹⁸ This error must be accepted if a calculation is performed in the x - y -plane. If the calculation is performed in the y - z -plane, a more realistic approach can be chosen by assuming that not the wall temperature, but the Stanton number is constant along the channel perimeter P . As for the calculation in the x - y -plane, the Stanton number for the cooling channels is obtained from the Prantl-Kármán model. The local heat fluxes $\dot{q}_{ch,yz}$, which are imposed as boundary condition for \dot{q}_w on the finite-element simulation in the y - z -plane via Eq. (4.12), are now obtained from Eq. (2.45). This way, the surface temperatures T_w along the perimeter P are not unrealistically forced to be constant.

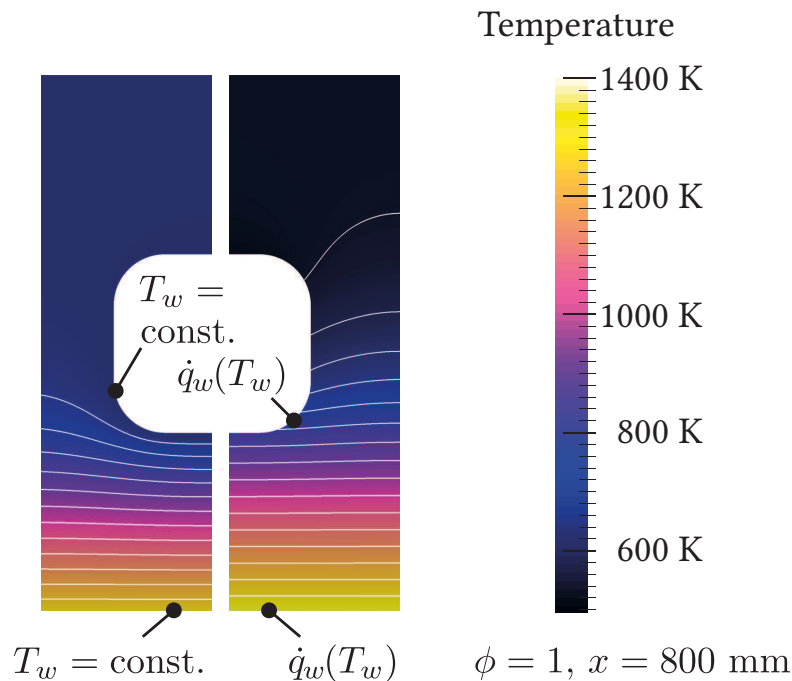


Figure 7.3: Comparison between constant temperature (left) and constant Stanton number boundary condition (right)

A two-dimensional calculation in the y - z -plane on the other hand is only realistic if the local temperature gradients $\partial T/\partial x$ are low. Therefore, without a full three-dimensional calculation, it is hard to say which model creates more realistic heat fluxes. In order to quantify the error caused by the 2D-abstraction, two magnitudes

$$\dot{Q}^{(yz)} = \int_P \dot{q}_{\text{cold}}^{(yz)} dP, \quad (7.2) \quad \text{and} \quad \dot{Q}^{(xy)} = \int_P \dot{q}_{\text{cold}}^{(xy)} dP, \quad (7.3)$$

are introduced, which denote the local heat flux derivative in dependence of the x -coordinate, obtained from the calculation in the x - y -plane, and the y - z -plane, respectively. The energy error is then expressed by the *normalized corrected sample standard deviation*,²¹⁹ which in case of two datapoints, here $\dot{Q}^{(xy)}$ and $\dot{Q}^{(yz)}$, reads

$$\mathfrak{s} = 2 \frac{|\dot{Q}^{(yz)} - \dot{Q}^{(xy)}|}{\dot{Q}^{(yz)} + \dot{Q}^{(xy)}}. \quad (7.4)$$

7.2. Mechanical Bearing

The temperature gradient between the hotgas and the coldgas side of the ceramic sandwich tiles will, due to thermal expansion, cause thermomechanical stresses and deformation. One problem in the construction of such structures is, that they should be kept as thin as possible in order to minimize thermal stresses, while one usually would strengthen the structure in order to reduce mechanical, non-thermal stresses.⁶⁸

Furthermore, the mechanical constraints should be kept as low as possible in order to minimize the stresses caused by thermal deformation. Two C/C-SiC design concepts which are worth mentioning are the tightening design of the X-38 experimental vehicle,²²⁰ and the design of the EXPERT reentry experiment,²²¹ which have both achieved an almost statically defined bearing. More detailed design guidelines for the mechanical bearing of C/C-SiC on metal are given in both English and German language by Krenkel.^{222,223}

For the present investigation, the panel structure from Fig. 7.1 was projected into the y - z -plane. A statically defined bearing was assumed. Due to the symmetry of the problem along the y -axis, only a half of the structure needed to be modeled, see Fig. 7.4. The wetted surfaces of the cooling channels were imposed with 20 bar, while the hotgas pressure, which is about forty times less, was not regarded.

With the hotgas pressure not being considered, the bearing which suppresses movement in the y -direction, Fig. 7.4 bottom right, becomes forceless due to symmetry conditions. The thermal deformation was assumed to be zero at 1693 K, which is the temperature of the liquid silicon infiltration process.²²⁴

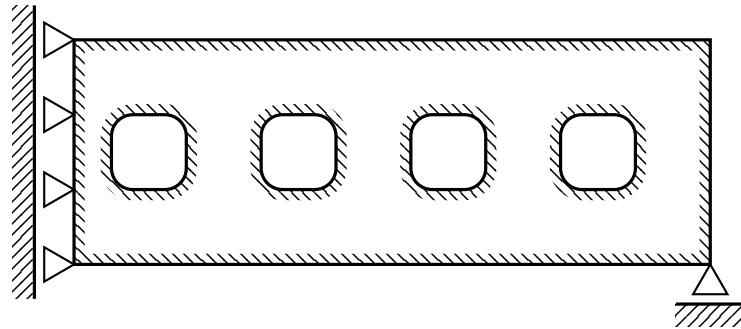


Figure 7.4: Symmetrical half model of C/C-SiC panel, statically defined mechanical bearing.

7.3. Thermal Stress Calculation

The modeling problem of the two-dimensional abstraction, as well as the dealing with the thermal boundary conditions, have been discussed in Sec. 7.1. The mechanical bearing has been discussed in Sec. 7.2. The Stanton numbers, (St) and the gas states (ρ, u, T) in dependence of the x -coordinate of both the hotgas and the coldgas have been obtained from the heat transfer analysis of the inlet, see Sec. 5, and the combustor, see Sec. 6. The thermomechanical stresses, in the y - z -plane, which are of special interest for the stability of the cooling channels, could now be calculated in a procedure, which is illustrated in Fig. 7.6. Herein, the structure shown in Fig. 7.4, was resolved into 21 000 biquadratic triangular elements of the type TRIM6, see App. A, and 84 000 degrees of freedom. The obtained thermomechanical stresses were ratified using the *Tsai-Wu criterion*, g , see App. B.2.

Two representative temperature plots and Tsai-Wu plots are depicted in Fig. 7.9 for the inlet positions $x = 700$ mm and $x = 1350$ mm. Corresponding plots for the combustor at $x = 250$ mm and $x = 650$ mm are shown in Fig. 7.10. The mechanical deformations are overscaled by a factor of 50. Since C/C-SiC has a negative thermal expansion ratio in fiber direction for temperatures below room temperature, the structure forms a concave bending at the cooled external inlet surface, while the bending of the internal hull structure is convex.

When compared to the x - y simulation, the surface temperatures in the y - z -simulations are approximately 100 K higher, see Fig. 7.7 and 7.8.

Significant energy deviations between the x - y and the y - z abstraction were found near the area of the separation bubble and the impingement of the first reflected shock on the hull structure. This can be explained by the increased heat loads at this position, which cause significant temperature gradients $\partial T/\partial x$, which are neglected in the y - z simulation.

A similar yet weaker effect was observed in the combustor simulation. In the area around the central injector. More reliable predictions could be made further downstream in the area, where ignition and combustion happen.

An interesting fact, which might turn out as useful for future design methodologies, is the almost linear relation between the temperature difference of the hotgas side surface temperature $T_{w,hot}^{(xy)}$ and the coldgas temperature $T_{cg}^{(xy)}$, which were both calculated in the x - y -simulation, and the maximal Tsai-Wu-criterion, which was calculated in the y - z -simulation. The plot is depicted in Fig. 7.5.

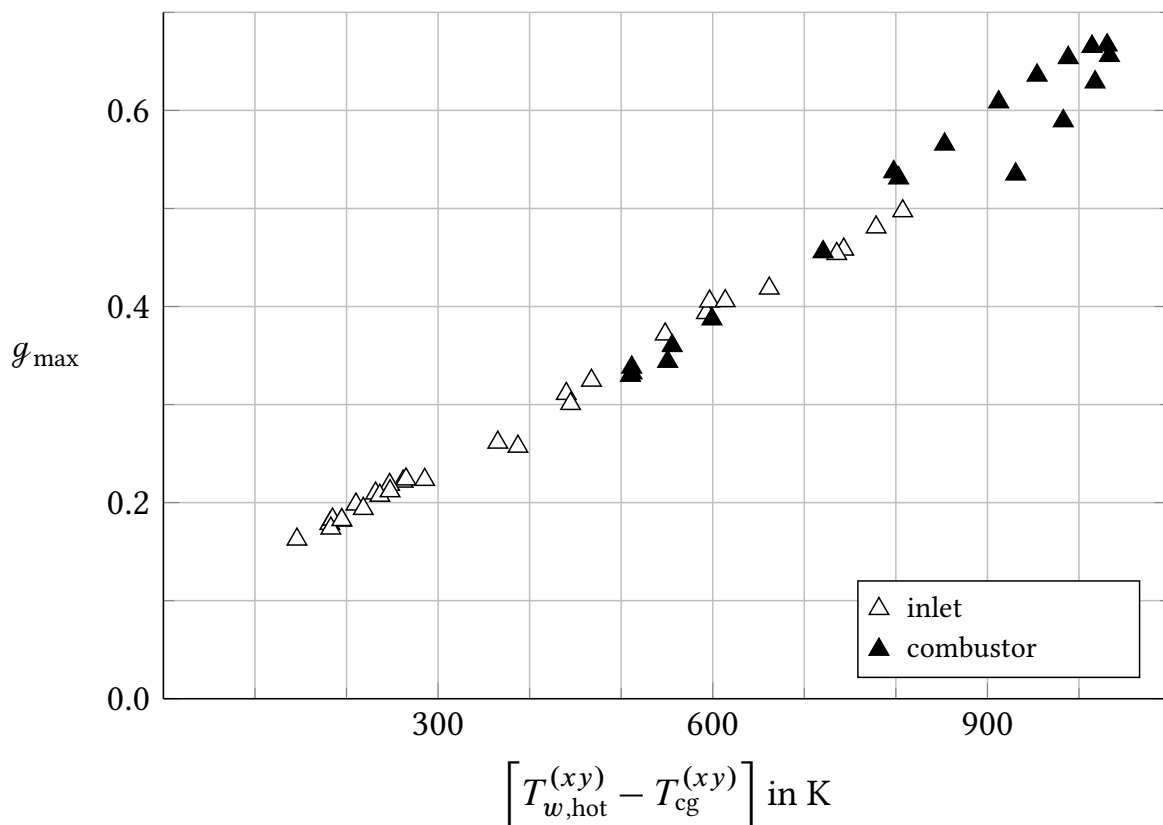


Figure 7.5: Relation between maximum Tsai-Wu criterion versus temperature difference of the hotgas surface and the coolgas versus.

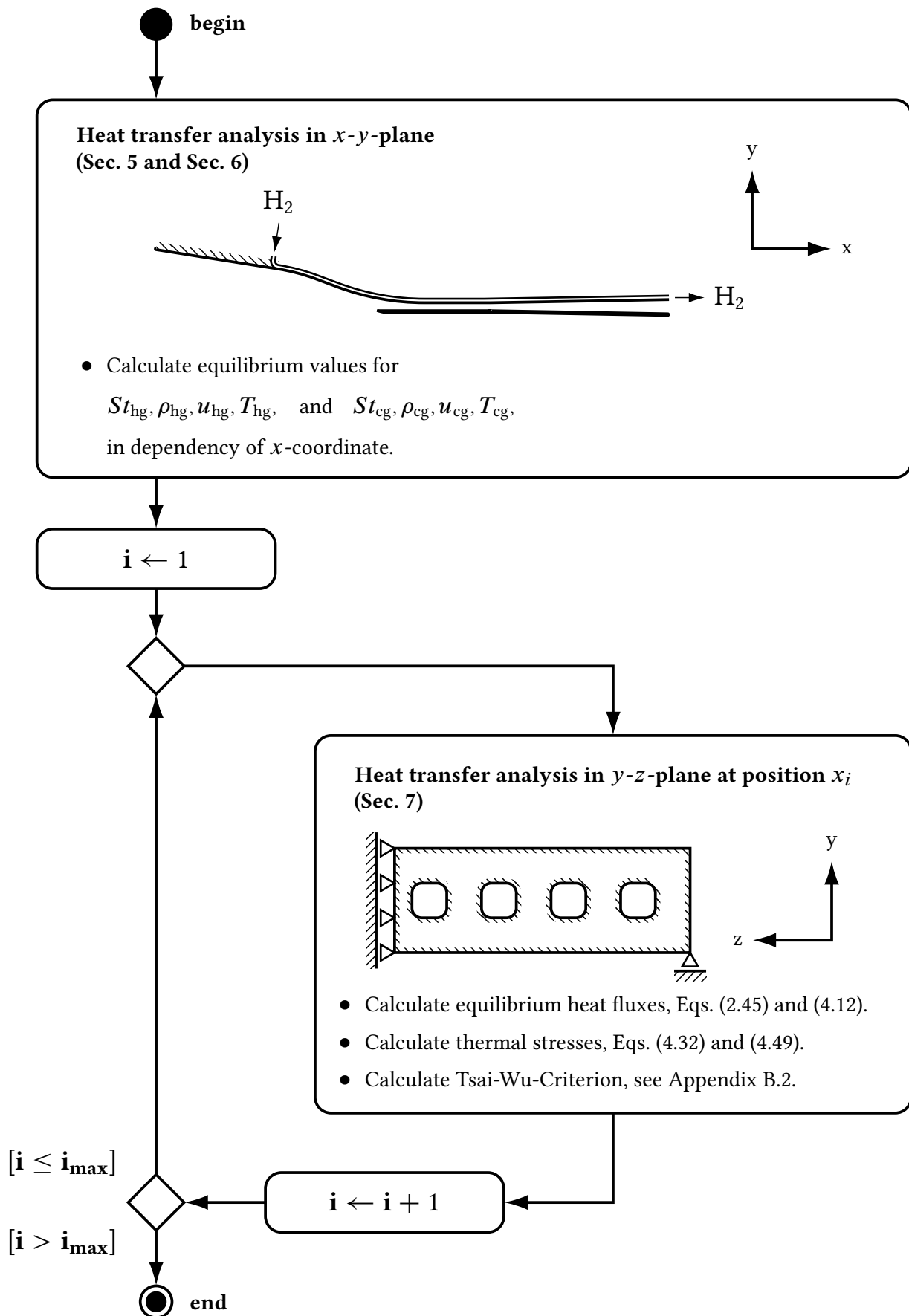


Figure 7.6: UML activity diagram for procedure of the thermomechanical investigation of the cooling channels.

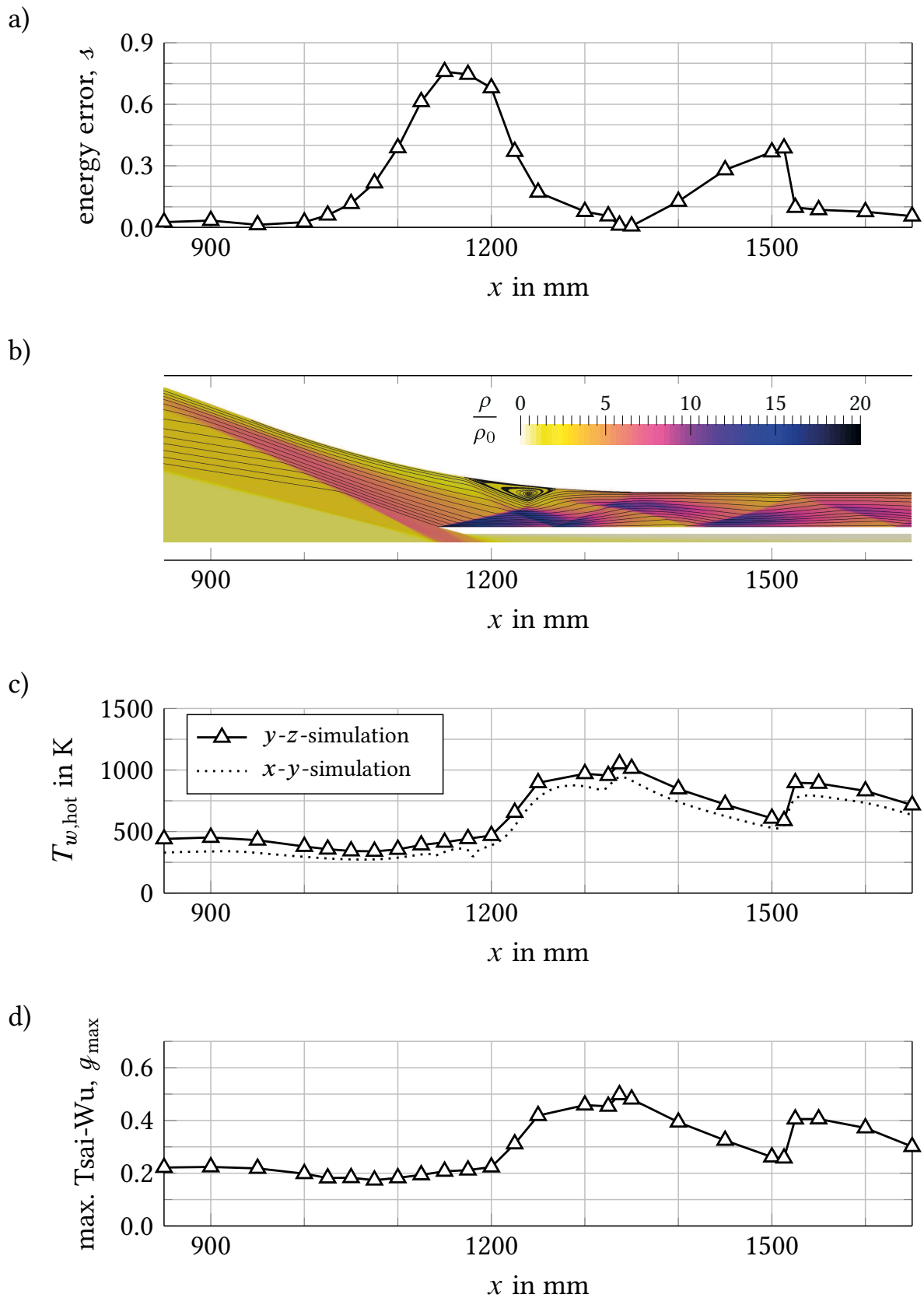
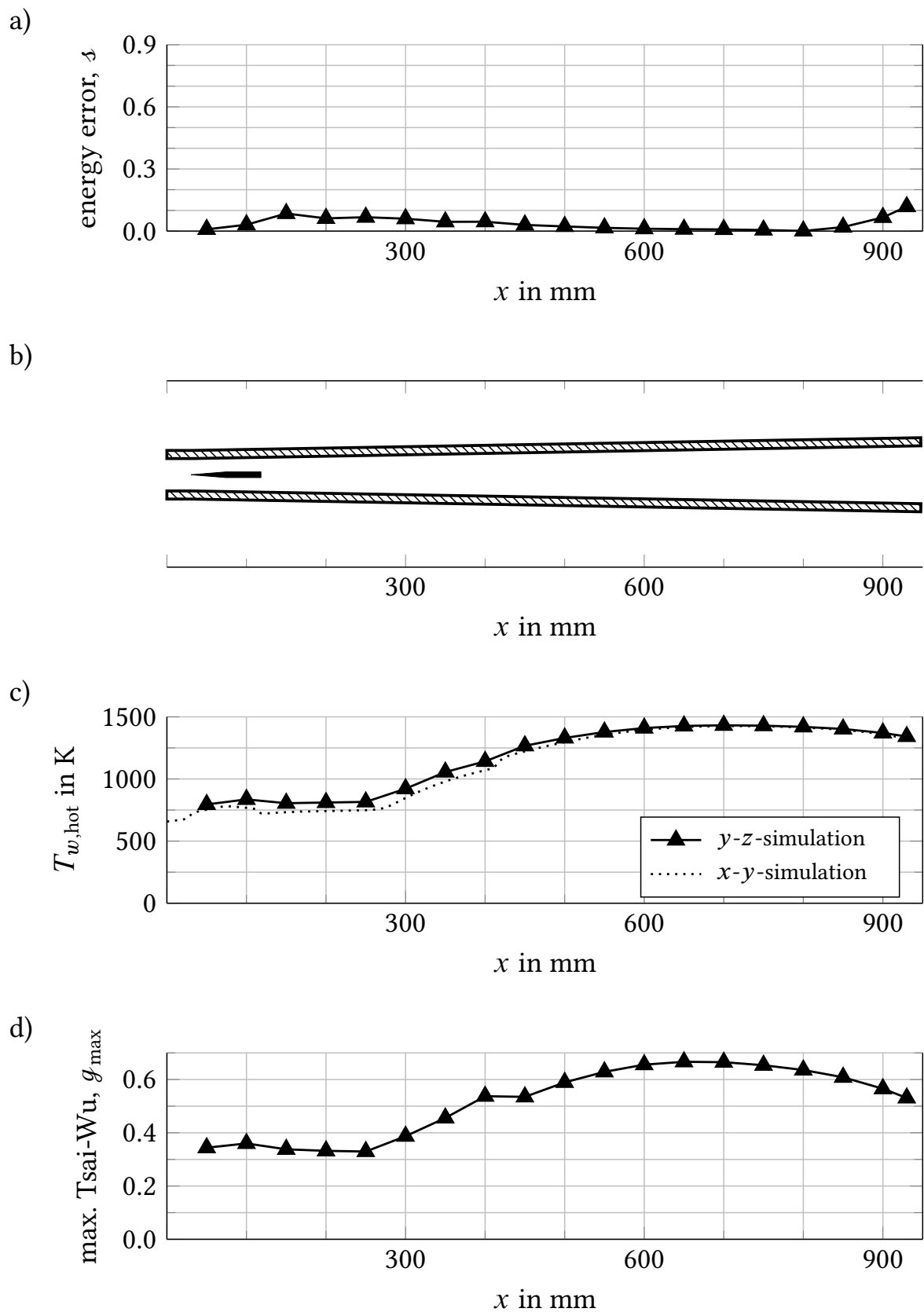


Figure 7.7: Inlet calculation along x -coordinate:

a) Energy error, b) numerical Schlieren image near lip,

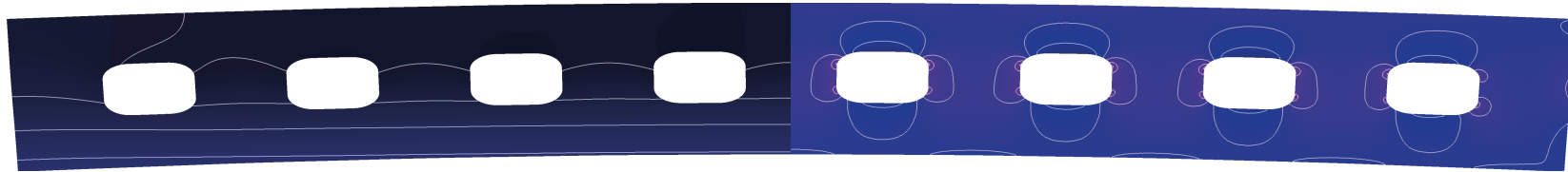
c) local surface temperature at hull side, d) maximum Tsai-Wu criterion.

Figure 7.8: Combustor calculation along x -coordinate:

- a) Energy error, b) combustor geometry,
 c) local surface temperature at hull side, d) maximum Tsai-Wu criterion.

x = 700 mm

Deformation scaled with factor 50.

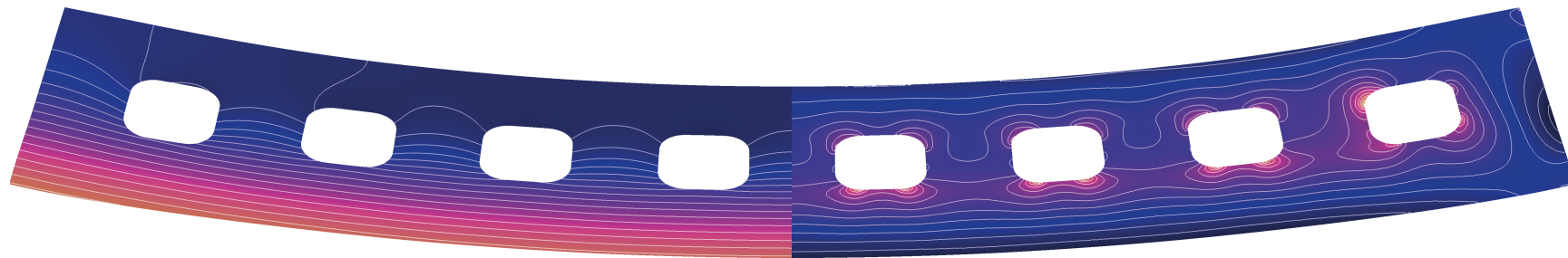


0 500 1000 1500

Temperature in K

-0.25 0 0.25 0.5

Tsai-Wu criterion

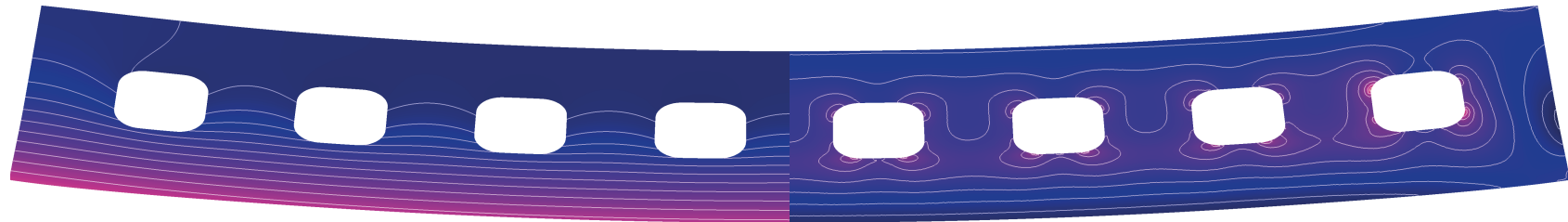


x = 1350 mm

Figure 7.9: Temperature field (left) and Tsai-Wu criterion (right) at inlet hull.

x = 250 mm

Deformation scaled with factor 50.

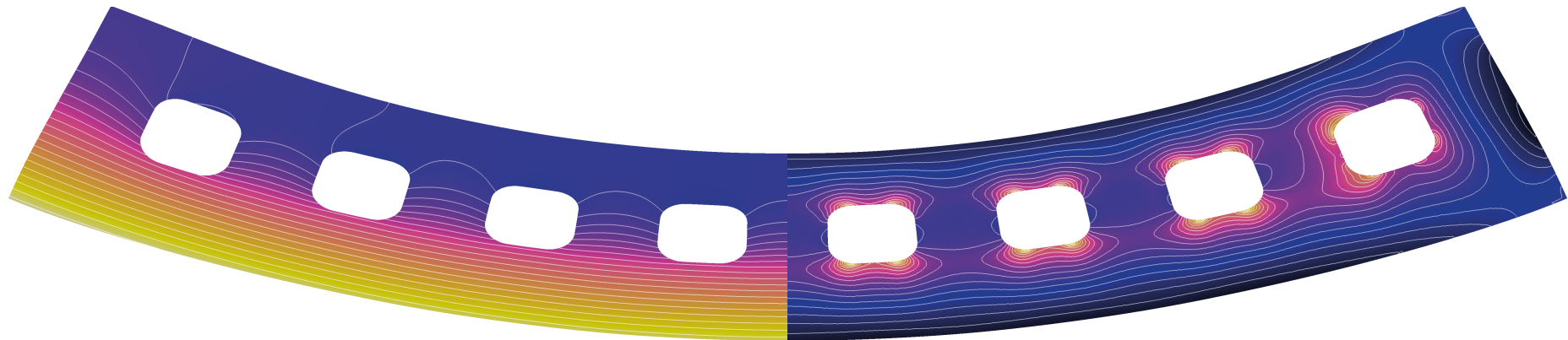


0 500 1000 1500

Temperature in K

-0.25 0 0.25 0.5

Tsai-Wu criterion



x = 650 mm

Figure 7.10: Temperature field (left) and Tsai-Wu criterion (right) at combustion chamber hull.

8. Conclusion and Outlook

In this work, a general methodology to estimate heat loads and equilibrium temperatures on a two-dimensional scramjet structure has been developed. It was shown that the structures of the inlet and the combustor system of a Mach 8 vehicle might be able to withstand the occurring thermal and mechanical loads, if they are regeneratively cooled.

The aerothermodynamic heat loads on the inlet structure were estimated using the Reynolds averaged Navier-Stokes solver FLOWer by the German Aerospace Centre DLR.⁸⁰ Hereby, the Menter-SSTk ω turbulence model was used,⁸¹ as recommended by Krause¹¹⁰ and Reinartz.²²⁵ The plausibility of the RANS simulation, which contains a perfect gas approach, was validated by comparing selected results with semi-empirical approaches from literature.

The aerothermodynamic heat loads on the structure of the combustion chamber were estimated by combining a one-dimensional combustion solver, which is based on the works of Walther¹⁶¹ and Scheuermann,²¹⁶ with a van Driest friction model for compressible non-adiabatic flow.¹²¹ Since this friction model was originally developed for the flat plate, it was modified to be applicable to channel flow and pipe flow. The friction and combustion processes resulting from this model have been validated against three-dimensional calculations by Rabadán Santana.²¹⁰ The implementation of the friction model, however, should be subject of further validation.

Hottel's method of crossed strings¹⁶⁸ was used for both the inlet and the combustor simulation in order to model surface radiation. Similarly to the preceding investigation by Reinartz,⁸³ the model by Hottel and Egbert⁸² for water vapor radiation by was implemented for the combustor simulation. A model for a rough estimation of the temperature of the central strut injector was suggested, and validated against measurements and calculations by Dröske²¹⁴ and Rust.²¹²

A regenerative cooling system similar to Sängers original design⁵ was considered, where the fuel feed was imagined to be driven by a turbopump, similar to the design of Kanda.⁵⁰ Since the hydrogen was assumed to be cryogenic in the inlet part, Leachman's real gas model⁸⁴ was used for the flow field of the channels. Along the combustion chamber, an calorically imperfect ideal gas was used.

The investigated inlet geometry is a modified version of Krause's two-dimensional inlet.¹¹⁰ The combustor geometry is a two-dimensional simplification of the geometry described by Rabadán Santana. Corresponding the baseline concept of the GRK 1095 design, a cruising velocity of $Ma = 8$, and a flight altitude of 30 km were chosen as characteristic boundary conditions.

The temperature distribution and the thermal deformation of the structure was modeled using the finite-element-method. An implicit Euler method was chosen as time-stepping method.

As material for the thermal protection system, the carbon fiber reinforced ceramic C/C-SiC was chosen. Available material data were collocated from literature and carefully extrapolated to the relevant temperature range. Since the ceramic structure was imagined to be coated with yttrium silicate, the optical properties of this substance were used for the radiative simulation. The Tsai-Wu criterion²²⁶ was chosen to quantify the mechanical stress on the structure. This criterion has been validated by Fink²²⁷ for its applicability to the ceramic material. Since not all necessary parameters for the case of interest were available, they had to be estimated using the theory of micromechanics, which is described in detail by Dvorak.²²⁸

It was observed that the stagnation temperature at the tip of the vehicle, the nose, can be kept in an acceptable range if the nose is rounded. Similar to the results by Fischer,²⁰¹ the separation bubble phenomenon at the lip of the inlet will cause the inlet to unstart if the wall temperature reaches a critical limit. It was shown that if the hydrogen fuel is stored cryogenically, it can be used to cool down the structure to uncritical conditions.

For geometric reasons, the cowl side of the structure can not be cooled regeneratively. However, a radiative cooling might suffice to keep the structure below its theoretical maximum service temperature of 2200 K.

A set of two-dimensional calculations perpendicular to the main flow direction revealed the limitations of the chosen approach. It was found that the surface temperatures can be generally predicted with an accuracy of 100 K. The area of high temperature gradients around the separation bubble at the lip, and the area around the central strut injector will require further attention in future investigations. Along the main flow direction, the relation between the local hot surface temperature and the local maximum of the Tsai-Wu criterion is close to linear, which might be useful in future design processes. During the simulations, both the flow field and the structure were kept within acceptable limits. If a statically defined mechanical bearing can be achieved, the cooling system will keep the thermal stresses low enough to prevent a system-wide rapid unscheduled disassembly.

For simplicity, the laminar-to-turbulent transition of the boundary layer along the external hull structure was assumed to be at one discrete x -position, see Fig. 5.6. The sensitivity of laminar to turbulent transition on the stability of the overall system behavior requires further attention. One starting point for a possible upcoming investigation might be the transition model discussed by Frauholz et al.²²⁹

The present investigation of the inlet flow field has been performed using a calorically perfect gas model. Using various semi-empiric approaches it could be shown that the perfect gas approach is, in a first step, justifiable, see Sec. 5.3.3. The literature research suggested that the SST- $k\omega$ turbulence model should be reliable in the present case. Especially with respect to the critical wall temperature at which inlet unstarting occurs (see Fig. 5.5), these assumptions need to be further investigated.

It was shown in Fig. 7.7, that the structural temperature near the separation bubble at the lip cannot be satisfactorily modeled with a two-dimensional abstraction. In order to get a better understanding the fluid-structure interaction near the separation bubble, a three dimensional model is required.

Temperature dependencies and hysteresis effects of the mechanical behavior of the material have been neglected in this investigation. However, the matrix of the chosen C/C-SiC ceramic contains approximately 10% silicon, which melts at 1687 K. The consequences for the mechanical behavior and strength of the ceramic need to be further investigated. The effect of the structure's thermal deformation on the flow field has not been investigated in this work. To perform this investigation, a three-dimensional geometry will be necessary, which contains sufficient information on the supporting metal structure and the ceramic-metal interface. Starting points for the design of that structure might be found in the constructions of the flight experiments EXPERT²²¹ and SHEFEX.²³⁰ Thermal deformation will also be relevant to the choice and design of the anti-oxidation coating, which protects the ceramic structure. Due to their different mechanical and thermal properties, shear stresses between the substrate and the layer will occur, which could potentially destroy the coating. These effects were observed for example in the Foton-M2 flight experiment.²³¹ In order to solve this problem, the utilization of so-called *functionally graded* coatings has been occasionally discussed in literature.^{232,233} The thermal loads, which have been found in this work, as well as the material theory discussed in App. B, will help to define the thermal and mechanical requirements of these coatings.

In order to control the thrust vector, a movable flap is sometimes proposed at the nozzle,²³⁴ see Fig. 1.1. However, since in the present design, the cowl side of the combustion chamber is passively cooled only, it will heat up to 2000 K, see Fig 5.16. In order to make the flap movable, it will probably be necessary to develop a more powerful cooling concept, for example by using heat pipes.⁵⁹

In order to optimize off-design performance of the inlet, a movable lip has been suggested in literature.²¹⁵ Similar to the flap, a more powerful cooling concept will be necessary if a moving structure is desired.

In order to reduce stagnation point heat loads, the nose of the inlet has been blunted, see Fig. D.3. The blunted nose induces a so-called entropy-layer, which is in detail explained by van Wie.¹⁸⁵ So far, the influence of the nose radius on the performance and robustness of the scramjet cycle is not fully understood. Detailed parameter studies should be performed in order to further investigate this behavior. Most likely, due to these changes in the boundary layer, the critical wall temperature, see Fig. 5.4, will decrease, while the combustor entry temperature T_3 will increase. This will probably lead to a more stable combustion process, with the cost of a lesser adiabatic kinetic efficiency.

A. Finite Element Formulation

The elements QUAM9 (quadrilateral membrane 9 nodes) and TRIM6 (triangular membrane 6 nodes) are second order Lagrangian elements, which perform very well for both the transient thermal conduction analysis and the static deformation and stress investigation of two-dimensional problems.²³⁵ Quadrilateral elements are primarily suitable for structured meshes, while triangular elements perform well for both structured and unstructured meshes.

A.1. Definition of Shape Functions

Local, dimensionless coordinates are introduced, in reference to which the element's interpolation functions, or shape functions, are evaluated. If within an element e , the nodal values \hat{f}_s^e of an arbitrary scalar function f are known, the function can be interpolated within the element, using the approximation

$$f \approx \phi_s \hat{f}_s^e, \quad (\text{A.1})$$

where ϕ_s are the shape function components. The components of the QUAM9 and TRIM6 elements are shown in Figs. A.2 and A.3. The shape functions are usually evaluated in relation to dimensionless parameter coordinates. A Cartesian coordinate system is used for the quadrilaterals, while a barycentric coordinate system is used for triangular elements (see Fig. A.1).

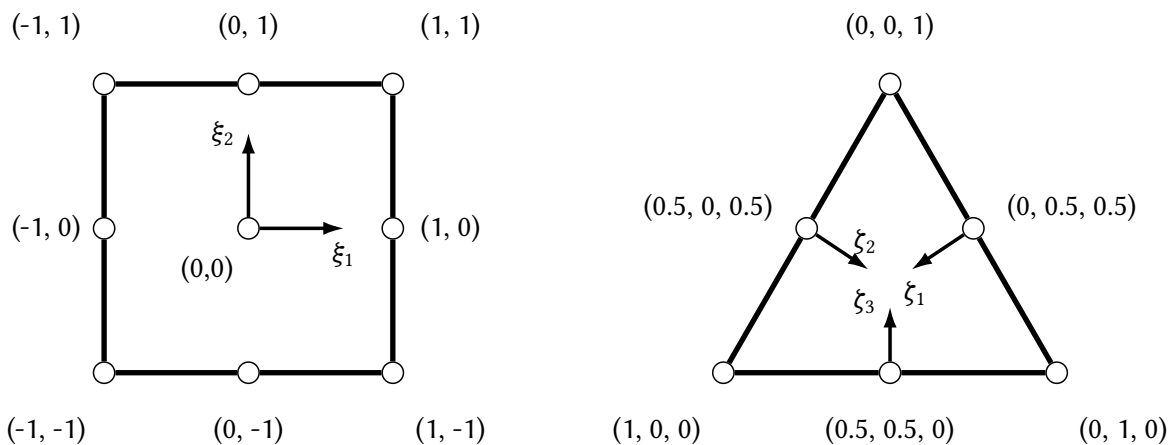


Figure A.1: Local Cartesian coordinate system of the QUAM9 element (left), and local barycentric coordinate system of the TRIM6 element (right).

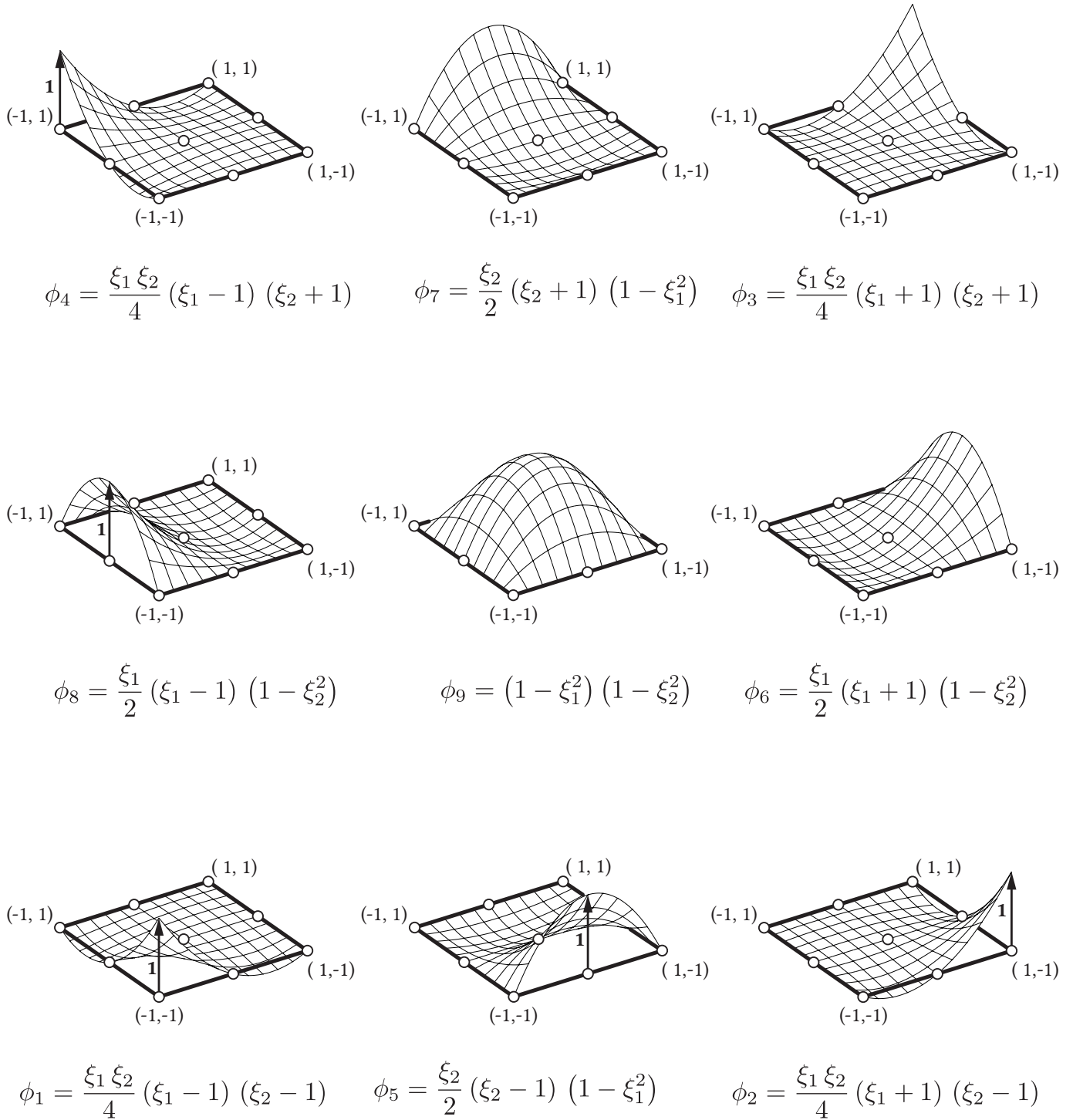


Figure A.2: Shape functions of the QUAM9 element.

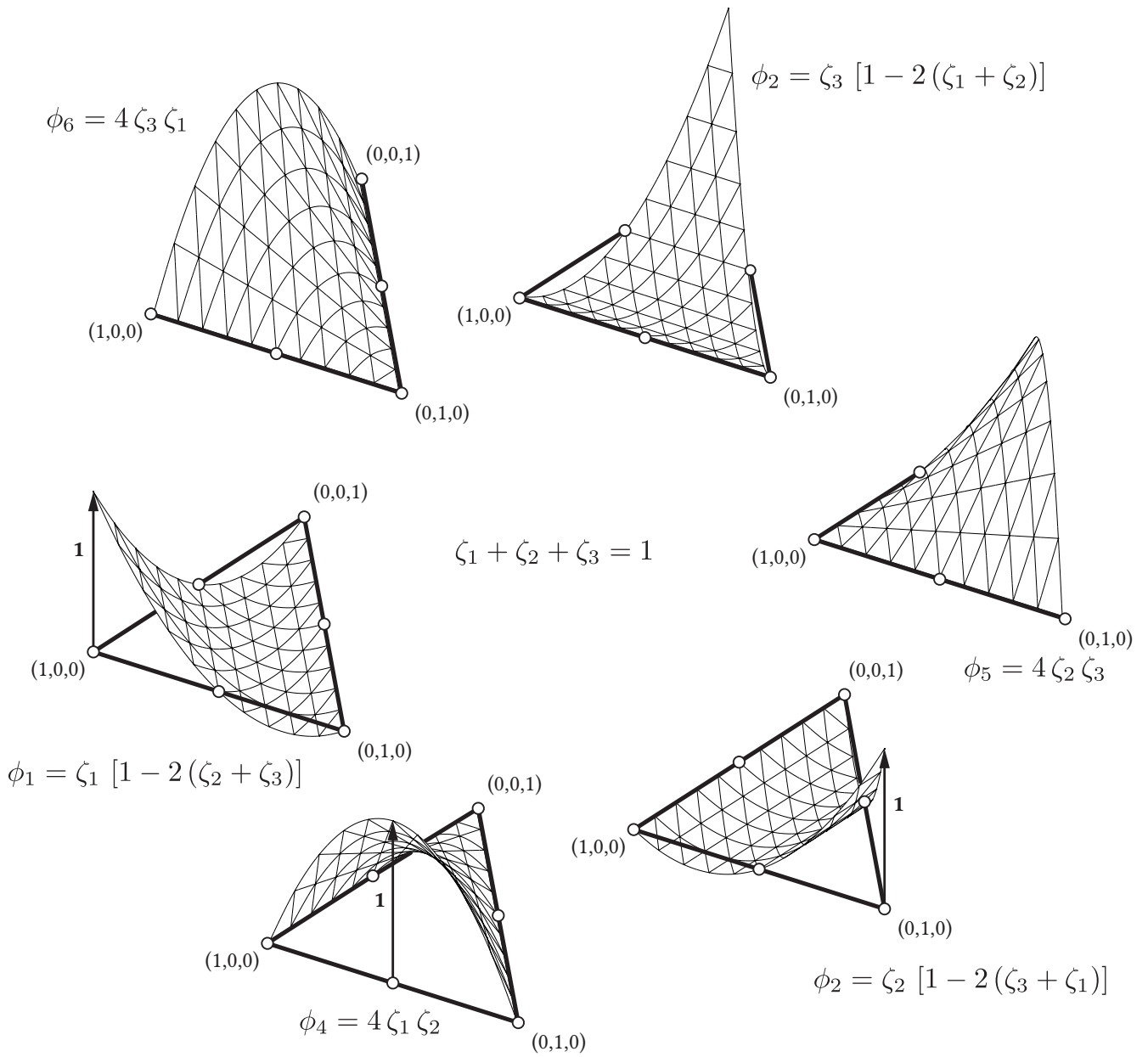


Figure A.3: Shape functions of the TRIM6 element.

A.2. Numerical Integration and Differentiation

For simplicity, the following equations are noted with the Cartesian coordinates ξ_q . They are also valid for barycentric coordinates ζ_q as well, if ζ_3 is substituted by

$$\zeta_3 = 1 - \zeta_1 - \zeta_2. \quad (\text{A.2})$$

Using the chain rule, it can be shown that the spacial deviations of f can be interpolated within the domain of the element Ω^e by

$$\frac{\partial f}{\partial x_j} = \frac{\partial \xi_q}{\partial x_j} \frac{\partial \phi_s}{\partial \xi_q} \hat{f}_s^e, \quad (\text{A.3})$$

where the components $\partial \xi_q / \partial x_j$ are found by inverting the Jacobian matrix

$$J_{jq} = \frac{\partial x_j}{\partial \xi_q} = \frac{\partial \phi_s}{\partial \xi_q} \hat{x}_{sj}^e. \quad (\text{A.4})$$

A scalar function g can be integrated over the elemental domain Ω_e , using the rules

$$G^e = \int_{\Omega^e} g \, dV^e \approx \int_{-1}^1 \int_{-1}^1 g |\det \mathbf{J}| \, d\xi_1 \, d\xi_2 \approx \sum_p \sum_q \tilde{v}_p \tilde{v}_q g(\tilde{\xi}_{p1}, \tilde{\xi}_{q2}) \left| \det \mathbf{J}(\tilde{\xi}_{p1}, \tilde{\xi}_{q2}) \right|, \quad (\text{A.5})$$

if a quadrilateral element is considered. For a triangular element, the interpolation rule reads

$$G^e = \int_{\Omega^e} g \, dV^e \approx \int_0^1 \int_0^{\xi_2} g |\det \mathbf{J}| \, d\xi_1 \, d\xi_2 \approx \sum_p \tilde{w}_p g(\tilde{\xi}_{p1}, \tilde{\xi}_{p2}) \left| \det \mathbf{J}(\tilde{\xi}_{p1}, \tilde{\xi}_{p2}) \right| \quad (\text{A.6})$$

The coordinates of $\tilde{\xi}_{pk}$, respectively $\tilde{\zeta}_{pk}$, and the weighting factors \tilde{v}_p and \tilde{w}_p can be found in standard literature.^{236,237}

If an integration of along an edge $\partial\Omega^e$ of a two-dimensional element is performed, the shape function becomes one-dimensional. The integration rule reads

$$\partial G^e = \int_{\partial\Omega^e} g \, dA^e \approx \int_{-1}^1 g \sqrt{\sum_j \left(\frac{\partial x_j}{\partial \xi} \right)^2} \, d\xi \approx \sum_p \tilde{w}_p g(\tilde{\xi}_p) \sqrt{\sum_j \left(\frac{\partial x_j}{\partial \xi} \Big|_{\tilde{\xi}_p} \right)^2}. \quad (\text{A.7})$$

A.3. Spatial Derivatives in Finite-Element-Analysis

Due to its C_0 -consistent representation of the deformation field, the Lagrangian element formulation does not allow a continuous representation of the stress field. More generally speaking, if f is a scalar function, which is represented in the finite-element field by Eq. (A.1), its spacial derivatives $\partial f / \partial x_j$, see Eq. (A.3), can not be represented continuously. Most post-processors smooth this difference by using a least squares method which is described in this paragraph.

Let \hat{f}^s be the known nodal values of the scalar field, and let

$$g^s = \frac{\partial f^s}{\partial x_j} \quad (\text{A.8})$$

be the spacial derivatives of f in j -direction which shall be found. These spacial derivatives are evaluated at the integration points within the adjacent elements, and extrapolated to the nodes using a least squares method.²³⁸ The algorithm reads:

Step 1: Choose suitable polynomial coefficients from the Gaussian triangle, so that

$$\boldsymbol{\psi}(\xi_1, \xi_2) = [1 \quad \xi_1 \quad \xi_2 \quad (\xi_1)^2 \quad \xi_1 \xi_2 \quad (\xi_2)^2 \quad \dots]^T \quad (\text{A.9})$$

Step 2: Loop over all elements e :

- a) Evaluate the Vandermonde-like coefficient matrix over all integration points p and the solution vector over all integration using Eq. (A.3), so that

$$\mathbf{V} = \sum_p \boldsymbol{\psi} \boldsymbol{\psi}^T |_{(\tilde{\xi}_{p1}, \tilde{\xi}_{p2})} \quad \text{and} \quad \mathbf{b} = \sum_p g |_{(\tilde{\xi}_{p1}, \tilde{\xi}_{p2})}. \quad (\text{A.10})$$

- b) Evaluate the coefficient vector \mathbf{c}

$$\mathbf{c} = \mathbf{V}^{-1} \mathbf{b}. \quad (\text{A.11})$$

- c) Extrapolate the nodal values in reference to the element e

$$\hat{g}_d^e = \mathbf{c}^T \boldsymbol{\psi}(\hat{\xi}_{d1}, \hat{\xi}_{d2}) \quad (\text{A.12})$$

Step 3: Average the nodal values \hat{g}_d over all elements m_d of which the node d is part of, so that

$$\hat{g}_d = \frac{\sum_{e=1}^{m_d} \Omega^e \hat{g}_d^e}{\sum_{e=1}^{m_d} \Omega^e}. \quad (\text{A.13})$$

B. Material Characterization of C/C-SiC

Carbon fiber reinforced carbon-silicon carbide (C/C-SiC) is a lightweight material for hot-temperature aerospace applications. It was developed during the German SFB 259 Collaborative Research Centre program, and was successfully flown on the FONTON-M2,²³¹ EXPERT²³⁹ and SHEFEX II²³ flight experiments. It is considered to be used in the combustion chamber of the upcoming Australian/American HIFire 8 scramjet flight experiment.²⁶

During the fabrication process of C/C-SiC, carbon fiber reinforced plastics (CFRPs) are pyrolyzed and infiltrated with liquid silicon.²⁴⁰ The silicon reacts with the pyrolyzed carbon matrix and forms beta-polymorphous silicon carbide. Various quotes cite a maximum service temperature of 2200 K for the composite,¹⁸³ the silicon carbide crystals are chemically stable to temperatures up to 2300 K.²⁴¹ In order to protect the material from thermal oxidation, it can be coated with yttrium silicate. The coating itself has been tested to up to 1800 K in ground and flight experiments,^{209,231} and is chemically stable up to 2200 K.^{184,242}

B.1. The Problem of Mechanical Modeling of C/C-SiC

The complex heterogeneous microstructure of C/C-SiC makes the prediction of material aging and failure very difficult. Due to the high brittleness of the composite, the determination of mechanical material properties through tension tests is very arduous. Phenomenological material models have been developed in the mid 1990s,^{227,243} and are continuously being refined.^{244,245} The most common variation of C/C-SiC is based on polyacrylonitrile (PAN) carbon fibers which are woven into a 0°/90° fabric and infiltrated with a phenol-like precursor. Different choices of the fiber material, fiber pretreatment, the fiber volume fraction of the CFRP raw material and the pyrolysis temperature lead to different volume and mass compositions of the final material.²²⁴ All data given in this work refer to the standard version, C/C-SiC XB, where the last two letters stand for *experimental basic*. There are six parameters needed to describe the mechanical behavior of the 0°/90° woven fabric. Some of these parameters are very difficult to measure, especially their development during material aging. In order to predict the mechanical properties on the basis of the mechanical properties of the components SiC, Si, C, and the carbon fibers, a micromechanical approach is therefore suggested in this section. The damage parameters $\tilde{\varphi}_f$ and $\tilde{\varphi}_m$ are introduced in order to describe the crack densities in the fibers and in the matrix. The parameters are fitted against literature data, and a brief discussion on the results and a recommended data-set is given.

B.1.1. The Self-Consistent Homogenization Approach

The theory of micromechanics is a homogenization approach which aims to predict effective material properties for composites. Its basic idea is that the composite can be described as a system of ellipsoidal inclusions and voids, as illustrated in Fig. B.1.

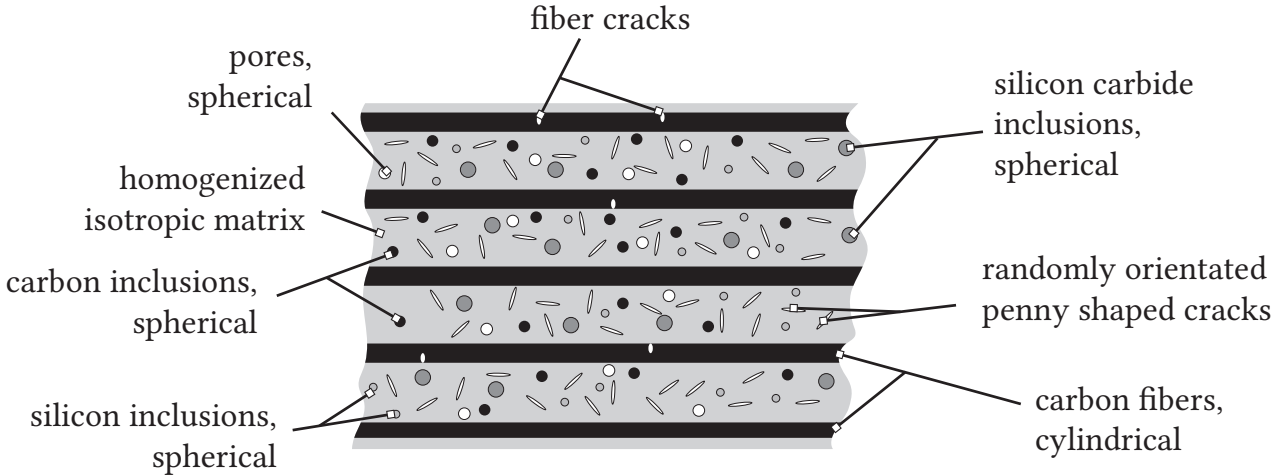


Figure B.1: Simplified model of the C/C-SiC material.

The *self-consistent* mixing model is based on the Eshelby's inclusion problem,^{246,247} and was first formulated by Hill.²⁴⁸ It states that if a number of r inclusions, each one having an elasticity \mathbf{C}^r , are embedded in a matrix with the elasticity \mathbf{C}^0 , the homogenized elasticity tensor $\bar{\mathbf{C}}$ can be formulated over

$$\bar{C}_{ijkl} = C_{ijkl}^m + \varphi^r (C_{ijmn}^r - C_{ijmn}^m) \mathcal{A}_{mnkl}^r. \quad (\text{B.1})$$

Herein, φ^r is the volume fraction of the r^{th} component, \mathcal{A} an influence tensor and m stands for the matrix. It depends implicitly on $\bar{\mathbf{C}}$ and needs to be found by solving the linear equation system

$$\mathcal{A}_{ijmn}^r \left[\mathcal{I}_{mnkl} + \mathcal{P}_{mnpq}^r (C_{pqkl}^r - \bar{C}_{pqkl}) \right] = \mathcal{I}_{ijkl}, \quad (\text{B.2})$$

where \mathcal{I} is the fourth order symmetric identity tensor²⁴⁹

$$\mathcal{I}_{ijkl} = \frac{1}{2} (\delta_{ik} \delta_{jl} + \delta_{il} \delta_{jk}), \quad (\text{B.3})$$

and \mathcal{P} is the *Hill polarization tensor*, which describes the relation between the strains within the inclusion to the strains in the embedding matrix.

It is defined as the surface integral²⁵⁰

$$\mathcal{P}_{ijkl} = \frac{1}{16\pi} \int_{\partial\Omega} \Gamma_{jk}^{-1} n_i n_l + \Gamma_{ik}^{-1} n_j n_l + \Gamma_{jl}^{-1} n_i n_k + \Gamma_{il}^{-1} n_j n_k \, d\partial\Omega, \quad (\text{B.4})$$

where $\partial\Omega$ is the surface of the inclusion Ω , \mathbf{n} the surface normal (see Fig. B.2), and Γ the *Kelvin-Christoffel stiffness*

$$\Gamma_{ik} = \bar{\mathcal{C}}_{ijkl} n_j n_l. \quad (\text{B.5})$$

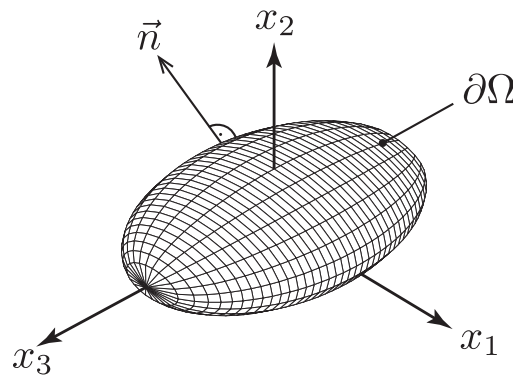


Figure B.2: Ellipsoid shape representing an inclusion or void.

Solving Eq. (B.4) numerically is difficult,²⁵¹ but there are analytical solutions for several special cases, which can be found for example in the works of Laws^{252e}, Lou and Stevens,^{253,254} and Qu.²⁵⁵

The elasticity tensor $\tilde{\mathcal{C}}$ of a cracked medium, which in its uncracked state has the elasticity $\bar{\mathcal{C}}$, can be modeled by introducing a damage tensor \mathcal{D} , which is defined over the implicit relations^{252, 256}

$$\mathcal{I}_{ijkl} = \mathcal{D}_{ijmn} \left(\mathcal{I}_{mnkl} - \mathcal{P}_{mnpq} \tilde{\mathcal{C}}_{pqkl} \right), \quad (\text{B.6})$$

$$\tilde{\mathcal{C}}_{ijkl} = \bar{\mathcal{C}}_{ijmn} \left(\mathcal{I}_{mnkl} - \lim_{a_3 \rightarrow 0} \tilde{\varphi} \mathcal{D}_{mnkl} \right), \quad (\text{B.7})$$

where $\tilde{\varphi}$ is the crack density, and a_3 the semi axis of the elliptic void (see Fig. B.2).

^eThere is a sign error in Laws' paper. The correct term, in Laws' notation, must read

$$P_{1313} = \frac{1}{16} [I_1 (L_{11}, -2(L_{11} + L_{13}), L_{11} + L_{33} + 2L_{13}) - I_2 (0, -1)].$$

B.1.2. Modeling of Fiber Degeneration

The material C/C-SiC XB is based on PAN-based carbon fibers of the type HTA40 E13 by Toho Tenax. The former product name HTA 5131 is also found in many publications. Its mechanical properties are listed in Tab. B.1. Generally, the elastic modulus $E_{f\parallel}$ in fiber direction is often given by the manufacturer. The elastic modulus $E_{f\perp}$ perpendicular to the fiber direction, and the shear modulus $G_{f\parallel\perp}$ are much harder to determine, and differ depending on the source.

Table B.1: Mechanical properties of Toho Tenax HTA40 E13.

	$E_{f\parallel}$	$E_{f\perp}$	$G_{f\parallel\perp}$	$\nu_{f\parallel\perp}$	$\nu_{\perp\perp}$
	GPa	GPa	GPa	-	-
de Kok ²⁵⁷	235	20	18	0.013	0.25
Schulte-Fischedick et al. ²⁵⁸	238	28	50	-	0.23
Green et al. ²⁵⁹	238	13	13	0.2	0.25
chosen values	238	28	18	0.013	0.25

It is known that the fibers are damaged during the pyrolysis process,²⁶⁰ and it is usually assumed that the damage does not increase further when the manufacturing process is finished. By modeling the damage as penny-shaped cracks perpendicular to the fiber direction (see Fig. B.1), Eqs. (B.6) and (B.7) deliver linear degenerations of $E_{f\parallel}$, $E_{f\perp}$, and $G_{f\parallel\perp}$, while $\nu_{f\parallel\perp}$ and $\nu_{f\perp\perp}$ remain constant.

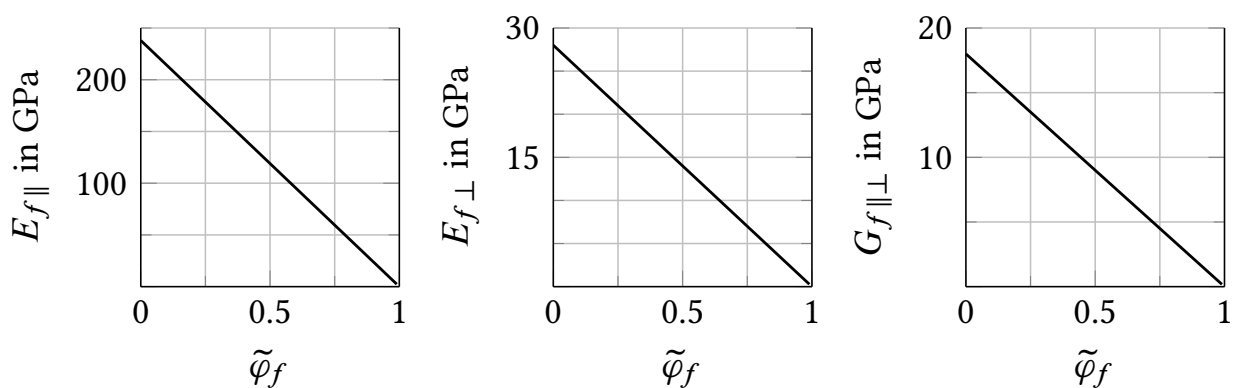


Figure B.3: Modeled degeneration of carbon fibers.

B.1.3. Modeling of Matrix Degeneration

The matrix consists of silicon carbide, as well as unreacted silicon and carbon. Mass- and volume fractions are taken from Krenkel²²⁴

Table B.2: Matrix composition of C/C-SiC XB and elastic properties of matrix components at room temperature.

			SiC	Si	C
mass fraction	ψ_m		0.636	0.124	0.240
volume fraction	φ_m		0.494	0.133	0.317
Young's modulus	E	GPa	436	166	5.66
shear modulus	G	GPa	188	68	2.16
density	ρ	kg/m^3	3220	2336	1840

The effective matrix properties can now be calculated using Eqs. (B.1) and (B.2). If the matrix is assumed to be isotropic, and spherical inclusions are assumed as illustrated in Fig. B.1, the data given in Tab. B.2 deliver the Young and shear moduli $E_m = 36$ GPa and $G_m = 13.6$ GPa for the undamaged matrix. If randomly oriented penny-shaped cracks are assumed, Eqs. (B.6) and (B.7) again deliver almost linear stiffness degenerations of E_m , and G_m in dependence of the crack density parameter $\tilde{\varphi}_m$.

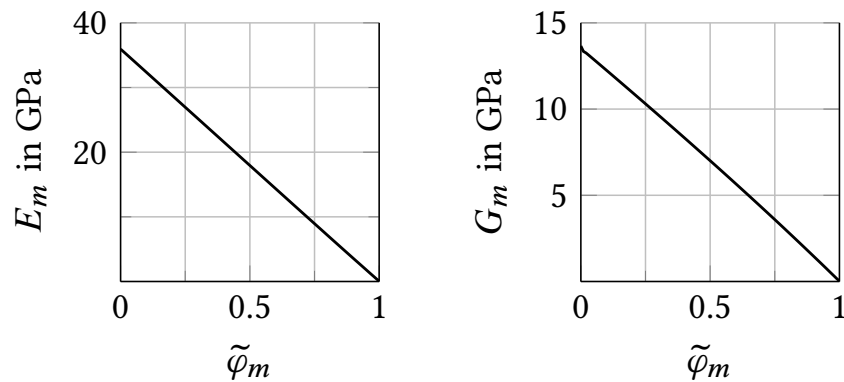


Figure B.4: Modeled degeneration of composite matrix.

B.1.4. Mechanical Properties of the Composite

The elastic properties for a $0^\circ/90^\circ$ laminate of C/C-SiC XB were calculated using the linear degeneration functions in the appendices B.1.2 and B.1.3, where the fiber volume fraction was assumed to be $\varphi_f = 0.65$.²²⁴ Two homogenization methods were used to evaluate the mechanical properties of the composite. The first method was Hill's self-consistent method from Eqs. (B.1) and (B.2), which in this context assumes perfect fiber-matrix bondings. For validation purposes, the same homogenization method was performed using the simplified mixture rules by Chamis,²⁶¹ which will not be discussed further at this point. By comparing the calculations with data from literature by Dinkler et al.,²⁴³ Hofmann et al.,²⁴⁴ and Glass et al.,²⁶² the fracture densities $\tilde{\varphi}_f = 0.38$ and $\tilde{\varphi}_m = 0.55$ were identified. The data are listed in Tab. B.3.

Table B.3: Elastic properties of C/C-SiC XB.

		Literature Data			Calculations		Chosen value
		Dinkler ²⁴³	Hofmann ²⁴⁴	Glass ²⁶²	Hill	Chamis	
E_1	GPa	60	58	60	59.57	59.49	60
E_2	GPa	60	58	60	60.57	59.49	60
E_3	GPa	30	20	20	19.31	18.01	20
G_{23}	GPa	15	6.6	8.9	8.03	8.20	8
G_{13}	GPa	15	9.06	8.8	8.03	8.20	8
G_{12}	GPa	16	5.14	8.8	9.4	9.52	9
ν_{23}		0.2	0.10	0.032	0.262	0.204	0.2
ν_{13}		0.2	0.10	0.032	0.262	0.204	0.2
ν_{12}		0.2	0.01	0.032	0.043	0.034	0.03

composite density: $\rho = 1900 \text{ kg/m}^3$

Both the self-consistent method and Chamis' simplified method approach the literature data very well. The predicted shear moduli and Poisson numbers are within the range of the literature data. On the basis of the literature data and the calculated data, a recommendation for the elastic properties is given.

The data in Tab. B.3 refer to room temperature (20°C). Although the elastic moduli E_m and G_m of the matrix slightly decrease with increasing temperature, measurements have shown that for temperatures up to 1600 K, the elastic properties are almost independent of the temperature.²⁶³ Further experiments have shown that the values for E_1 and E_2 are not constant, but degenerate due to material fatigue.²²⁷ Therefore, the data given in Tab. B.3 are to be understood as averaged values.

B.2. Tsai-Wu Failure Criterion for C/C-SiC

The *Tsai-Wu yield criterion* g can be understood as a generalized *von Mises yield criterion*, which can be applied to orthotropic materials. In Voigt-notation, it reads for the two-dimensional case²²⁶

$$g = \begin{bmatrix} \sigma_{11} \\ \sigma_{22} \\ \tau_{12} \end{bmatrix}^T \begin{bmatrix} \mathcal{F}_{1111} & \mathcal{F}_{1122} & 0 \\ \mathcal{F}_{2211} & \mathcal{F}_{2222} & 0 \\ 0 & 0 & \mathcal{F}_{1212} \end{bmatrix} \begin{bmatrix} \sigma_{11} \\ \sigma_{22} \\ \tau_{12} \end{bmatrix} + \begin{bmatrix} f_{11} \\ f_{22} \\ 0 \end{bmatrix}^T \begin{bmatrix} \sigma_{11} \\ \sigma_{22} \\ \tau_{12} \end{bmatrix} \stackrel{!}{<} 1. \quad (\text{B.8})$$

with the parameters

$$\mathcal{F}_{1111} = \frac{1}{X_t X_c}, \quad (\text{B.9}) \quad \text{and} \quad \mathcal{F}_{2222} = \frac{1}{Y_t Y_c}, \quad (\text{B.10})$$

where X_t and Y_t are the uniaxial yield stresses against tension, and X_c and Y_c are the uniaxial yield stresses against compression. The shear parameter

$$\mathcal{F}_{1212} = \frac{1}{S^2} \quad (\text{B.11})$$

depends on the maximal shear stress S . Fink explained in detail the difficulty of measuring the coupling term \mathcal{F}_{1122} .²⁶⁰ For preliminary calculations, the value $\mathcal{F}_{1122} = \mathcal{F}_{2211}$ can be assumed as zero.²⁶⁴ The remaining parameters read

$$f_{11} = \frac{1}{X_t} - \frac{1}{X_c}, \quad (\text{B.12}) \quad \text{and} \quad f_{22} = \frac{1}{Y_t} - \frac{1}{Y_c}. \quad (\text{B.13})$$

Values for X_t , X_c and S can be taken from literature. If the plane of the laminate is considered, it is $Y_t = X_t$ and $Y_c = X_c$.

If the considered plane is perpendicular to one fiber direction and perpendicular to the plane of the laminate, values for Y_t and Y_c can be estimated as follows:

If σ is the stress of the composite, the matrix stress σ^m can be estimated as²²⁸

$$\sigma_{ij}^m = \mathcal{B}_{ijkl}^m \sigma_{kl}, \quad (\text{B.14})$$

where the compliance influence \mathcal{B}^m is determined by the rule

$$\mathcal{B}_{ijkl}^m = C_{ijmn}^m \mathcal{A}_{mnpq}^m \tilde{\mathcal{M}}_{pqkl}. \quad (\text{B.15})$$

Herein, \mathcal{A}^m is the influence tensor of the matrix, which reads

$$\mathcal{A}_{ijkl}^m = \frac{1}{\varphi^m} \left[\mathcal{I}_{ijkl} - \varphi^r \mathcal{A}_{ijkl}^r \right], \quad (\text{B.16})$$

and $\tilde{\mathcal{M}}$ is the compliance tensor of the composite

$$\mathcal{I}_{ijkl} = \tilde{\mathcal{C}}_{ijmn} \tilde{\mathcal{M}}_{mnkl}. \quad (\text{B.17})$$

One can now numerically reproduce an uniaxial tension test by setting $\sigma_{11} = X_t$ and estimate the matrix stress σ^m over Eq. (B.14). Since the fibers do not carry any load perpendicular to the plane of the laminate, the resulting von Mises stress of the matrix provides a good first estimation for Y_t . In the same way, a compression test can be recreated by setting $\sigma_{11} = X_c$, and a value for Y_c can be estimated. The values are listed in Tab. B.4.

Table B.4: Tsai-Wu parameters for C/C-SiC XB.

			source
X_t	MPa	80	Krenkel ²⁶⁵
X_c	MPa	250	Fink ²⁶⁰
Y_t	MPa	20	<i>this work</i>
Y_c	MPa	60	<i>this work</i>
S	MPa	28	Krenkel ²⁶⁵

B.3. Thermal Conductivity of C/C-SiC

Experimental data for the thermal conductivity of C/C-SiC XB have been published by Krenkel.²⁶⁵ The data are plotted in Fig. B.5. It is assumed that the thermal conductivity is not affected by mechanical material fatigue.

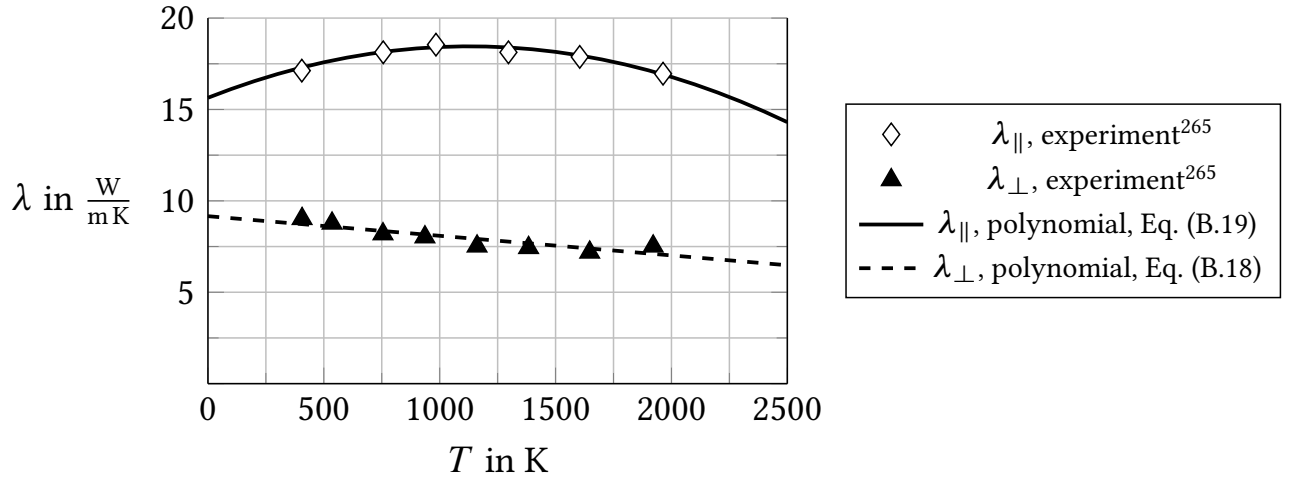


Figure B.5: Thermal conductivity of C/C-SiC and polynomial.

The data were fitted with two polynomials

$$\lambda_{\parallel} = \left(\frac{\text{W}}{\text{mK}}\right) \sum_{i=0}^2 a_i \left(\frac{T}{\text{K}}\right)^i, \quad (\text{B.18}) \quad \text{and} \quad \lambda_{\perp} = \left(\frac{\text{W}}{\text{mK}}\right) \sum_{i=0}^1 b_i \left(\frac{T}{\text{K}}\right)^i, \quad (\text{B.19})$$

where the polynomial coefficients are given in Tab. B.5.

Table B.5: Polynomial coefficients for the thermal conductivity of C/C-SiC.

a_0	$-2.2075 \cdot 10^{-6}$	b_0	$-1.0737 \cdot 10^{-3}$
a_1	$4.9853 \cdot 10^{-3}$	b_1	$9.1618 \cdot 10^0$
a_2	$1.5640 \cdot 10^1$		

B.4. Specific Heat Capacity of C/C-SiC

The specific heat capacity of a C/C-SiC material very similar to the XB type has been published by Brandt et al,²⁶⁶ for a range between 500 K and 1000 K (see Fig. B.6).

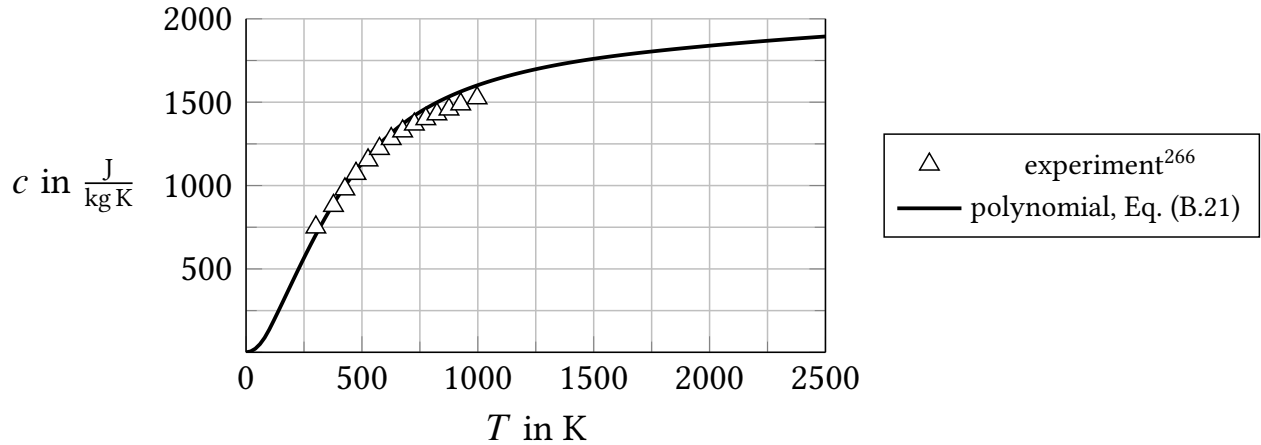


Figure B.6: Experimental data for the specific heat of C/C-SiC and polynomial.

Since the specific heat capacity of a composite can be mass averaged from the specific heat capacities of the components, so that

$$c = \sum_r \psi_r c_r, \quad (\text{B.20})$$

a smooth polynomial for the range between 0 K and 2500 K was created using the *JANAF thermochemical tables* database⁹⁷

$$c = \begin{cases} \left(\frac{\text{J}}{\text{kgK}}\right) \sum_{i=0}^{10} c_i \left(\frac{T}{\text{K}}\right)^i & \text{if } T > 100 \text{ K,} \\ \left(\frac{\text{J}}{\text{kgK}}\right) \sum_{i=2}^3 d_i \left(\frac{T}{\text{K}}\right)^i & \text{else.} \end{cases} \quad (\text{B.21})$$

The coefficients for c are listed in Tab. B.6.

Table B.6: Polynomial coefficients for the specific heat capacity of C/C-SiC.

c_0	$-8.8072 \cdot 10^1$	c_7	$-7.1361 \cdot 10^{-18}$
c_1	$1.5400 \cdot 10^0$	c_8	$1.6001 \cdot 10^{-21}$
c_2	$9.6423 \cdot 10^{-3}$	c_9	$-2.0511 \cdot 10^{-25}$
c_3	$-2.9997 \cdot 10^{-5}$	c_{10}	$1.1472 \cdot 10^{-29}$
c_4	$4.2648 \cdot 10^{-8}$		
c_5	$-3.6419 \cdot 10^{-11}$	d_2	$1.3662 \cdot 10^{-2}$
c_6	$2.0006 \cdot 10^{-14}$	d_3	$-3.4449 \cdot 10^{-7}$

B.5. Thermal Expansion of C/C-SiC

Experimental data for the thermal expansion of C/C-SiC XB have been given by Krenkel²⁶⁵ (see Fig. B.7).

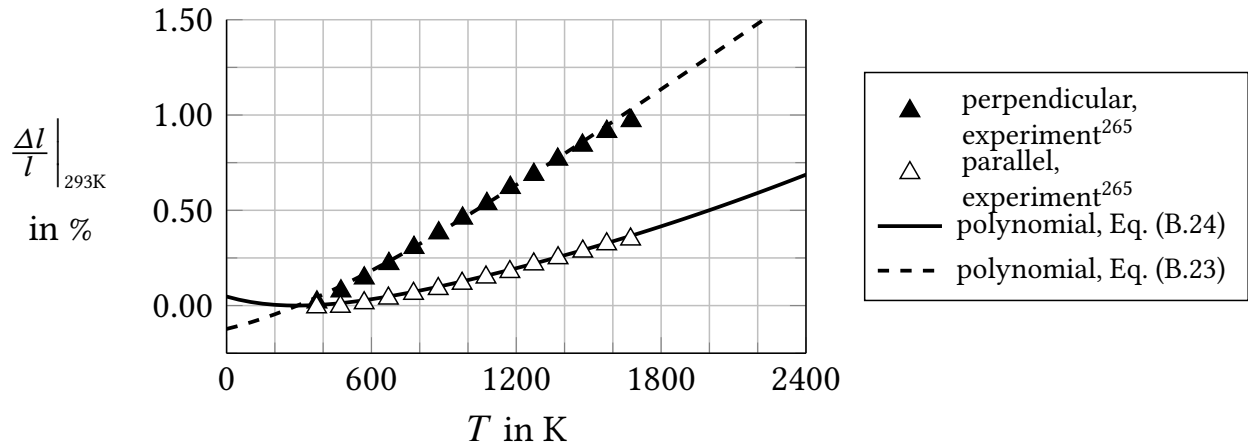


Figure B.7: Experimental data and polynomials for α of C/C-SiC.

The thermal expansion is defined over the tangent expansion coefficient α , so that

$$\frac{\Delta l}{l} = \exp \left(\int_{T_0}^T \alpha \, dT \right) - 1. \quad (\text{B.22})$$

Two polynomials of the shape

$$\alpha_{\parallel} = \left(\frac{1}{\text{K}} \right) \sum_{i=0}^5 f_i \left(\frac{T}{\text{K}} \right)^i \quad (\text{B.23}) \quad \text{and} \quad \alpha_{\perp} = \left(\frac{1}{\text{K}} \right) \sum_{i=0}^4 g_i \left(\frac{T}{\text{K}} \right)^i \quad (\text{B.24})$$

were created, where the coefficients are given in Tab. B.7. According to the data given by Krenkel, α_{\parallel} becomes negative below approximately 300 K.

Table B.7: Polynomial coefficients for thermal expansion of C/C-SiC.

f_0	$-3.6667 \cdot 10^{-6}$	g_0	$3.0497 \cdot 10^{-6}$
f_1	$1.7128 \cdot 10^{-8}$	g_1	$8.7556 \cdot 10^{-9}$
f_2	$-1.8260 \cdot 10^{-11}$	g_2	$-5.4979 \cdot 10^{-12}$
f_3	$1.0238 \cdot 10^{-14}$	g_3	$1.6171 \cdot 10^{-15}$
f_4	$-2.7798 \cdot 10^{-18}$	g_4	$-1.8885 \cdot 10^{-19}$
f_5	$2.9304 \cdot 10^{-22}$		

C. Caloric and Transport Properties of Dry Air

The Gordon-McBride database is one of the most complete databases for caloric properties c_p and h , and transport properties μ and λ of various gases.

For quick on-hand calculations considering dry air, however, it is feasible to have the functions, which model the caloric properties and transport properties, directly available. For that purpose, these functions are given in this section.

C.1. Caloric Properties of Dry Air

The polynomials for the specific heat capacity c_p° , the specific enthalpy h° and entropy s° at reference pressure $p^\circ = 1$ bar are calculated from the NASA CEA database^{98,99}

$$\frac{c_p^\circ}{R} = \frac{a_1}{T^2} + \frac{a_2}{T} + a_3 + a_4 T + a_5 T^2 + a_6 T^3 + a_7 T^4, \quad (\text{C.1})$$

$$\frac{h^\circ}{R} = -\frac{a_1}{T} + a_2 \ln T + a_3 T + a_4 \frac{T^2}{2} + a_5 \frac{T^3}{3} + a_6 \frac{T^4}{4} + a_7 \frac{T^5}{5} + b_1, \quad (\text{C.2})$$

$$\frac{s^\circ}{R} = -\frac{a_1}{2T^2} - \frac{a_2}{T} + a_3 \ln T + a_4 T + a_5 \frac{T^2}{2} + a_6 \frac{T^3}{3} + a_7 \frac{T^4}{4} + b_2. \quad (\text{C.3})$$

where R is the specific gas constant. Units are J, kg and K . The polynomial is split into two intervals, the constants are given in Tab. C.1.

Table C.1: Polynomial coefficients for the specific heat capacity, Eq. (C.1) specific enthalpy Eq. (C.2) and entropy Eq. (C.3) of dry air.

200 K $\leq T \leq$ 1000 K		1000 K $< T \leq$ 6000 K	
a_1	$1.0099 \cdot 10^4$	a_1	$2.4122 \cdot 10^5$
a_2	$-1.9681 \cdot 10^2$	a_2	$-1.2571 \cdot 10^3$
a_3	$5.0091 \cdot 10^0$	a_3	$5.1438 \cdot 10^0$
a_4	$-5.7607 \cdot 10^{-3}$	a_4	$-2.1356 \cdot 10^{-4}$
a_5	$1.0668 \cdot 10^{-5}$	a_5	$7.0620 \cdot 10^{-8}$
a_6	$-7.9400 \cdot 10^{-9}$	a_6	$-1.0717 \cdot 10^{-11}$
a_7	$2.1852 \cdot 10^{-12}$	a_7	$6.5820 \cdot 10^{-16}$
b_1	$-1.7651 \cdot 10^2$	b_1	$6.4574 \cdot 10^3$
b_2	$-4.4879 \cdot 10^0$	b_2	$-8.7089 \cdot 10^0$

C.2. Transport Properties of Dry Air

For preliminary estimations of the dynamic shear viscosity μ of dry air, Sutherland's correlation²⁶⁷

$$\mu = \mu_0 \left(\frac{T}{T_0} \right)^{\frac{3}{2}} \frac{T_0 + C_\mu}{T + C_\mu}, \quad (\text{C.4})$$

which is deduced from gaskinetic considerations, is often used. A corresponding correlation for the thermal conductivity λ of dry air was given by Hansen²⁶⁸

$$\lambda = \lambda_0 \left(\frac{T}{T_0} \right)^{\frac{3}{2}} \frac{T_0 + C_\lambda}{T + C_\lambda}, \quad (\text{C.5})$$

where the constants C_μ and C_λ are given in Tab. C.2. When compared to the Gordon-McBride database however, Sutherland's correlation underestimates μ between 5% and 10%. Hansen's correlation for λ is even 15% to 25% off. Within this work, new values for C_μ and C_λ have been determined by performing a genetic approximation of data given by the Gordon-McBride database. By using the new parameters, within the interval $300 \text{ K} \leq T \leq 2000 \text{ K}$, the dynamic viscosity μ is approximated with 2 % accuracy, the thermal conductivity λ is about 5 % exact.

Table C.2: Calibration parameters for the Sutherland and Hansen correlations.

		original value ^{267, 268}	recommended value
T_0	K	273.15	398.15
C_μ	K	110.40	164.52
C_λ	K	112.00	281.05
μ_0	$\text{Pa} \cdot 10^6$	17.16	22.88
λ_0	$\text{W}/(\text{mK}) \cdot 10^3$	23.36	32.36

D. Inlet Design Methodology

A two-dimensional double ramp configuration with a blunted nose and rounded corners is considered. The geometry parameters of this configuration are illustrated in Fig. 5.1.

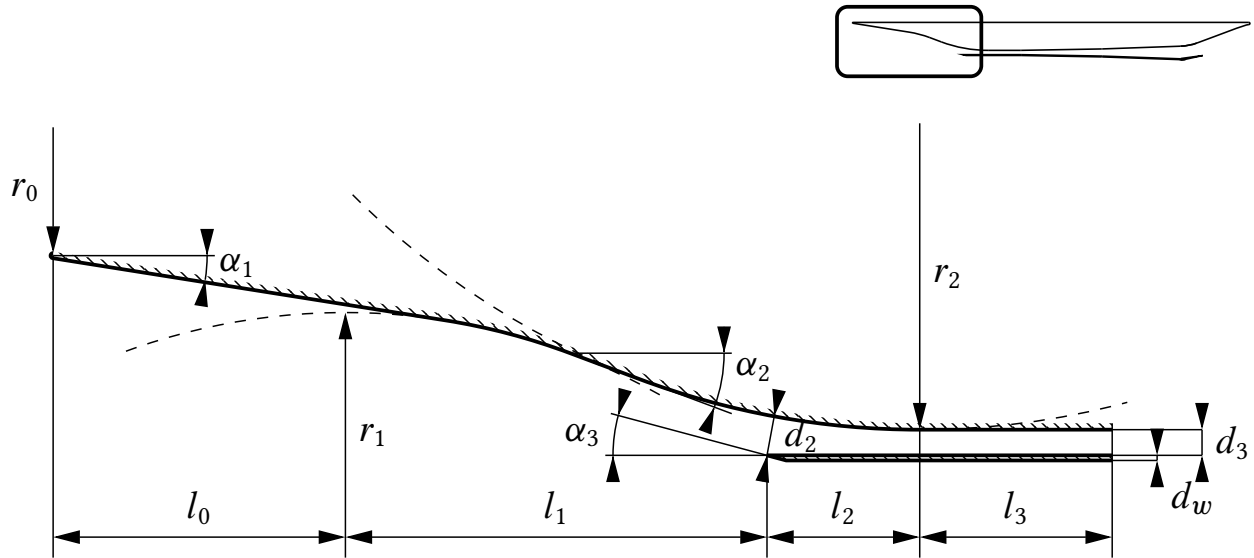


Figure 5.1: Variables for the inlet geometry.

The most important design parameters are the two ramp angles α_1 and α_2 . The choice of the angles depends on the cruising speed and flight altitude. Using a trial and error approach, the angles can initially be estimated using Anderson's method of characteristics,²⁶⁹ which performs an inviscid simulation of both the external and internal flow field. Final adjustments can be made during various Reynolds averaged Navier Stokes simulations. This approach was used and experimentally verified by Häberle and Gülhan¹⁸¹ to design a sharp-edged configuration. The present configuration is based on Häberle's sharp-edged design.

Next, the internal duct height d_3 needs to be determined. In the present case, it was chosen to meet the size of the experimental scramjet combustor at the Institute of Aerospace Thermodynamics (ITLR) of University of Stuttgart. Analytical investigations of the flow state at the stagnation point reveal that the heat load at the stagnation point is reciprocal to the square root of the nose radius r_0 .²⁰⁶ Blunting the nose however decreases the inlet performance and increases the risk of unstarting. The curved bowshock induces an overpressurization in the boundary layer which alters capture and transition behavior of the flow field.

This entropy layer has for example been mentioned by van Wie.¹⁸⁵ To prevent a boundary layer separation at the kink between the first and the second ramp, the corner can be rounded. In a similar way, the size of the separation bubble at the duct can be influenced by the radius r_2 . In the present configuration, these radii have been chosen on a trial and error based approach.

Once the two angles α_1 and α_2 , the duct height d_3 and the three radii r_0 , r_1 and r_2 are chosen, the inviscid shock system along the structure has to be modeled to find the remaining parameters that define the geometry. In an intermediate step, a sharp-edged configuration as illustrated in Fig. D.2 is considered. Using the oblique shock equations, the Mach numbers Ma_1 and Ma_2 downstream from the bow shock, as well as the shock angles β_1 and β_2 can be determined.

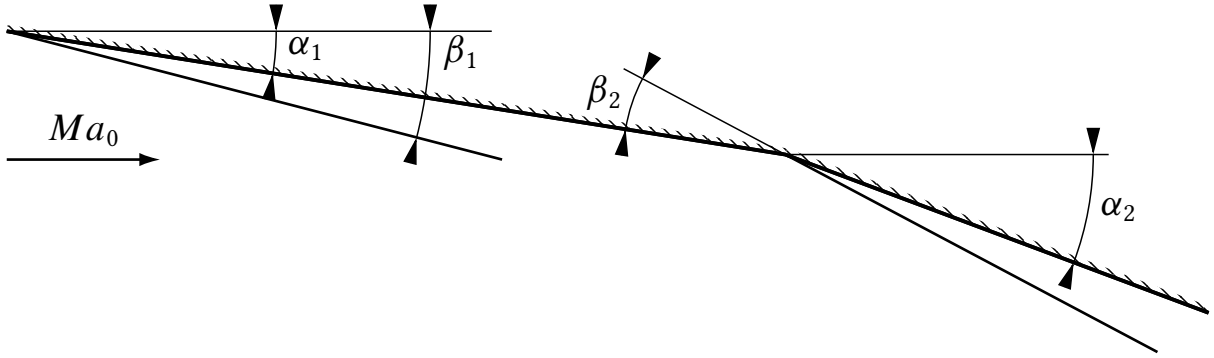


Figure D.2: Sharp-edged external shock system.

Having determined the shock angle β_1 , the shape of the curved shock along the blunted ramp, see Fig. D.4, can be estimated using a correlation provided by Bilig²⁷⁰

$$y \approx -\frac{\sqrt{(\Delta + r_0 + x) (2 r_c (\cot \beta_1)^2 + \Delta + r_0 + x)}}{\cot \beta_1}, \quad (\text{D.1})$$

where Δ is the shock standoff distance²⁷¹

$$\frac{\Delta}{r_0} \approx 0.386 \exp\left(\frac{4.67}{Ma_0^2}\right), \quad (\text{D.2})$$

and r_c is the vertex radius of curvature²⁷⁰

$$\frac{r_c}{r_0} \approx 1.386 \exp\left(\frac{1.8}{(Ma_0 - 1)^{\frac{3}{4}}}\right). \quad (\text{D.3})$$

The coordinate system was chosen to originate in the center of the circle that describes the shape of the blunted nose. The resulting shock shape is illustrated in Fig. D.3. The curved shock, which is approximated using Eq. (D.1), gradually merges into an oblique shock with the shock angle β_1 .

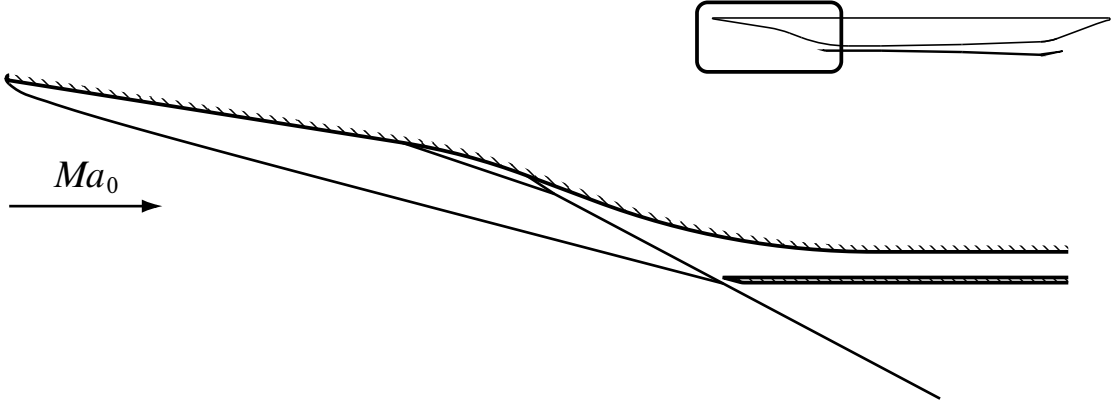


Figure D.3: Inviscid blunt edged external shock system.

If the shock shape of the uninclined side is needed as well, a correlation^f from Lukasiewicz²⁰³ can be used, which is valid for $\gamma = 1.4$

$$y \approx \frac{1.54 r_0 C_d Ma_0^2}{Ma_0^2 \left(\frac{2r_0 C_d}{x+r_0} \right)^{\frac{2}{3}} - 1.09} + r_0, \quad (\text{D.4})$$

where $C_d \approx 1.4$ is the drag coefficient of a corresponding cylinder in crossflow. Generally, internal compression in the duct is desired. The internal compression ratio

$$C_r = \frac{d_2}{d_3} \quad (\text{D.5})$$

must be small enough to keep the internal Mach numbers supersonic. As an estimation for an appropriate compression ratio, a criterion by Oswatitsch,²⁷² and Kantrowitz and Donaldson²⁷³ can be used

$$C_r \approx \left[\frac{2\gamma}{\gamma+1} - \frac{\gamma-1}{(\gamma+1)Ma_2^2} \right]^{\frac{1}{1-\gamma}} \left[\frac{\gamma-1}{\gamma+1} + \frac{2}{(\gamma+1)Ma_2^2} \right]^{-\frac{1}{2}}, \quad (\text{D.6})$$

where γ is the ratio of specific heats.

^f the correlations Eq. (D.4) and Eq. (D.1) were modified to be consistent with the coordinate system in Fig. D.4

The distance l_2 between the top of the lip and the center of the second circle must be chosen so that the entry height h_2 of the duct fulfills Eq. (D.6). The distance $l_1 + l_2$ between the two circles must be chosen so that the second shock closely passes the lip. The angle α_3 at the tip of the lip must be chosen so that no oblique shock is generated at the lip

$$\alpha_3 < \alpha_1 + \beta_2. \quad (\text{D.7})$$

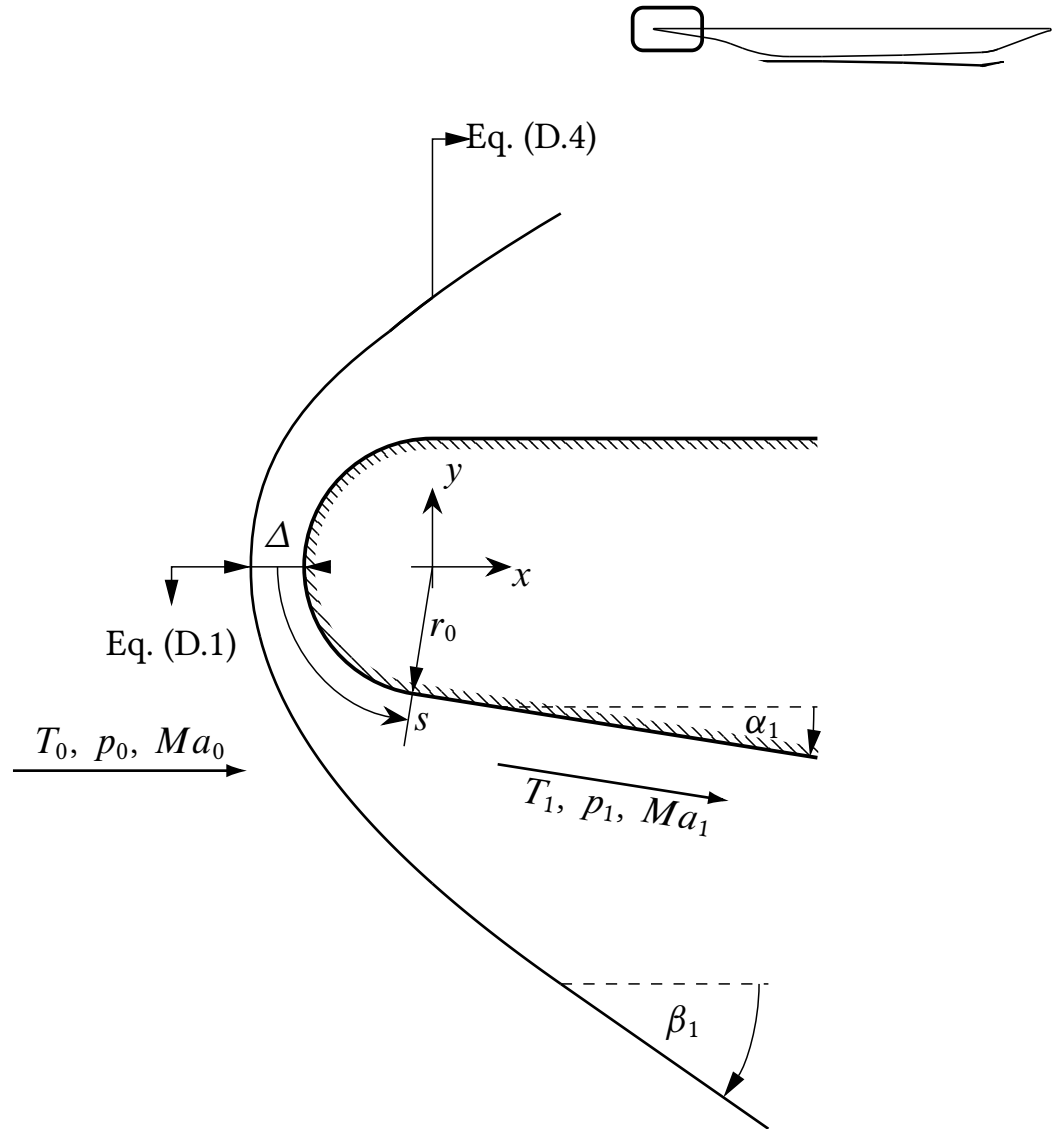


Figure D.4: Shock system around a blunted edge.

Having determined the length scales l_1 and l_2 , the horizontal distance l_0 between the center of the nose circle and the circle of the kink can be evaluated. Finally, the vertical position of the center of the kink's circle is determined. For special reasons, latter is not drawn in Fig. 5.1.

The first of two conditions which determine these two unknowns is, that for continuity reasons, the first ramp must touch the first circle. The second condition is that the first and the second shock must intersect closely above the tip of the lip to minimize the spillage. The isolator length l_3 needs to be chosen so that the inlet flow is not disturbed by boundary layer separations induced in the combustor. These subsonic boundary layer separations are forced upstream by the pressure rise caused by the combustion. In the worst case scenario, these local boundary layer separations grow upstream until they connect with the separation bubble at the duct and unstart the inlet. Determining an isolator length cannot be done without knowledge of the flow field in the combustion chamber. For the estimation of l_3 , there is a frequently quoted empirical relation by Waltrup and Billig²⁷⁴ reading

$$\frac{l_3}{d_3} \approx \frac{\sqrt{\frac{\theta}{d_3}}}{\sqrt[4]{Re_\theta}} \frac{50 \left(\frac{p_c}{p_{2.1}} - 1 \right) + 170 \left(\frac{p_c}{p_{2.1}} - 1 \right)^2}{Ma_{2.1}^2 - 1}, \quad (\text{D.8})$$

where $p_{2.1}$ and $Ma_{2.1}$ are pressure and Mach number above the midpoint of the second circle, p_c the maximal pressure in the combustion chamber, and θ the momentum thickness of the boundary layer. If the effects of the entropy layer, which is induced by the curved shock at the blunted edge is neglected, the momentum thickness θ at the hull side of the internal flow field can be estimated using a correlation from literature.²⁷⁵ As the maximal pressure p_c within the combustor needs to be known, l_3 must be determined iteratively. Since Eq. (D.8) has been calibrated against experimental data for axisymmetric flows, it only provides a rough estimation for the optimal isolator length l_3 for the present configuration. Assuming a maximal combustor pressure of $p_c \approx 130\,000$ Pa and a momentum thickness of $\theta \approx 2.5$ mm, Eq. (D.8) delivers an isolator length of $l_3 \approx 300$ mm. The chosen geometry parameters as well as approximate values for l_0 to l_3 are listed in Tab. 5.1

E. Hydrogen–Air Combustion Mechanism

This reaction scheme is based on Jachimowski's 33-reaction scheme for scramjet combustion.^{276,277} This is the reduced form as given by Gerlinger et al.¹⁶⁰ It is validated for hypersonic flight with $Ma_0 < 12$, and was used by Scheuermann²⁷⁸ and Rabadán Santana.²¹⁰ Units are seconds, moles, cubic centimeters, calories, and Kelvin.

See also Eqs. (3.4ff).

Table E.1: Hydrogen–Air Reaction Scheme

j	Reaction j	\tilde{A}_j	\tilde{n}_j	\tilde{E}_j
(1)	$\text{O}_2 + \text{H}_2 \rightleftharpoons \text{H} + \text{HO}_2$	1.0×10^{14}	0.0	56000
(2)	$\text{O}_2 + \text{H} \rightleftharpoons \text{O} + \text{OH}$	2.6×10^{14}	0.0	16800
(3)	$\text{O} + \text{H}_2 \rightleftharpoons \text{OH} + \text{H}$	1.8×10^{10}	1.0	8900
(4)	$\text{OH} + \text{H}_2 \rightleftharpoons \text{H} + \text{H}_2\text{O}$	2.2×10^{13}	0.0	5150
(5)	$2 \text{OH} \rightleftharpoons \text{O} + \text{H}_2\text{O}$	6.3×10^{12}	0.0	1090
(6)	$\text{OH} + \text{H} \rightleftharpoons \text{H}_2\text{O} + \text{M}$	2.2×10^{22}	-2.0	0
(7)	$2 \text{H} \rightleftharpoons \text{H}_2 + \text{M}$	6.4×10^{17}	-1.0	0
(8)	$\text{O} + \text{H} \rightleftharpoons \text{OH} + \text{M}$	6.0×10^{16}	-0.6	0
(9)	$\text{O}_2 + \text{H} \rightleftharpoons \text{HO}_2 + \text{M}$	2.1×10^{15}	0.0	-1000
(10)	$\text{H} + \text{HO}_2 \rightleftharpoons 2 \text{OH}$	1.4×10^{14}	0.0	1080
(11)	$\text{H} + \text{HO}_2 \rightleftharpoons \text{O} + \text{H}_2\text{O}$	1.0×10^{13}	0.0	1080
(12)	$\text{O} + \text{HO}_2 \rightleftharpoons \text{O}_2 + \text{OH}$	1.5×10^{13}	0.0	950
(13)	$\text{OH} + \text{HO}_2 \rightleftharpoons \text{O}_2 + \text{H}_2\text{O}$	8.0×10^{12}	0.0	0
(14)	$2 \text{HO}_2 \rightleftharpoons \text{O}_2 + \text{H}_2\text{O}_2$	2.0×10^{12}	0.0	0
(15)	$\text{H} + \text{H}_2\text{O}_2 \rightleftharpoons \text{H}_2 + \text{HO}_2$	1.4×10^{12}	0.0	3600
(16)	$\text{O} + \text{H}_2\text{O}_2 \rightleftharpoons \text{OH} + \text{HO}_2$	1.4×10^{13}	0.0	6400
(17)	$\text{OH} + \text{H}_2\text{O}_2 \rightleftharpoons \text{H}_2\text{O} + \text{HO}_2$	6.1×10^{12}	0.0	1430
(18)	$\text{H}_2\text{O}_2 \rightleftharpoons 2 \text{OH} + \text{M}$	1.2×10^{17}	0.0	45500
(19)	$2 \text{O} \rightleftharpoons \text{O}_2 + \text{M}$	6.0×10^{13}	0.0	-1800

Bibliography

- ¹ “Aircraft Propulsion System Performance Station Designation,” Tech. Rep. AS755F, Society of Automotive Engineers, Warrendale, PA, 2014.
- ² “U.S. Standard Atmosphere,” Tech. Rep. NASA-TM-X-74335, National Aeronautics and Space Administration, National Oceanic and Atmospheric Administration, United States Department of the Air Force, Washington, DC, Oct. 1976.
- ³ Heiser, W. H. and Pratt, D. T., *Hypersonic Airbreathing Propulsion*, AIAA Education Series, American Institute of Aeronautics and Astronautics, Washington, DC, 1994.
- ⁴ Krehl, P., *Handbook of Shock Waves, Three Volume Set*, Vol. 1, chap. History of Shock Waves, Academic Press, San Diego, CA, 1st ed., 2000, pp. 1–142.
- ⁵ Sänger, E. and Bredt, I., “Über einen Raketenantrieb für Fernbomber,” Tech. Rep. UM 3538, Deutsche Luftfahrtforschung, Aug. 1944.
- ⁶ Jenkins, D. R., Landis, T., and Miller, J., “America X-Vehicles,” Tech. Rep. Monographs in Aerospace History, No. 31, SP-2003-4531, National Aeronautics and Space Administration, Washington, DC, June 2003.
- ⁷ Curran, E. T., “Scramjet Engines: The First Forty Years,” *Journal of Propulsion and Power*, Vol. 17, No. 6, pp. 1138–1148, Nov. 2001, doi: 10.2514/2.5875.
- ⁸ Czysz, P. A. and Bruno, C., *Future Spacecraft Propulsion Systems*, Springer Verlag, Berlin Heidelberg, Germany, 2nd ed., 2009.
- ⁹ Heppenheimer, T. A., *Facing the Heat Barrier: A History of Hypersonics*, No. NASA SP-2007-4232 in NASA History Series, National Aeronautics and Space Administration, Washington, DC, 2007.
- ¹⁰ Gouskov, O., Kopchenov, V., Lomkov, K., Roudakov, A., and Semenov, V., “CFD in the Preparation and Data Processing of Scramjet Testing on Hypersonic Flight Beds,” *7th AIAA International Space Plane and Hypersonic Systems and Technology Conference, Norfolk VA*, American Institute of Aeronautics and Astronautics, Norfolk, VA, 1996, doi: 10.2514/6.1996-4562.
- ¹¹ Voland, R., Auslender, A., Smart, M., Roudakov, A., Semenov, V., and Kopchenov, V., “CIAM/NASA Mach 6.5 Scramjet Flight and Ground Test,” *9th International Space Planes and Hypersonic Systems and Technologies Conference*, American Institute of Aeronautics and Astronautics, Norfolk, VA, 1999, doi: 10.2514/6.1999-4848.

- ¹² Serre, L. and Falempin, F., “Promethee - The French Military Hypersonic Propulsion Program,” *12th AIAA International Space Planes and Hypersonic Systems and Technologies*, American Institute of Aeronautics and Astronautics, Norfolk, VA, 2002, doi: 10.2514/6.2003-6950.
- ¹³ Peebles, C., *Eleven Seconds into the Unknown - A History of the Hyper-X Program*, American Institute of Aeronautics and Astronautics, Washington, DC, 2011.
- ¹⁴ Hass, N. E., “Flight Data Analysis of the HYSHOT Flight #2 Scramjet,” , pp. 1–17, Sept. 2005.
- ¹⁵ Rondeau, M. C. M. and Timothy R Jorris, “X-51A Scramjet Demonstrator Program: Waverider Ground and Flight Test,” *SFTE th International SETP Southwest Flight Test Symposium*, Fort Worth, TX, Oct. 2013.
- ¹⁶ Falempin, F. and Serre, L., “French Flight Testing Program LEA - Status in 2011,” *17th AIAA International Space Planes and Hypersonic Systems and Technologies Conference*, American Institute of Aeronautics and Astronautics, San Francisco, CA, April 2011, doi: 10.2514/6.2011-2200.
- ¹⁷ Bissinger, N., Koschel, W., Sacher, P. W., and Walther, R., “Scramjet Investigations within the German Hypersonics Technology Program (1993-1996),” *Scramjet Propulsion*, edited by E. T. Curran and S. N. B. Murthy, American Institute of Aeronautics and Astronautics, Reston ,VA, 2000, pp. 119–158.
- ¹⁸ Janovsky, R., Wienss, W., and Kovaltschuk, V., “The Hypersonic Technology Demonstrator D2,” *8th AIAA International Space Planes and Hypersonic Systems and Technologies Conference*, American Institute of Aeronautics and Astronautics, Norfolk, VA, April 1998, doi: 10.2514/6.1998-1645.
- ¹⁹ Jacob, D., Sachs, G., and Wagner, S., editors, *Basic Research and Technologies for Two-Stage-to-Orbit Vehicles: Final Report of the Collaborative Research Centres 253, 255 and 259*, Sonderforschungsberichte der Deutschen Forschung, John Wiley and Sons, Inc., Weinheim, Germany, 2006.
- ²⁰ Weigand, B. and Gaisbauer, U., “An Overview on the Structure and Work of the DFG Research Training Group GRK 1095: Aero-Thermodynamic Design of a Scramjet Propulsion System,” *16th AIAA/DLR/DGLR International Space Planes and Hypersonic Systems and Technologies Conference*, American Institute of Aeronautics and Astronautics, Bremen, Germany, Oct. 2009, doi: 10.2514/6.2009-7276.

- 21 Püttmann, N. and Longo, J., “The Flight of SHEFEX,” *57th International Astronautical Congress*, American Institute of Aeronautics and Astronautics, Valencia, Spain, Aug. 2006, doi: 10.2514/6.IAC-06-D2.6.01.
- 22 Gülhan, A., Neeb, D., Thiele, T., and Siebe, F., “Aerothermal Postflight Analysis of the Sharp Edge Flight Experiment-II,” *Journal of Spacecraft and Rockets*, pp. 1–25, Dec. 2015, doi: 10.2514/1.A33275.
- 23 Böhrk, H., “Transpiration-Cooled Hypersonic Flight Experiment: Setup, Flight Measurement, and Reconstruction,” *Journal of Spacecraft and Rockets*, Vol. 52, No. 3, pp. 674–683, May 2015, doi: 10.2514/1.A33144.
- 24 Weihs, H., “Sounding Rockets for Entry Research: SHEFEX Flight Test Program,” *Proceedings of the 21st ESA Symposium on Rocket and Balloon Programmes*, Thun, Switzerland, June 2013, pp. 143–152.
- 25 Bowcutt, K., Paull, A., Dolvin, D., and Smart, M., “HIFiRE: An International Collaboration to Advance the Science and Technology of Hypersonic Flight,” *28th International Congress of the Aeronautical Sciences*, Brisbane, Australia, Sept. 2012.
- 26 Glass, D. E., Capriotti, D. P., Reimer, T., Kütemeyer, M., and Smart, M., “Testing of DLR C/C-SiC for HIFiRE 8 Scramjet Combustor,” *7th European Workshop on Thermal Protection Systems and Hot Structures*, 8.-10. April 2013, ESA/ESTEC, Noordwijk, The Netherlands, April 2013.
- 27 Smart, M., “Sustained Hypersonic Flight – It’s harder than Rocket Science,” *Ultra-High Temperature Ceramics: Materials for Extreme Environment Applications III*, edited by G. Franks and C. Tallon, ECI Symposium Series, University of Melbourne, Australia, 2015.
- 28 Rolim, T. C., Toro, P. G. d. P., Minucci, M. A. S., Oliveira, A. d. C. d., and Follador, R. d. C., “Experimental Results of a Mach 10 Conical-Flow Derived Waverider to 14-X Hypersonic Airspace Vehicle,” *Journal of Aerospace Technology and Management*, Vol. 3, No. 2, pp. 127–136, 2011, doi: 10.5028/jatm.2011.03027510.
- 29 de Lima Cardoso, R. and de Paula Toro, P. G., “Brazilian 14-XS Hypersonic Scramjet Aerospace Vehicle: Dimensional Design at Mach Number 7,” *22nd International Congress of Mechanical Engineering*, Nov. 2013, pp. 1787–1795.
- 30 Thomalla, V. K., “Volle Kraft Voraus,” *Flug Revue*, Vol. 61, No. 1, pp. 36–41, 2016.
- 31 Harrington, J. and Barnstorff, K., “NASA Invests in Future of Aviation with Supersonic Research Projects,” press release, July 2015.

- ³² Prampolini, M. and Coraboeuf, Y., "Ultra-Rapid Air Vehicle and Related Method for Aerial Locomotion," July 14 2015, US Patent 9,079,661.
- ³³ Steinke, S., "Der Hyperschalltraum," *Flug Revue*, Vol. 60, No. 10, pp. 30–32, October 2015.
- ³⁴ Smith, T. and Bowcutt, K., "First and Second Stage Aircraft Coupled in Tandem," Feb. 17 2015, US Patent 8,955,791.
- ³⁵ Button, K., "Making a Money Saver," *Aerospace America*, Vol. 54, No. 6, pp. 16–19, June 2016.
- ³⁶ Varvill, R. and Bond, A., "The SKYLON Spaceplane - Progress to Realisation," *Journal of the British Interplanetary Society*, Vol. 61, pp. 412–418, Aug. 2008.
- ³⁷ Schechter, E., "Going Hypersonic," *Aerospace America*, Vol. 52, No. 7-8, pp. 10–12, July-August 2014.
- ³⁸ Erdos, J., "Skeptical about the SABRE engine," *Aerospace America*, Vol. 52, No. 9, pp. 3, September 2014.
- ³⁹ Button, K., "Will Skylon fly?" *Aerospace America*, Vol. 54, No. 3, pp. 8–11, March 2016.
- ⁴⁰ Schwarz, K., "Hyperschall-Studie "SR-72"," *Flug Revue*, Vol. 59, No. 1, pp. 51, Januar 2014.
- ⁴¹ Peck, M., "Über Drones," *Aerospace America*, Vol. 54, No. 5, pp. 16–22, May 2016.
- ⁴² Nagappa, R., "Going too fast: Time to ban hypersonic missile tests?: An Indian response," *Bulletin of the Atomic Scientists*, Vol. 71, No. 5, pp. 9–12, Sept. 2015, doi: 10.1177/0096340215599773.
- ⁴³ Mehta, U. B. and Bowles, J. V., "Two-Stage-to-Orbit Spaceplane Concept with Growth Potential," *Journal of Propulsion and Power*, Vol. 17, No. 6, pp. 1149–1161, Nov. 2001, doi: 10.2514/2.5886.
- ⁴⁴ Smart, M. K. and Tetlow, M. R., "Orbital Delivery of Small Payloads Using Hypersonic Airbreathing Propulsion," *Journal of Spacecraft and Rockets*, Vol. 46, No. 1, pp. 117–125, Jan. 2009, doi: 10.2514/1.38784.
- ⁴⁵ Curtis, H., *Orbital Mechanics for Engineering Students*, Elsevier, Burlington, MA, 2005.

- ⁴⁶ Messerschmid, E. and Fasoulas, S., *Raumfahrtsysteme: Eine Einführung mit Übungen und Lösungen*, Springer Verlag, Berlin Heidelberg, Germany, 4th ed., 2010.
- ⁴⁷ Sutton, G. P., “History of Liquid-Propellant Rocket Engines in Russia, Formerly the Soviet Union,” *Journal of Propulsion and Power*, Vol. 19, No. 6, pp. 1008–1037, Nov. 2003, doi: 10.2514/2.6943.
- ⁴⁸ Scotti, S., Martin, C., and Lucas, S., “Active Cooling Design for Scramjet Engines using Optimization Methods,” *29th Structures, Structural Dynamics and Materials Conference*, American Institute of Aeronautics and Astronautics, Williamsburg, VA, 1988, pp. 420–430, doi: 10.2514/6.1988-2265.
- ⁴⁹ Daniau, E., Bouchez, M., Herbinet, O., Marquaire, P.-M., Gascoin, N., and Gillard, P., “Fuel Reforming for Scramjet Thermal Management and Combustion Optimization,” *AIAA/CIRA 13th International Space Planes and Hypersonics Systems and Technologies Conference*, American Institute of Aeronautics and Astronautics, Capua, Italy, May 2005, doi: 10.2514/6.2005-3403.
- ⁵⁰ Kanda, T., Masuya, G., and Wakamatsu, Y., “Propellant Feed System of a Regeneratively Cooled Scramjet,” *Journal of Propulsion and Power*, Vol. 7, No. 2, pp. 299–301, March 1991, doi: 10.2514/3.23325.
- ⁵¹ Kanda, T., Masuya, G., Wakamatsu, Y., Chinzei, N., and Kanmuri, A., “Parametric Study of Airframe-Integrated Scramjet Cooling Requirement,” *Journal of Propulsion and Power*, Vol. 7, No. 3, pp. 431–436, May 1991, doi: 10.2514/3.23344.
- ⁵² *The Jet Engine*, Rolls-Royce plc, Derby, UK, 5th ed., 1996, p. 37f.
- ⁵³ Urlaub, A., *Flugtriebwerke*, Springer Verlag, Berlin Heidelberg, Germany, 2nd ed., 1995, p. 303.
- ⁵⁴ Schubert, S., *Untersuchung von Strömungsfeld und Wärmeübergang in einem berippten Multipass-System zur internen Kühlung von Gasturbinenschaufeln*, Ph.D. thesis, University of Stuttgart, Germany, June 2005.
- ⁵⁵ Bogard, D. G. and Thole, K. A., “Gas Turbine Film Cooling,” *Journal of Propulsion and Power*, Vol. 22, No. 2, pp. 249–270, March 2006, doi: 10.2514/1.18034.
- ⁵⁶ Langener, T., Wolfersdorf, J. V., and Steelant, J., “Experimental Investigations on Transpiration Cooling for Scramjet Applications Using Different Coolants,” *AIAA Journal*, Vol. 49, No. 7, pp. 1409–1419, July 2011, doi: 10.2514/1.J050698.

- ⁵⁷ Arai, M. and Suidzu, T., "Porous Ceramic Coating for Transpiration Cooling of Gas Turbine Blade," *Journal of Thermal Spray Technology*, Vol. 22, No. 5, pp. 690–698, Jan. 2013, doi: 10.1007/s11666-013-9883-1.
- ⁵⁸ Glass, D. E., Merrigan, M., and Sena, J. T., "Fabrication and Testing of Mo-Re Heat Pipes Embedded in Carbon/Carbon," Tech. Rep. NASA/CR-1998-207642, National Aeronautics and Space Administration, Langley Research Center, Hampton, VA, March 1998.
- ⁵⁹ Glass, D. E., Merrigan, M., Sena, J. T., and Reid, R. S., "Fabrication and Testing of a Leading-Edge-Shaped Heat Pipe," Tech. Rep. NASA/CR-1998-208720, National Aeronautics and Space Administration, Langley Research Center, Hampton, VA, Oct. 1998.
- ⁶⁰ Musielak, D., "High-Speed Air-Breathing Propulsion," *Aerospace America*, Vol. 48, No. 12, pp. 57, December 2010.
- ⁶¹ Harsha, P., Keel, L., Castrogiovanni, A., and Sherrill, R., "X-43A Vehicle Design and Manufacture," *AIAA/CIRA 13th International Space Planes and Hypersonics Systems and Technologies Conference*, American Institute of Aeronautics and Astronautics, Capua, Italy, May 2005, doi: 10.2514/6.2005-3334.
- ⁶² Musielak, D., "National Hypersonic Centers: Fast Track to Truly Fast Flight," *Aerospace America*, Vol. 50, No. 6, pp. 40–45, June 2012.
- ⁶³ Lewis, M., "X-51 Scrams into the Future," *Aerospace America*, Vol. 48, No. 10, pp. 26–31, October 2010.
- ⁶⁴ Dittert, C., Böhrk, H., and Weihs, H., "Wall Thickness Optimization of a Transpiration-Cooled Sharp Leading Edge at Atmospheric Re-Entry," *Proceedings of the 13th International Conference on Porous Media and its Applications in Science and Engineering, June 22nd-27th, 2014*, Kona, HI, June 2014.
- ⁶⁵ Segal, C., *The Scramjet Engine - Processes and Characteristics*, Cambridge University Press, New York, NY, 1st ed., 2009.
- ⁶⁶ Bouchez, M., Cahuzac, G., and Beyer, S., "PTAH-SOCAR Fuel-Cooled Composite Materials Structure for Dual-Mode Ramjet and Liquid Rocket Engines," *40th AIAA/ASME/SAE/ASEE Joint Propulsion Conference and Exhibit*, American Institute of Aeronautics and Astronautics, Fort Lauderdale, FL, July 2004, doi: 10.2514/6.2004-3653.

- ⁶⁷ RTO-EN-AVT-185 - *High Speed Propulsion: Engine Design - Integration and Thermal Management*, chap. Bouchez, M.: Scramjet Thermal Management, NATO Science and Technology Organization, September 2010.
- ⁶⁸ Glass, D., "Ceramic Matrix Composite (CMC) Thermal Protection Systems (TPS) and Hot Structures for Hypersonic Vehicles," *15th AIAA International Space Planes and Hypersonic Systems and Technologies Conference*, Dayton, OH, April 2008, doi: 10.2514/6.2008-2682.
- ⁶⁹ Pagel, L. L. and Warmbold, W. R., "Active Cooling of a Hydrogen-Fueled Scramjet Engine." *Journal of Aircraft*, Vol. 6, No. 5, pp. 472–474, Sept. 1969, doi: 10.2514/3.44088.
- ⁷⁰ Kanda, T., "Study of the Intensive Combustion in the Scramjet Engine," *34th AIAA/ASME/SAE/ASEE Joint Propulsion Conference and Exhibit*, American Institute of Aeronautics and Astronautics, Cleveland, OH, 1998, doi: 10.2514/6.1998-3123.
- ⁷¹ Mitani, T., Chinzei, N., and Kanda, T., "Reaction and Mixing-Controlled Combustion in Scramjet Engines," *Journal of Propulsion and Power*, Vol. 17, No. 2, pp. 308–314, March 2001, doi: 10.2514/2.5743.
- ⁷² Qin, J., Zhang, S., Bao, W., Duan, Y. J., Zhou, W., and Yu, D., "Off-Design Condition Cooling Capacity Analysis of Recooling Cycle for a Scramjet," *Journal of Propulsion and Power*, Vol. 28, No. 6, pp. 1285–1292, Nov. 2012, doi: 10.2514/1.B34455.
- ⁷³ Zander, F. and Morgan, R. G., "Transient Heat Analysis of a Carbon Composite Scramjet Combustion Chamber," *16th Australasian Fluid Mechanics Conference Crown Plaza Gold Coast Australia*, Crown Plaza, Gold Coast, Australia, Dec. 2007.
- ⁷⁴ Morgan, R. G. and Zander, F., "Radiatively Cooled Scramjet Combustor," *Shock Waves*, Springer Berlin Heidelberg, Berlin, Heidelberg, 2009, pp. 1135–1140.
- ⁷⁵ Eckert, E. R. G., "Engineering Relations for Friction and Heat Transfer to Surfaces in High Velocity Flow," *Journal of the aeronautical sciences*, Vol. 22, No. 8, pp. 585–587, 1955.
- ⁷⁶ Stollery, J. L. and Coleman, G. T., "A Correlation between Pressure and Heat Transfer Distributions at Supersonic and Hypersonic Speeds," *Aeronautical Quarterly*, Vol. 26, No. 4, pp. 304–312, Nov. 1975.

- ⁷⁷ Meador, W. E. and Smart, M. K., "Reference Enthalpy Method Developed from Solutions of the Boundary-Layer Equations," *AIAA Journal*, Vol. 43, No. 1, pp. 135–139, Jan. 2005, doi: 10.2514/1.2656.
- ⁷⁸ Crow, A. J., Boyd, I. D., and Terrapon, V. E., "Radiation Modeling of a Hydrogen Fueled Scramjet," *Journal of Thermophysics and Heat Transfer*, Vol. 27, No. 1, pp. 11–21, Jan. 2013, doi: 10.2514/1.T3751.
- ⁷⁹ Capra, B. R., Brown, L. M., Boyce, R. R., and Tirtey, S. C., "Aerothermal–Structural Analysis of a Rocket-Launched Mach 8 Scramjet Experiment: Ascent," *Journal of Spacecraft and Rockets*, Vol. 52, No. 3, pp. 684–696, May 2015, doi: 10.2514/1.A33112.
- ⁸⁰ Kroll, N., Rossow, C.-C., Becker, K., and Thiele, F., "The MEGAFLOW project," *Aerospace Science and Technology*, Vol. 4, No. 4, pp. 223–237, June 2000, doi: 10.1016/S1270-9638(00)00131-0.
- ⁸¹ Menter, F. R., "Two-Equation Eddy-Viscosity Turbulence Models for Engineering Applications," *AIAA Journal*, Vol. 32, No. 8, pp. 1598–1605, Aug. 1994, doi: 10.2514/3.12149.
- ⁸² Hottel, H. C. and Egbert, R. B., "Radiant Heat Transmission from Water Vapor," *Transactions of the American Institute of Chemical Engineers*, Vol. 38, pp. 531–568, 1942.
- ⁸³ Reinartz, B., *Wärmebelastung der Brennkammer eines Staustahltriebwerks mit Überschallverbrennung*, Ph.D. thesis, RWTH Aachen University, Aachen, Germany, October 2000.
- ⁸⁴ Leachman, J. W., Jacobsen, R. T., Penoncello, S. G., and Lemmon, E. W., "Fundamental Equations of State for Parahydrogen, Normal Hydrogen, and Orthohydrogen," *Journal of Physical and Chemical Reference Data*, Vol. 38, No. 3, pp. 721, 2009, doi: 10.1063/1.3160306.
- ⁸⁵ Vidal, J., *Thermodynamics - Applications in Chemical Engineering and the Petroleum Industry*, Publication IFP, Editions Technips, Paris, France, 4th ed., 2003, p. 112ff.
- ⁸⁶ Soave, G., "Equilibrium Constants from a Modified Redlich-Kwong Equation of State," *Chemical Engineering Science*, Vol. 27, No. 6, pp. 1197–1203, June 1972, doi: 10.1016/0009-2509(72)80096-4.

- ⁸⁷ Peng, D.-Y. and Robinson, D. B., "A New Two-Constant Equation of State," *Industrial & Engineering Chemistry Fundamentals*, Vol. 15, No. 1, pp. 59–64, Feb. 1976, doi: 10.1021/i160057a011.
- ⁸⁸ Mahmoodi, P. and Sedigh, M., "A consistent and precise alpha function for cubic equations of state," *Fluid Phase Equilibria*, Vol. 436, pp. 69–84, March 2017, doi: 10.1016/j.fluid.2016.12.015.
- ⁸⁹ Aznar, M. and Telles, A. S., "A Data Bank of Parameters for the Attractive Coefficient of the Peng-Robinson Equation of State," *Brazilian Journal of Chemical Engineering*, Vol. 14, 03 1997, doi: 10.1590/S0104-66321997000100003.
- ⁹⁰ Young, A. F., Pessoa, F. L. P., and Ahón, V. R. R., "Comparison of 20 Alpha Functions Applied in the Peng–Robinson Equation of State for Vapor Pressure Estimation," *Industrial & Engineering Chemistry Research*, Vol. 55, No. 22, pp. 6506–6516, June 2016, doi: 10.1021/acs.iecr.6b00721.
- ⁹¹ Jaubert, J.-N. and Privat, R., "Relationship between the binary interaction parameters (k_{ij}) of the Peng-Robinson and those of the Soave-Redlich-Kwong equations of state: Application to the definition of the PR2SRK model," *Fluid Phase Equilibria*, Vol. 295, No. 1, pp. 26–37, Aug. 2010, doi: 10.1016/j.fluid.2010.03.037.
- ⁹² Lee, B. I. and Kesler, M. G., "A Generalized Thermodynamic Correlation Based on Three-Parameter Corresponding States," *AIChE Journal*, Vol. 21, No. 3, pp. 510–527, May 1975, doi: 10.1002/aic.690210313.
- ⁹³ Muñoz, F. and Reich, R., "New Parameters for the Lee-Kesler Correlation Improve Liquid Density Predictions," *Fluid Phase Equilibria*, Vol. 13, pp. 171–178, Jan. 1983, doi: 10.1016/0378-3812(83)80091-0.
- ⁹⁴ Weigand, B., Köhler, J., and von Wolfersdorf, J., *Thermodynamik kompakt*, chap. 4.2 Zustandsgleichungen, Springer Verlag, Berlin, 1st ed., 2008, p. 52f.
- ⁹⁵ Rao, Y. V. C., *Chemical Engineering Thermodynamics*, Universities Press, India, 1997, p. 272f.
- ⁹⁶ Hirschel, E. H., *Basics of Aerothermodynamics*, Springer International Publishing, Heidelberg, Germany, 2nd ed., 2015.
- ⁹⁷ Stull, D. R., *JANAF thermochemical tables*, United States, Dep. of Commerce, National Bureau of Standards, Washington, DC : US Government Pr. Office, 2nd ed., 1971.

- ⁹⁸ Gordon, S. and McBride, B. J., “Computer Program for Calculation of Complex Chemical Equilibrium Compositions and Applications I. Analysis,” Oct. 1994.
- ⁹⁹ Gordon, S. and McBride, B. J., “Computer Program for Calculation of Complex Chemical Equilibrium Compositions and Applications II. User’s Manual and Program Description,” June 1996.
- ¹⁰⁰ Kleiber, M. and Joh, R., *VDI Heat Atlas*, chap. D1 Calculation Methods for Thermophysical Properties, Springer Verlag, Berlin Heidelberg, Germany, 2nd ed., 2010, pp. 979–988.
- ¹⁰¹ Kouremenos, D. A. and Antonopoulos, K. A., “Isentropic Exponents of Real Gases and Application for the Air at Temperatures from 150 K to 450 K,” *Acta Mechanica*, Vol. 65, No. 1-4, pp. 81–99, Jan. 1987, doi: 10.1007/BF01176874.
- ¹⁰² Gad-el Hak, M., “Questions in Fluid Mechanics: Stokes’ Hypothesis for a Newtonian, Isotropic Fluid,” *Journal of Fluids Engineering*, Vol. 117, No. 1, pp. 3–3, 1995, doi: 10.1115/1.2816816.
- ¹⁰³ Fujii, K. and Hornung, H. G., “Experimental Investigation of High-Enthalpy Effects on Attachment-Line Boundary-Layer Transition,” *AIAA Journal*, Vol. 41, No. 7, pp. 1282–1291, July 2003, doi: 10.2514/2.2096.
- ¹⁰⁴ Emanuel, G., “Effect of Bulk Viscosity on a Hypersonic Boundary Layer,” *Physics of Fluids A: Fluid Dynamics*, Vol. 4, No. 3, pp. 491–5, 1992, doi: 10.1063/1.858322.
- ¹⁰⁵ Schlichting, H. and Gersten, K., *Grenzschicht-Theorie*, chap. Feldgleichungen für die Strömungen Newtonscher Fluide: Energiegleichung, Springer, Berlin Heidelberg, Germany, 10th ed., 2006, pp. 68–72.
- ¹⁰⁶ Ladyzhenskaya, O. A., “Sixth Problem of the Millennium: Navier-Stokes Equations, Existence and Smoothness,” *Russian Mathematical Surveys*, Vol. 58, No. 2, pp. 251–286, Oct. 2007, doi: 10.1070/RM2003v058n02ABEH000610.
- ¹⁰⁷ Buckingham, E., “On Physically Similar Systems; Illustrations of the Use of Dimensional Equations,” *Physical Review*, Vol. 4, No. 4, pp. 345–376, Oct. 1914, doi: 10.1103/PhysRev.4.345.
- ¹⁰⁸ Rudolph, S., *Übertragung von Ähnlichkeitsbegriffen*, Habilitationsschrift, ISD Verlag, Universität Stuttgart, 2002.
- ¹⁰⁹ Kays, W. M. and Crawford, M. E., *Convective Heat and Mass Transfer*, Mc Graw-Hill, New York, NY, 3rd ed., 1993.

- ¹¹⁰ Krause, M., Reinartz, B., and Ballmann, J., “Numerical Computations for Designing a Scramjet Intake,” *28th International Congress of the Aeronautical Sciences*, Hamburg, Germany, Aug. 2006.
- ¹¹¹ Kays, W. M., “Turbulent Prandtl Number—Where Are We?” *Journal of Heat Transfer*, Vol. 116, No. 2, pp. 284–12, 1994, doi: 10.1115/1.2911398.
- ¹¹² Colburn, A. P., “A Method of Correlating Forced Convection Heat-Transfer Data and a Comparison with Fluid Friction,” *Transactions of the American Institute of Chemical Engineers*, Vol. 29, pp. 174–210, 1933, doi: 10.1016/0017-9310(64)90125-5.
- ¹¹³ Lin, H. T., “The Analogy Between Fluid Friction and Heat Transfer of Laminar Forced Convection on a Flat Plate,” *Wärme- und Stoffübertragung*, Vol. 29, No. 3, pp. 181–184, Jan. 1994, doi: 10.1007/BF01548602.
- ¹¹⁴ van Driest, E. R., “The Turbulent Boundary Layer with Variable Prandtl Number,” Tech. Rep. AL-1914, North American Aviation Inc., Downey, California, Jan. 1954.
- ¹¹⁵ Nikuradse, J., “Gesetzmäßigkeiten der turbulenten Strömung in glatten Röhren,” Tech. Rep. Forschungsheft 356, Berlin, Germany, Oct. 1932.
- ¹¹⁶ Ackermann, G., “Plattenthermometer in Strömung mit großer Geschwindigkeit und turbulenter Grenzschicht,” *Forschung auf dem Gebiet des Ingenieurwesens A*, Vol. 13, No. 6, pp. 226–234, Nov. 1942.
- ¹¹⁷ Prandtl, L., “Über Flüssigkeitsbewegung bei sehr kleiner Reibung,” *Verhandlungen des III. Internationalen Mathematiker-Kongresses*, Heidelberg, Germany, 1904, pp. 484–491.
- ¹¹⁸ Kármán, T. v., “Mechanical Similitude and Turbulence,” Tech. Rep. NACA-TM-611, National Advisory Committee for Aeronautics, Washington, DC, 1930.
- ¹¹⁹ Prandtl, L., “Neuere Ergebnisse der Turbulenzforschung,” *VDI Zeitschrift*, Vol. 7, No. 5, pp. 105–114, 1933.
- ¹²⁰ Crocco, L., “Lo strato limite laminare nei gas,” *Associazione culturale aeronautica*, Vol. 187, 1946.
- ¹²¹ van Driest, E. R., “Turbulent Boundary Layer in Compressible Fluids,” *Journal of the aeronautical sciences*, Vol. 18, No. 3, pp. 145–160, March 1951, doi: 10.2514/2.7048.

- ¹²² Schlichting, H. and Gersten, K., *Grenzschicht-Theorie*, Springer, Berlin Heidelberg, Germany, 10th ed., 2006, p. 117f.
- ¹²³ Schlichting, H., *Boundary-Layer Theory*, Mc Graw-Hill series in mechanical engineering, Mc Graw-Hill, 7th ed., 1979.
- ¹²⁴ McLean, D., *Understanding Aerodynamics: Arguing from the Real Physics*, John Wiley & Sons, Ltd., West Sussex, UK, 1st ed., 2013, p. 108.
- ¹²⁵ Shapiro, A. H., *The Dynamics and Thermodynamics of Compressible Fluid Flow*, Vol. 1, chap. Generalized One-Dimensional Continous Flow, John Wiley & Sons, Inc., 1953, p. 219ff.
- ¹²⁶ Blasius, H., "Grenzschichten in Flüssigkeiten mit kleiner Reibung," *ZAMM - Zeitschrift für Angewandte Mathematik und Mechanik*, , No. 56, pp. 1–37, 1908.
- ¹²⁷ Falkner, V. M. and Skan, S. W., "Solutions of the Boundary-Layer Equations," *The London, Edinburgh, and Dublin Philosophical Magazine and Journal of Science: Series 7*, Vol. 12, No. 80, pp. 865–896, 1931, doi: 10.1080/14786443109461870.
- ¹²⁸ Rohsenow, W. M., Hartnett, J. P., and Ganic, E. N., *Handbook of Heat Transfer Fundamentals*, Mcgraw-Hill, Texas, 2nd ed., 1985, pp. 8–412ff.
- ¹²⁹ Higgins, K., "Comparision of Engineering Correlations for Predicting Heat Transfer in Zero-Pressure-Gradient Compressible Boundary Layers with CFD and Experimental Data," Tech. Rep. DSTO–TR–2159, Australian Government, Department of Defence, Victoria, Australia, 2008.
- ¹³⁰ Spalding, D. B., "A Single Formula for the "Law of the Wall"," *Journal of Applied Mechanics*, Vol. 28, No. 3, pp. 455–4, 1961, doi: 10.1115/1.3641728.
- ¹³¹ Österlund, J. M., Johansson, A. V., Nagib, H. M., and Hites, M. H., "A Note on the Overlap Region in Turbulent Boundary Layers," *Physics of Fluids*, Vol. 12, No. 1, pp. 1–4, 2000, doi: 10.1063/1.870250.
- ¹³² Schultz-Grunow, F., "New Frictional Resistance Law for Smooth Plates," Tech. Rep. NACA-TM-986, Sept. 1941.
- ¹³³ Dutton, R. A., "The Velocity Distribution in a Turbulent Boundary Layer on a Flat Plate," Tech. rep., 1959.
- ¹³⁴ Coles, D., "The Law of the Wake in the Turbulent Boundary Layer," *Journal of Fluid Mechanics*, Vol. 1, No. 02, pp. 191–226, July 1956, doi: 10.1017/S0022112056000135.

- ¹³⁵ Cebeci, T. and Smith, A. M. O., *Analysis of Turbulent Boundary Layers*, Vol. 15 of *Applied Mathematics and Mechanics*, Academic Press, New York, NY, 1974, p. 221.
- ¹³⁶ Das, D. K., “A Simple Theory for Calculating Turbulent Boundary Layers Under Arbitrary Pressure Gradients,” *International Journal of Engineering and Fluid Mechanics*, Vol. 1, No. 1, pp. 83–99, April 1988.
- ¹³⁷ Schlichting, H. and Gersten, K., *Grenzschicht-Theorie*, chap. Turbulente Grenzschichten ohne Kopplung des Geschwindigkeitsfeldes an das Temperaturfeld, Springer, Berlin Heidelberg, Germany, 10th ed., 2006, pp. 557–610.
- ¹³⁸ George, W. K., “Is there a universal log law for turbulent wall-bounded flows?” *Philosophical Transactions of the Royal Society A: Mathematical, Physical and Engineering Sciences*, Vol. 365, No. 1852, pp. 789–806, March 2007, doi: 10.1098/rsta.2006.1941.
- ¹³⁹ Petukhov, B. S., “Heat Transfer and Friction in Turbulent Pipe Flow with Variable Physical Properties,” Vol. 6, pp. 503–564, 1970, doi: 10.1016/S0065-2717(08)70153-9.
- ¹⁴⁰ Fernholz, H., “Geschwindigkeitsprofile, Temperaturprofile und halbempirische Gesetze in kompressiblen turbulenten Grenzschichten bei konstantem Druck,” *Ingenieur-Archiv*, Vol. 38, No. 4-5, pp. 311–328, 1969, doi: 10.1007/BF00536174.
- ¹⁴¹ Bradshaw, P., “An Improved Van Driest Skin-Friction Formula for Compressible Turbulent Boundary Layers,” *AIAA Journal*, Vol. 15, No. 2, pp. 212–214, Feb. 1977, doi: 10.2514/3.7315.
- ¹⁴² Jischa, M., *Konvektiver Impuls-, Wärme- und Stoffaustausch*, chap. Turbulenter Wärme- und Stoffaustausch, Friedr. Vieweg & Sohn Verlag, Braunschweig, Germany, 1982, pp. 254–313.
- ¹⁴³ Kempf, G., “Flächenwiderstand,” *Werft - Reederei - Hafen*, Vol. 5, pp. 521–528, 1924.
- ¹⁴⁴ Huang, P. G. and Coleman, G. N., “Van Driest Transformation and Compressible Wall-Bounded Flows,” *AIAA Journal*, Vol. 32, No. 10, pp. 2110–2113, Oct. 1994, doi: 10.2514/3.12259.
- ¹⁴⁵ Huang, P. G. and Coleman, G. N., “Errata Van Driest Transformation and Compressible Wall-Bounded Flows,” *AIAA Journal*, Vol. 33, No. 9, pp. 1756b–1756b, Sept. 1995, doi: 10.2514/3.48353.

- ¹⁴⁶ Messe, C., “A Modified van Driest Method for Compressible and Supersonic Channel Flows and Pipe Flows,” *53rd AIAA/SAE/ASEE Joint Propulsion Conference*, American Institute of Aeronautics and Astronautics, Atlanta, GA, July 2017, doi: 10.2514/6.2017-4743.
- ¹⁴⁷ Pianko, M. and Wazelt, F., “Suitable Averaging Techniques in Non-Uniform Internal Flows,” Tech. Rep. AGARD-AR-182, North Atlantic Treaty Organization, Essex, UK, June 1983.
- ¹⁴⁸ Lindgren, E. R., “Experimental Study on Turbulent Pipe Flows of Distilled Water,” Tech. Rep. 1AD0621071, Oklahoma State University, Stillwater, OK, 1965.
- ¹⁴⁹ White, F., *Viscous Fluid Flow*, Mc Graw-Hill, 3rd ed., 2006.
- ¹⁵⁰ Guo, J. and Julien, P., “Modified Log-Wake Law for Turbulent Flow in Smooth Pipes,” *Journal of Hydraulic Research*, Vol. 43, No. 4, pp. 431–434, July 2005.
- ¹⁵¹ Nikuradse, J., “Gesetzmäßigkeiten der turbulenten Strömung in glatten Rohren (Nachtrag),” *Forschung im Ingenieurwesen*, Vol. 4, No. 1, pp. 44–44, Feb. 1933, doi: 10.1007/BF02716946.
- ¹⁵² Williams, W. C., “If the Dittus and Boelter equation is really the McAdams equation, then should not the McAdams equation really be the Koo equation?” *International Journal of Heat and Mass Transfer*, Vol. 54, No. 7-8, pp. 1682–1683, March 2011, doi: 10.1016/j.ijheatmasstransfer.2010.11.047.
- ¹⁵³ Messe, C., “A Refined Formulation for One-Dimensional Modeling of Compressible and Supersonic Reacting Flows,” *53rd AIAA/SAE/ASEE Joint Propulsion Conference*, American Institute of Aeronautics and Astronautics, Atlanta, GA, July 2017, doi: 10.2514/6.2017-4989.
- ¹⁵⁴ Hayes, W. D. and Probstein, R. F., *Hypersonic Flow Theory*, Academic Press, New York, NY, 1959.
- ¹⁵⁵ Anderson, J. D., *Hypersonic and High Temperature Gas Dynamics*, AIAA Education Series, Mc Graw-Hill, 2nd ed., 2006.
- ¹⁵⁶ Franke, H., editor, *Lexikon der Physik, Band 3: S-Z*, Franckh’sche Verlangshandlung, W. Keller & Co., Stuttgart, Germany, 3rd ed., 1969.
- ¹⁵⁷ Anderson, J. D., *Modern Compressible Flow: With Historical Perspective*, Mc Graw-Hill, 3rd ed., 2003.

- ¹⁵⁸ Vortmeyer, D. and Kabelac, S., *VDI Heat Atlas*, chap. K3 Gas Radiation: Radiation from Gas Mixtures, Springer Verlag, Berlin Heidelberg, Germany, 2nd ed., 2010, pp. 979–988.
- ¹⁵⁹ Fehlberg, E., “Klassische Runge-Kutta-Formeln vierter und niedrigerer Ordnung mit Schrittweiten-Kontrolle und ihre Anwendung auf Wärmeleitungsprobleme,” *Computing*, Vol. 6, No. 1-2, pp. 61–71, March 1970, doi: 10.1007/BF02241732.
- ¹⁶⁰ Gerlinger, P., Möbus, H., and Brüggemann, D., “An Implicit Multigrid Method for Turbulent Combustion,” *Journal of Computational Physics*, Vol. 167, No. 2, pp. 247–276, March 2001, doi: 10.1006/jcph.2000.6671.
- ¹⁶¹ Walther, R., *Ein Differenzenverfahren für chemisch reagierende Strömungen*, Ph.D. thesis, University of Stuttgart, Germany, 1985.
- ¹⁶² Murthy, S., *Scramjet Propulsion, Progress in Astronautics and Aeronautics, Vol. 189*, chap. Basic Performance Assessment of Scram Combustors, American Institute of Aeronautics and Astronautics, Reston, VA, 2000, pp. 597–695.
- ¹⁶³ Scheuermann, T., Chin, J., and von Wolfersdorfs, J., “One-Dimensional Modelling of a Scramjet Combustor Reacting Flow,” *5th AIAA International Space Planes and Hypersonic Systems and Technologies Conference*, Dayton, OH, 2008, doi: 10.2514/6.2008-2643.
- ¹⁶⁴ Pulsonetti, M., Erdos, J., and Early, K., “An Engineering Model for Analysis of Scramjet Combustor Performance with Finite Rate Chemistry,” *AIAA/ASME/SAE/ASEE 24th Joint Propulsion Conference*, American Institute of Aeronautics and Astronautics, Boston, MA, July 1988, doi: 10.2514/6.1988-3258.
- ¹⁶⁵ Messerschmid, E. and Fasoulas, S., *Raumfahrtsysteme: Eine Einführung mit Übungen und Lösungen*, chap. Thermalkontrollsysteme, Springer Verlag, Berlin Heidelberg, Germany, 4th ed., 2011, pp. 333–370.
- ¹⁶⁶ Rao, Y. V. C., *Heat Transfer*, Universities Press, India, 2001, p. 255.
- ¹⁶⁷ Howell, J. R., “Calculation of Radiant Heat Exchange by the Monte Carlo Method,” *Winter Annual Meeting of the American Society of Mechanical Engineers*, Chicago, Illinois, Nov. 1965.
- ¹⁶⁸ Hottel, H. C., *Heat Transmission*, chap. Radiant Heat Transmission, Mc Graw-Hill, New York, NY, 3rd ed., 1954, pp. 55–125.

- ¹⁶⁹ Siegel, R., Howell, J. R., and Lohrengel, J., *Wärmeübertragung durch Strahlung - Teil 2: Strahlungsaustausch zwischen Oberflächen und in Umhüllungen*, Springer Verlag, Heidelberg, Germany, 1988, p. 102.
- ¹⁷⁰ Argyris, J. H., “Energy Theorems and Structural Analysis: a Generalized Discourse with Applications on Energy Principles of Structural Analysis Including the Effects of Temperature and Non-Linear Stress-Strain Relations,” *Aircraft Engineering and Aerospace Technology*, Vol. 26, No. 10, pp. 347–356, Oct. 1954, doi: 10.1108/eb032482.
- ¹⁷¹ Turner, M. J., Clough, R. W., Martin, H. C., and Topp, L. P., “Stiffness and Deflection Analysis of Complex Structures,” *Journal of the aeronautical sciences*, Vol. 23, No. 9, pp. 805–823, Sept. 1956, doi: 10.2514/8.3664.
- ¹⁷² Bathe, K.-J., *Finite Element Procedures*, Klaus-Jürgen Bathe, Watertown, MA, 2nd ed., 2014.
- ¹⁷³ Zienkiewicz, O. C., Taylor, R. L., and Fox, D. D., *The Finite Element Method for Solid and Structural Mechanics*, Butterworth-Heinemann, Oxford, UK, 7th ed., 2013.
- ¹⁷⁴ Brenner, S. C. and Scott, L. R., *The Mathematical Theory of Finite Element Methods*, Texts in Applied Mathematics, Springer Science+Business Media, LLC, New York, NY, 3rd ed., 2008.
- ¹⁷⁵ Argyris, J. and Mlejnek, H.-P., *Die Methode der Finiten Elemente*, Vol. 1-3, Viewig & Sohn Verlag, Braunschweig, Germany, 1986-1988.
- ¹⁷⁶ Lewis, R. W., Morgan, K., Thomas, H. R., and Seetharamu, K. N., *The Finite Element Method in Heat Transfer Analysis*, 2nd, John Wiley & Sons, New York, NY, 1996.
- ¹⁷⁷ Lewis, R. W., Morgan, K., Thomas, H. R., and Seetharamu, K. N., *The Finite Element Method in Heat Transfer Analysis*, John Wiley & Sons, New York, NY, 2nd ed., 1996, p. 82ff.
- ¹⁷⁸ van der Vorst, H. A., “Bi-CGSTAB: A Fast and Smoothly Converging Variant of Bi-CG for the Solution of Nonsymmetric Linear Systems,” *SIAM Journal on Scientific and Statistical Computing*, Vol. 13, No. 2, pp. 631–644, March 1992, doi: 10.1137/0913035.
- ¹⁷⁹ Gummert, P. and Reckling, K.-A., *Mechanik*, chap. Statik deformierbarer Systeme, Friedr. Vieweg & Sohn Verlag, 1986, pp. 266–443.

- ¹⁸⁰ Kochendörfer, R. and Krenkel, W., “CMC-Intake Ramp for Hypersonic Propulsion Systems,” *2nd International Conference on High Temperature Composite Materials (HT-CMC-2)*, pp. 13–22, Aug. 1995.
- ¹⁸¹ Häberle, J. and Gülhan, A., “Investigation of Two-Dimensional Scramjet Inlet Flowfield at Mach 7,” *Journal of Propulsion and Power*, Vol. 24, No. 3, pp. 446–459, May 2008, doi: 10.2514/1.33545.
- ¹⁸² Heinrich, R., “Die Duale Zeitschrittmethode zur Simulation instationärer, dreidimensionaler, viskoser Strömungen,” *GAMM-Tagung, Regensburg*, 1997.
- ¹⁸³ Shuxin, B., Yonggang, T., Yicong, Y., and Hong, Z., *MAX Phases and Ultra-High Temperature Ceramics for Extreme Environments*, chap. MAX Phases and Ultra-High Temperature Ceramics for Extreme Environments, IGI Global, Hershey, PA, 2013, pp. 323–353.
- ¹⁸⁴ Seifert, H. J., Wagner, S., Fabrichnaya, O., Lukas, H. L., Aldinger, F., Ullmann, T., Schmucker, M., and Schneider, H., “Yttrium Silicate Coatings on Chemical Vapor Deposition-SiC-Precoated C/C-SiC: Thermodynamic Assessment and High-Temperature Investigation,” *Journal of the American Ceramic Society*, Vol. 88, No. 2, pp. 424–430, Feb. 2005, doi: 10.1111/j.1551-2916.2005.00077.x.
- ¹⁸⁵ van Wie, D., *Scramjet Propulsion, Progress in Astronautics and Aeronautics, Vol. 189*, chap. Scramjet Inlets, American Institute of Aeronautics and Astronautics, Reston, VA, 2000, pp. 447–511.
- ¹⁸⁶ Pagel, L. L. and Warmbold, W. R., “Active Cooling of a Hydrogen-Fueled Scramjet Engine,” *Journal of Aircraft*, Vol. 6, pp. 472–474, 1969.
- ¹⁸⁷ Shore, C. P., “Review of Convectively Cooled Structures for Hypersonic Flight,” Tech. Rep. NASA-TM-87740, NASA Langley Research Center, Hampton, Virginia, May 1986.
- ¹⁸⁸ Johnson, D. and Robinson, J., “X-43D Conceptual Design and Feasibility Study,” *AIAA/CIRA 13th International Space Planes and Hypersonics Systems and Technologies Conference*, American Institute of Aeronautics and Astronautics, Capua, Italy, 2005, doi: 10.2514/6.2005-3416.
- ¹⁸⁹ Yoshida, M., Sudo, T., and Bosaka, M., “Evaluation of Cryogenic CFRP Tank Elements under Pressurized Liquid Hydrogen,” Tech. Rep. NALRP2001031, National Aerospace Laboratory, Tokyo, Japan, Jan. 2001.

- ¹⁹⁰ Moses, P., Bouchard, K., Vause, R., Pinckney, S., Taylor III, L., Ferlemann, S., Leonard, C., Robinson, J., Martin, J., Petley, D., and e, a., "An Airbreathing Launch Vehicle Design with Turbine-Based Low-speed Propulsion and Dual Mode Scramjet High-Speed Propulsion," *9th International Space Planes and Hypersonic Systems and Technologies Conference*, American Institute of Aeronautics and Astronautics, Norfolk, VA, Nov. 1999, doi: 10.2514/6.1999-4948.
- ¹⁹¹ "NASA Space Vehicle Design Criteria (Chemical Propulsion): Liquid Rocket Engine Centrifugal Flow Turbopumps," Tech. Rep. NASA SP-8109, National Aeronautics and Space Administration, Nov. 1973.
- ¹⁹² Kamijo, K. and Hirata, K., "Performance of Small High Speed Cryogenic Pumps," *Journal of Fluids Engineering*, Vol. 107, No. 2, pp. 197–7, 1985, doi: 10.1115/1.3242460.
- ¹⁹³ Bohl, W., *Strömungsmaschinen*, Vol. 2, Vogel Fachbuch, Würzburg, Germany, 6th ed., 1999, p. 40.
- ¹⁹⁴ Bouchez, M. and Beyer, S., "PTAH-SOCAR Fuel-Cooled Composite Materials Structure for Dual-Mode Ramjet and Liquid Rocket Engines - 2005 Status," *AIAA/CIRA 13th International Space Planes and Hypersonics Systems and Technologies Conference*, American Institute of Aeronautics and Astronautics, Capua, Italy, May 2005, doi: 10.2514/6.2005-3434.
- ¹⁹⁵ Gülich, J. F., *Kreiselpumpen: Handbuch für Entwicklung, Anlagenplanung und Betrieb*, chap. Verhalten der Kreiselpumpen in Anlagen, Springer-Verlag, Berlin Heidelberg, Germany, 2013, pp. 809–862.
- ¹⁹⁶ Bouchez, M., Cahuzac, G., Beyer, S., and Avrashkov, V., "PTAH-SOCAR Fuel-Cooled Composite Materials Structure in 2003," *12th AIAA International Space Planes and Hypersonic Systems and Technologies*, American Institute of Aeronautics and Astronautics, Norfolk, VA, Dec. 2003, doi: 10.2514/6.2003-6919.
- ¹⁹⁷ Bouchez, M., Beyer, S., and Schmidt, S., "PTAH-SOCAR Fuel-Cooled Composite Materials Structure : 2011 Status," *17th AIAA International Space Planes and Hypersonic Systems and Technologies Conference*, American Institute of Aeronautics and Astronautics, San Francisco, CA, April 2011, doi: 10.2514/6.2011-2208.
- ¹⁹⁸ Jacobsen, R. T., Leachman, J. W., Penoncello, S. G., and Lemmon, E. W., "Current Status of Thermodynamic Properties of Hydrogen," *International Journal of Thermophysics*, Vol. 28, No. 3, pp. 758–772, Aug. 2007, doi: 10.1007/s10765-007-0226-7.

- ¹⁹⁹ Reinartz, B., Ballmann, J., and Boyce, R., “Numerical Investigation of Wall Temperature and Entropy Layer Effects on Double Wedge Shock / Boundary Layer Interactions,” *14th AIAA/AHI Space Planes and Hypersonic Systems and Technologies Conference*, American Institute of Aeronautics and Astronautics, Canberra, Australia, Nov. 2006, doi: 10.2514/6.2006-8137.
- ²⁰⁰ Frauholz, S., Bosco, A., Reinartz, B. U., Müller, S., and Behr, M., “Investigation of Hypersonic Intakes Using Reynolds Stress Modeling and Wavelet-Based Adaptation,” *AIAA Journal*, Vol. 52, No. 12, pp. 2765–2781, Dec. 2014, doi: 10.2514/1.J052966.
- ²⁰¹ Fischer, C. and Olivier, H., “Experimental Investigation of the Internal Flow Field of a Scramjet Engine,” *16th AIAA/DLR/DGLR International Space Planes and Hypersonic Systems and Technologies Conference*, Bremen, Germany, Oct. 2009.
- ²⁰² Hirschel, E. H., *Basics of Aerothermodynamics*, chap. Real-Gas Aerothermodynamic Phenomena, Springer International Publishing, Heidelberg, Germany, 2nd ed., 2015, p. 111ff.
- ²⁰³ Lukasiewicz, J., “Blast-Hypersonic Flow Analogy Theory and Application,” *American Rocket Society Journal*, Vol. 32, No. 9, pp. 1341–1346, Nov. 1962, doi: 10.2514/8.6281.
- ²⁰⁴ Baradell, D. L. and Bertram, M. H., “The Blunt Plate in Hypersonic Flow,” Tech. Rep. NASA-TN-D-408, National Aeronautics and Space Administration, Langley Field, VA, Oct. 1960.
- ²⁰⁵ Oliver, R. E., “An Experimental Investigation of Flow About Simple Blunt Bodies at a Nominal Mach Number of 5.8,” *Journal of the aeronautical sciences*, Vol. 23, No. 2, pp. 177–179, Feb. 1956.
- ²⁰⁶ Lees, L., “Laminar Heat Transfer Over Blunt-Nosed Bodies at Hypersonic Flight Speeds,” *Journal of Jet Propulsion*, Vol. 26, No. 4, pp. 259–269, April 1956, doi: 10.2514/8.6977.
- ²⁰⁷ Kemp Jr, J. H., “Hypersonic Viscous Interaction on Sharp and Blunt Inclined Plates,” *AIAA Journal*, Vol. 7, No. 7, pp. 1280–1289, July 1969, doi: 10.2514/3.5335.
- ²⁰⁸ Nguyen, T., Vukovic, M., Behr, M., and Reinartz, B., “Numerical Simulations of Successive Distortions in Supersonic Turbulent Flow,” *AIAA Journal*, Vol. 50, No. 11, pp. 2365–2375, Nov. 2012, doi: 10.2514/1.J051465.

- ²⁰⁹ Pidan, S., Auweter-Kurtz, M., Herdrich, G., and Fertig, M., “Recombination Coefficients and Spectral Emissivity of Silicon Carbide-Based Thermal Protection Materials,” *Journal of Thermophysics and Heat Transfer*, Vol. 19, No. 4, pp. 566–571, Oct. 2005, doi: 10.2514/1.12814.
- ²¹⁰ Santana, E. J. R., *Numerical Investigation of a Generic Supersonic Combustion Chamber under Realistic Flight Conditions*, Ph.D. thesis, University of Stuttgart, Germany, 2015.
- ²¹¹ Gerlinger, P., Kasal, P., Schneider, F., von Wolfersdorf, J., Weigand, B., and Eigner, M., *Basic Research and Technologies for Two-Stage-to-Orbit Vehicles: Final Report of the Collaborative Research Centres 253, 255 and 259*, chap. Experimental and Numerical Investigation of Lobed Strut Injectors for Supersonic Combustion, Sonderforschungsberichte der Deutschen Forschung, John Wiley and Sons, Inc., Weinheim, Germany, 2006, pp. 365–382.
- ²¹² Rust, B., Gerlinger, P., Lourier, J.-M., Aigner, M., and Kindler, M., “Numerical Simulation of the Internal and External Flowfields of a Scramjet Fuel Strut Injector Including Conjugate Heat Transfer,” *17th AIAA International Space Planes and Hypersonic Systems and Technologies Conference*, American Institute of Aeronautics and Astronautics, San Francisco, CA, April 2011, doi: 10.2514/6.2011-2207.
- ²¹³ Fuhrmann, T., *Auslegung und Betriebsverhalten von SCRamjet-Antriebssystemen für Raumtransporter-Hyperschallflugzeuge*, Ph.D. thesis, Technical University of Munich, Germany, 2009.
- ²¹⁴ Dröske, N., Förster, F. J., Weigand, B., and von Wolfersdorf, J., “Investigation of Heat Loads onto an Internally Cooled Strut Injector for Scramjet Application,” *20th AIAA International Space Planes and Hypersonic Systems and Technologies Conference*, American Institute of Aeronautics and Astronautics, Glasgow, Scotland, July 2015, doi: 10.2514/6.2015-3555.
- ²¹⁵ Hohn, O., *Auslegung und Charakterisierung eines dreidimensionalen Scramjet-Einlaufs mit hohem Verdichtungsverhältnis und variabler Innenkontraktion*, Ph.D. thesis, University of Stuttgart, Germany, 2014.
- ²¹⁶ Scheuermann, T., *Untersuchungen zur Verbrennung in einer SCRamjet-Brennkammer*, Ph.D. thesis, University of Stuttgart, Germany, 2010.
- ²¹⁷ Riccius, J., Haidn, O., and Zametaev, E., “Influence of Time Dependent Effects on the Estimated Life Time of Liquid Rocket Combustion Chamber Walls,”

- 40th AIAA/ASME/SAE/ASEE Joint Propulsion Conference and Exhibit*, American Institute of Aeronautics and Astronautics, Fort Lauderdale, FL, July 2004, doi: 10.2514/6.2004-3670.
- ²¹⁸ Jankovsky, R. S., Arya, V. K., Kazaroff, J. M., and Halford, G. R., “Structurally Compliant Rocket Engine Combustion Chamber: Experimental and Analytical Validation,” *JANNAF Propulsion Meeting*, Monterey, CA, Nov. 1993.
- ²¹⁹ Bronstein, I. N., Semendjajew, K. A., Musiol, G., and Mühlig, H., “Taschenbuch der Mathematik,” 2001.
- ²²⁰ Harald, H. and Weihs, H., “Development of a CMC Nose Cap System for X-38,” *International Symposium on Atmospheric Reentry Vehicles and Systems*, Arca-chon, France, 1999.
- ²²¹ Reimer, T. and Laux, T., “Thermal and Mechanical Design of the Expert C/C-SiC Nose,” *5th European Workshop on Thermal Protection Systems and Hot Structures*, Noordwijk, NL, May 2006.
- ²²² Krenkel, W., *Handbook of Ceramic Composites*, chap. Carbon Fibre Reinforced Silicon Carbide Composites (C/SiC, C/C-SiC), Kluwer Academic Publishers, Boston Dordrecht London, 2005, pp. 117–148.
- ²²³ Krenkel, W., *Handbuch Konstruktion*, chap. Konstruieren mit technischer Keramik, Carl Hanser Verlag GmbH & Co. KG, Munich, Germany, 2012, pp. 45–102.
- ²²⁴ Krenkel, W., “Cost Effective Processing of CMC Composites by Melt Infiltration (LSI-Process),” *25th Annual Conference on Composites, Advanced Ceramics, Materials, and Structures: A: Ceramic Engineering and Science Proceedings*, Vol. 22, No. 23, pp. 443–454, Jan. 2001, doi: 10.1002/9780470294680.ch52.
- ²²⁵ Reinartz, B. U., “Performance Analysis of a 3D Scramjet Intake,” *26th Congress of the International Council of the Aeronautical Sciences*, Anchorage, AK, Sept. 2008.
- ²²⁶ Tsai, S. W. and Wu, E. M., “A General Theory of Strength for Anisotropic Materials,” *Journal of Composite Materials*, Vol. 5, No. 1, pp. 58–80, Jan. 1971, doi: 10.1177/002199837100500106.
- ²²⁷ Fink, A., Dinkler, D., and Kröplin, B., “A Phenomenological Material Model for Fiber Reinforced Ceramics,” *Zeitschrift für Flugwissenschaften und Weltraumforschung*, Vol. 19, No. 3, pp. 197–204, Feb. 1995.

- ²²⁸ Dvorak, G., *Micromechanics of Composite Materials*, Vol. 186 of *Solid Mechanics and its Applications*, Springer Verlag, 2013.
- ²²⁹ Frauholz, S., Reinartz, B. U., Müller, S., and Behr, M., “Transition Prediction for Scramjets Using γ -Re θ t Model Coupled to Two Turbulence Models,” *Journal of Propulsion and Power*, Vol. 31, No. 5, pp. 1404–1422, Sept. 2015, doi: 10.2514/1.B35630.
- ²³⁰ Böhrk, H. and Beyermann, U., “Secure Tightening of a CMC Fastener for the Heat Shield of Re-Entry Vehicles,” *Composite Structures*, Vol. 92, No. 1, pp. 107–112, Jan. 2010, doi: 10.1016/j.compstruct.2009.07.002.
- ²³¹ Ullmann, T., Reimer, T., Hald, H., Zeiffer, B., and Schneider, H., “Reentry Flight Testing of a C/C-SiC Structure with Yttrium Silicate Oxidation Protection,” *14th AIAA/AHI Space Planes and Hypersonic Systems and Technologies Conference, AIAA 2006-8127*, American Institute of Aeronautics and Astronautics, Canberra, Australia, Nov. 2006, doi: 10.2514/6.2006-8127.
- ²³² Laux, T., Killinger, A., Auweter-Kurtz, M., Gadow, R., and Wilhelmi, H., “Functionally Graded Ceramic Materials for High Temperature Applications for Space Planes,” *Materials Science Forum*, Vol. 308-311, pp. 428–433, 1999, doi: 10.4028/www.scientific.net/MSF.308-311.428.
- ²³³ Messe, C., Kliche, D., Wallmersperger, T., Kröplin, B., and Mundt, C., “Modeling and Simulation of Heat Transfer on Functionally Graded Materials for Hot Structures in Scramjet Engines,” *10th AIAA/ASME Joint Thermophysics and Heat Transfer Conference*, American Institute of Aeronautics and Astronautics, Chicago, IL, July 2010, doi: 10.2514/6.2010-4896.
- ²³⁴ Meiss, J.-H., Schröder, W., and Meinke, M., “Numerical Investigation to Enhance the Thrust Vector of a Scramjet Nozzle,” *17th AIAA International Space Planes and Hypersonic Systems and Technologies Conference*, American Institute of Aeronautics and Astronautics, San Francisco, CA, April 2011, doi: 10.2514/6.2011-2346.
- ²³⁵ Argyris, J. H. and Willam, K. J., “Some Considerations for the Evaluation of Finite Element Models,” *Nuclear Engineering and Design*, Vol. 28, No. 1, pp. 76–96, July 1974, doi: 10.1016/0029-5493(74)90089-2.
- ²³⁶ Albrecht, J. and Collatz, L., “Zur numerischen Auswertung mehrdimensionaler Integrale,” *Zeitschrift für Angewandte Mathematik und Mechanik*, Vol. 38, No. 1-2, pp. 1–15, Jan. 1958, doi: 10.1002/zamm.19580380102.

- ²³⁷ Cowper, G. R., "Gaussian Quadrature Formulas for Triangles," *International Journal for Numerical Methods in Engineering*, pp. 405–408, April 1973, doi: 10.1002/nme.1620070316.
- ²³⁸ Hinton, E. and Campbell, J. S., "Local and Global Smoothing of Discontinuous Finite Element Functions Using a Least Squares Method," *International Journal for Numerical Methods in Engineering*, Vol. 8, No. 3, pp. 461–480, 1974, doi: 10.1002/nme.1620080303.
- ²³⁹ Reimer, T., "The EXPERT C/C-SiC Nose Cap - System Design and Thermomechanical Layout," *AIAA/CIRA 13th International Space Planes and Hypersonics Systems and Technologies Conference, AIAA 2005-3262*, American Institute of Aeronautics and Astronautics, Capua, Italy, May 2005, doi: 10.2514/6.2005-3262.
- ²⁴⁰ Krenkel, W., "From Polymer to Ceramics: Low Cost Manufacturing of Ceramic Matrix Composite Materials," *Molecular Crystals and Liquid Crystals Science and Technology. Section A. Molecular Crystals and Liquid Crystals*, Vol. 354, No. 1, pp. 353–364, Dec. 2000, doi: 10.1080/10587250008023627.
- ²⁴¹ Baumann, H. N., "The Relationship of Alpha and Beta Silicon Carbide," *Journal of The Electrochemical Society*, Vol. 99, No. 3, pp. 109–6, 1952, doi: 10.1149/1.2779671.
- ²⁴² Chambers, J. J. and Parsons, G. N., "Physical and Electrical Characterization of Ultrathin Yttrium Silicate Insulators on Silicon," *Journal of Applied Physics*, Vol. 90, No. 2, pp. 918–17, 2001, doi: 10.1063/1.1375018.
- ²⁴³ Dinkler, D., Fink, A., and Kröplin, B., "Constitutive Laws for Fibre Reinforced Ceramics," *5th International Aerospace Planes and Hypersonics Technologies Conference*, American Institute of Aeronautics and Astronautics, Munich, Germany, Nov. 1993, doi: 10.2514/6.1993-5038.
- ²⁴⁴ Hofmann, S., Öztürk, B., Koch, D., and Voggenreiter, H., "Experimental and Numerical Evaluation of Bending and Tensile Behaviour of Carbon-Fibre Reinforced SiC," *Composites Part A*, Vol. 43, No. 11, pp. 1877–1885, Nov. 2012, doi: 10.1016/j.compositesa.2012.07.017.
- ²⁴⁵ Breede, F., Frieß, M., Jemmali, R., Koch, D., Voggenreiter, H., Frenzel, V., and Drechsler, K., "Mechanical and Microstructural Characterization of C/C-SiC Manufactured via Triaxial and Biaxial Braided Fiber Preforms," *Mechanical Properties and Performance of Engineering Ceramics and Composites VI, 36th International Conference and Expo on Advanced Ceramics and Composites*, edited

- by D. Singh, J. Salem, M. Halbig, and S. Mathur, John Wiley & Sons, Inc., Hoboken, NJ, USA, Dec. 2012, pp. 183–194.
- ²⁴⁶ Eshelby, J. D., “The Determination of the Elastic Field of an Ellipsoidal Inclusion, and Related Problems,” *Proceedings of the Royal Society of London. Series A, Mathematical and Physical Sciences*, Vol. 241, pp. 376–396, Aug. 1957, doi: 10.1098/rspa.1957.0133.
- ²⁴⁷ Eshelby, J. D., “The Elastic Field Outside an Ellipsoidal Inclusion,” *Proceedings of the Royal Society of London. Series A, Mathematical and Physical Sciences*, Vol. 252, No. 1271, pp. 561–569, Oct. 1957.
- ²⁴⁸ Hill, R., “A Self-Consistent Mechanics of Composite Materials,” *Journal of the Mechanics and Physics of Solids*, Vol. 13, No. 4, pp. 213–222, Aug. 1965, doi: 10.1016/0022-5096(65)90010-4.
- ²⁴⁹ Itskov, M., “On the Theory of Fourth-Order Tensors and their Applications in Computational Mechanics,” *Computer Methods in Applied Mechanics and Engineering*, Vol. 189, No. 2, pp. 419–438, Sept. 2000, doi: 10.1016/S0045-7825(99)00472-7.
- ²⁵⁰ Suvorov, A. P. and Dvorak, G. J., “Rate form of the Eshelby and Hill tensors,” *International Journal of Solids and Structures*, Vol. 39, No. 21-22, pp. 5659–5678, Oct. 2002, doi: 10.1016/S0020-7683(02)00369-4.
- ²⁵¹ Gavazzi, A. C. and Lagoudas, D. C., “On the Numerical Evaluation of Eshelby’s Tensor and its Application to Elastoplastic Fibrous Composites,” *Computational Mechanics*, Vol. 7, No. 1, pp. 13–19, 1990, doi: 10.1007/BF00370053.
- ²⁵² Laws, N., “A Note on Penny-Shaped Cracks in Transversely Isotropic Materials,” *Mechanics of Materials*, Vol. 4, No. 2, pp. 209–212, June 1985, doi: 10.1016/0167-6636(85)90017-1.
- ²⁵³ Luo, J. and Stevens, R., “Micromechanics of Randomly Oriented Ellipsoidal Inclusion Composites. Part I: Stress, Strain and Thermal Expansion,” *Journal of Applied Physics*, Vol. 79, No. 12, pp. 9047–9056, 1996, doi: 10.1063/1.362638.
- ²⁵⁴ Luo, J. and Stevens, R., “Micromechanics of Randomly Oriented Ellipsoidal Inclusion Composites. Part II: Elastic Moduli,” *Journal of Applied Physics*, Vol. 79, No. 12, pp. 9057–9063, 1996, doi: 10.1063/1.362639.
- ²⁵⁵ Qu, J. and Cherkaoui, M., *Fundamentals of Micromechanics of Solids*, John Wiley & Sons, Inc., Hoboken, New Jersey, 1st ed., 2006.

- ²⁵⁶ Budiansky, B. and O'Connell, R. J., "Elastic Moduli of a Cracked Solid," *International Journal of Solids and Structures*, Vol. 12, No. 2, pp. 81–97, Jan. 1976, doi: 10.1016/0020-7683(76)90044-5.
- ²⁵⁷ de Kok, J. M. M., Meijer, H. E. H., and Peijs, A. A. J. M., "The Influence of Matrix Plasticity on the Failure Strain of Transversely Loaded Composite Materials," *9th International Conference on Composite Materials*, Madrid, Spain, July 1993, pp. 242–249.
- ²⁵⁸ Schulte-Fischedick, J., Seiz, S., Lützenburger, N., Wanner, A., and Voggenreiter, H., "The Crack Development on the Micro- and Mesoscopic Scale During the Pyrolysis of Carbon Fibre Reinforced Plastics to Carbon/Carbon Composites," *Composites Part A: Applied Science and Manufacturing*, Vol. 38, No. 10, pp. 2171–2181, Oct. 2007, doi: 10.1016/j.compositesa.2007.06.013.
- ²⁵⁹ Green, S. D., Matveev, M. Y., Long, A. C., Ivanov, D., and Hallett, S. R., "Mechanical Modelling of 3D Woven Composites Considering Realistic Unit Cell Geometry," *Composite Structures*, Vol. 118, No. C, pp. 284–293, Dec. 2014, doi: 10.1016/j.compstruct.2014.07.005.
- ²⁶⁰ Fink, A., *Ein Grenzflächenmodell zur Beschreibung des mechanischen Verhaltens faserverstärkter Keramiken*, Ph.D. thesis, Institute for Statics and Dynamics of Aerospace Structures, University of Stuttgart, Germany, 1995.
- ²⁶¹ Chamis, C. C., "Simplified Composite Micromechanics Equations for Strength, Fracture Toughness, Impact Resistance and Environmental Effects," Tech. Rep. NASA TM 83693, Cleveland, Ohio, Jan. 1984.
- ²⁶² Glass, D. E., Capriotti, D., Reimer, T., Küttemeyer, M., and Smart, M., "Testing of DLR C/C-SiC and C/C for HIFiRE 8 Scramjet Combustor," *19th AIAA International Space Planes and Hypersonic Systems and Technologies Conference*, American Institute of Aeronautics and Astronautics, Atlanta, GA, June 2014, doi: 10.2514/6.2014-3089.
- ²⁶³ Frieß, M., Krenkel, W., Kochendörfer, R., Brandt, R., Neuer, G., and Maier, H.-P., *Basic Research and Technologies for Two-Stage-to-Orbit Vehicles: Final Report of the Collaborative Research Centres 253, 255 and 259*, chap. High Temperature Materials and Hot Structures, Sonderforschungsberichte der Deutschen Forschung, John Wiley and Sons, Inc., Weinheim, Germany, 2006, pp. 499–580.
- ²⁶⁴ Narayanaswami, R. and Adelman, H. M., "Evaluation of the Tensor Polynomial and Hoffman Strength Theories for Composite Materials," *Journal of Composite Materials*, Vol. 11, No. 4, pp. 366–377, Oct. 1977, doi: 10.1177/002199837701100401.

- ²⁶⁵ Krenkel, W., *Keramische Verbundwerkstoffe*, WILEY-VCH Verlag GmbH, Weinheim, 1st ed., 2003.
- ²⁶⁶ Brandt, R., Frieß, M., and Neuer, G., “Thermal Conductivity, Specific Heat Capacity, and Emissivity of Ceramic Matrix Composites at High Temperatures,” *High Temperatures-High Pressures*, Vol. 35/36, No. 2, pp. 169–177, 2003, doi: 10.1068/htjr105.
- ²⁶⁷ Sutherland, W., “The Viscosity of Gases and Molecular Force,” *Philosophical Magazine Series 5*, Vol. 36, No. 223, pp. 507–531, Dec. 1893, doi: 10.1080/14786449308620508.
- ²⁶⁸ Hansen, C. F., “Approximations for the Thermodynamic and Transport Properties of High-Temperature Air,” Tech. Rep. NACA TN-4150, March 1958.
- ²⁶⁹ Anderson, B. H., “Design of Supersonic Inlets by a Computer Program Incorporating the Method of Characteristics,” Tech. Rep. NASA-TN-D-4960, NASA Lewis Research Center, Cleveland, OH, Jan. 1969.
- ²⁷⁰ Billig, F. S., “Shock-Wave Shapes around Spherical- and Cylindrical-Nosed Bodies.” *Journal of Spacecraft and Rockets*, Vol. 4, No. 6, pp. 822–823, June 1967, doi: 10.2514/3.28969.
- ²⁷¹ Ambrosio, A. and Wortmann, A., “Stagnation Point Shock Detachment Distance for Flow Around Spheres and Cylinders,” *ARS Journal*, Vol. 32, No. 2, pp. 281, 1962, doi: 10.2514/8.5988.
- ²⁷² Oswatitsch, K., “Pressure Recovery for Missiles with Reaction Propulsion at High Supersonic Speeds,” Tech. Rep. NACA-TM-1140, National Advisory Committee for Aeronautics, July 1947.
- ²⁷³ Kantrowitz, A. and Donaldson, C. d., “Preliminary Investigation of Supersonic Diffusers,” Tech. Rep. NACA-ACR-L5D20, National Advisory Committee for Aeronautics, Langley Field, VA, May 1945.
- ²⁷⁴ Waltrup, P. J. and Billig, F. S., “Prediction of Precombustion Wall Pressure Distributions in Scramjet Engines,” *Journal of Spacecraft and Rockets*, Vol. 10, No. 9, pp. 620–622, Sept. 1973, doi: 10.2514/3.27782.
- ²⁷⁵ Hirschel, E. H. and Weiland, C., *Selected Aerothermodynamic Design Problems of Hypersonic Flight Vehicles*, Vol. 229 of *Progress in Astronautics and Aeronautics*, Springer International Publishing, Heidelberg, Germany, 2009.

- ²⁷⁶ Jachimowski, C. J., “An Analytical Study of the Hydrogen-Air Reaction Mechanism with Application to Scramjet Combustion,” Tech. Rep. NASA-TP-2791, Hampton, VA, Feb. 1988.
- ²⁷⁷ Wilson, G. J. and MacCormack, R. W., “Modeling Supersonic Combustion using a Fully Implicit Numerical Method,” *AIAA Journal*, Vol. 30, No. 4, pp. 1008–1015, April 1992, doi: 10.2514/3.11021.
- ²⁷⁸ Scheuermann, T., Chun, J., and von Wolfersdorf, J., “One-Dimensional Modelling of a Scramjet Combustor Reacting Flow,” *15th AIAA International Space Planes and Hypersonic Systems and Technologies Conference*, American Institute of Aeronautics and Astronautics, Dayton, OH, April 2008, doi: 10.2514/6.2008-2643.

ISBN 978-3-942807-05-0